

2013-08-01

Catalytic Applications of Bio-inspired Nanomaterials

Dennis Kien B. Pacardo

University of Miami, d.pacardo@umiami.edu

Follow this and additional works at: https://scholarlyrepository.miami.edu/oa_dissertations

Recommended Citation

Pacardo, Dennis Kien B., "Catalytic Applications of Bio-inspired Nanomaterials" (2013). *Open Access Dissertations*. 1074.
https://scholarlyrepository.miami.edu/oa_dissertations/1074

This Open access is brought to you for free and open access by the Electronic Theses and Dissertations at Scholarly Repository. It has been accepted for inclusion in Open Access Dissertations by an authorized administrator of Scholarly Repository. For more information, please contact repository.library@miami.edu.

UNIVERSITY OF MIAMI

CATALYTIC APPLICATIONS OF BIO-INSPIRED NANOMATERIALS

By

Dennis Kien Balaong Pacardo

A DISSERTATION

Submitted to the Faculty
of the University of Miami
in partial fulfillment of the requirements for
the degree of Doctor of Philosophy

Coral Gables, Florida

August 2013

©2013
Dennis Kien Balaong Pacardo
All Rights Reserved

UNIVERSITY OF MIAMI

A dissertation submitted in partial fulfillment of
the requirements for the degree of
Doctor of Philosophy

CATALYTIC APPLICATIONS OF BIO-INSPIRED NANOMATERIALS

Dennis Kien Balaong Pacardo

Approved:

Marc R. Knecht, Ph.D.
Professor of Chemistry

M. Brian Blake, Ph.D.
Dean of the Graduate School

Francisco M. Raymo, Ph.D.
Professor of Chemistry

Norito Takenaka, Ph.D.
Professor of Chemistry

Sung Jin Kim, Ph.D.
Professor of Electrical and
Computer Engineering

PACARDO, DENNIS KIEN BALAONG
Catalytic Applications of Bio-inspired Nanomaterials

(Ph.D., Chemistry)
(August 2013)

Abstract of a dissertation at the University of Miami.

Dissertation supervised by Professor Marc R. Knecht.
No. of pages in text. (193)

The biomimetic synthesis of Pd nanoparticles was presented using the Pd4 peptide, TSNAVHPTLRHL, isolated from combinatorial phage display library. Using this approach, nearly monodisperse and spherical Pd nanoparticles were generated with an average diameter of 1.9 ± 0.4 nm. The peptide-based nanocatalyst were employed in the Stille coupling reaction under energy-efficient and environmentally friendly reaction conditions of aqueous solvent, room temperature and very low catalyst loading. To this end, the Pd nanocatalyst generated high turnover frequency (TOF) value and quantitative yields using ≥ 0.005 mol% Pd as well as catalytic activities with different aryl halides containing electron-withdrawing and electron-donating groups. The Pd4-capped Pd nanoparticles followed the atom-leaching mechanism and were found to be selective with respect to substrate identity. On the other hand, the naturally-occurring R5 peptide (SSKKSYSYSGSKGSKRRIL) was employed in the synthesis of biotemplated Pd nanomaterials which showed morphological changes as a function of Pd:peptide ratio. TOF analysis for hydrogenation of olefinic alcohols showed similar catalytic activity regardless of nanomorphology. Determination of catalytic properties of these bio-inspired nanomaterials are important as they serve as model system for alternative green catalyst with applications in industrially important transformations.

To my parents, Mr. Eriberto Pacardo and Mrs. Evelyn Pacardo.

Acknowledgments

As my graduate school career comes to a close, I would like to express my gratitude and appreciation to a lot of people who shared their knowledge, experiences, time, love and acts of kindness.

First and foremost, a big thank you to my research adviser, Dr. Marc R. Knecht, for giving me a chance to work in his research group, for his mentorship, motivation and guidance. I would also like to thank the members of my graduate committee, Dr. Francisco M. Raymo, Dr. Norito Takenaka and Dr. Sung Jin Kim for sharing their valuable expertise. I would also like to acknowledge our research collaborators Dr. Joseph M. Slocik and Dr. Rajesh R. Naik. To my awesome co-worker, roommate and friend, Rohit Bhandari, thank you very much for your encouragement, support and understanding. To the other members of the lab, Nicholas Bedford, Nicholas Merrill, Beverly Briggs, Michelle Nguyen, Andy Tang, Randy Lawrence, Ryan Coppage and Manish Sethi, thank you for making the lab environment fun.

I would also like to express my appreciation to my friends Nick Caraquel, Major Gooyit, Reyna Lim and Nikki Magdaong for their support and sense of humor. I would also like to thank my mentor, Dr. Titos Quibuyen for encouraging me to pursue graduate studies.

Lastly, I would like to thank my family, Michael Louie Pacardo, Shyla Joy Pacardo and most of all my beloved parents, Mr. Eriberto Pacardo and Mrs. Evelyn Pacardo for their unconditional love and support. *Maraming salamat po!*

TABLE OF CONTENTS

	Page
List of Figures	ix
List of Tables	xii
List of Abbreviations	xiii
Summary.....	1
Chapter 1: Introduction	6
1.1 Metal-catalyzed C-C Coupling Reactions	6
1.2 Synthetic Scheme for the Fabrication of Pd Nanoparticles	10
1.3 C-C Coupling Reaction Mechanism for Pd Nanocatalyst	12
1.4 Pd Nanoparticles in Stille Coupling Reaction	25
1.5 Pd Nanoparticles in Suzuki Coupling Reaction	35
1.6 Pd Nanoparticles in Heck Coupling Reaction	50
1.7 Summary and Conclusions	58
Chapter 2: Biomimetic Synthesis of Green Pd Nanocatalyst for the Stille Coupling Reaction	60
2.1 Overview of Study	60
2.2 Motivation	60
2.3 Methods	64
2.3.1 Chemicals	64
2.3.2 Peptide Synthesis	64

2.3.3 Preparation of Pd Nanoparticle	65
2.3.4 Catalytic Reactions	65
2.3.5 TOF Measurements	66
2.3.6 Characterization	66
2.4 Results and Discussion	67
2.5 Summary and Conclusions	80
Chapter 3: Interrogating the Catalytic Mechanism of Nanoparticle Mediated Stille Coupling Reactions Employing Bio-inspired Pd Nanocatalysts	82
3.1 Overview of Study	82
3.2 Motivation	83
3.3 Methods	87
3.3.1 Chemicals	87
3.3.2 Preparation of Pd Nanoparticles	88
3.3.3 TOF Measurements	89
3.3.4 Temperature Controlled Stille Coupling	90
3.3.5 Effects of the Transmetalation Agent	90
3.3.6 QCM Analysis	91
3.4 Results and Discussion	91
3.5 Summary and Conclusions	107
Chapter 4: Exploring the Mechanism of Stille C-C Coupling via Peptide-capped Pd Nanoparticles Results in Low Temperature Reagent Selectivity	109

4.1 Overview of Study	109
4.2 Motivation	109
4.3 Methods	113
4.3.1 Chemicals	113
4.3.2 Characterization	114
4.3.3 Catalytic Reactions with Multiple Aryl Halides	115
4.3.4 Aryl Dihalide Reactivity	116
4.4 Results and Discussion	117
4.5 Summary and Conclusions	133
Chapter 5: Probing the Selectivity of Peptide-templated Pd Nanoparticles as Catalyst for Hydrogenation of Olefinic Alcohols	135
5.1 Overview of Study	135
5.2 Motivation	136
5.3 Methods	140
5.3.1 Chemicals	140
5.3.2 Synthesis of Peptide-templated Pd Nanoparticles	141
5.3.3 Catalytic Hydrogenation Reaction	141
5.3.4 Characterization and Retention Factor Determination	142
5.4 Results and Discussion	142
5.5 Summary and Conclusions	158

Chapter 6: Additional Information	160
6.1 Additional Information to Chapter 2	160
6.2 Additional Information to Chapter 5	175
6.2.1 Calculations for 4-penten-1-ol	175
6.2.2 Calculations for stepwise hydrogenation	176
References	178

List of Figures

Figure 1.1 General mechanism of Pd-catalyzed C-C coupling	7
Figure 1.2 Select Pd-catalyzed C-C coupling reactions	8
Figure 1.3 Photograph and schematic diagram of a two-component reactor.....	13
Figure 1.4 Transfer mechanisms for leached Pd species	16
Figure 1.5 Illustration of crystallinity changes for Pd and Au-Pd nanoparticles	17
Figure 1.6 Characterization of Pd nanoparticles before and after catalysis	19
Figure 1.7 Diagram of XAS reaction set up and TOF analysis for Suzuki reaction	22
Figure 1.8 Synthesis of dendrimer-encapsulated Pd nanoparticles for Stille reaction	27
Figure 1.9 Synthesis of GnDenP-Pd nanoparticles and their use in Stille reaction	30
Figure 1.10 Synthesis and TEM images of R5-templated Pd nanoparticles networks	33
Figure 1.11 SEM and TEM images of Pd PANI nanoparticles in Suzuki reaction	41
Figure 1.12 Suzuki reaction using dendritic bromobenzene as substrate	48
Figure 1.13 CD-capped Pd nanoparticles for Suzuki coupling reaction	50
Figure 1.14 Scheme of the Pd complex immobilized inside the dendrimer	54
Figure 2.1 Synthetic scheme of Pd ₄ -capped Pd nanoparticles in Stille reaction	63
Figure 2.2 UV-vis spectra of Pd ₄ -capped Pd nanoparticles	69
Figure 2.3 TEM analysis of Pd ₄ -capped Pd nanoparticles	70
Figure 2.4 Characterization of the products of Stille coupling reaction	73
Figure 2.5 Analysis of catalytic activity of Pd ₄ -capped Pd nanoparticles	75
Figure 3.1 Schematic diagram of the atom-leaching mechanism	84
Figure 3.2 TEM and HRTEM images of Pd ₄ -capped Pd nanoparticles	92
Figure 3.3 TOF analysis using different Pd nanoparticle loadings	93

Figure 3.4 Effects of temperature on catalytic activity of Pd nanoparticles	94
Figure 3.5 UV-vis and TEM analysis of Pd nanoparticles at 70°C	98
Figure 3.6 Reactivity analysis using divinyl trichloride	99
Figure 3.7 QCM analysis showing particle leaching	106
Figure 4.1 Scheme for reagent selectivity of peptide-capped Pd nanoparticles	111
Figure 4.2 Results of competition experiment using iodo- and bromobenzoic acid	118
Figure 4.3 Time-resolved analysis of Stille coupling using Pd nanoparticles	121
Figure 4.4 Reaction scheme for Stille coupling using 3-bromo-5-iodobenzoic acid	125
Figure 4.5 Reaction scheme for Stille coupling using 3,5-diiodobenzoic acid	128
Figure 5.1 TEM analysis of biotemplated Pd nanomaterials	143
Figure 5.2 Isomerization of olefinic alcohols	147
Figure 5.3 TOF analysis of competition hydrogenation reactions	149
Figure 5.4 Reaction scheme for hydrogenation of 1,4-pentadien-3-ol	154
Figure 5.5 Reaction scheme for hydrogenation of 3-methyl-1-pentyn-3-ol	156
Figure 6.1 TEM image of R5-templated Pd nanoparticles	160
Figure 6.2 Characterization of Stille coupling products using 4-iodobenzoic acid	161
Figure 6.3 Characterization of Stille coupling products using 3-iodobenzoic acid	162
Figure 6.4 Characterization of Stille coupling products using 2-iodobenzoic acid	163
Figure 6.5 Characterization of Stille coupling products using 4-bromobenzoic acid	164
Figure 6.6 Characterization of Stille coupling products using 4-bromobenzoic acid after 7 days and 0.10mol% Pd	165
Figure 6.7 Characterization of Stille coupling products using 4-bromobenzoic acid after 3 days and 0.50mol% Pd	166

Figure 6.8 Characterization of Stille coupling products using 4-bromobenzoic acid after 7 days and 0.50mol% Pd	167
Figure 6.9 Characterization of Stille coupling products using 4-chlorobenzoic acid	168
Figure 6.10 Characterization of Stille coupling products using 4-iodophenol	169
Figure 6.11 Characterization of Stille coupling products using 4-bromophenol after 3 days and 0.10mol% Pd	170
Figure 6.12 Characterization of Stille coupling products using 4-bromophenol after 7 days and 0.10mol% Pd	171
Figure 6.13 Characterization of Stille coupling products using 4-bromophenol after 3 days and 0.50mol% Pd	172
Figure 6.14 Characterization of Stille coupling products using 4-bromophenol after 7 days and 0.50mol% Pd	173
Figure 6.15 Characterization of Stille coupling products using 4-chlorophenol	174
Figure 6.16 Characterization of Stille coupling products in ethanol/KOH	174

List of Tables

Table 1 Pd binding peptides isolated via phage display	68
Table 2 Stille coupling reactions using Pd ₄ -capped Pd nanoparticles	77
Table 3 Aryl dihalides substrates for Stille coupling reactions	124
Table 4 Effect of halogen group positions in Stille coupling reactions	130
Table 5 TOF analysis for hydrogenation of olefinic alcohols	144

List of Abbreviations

Abbreviation	Definition
BC	bacterial cellulose
BPCA	biphenylcarboxylic acid
CD	cyclodextrin
CN	coordination number
DEN	dendrimer encapsulated nanoparticle
DME	dimethoxyethane
DMF	dimethylformamide
DSN	dendrimer stabilized nanoparticle
DVT	divinyltin dichloride
EDX	energy dispersive x-ray
EXAFS	extended x-ray absorption fine structure
FMOCl	fluorenylmethyloxycarbonyl chloride
GC-FID	gas chromatography – flame ionization detector
GC-MS	gas chromatography – mass spectrometry
HRTEM	high resolution transmission electron microscopy
ICP	inductively coupled plasma
ICP-AES	inductively coupled plasma – atomic emission spectrometry
ICP-MS	inductively coupled plasma – mass spectrometry
ICP-XRF	inductively coupled plasma – x-ray fluorescence
MALDI – TOF	matrix assisted laser desorption/ionization – time-of-flight

MSTFA	<i>N</i> -methyl- <i>N</i> -(trimethylsilyl)trifluoroacetamide
NMR	nuclear magnetic resonance
NPN	nanoparticle network
PAMAM	poly(amido amine)
PANI	polyaniline
PC	propylene carbonate
PEG	polyethylene glycol
PPI	poly(propylene imine)
PVP	polyvinyl pyrrole
QCM	quartz crystal microbalance
SAED	selected area electron diffraction
SEM	scanning electron microscopy
TBP	4- <i>t</i> -butylphenol
TEM	transmission electron microscopy
TLC	thin layer chromatography
TOAG	tetraoctylammonium glycolate
TOF	turnover frequency
TON	turnover number
VBA	4-vinylbenzoic acid
XAS	x-ray absorption spectroscopy
XPS	x-ray photoelectron spectroscopy

Summary

The main objective of my research is to study the catalytic applications of peptide-capped and peptide-templated Pd nanoparticles in ambient reaction conditions. Taking inspiration from nature, the biomimetic synthesis of Pd nanoparticles was achieved by exploiting the biotic/abiotic interactions between biological molecules and inorganic metals. From these interactions, binding of Pd metal precursor was achieved through the amino- and/or carboxylic groups of naturally occurring peptides and those isolated through phage display technique. In this report, the peptide-based Pd nanoparticles were employed as catalyst for Stille carbon-carbon (C-C) coupling reactions using aryl halides and hydrogenation of olefinic alcohols in energy-neutral and environmentally-friendly reaction conditions. These transformations are widely studied due to their applications in a variety of industrially relevant processes specifically, the synthesis of new materials, pharmaceuticals, and natural products. The Pd catalyzed C-C coupling reactions were developed several decades ago by pioneering researchers namely Heck, Suzuki and Negishi who were awarded the 2010 Nobel Prize in Chemistry. Since then, these reactions were modified and improved by other researchers such as Stille, Sonogashira and Kumada who also made significant contributions to the development of Pd-catalyzed reactions. Although the C-C coupling reactions were efficient and widely applicable, the reaction conditions, which include the use of toxic organic solvents, high temperatures and large catalyst loading, need to be improved in order to lessen their ecological impact and utilization of limited resources. Thus, with the advent of nanotechnology, novel synthetic methods allow the production of new Pd nanocatalysts with unique properties

and applications. These nanomaterials were employed for different C-C coupling reactions under mild conditions such as aqueous solution, room temperature and low catalyst loading. The synthetic processes, and applications of different Pd nanoparticles for C-C bond formation were described in **Chapter 1**, together with a brief history of the pioneering works of Heck, Suzuki, Negishi, Stille and Sonogashira. Moreover, the two proposed catalytic mechanisms for Pd nanoparticles namely, surface-based reaction and atom-leaching mechanisms, were also discussed using recently published literatures.

Initial study on the role of peptides as stabilizers for the biomimetic synthesis of Pd nanoparticles was done using the Pd4 peptide (TSNAVHPTLRHL) isolated using phage display technique. Computational studies revealed that the histidine residues at positions 6 and 11 in the sequence bind strongly to the Pd metal surface. These binding conformation allow stabilization of the nanoparticles as well as provide an open space for substrate interaction in catalysis. UV-vis and TEM analyses revealed the formation of peptide-capped Pd nanoparticles with average diameter of 1.9 ± 0.4 nm which is ideal for catalytic applications. As such the Pd4-Pd nanoparticles were used for Stille coupling reaction between aryl halides and organostannane reagent under ambient conditions of aqueous solution, room temperature and low catalyst loading. The results of the synthesis, characterization and catalytic applications of peptide-capped Pd nanoparticles were thoroughly discussed in **Chapter 2**. Characterization of the products of Stille coupling reaction using ^1H NMR and GC-MS were also presented in this chapter with additional information on **Chapter 6**.

Once the catalytic applications of Pd4-capped Pd nanoparticles were established, the reaction mechanism was then explored using TOF measurements at different catalyst

loadings. In this project, the results showed that the TOF values decrease as we increase the concentration of the catalyst in the reaction. This suggests an atom-leaching mechanism wherein the catalytically active Pd atom was abstracted from the nanoparticle surface during oxidative addition. After the initial catalytic cycle, the Pd atom can again catalyze the remaining substrates or it can be quenched at the nanoparticle surface or it can combine with other Pd atoms and precipitate out as Pd black. Results indicate that at higher catalyst loading, formation of Pd black occurs at a higher rate thereby decreasing the TOF values obtained. QCM analysis corroborated the results of the TOF analysis wherein the presence of 4-iodobenzoic acid lead to the decrease in the mass of Pd-coated gold chip indicating leaching of Pd atoms. The effect of elevated temperatures on the reactivity of the nanocatalyst in Stille coupling reaction was also investigated using less active substrate, 4-bromobenzoic acid. Results showed that a mild temperature increase to 40°C significantly increases the reactivity of the catalyst generating ~ 75% yield of the product after 24 h. Control reactions involving UV-vis and TEM analyses showed that the peptide-capped Pd nanoparticles were stable at elevated temperature of 70°C. These results, together with the effects of changing the transmetalation reagent, were presented in **Chapter 3**. With the catalytic application and reaction mechanism established for the peptide-capped Pd nanoparticles, the selectivity of the catalyst was then investigated.

Initially, the fate of the Pd atoms after the initial catalytic cycle was probed by using a competition reaction between two aryl halide substrates, 4-iodobenzoic acid and 4-bromobenzoic acid. However, results showed that at room temperature only the iodo-substrate undergoes coupling reaction while the bromo-substrate required thermal activation at 40°C for reactivity. 4-Chlorobenzoic acid was also used in competition with

iodo- and bromo-substrates but it does not show any reactivity at the given reaction conditions. Thus, the selectivity of the peptide-capped Pd nanoparticles was established as a function of substrate identity wherein iodo-substrates were highly reactive at room temperature while bromo-substrates required mild heating and chloro-substrates did not react at all. These results were in accordance with the strength of the carbon-halogen bond wherein $C-I < C-Br < C-Cl$. These *intermolecular* competition reactions were fully described and presented in **Chapter 4**. Furthermore, the *intramolecular* competition reactions between two different halide groups were also explored using aryl dihalide substrates. The results showed similar reactivity trends as with the intermolecular systems with regards to halide identity but changes in the electronics of aryl ring presented interesting catalytic results.

Another peptide sequence was used for the synthesis of Pd nanoparticles. The naturally occurring R5 peptide, SSKKSGSYSGSKGSKRRIL, was extracted from the cell walls of diatoms responsible for precipitation of silica. In this peptide, the –RRIL motif self-assembles in solution forming a bioscaffold that can serve as template for nanoparticle formation. Interestingly, the size and shape of Pd nanoparticles formed in the R5 template varies as the Pd:peptide ratio was changed from spherical nanoparticles for Pd60, to nanoribbons for Pd90 and nanoparticle networks for Pd120. These R5-templated Pd nanoparticles were then used for catalytic hydrogenation of different olefinic alcohols at room temperature. The results were shown in **Chapter 5**, wherein statistically similar TOF values were obtained for each alcohol substrates regardless of particle morphology. Interestingly, higher average TOF values were obtained for secondary and tertiary alcohols compared with primary alcohols. These results were due to the high degree of

isomerization in primary alcohols, impeding the formation of hydrogenated product. On the other hand, only moderate amounts of isomers were formed for secondary alcohols while no isomerization was observed for tertiary alcohols. Competition reactions using allyl alcohol against another olefinic alcohols were also performed. In these experiments, the R5-templated Pd nanoparticles exhibited non-specific catalytic activity wherein both substrates simultaneously react during the hydrogenation reaction. However, the effects of isomerization and substrate molecular size, altered the TOF values obtained in the competition reaction compared when the substrates were hydrogenated separately. Finally, the biotemplated Pd nanoparticles showed stepwise reaction mechanism for the hydrogenation of substrates with two reactive centers.

Chapter 1. Introduction

1.1 Metal-catalyzed C-C Coupling Reactions

Transition metals have played an important role in synthetic chemistry as they have the unique capacity of activating various organic compounds towards chemical transformation and/or generation of new bonds. As such, organic ligand-stabilized metal catalysts based on Mg,¹⁻⁴ Fe,⁵⁻⁹ Ni,¹⁰⁻¹⁶ Au,¹⁷⁻²³ Ag,²⁴⁻³⁰ Pd,³¹⁻⁴² and Pt⁴³⁻⁴⁹ have been synthesized to afford industrially important transformations such as carbon-carbon (C-C) coupling reactions, alkylation, hydrogenation, oxygen and nitro-group reduction, and carbon dioxide oxidation. These reactions, however, typically involve the use of organic solvents, high temperatures, and high metal loadings. Furthermore, these processes also produce toxic by-products and are becoming economically unsustainable and environmentally unviable.^{50, 51} As such, new processes are being developed to reduce the energy consumption and ecological impact of these reactions that are essential to maintain current technological advances.⁵²

One reaction that has garnered significant attention over the past decade is the C-C coupling reaction using Pd-based catalysts due to its applications in pharmaceutical, natural products, and materials synthesis.⁵³⁻⁵⁶ The coupling reaction, shown in Figure 1.1, typically involves the formation of a new C-C bond between an electrophile (usually an aryl or vinyl halide) and a nucleophile (either an olefin or organometallic reagent), using zerovalent Pd metal to drive the reaction. The first step in the coupling is oxidative

addition wherein Pd^0 reacts with the electrophile by insertion between the C-X bond to form an organopalladate complex, oxidizing the Pd^0 to Pd^{2+} . The nucleophilic component will then attack the organopalladate complex either through transmetalation or alkene insertion, positioning the two carbon groups closer to each other on the metal surface. After reductive elimination, the new C-C bond is formed, the product is released, and the Pd^{2+} is reduced back to Pd^0 .

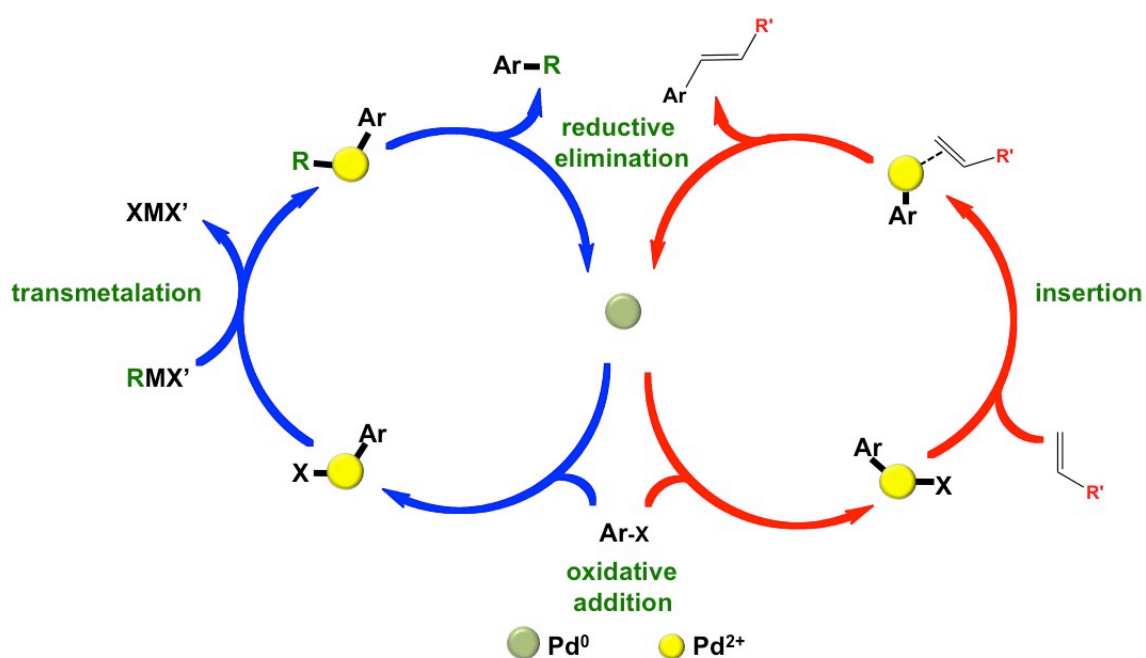


Figure 1.1 General mechanism of Pd-catalyzed C-C coupling reactions.

The modern use of Pd catalysts for C-C coupling reactions was pioneered by Heck with the publication of his work in 1972 on Pd-catalyzed arylation of olefins to produce substituted olefinic compounds.⁵⁷ In this reaction, catalytic quantities of Pd were used to form new C-C bonds between aromatic and olefinic compounds producing a standard protocol for metal-catalyzed coupling reactions.⁵⁷ For many years thereafter, several Pd-

catalyzed coupling reactions (Figure 1.2)^{52, 58} were developed by different groups by modifying the nucleophilic component of the reaction. Sonogashira used alkynes instead

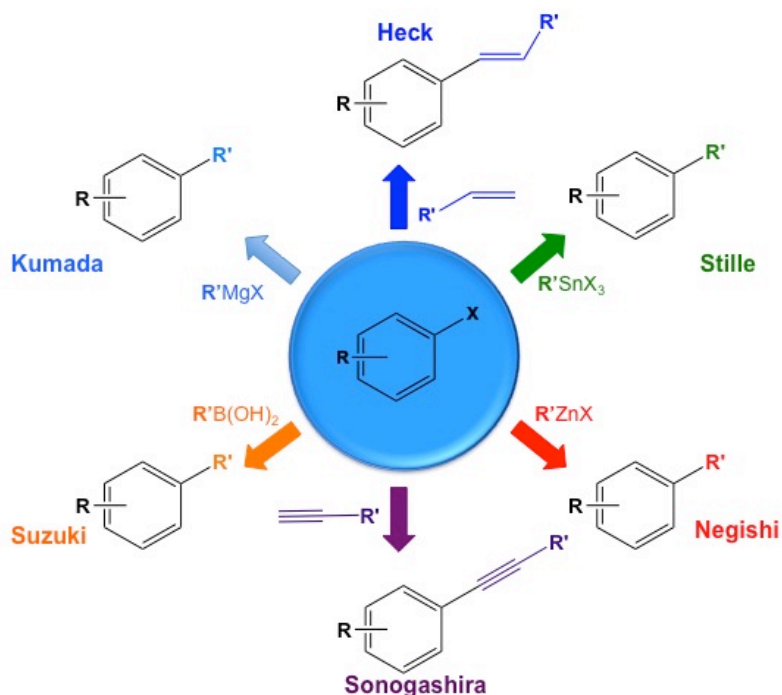


Figure 1.2 Select Pd-catalyzed C-C coupling reactions.

of alkenes for cross-coupling reactions with aryl halides.⁵⁹ Stille, on the other hand, initiated the use of organometallic reagents as the nucleophile by using organostannane compounds for the Pd-catalyzed coupling reaction with aryl halides;⁶⁰ however, the toxic nature of tin compounds limited their large-scale use. As an alternative to tin reagents, less toxic organometallic compounds such as organozinc was used by Negishi in the coupling reaction generating a mild and highly selective transmetalation agent that can tolerate a variety of functional groups.⁶¹ Kumada used organomagnesium reagents for transmetalation,⁶² although the highly reactive Grignard reagent also restricted their applications to a selection of functionalities. As an alternative to highly toxic tin and

highly reactive Grignard transmetalation agents, Suzuki developed boron-based organometallic reagents for coupling reactions with aryl halides,^{63, 64} generating a non-toxic and practical alternative that can be used under mild reaction conditions. In this reaction, activation of organoboron by a base is required to produce the boronate intermediate that initiates transmetalation, where a wide variety of functional groups can be employed.

The importance of Pd-catalyzed C-C coupling reactions in organic and material synthesis, as well as industrial applications, was recognized by the 2010 Nobel Prize in Chemistry for the pioneering works of Heck, Suzuki, and Negishi.^{65, 66} In more recent times, technological advancements have led to novel synthetic approaches for producing highly active Pd catalysts by using different types of organic-based stabilizers that can control the reactivity and selectivity of the metal catalyst. Furthermore, these new Pd materials have unique characteristics and properties that enable their use in catalytic transformations for a wide array of applications in material,⁶⁷⁻⁶⁹ natural products,⁷⁰⁻⁷⁵ and pharmaceutical synthesis.^{54, 76, 77}

With the advent of nanotechnology, new synthetic strategies for the generation of Pd nanocatalysts have been developed with particular emphasis on the control of the particle size, shape, and functionality.⁷⁸⁻⁸³ Since nanomaterials encompass the gap between the atomic level and bulk materials, interesting physical, chemical, electronic, and optical properties can be obtained,^{81, 84, 85} thereby generating a new class of structures for specific applications. Modern synthetic methods allow for the production of nanosized catalysts with optimized surface-to-volume ratios, allowing for more efficient catalytic reactivity as compared to traditional small molecule materials. The use of Pd nanoparticles for C-C

catalysis marks a transition from using traditional organic solvent-based and high temperature reactions toward more ambient conditions such as aqueous solutions, mild temperatures, and low catalyst loadings.⁸⁶⁻⁸⁸ This is achieved by employing highly functionalized stabilizers such as dendrimers,^{33, 86, 89-93} proteins,³¹ peptides,^{87, 88, 94} and other small molecules.⁹⁵⁻⁹⁸ These materials allow for size-specific interactions, as well as control over the nanoparticle shape, thereby generating solution stability, but at the same time exposing active sites for interaction with substrates.

This chapter will cover select recent advances regarding the use of Pd nanoparticles for C-C coupling reactions. Due to the large volume of work done in this area, this report will mostly focus on homogeneous Pd nanoparticles; however, it will not discuss bimetallic catalysts for coupling reactions. Emphasis will be given to Pd nanoparticles used in energy-efficient and environmentally benign catalytic reactions, as well as information regarding their catalytic mechanisms.

1.2 Synthetic Scheme for the Fabrication of Pd nanoparticles

There are several common methods employed for the synthesis of Pd nanoparticles such as chemical reduction,^{37, 38, 86, 94} vapor phase deposition,⁹⁹⁻¹⁰¹ laser ablation,¹⁰²⁻¹⁰⁵ sonochemical reduction,¹⁰⁶⁻¹¹⁰ electrochemical methods,^{39, 111-113} seed-mediated approaches,^{35, 114} and microwave reduction.^{40, 115-117} For this review, however, we will focus on the chemical reduction approach, which typically involves the use of metal salts as a precursor, organic and/or biological ligands as surface passivants, and a reductant to reduce the metal ions to the zerovalent state. Using this method, the metal precursor,

which is usually K_2PdCl_4 ⁸⁸ or K_2PdCl_6 ,¹¹⁸ is dissolved in aqueous solution and added to a separate ligand solution. In this process, the interaction of metal ions and ligands can lead to a ligand-to-metal charge transfer band in UV-vis analysis.^{88, 119, 120} Upon addition of a reducing agent, typically $NaBH_4$, the metal ions are reduced to form metallic Pd nanoparticles as evidenced by the formation of dark brown solution with a broad absorbance spectrum.^{86, 88, 94} During the reduction process, several nucleation sites are generated, thus resulting in rapidly growing nanoparticles that can ripen and precipitate as bulk metal in the absence of stabilizing agents. As such, the ligands present in the reaction prevent particle agglomeration and control the size and shape of the resulting nanoparticles. By design, these stabilizing agents do not completely coat the nanoparticles, which, therefore, allows for surface accessibility by the substrates in the reaction; however, the porous network of ligands can also be designed control access to the metal surface to develop catalytic selectivity. Commonly used stabilizers in Pd nanoparticle synthesis are amine-,¹²¹⁻¹²³ thiol-,¹²⁴⁻¹²⁷ and phosphorus-based ligands,¹²⁸⁻¹³⁰ polymers,^{34, 38, 96, 97} dendrimers,^{86, 89, 90, 92, 119} surfactants,¹³¹⁻¹³³ ionic liquids,¹³⁴⁻¹³⁷ and biomacromolecules such as peptides.^{87, 88, 94}

While this method has produced a variety of homogeneous nanocatalysts for different C-C coupling reactions, their wide scale application in industry has not yet been realized due to the difficulty in recovering and recycling of the catalyst. In this regard, attaching the nanoparticles to a solid support offers an alternative process for easier catalyst recovery and recyclability. Although there are many advantages for homogeneous catalysts such as efficiency and selectivity,¹³⁸⁻¹⁴⁰ supported nanocatalysts can be more practical, easily separated, and cost-effective in large-scale use. They also greatly reduce

the amount of metal impurities in the isolated products, thus lowering the degree of separation required post reaction. Solid supports such as carbon nanotubes,¹⁴¹⁻¹⁴⁴ metal oxides,¹⁴⁵⁻¹⁴⁸ silica,¹⁴⁹⁻¹⁵¹ alumina,¹⁵²⁻¹⁵⁴ zeolites,¹⁵⁵⁻¹⁵⁷ clays,¹⁵⁸ polymer coatings,¹⁵⁹⁻¹⁶¹ molecular sieves,¹⁶² aerogels,^{163, 164} and naturally occurring porous diatomite¹⁶⁵ have been used to immobilized Pd nanoparticles. The synthesis of solid-supported nanocatalyst generally involves the adsorption, grafting, or attachment of the stabilizing agent to the solid material, after which Pd ions are introduced to interact with the ligands, followed by reduction. The solid materials can be easily separated via filtration, washed to remove excess ligands, and redispersed in various solvents for catalytic application.

1.3 C-C Coupling Reaction Mechanism for Pd Nanocatalyst

Nanoparticles have gained significant attention due to their enhanced surface-to-volume ratio generating more efficient exposure of the catalytic materials. In C-C coupling, the nature of the nanocatalyst and the actual catalytic mechanism remain a subject of intense debate. The colloidal nature of Pd nanoparticles suggests that they can act as homogeneous or heterogeneous catalysts in solution and, as such, two catalytic mechanisms are possible. On one side, researchers suggest that the reaction occurs directly at the surface of the nanoparticles without inducing changes in the material structure, size, and shape, indicating a purely heterogeneous nature of the catalyst.^{52, 166} On the other hand, substrates could interact with the active metal surface and abstract atoms from the nanoparticle surface, from which the catalytic cycle could then occur in solution. This homogeneous process, often referred to as the atom-leaching mechanism,

results in the nanoparticles serving as a reservoir of active catalytic species.^{52, 167} In this process, Pd atoms are abstracted from the surface of the nanoparticles during oxidative addition.

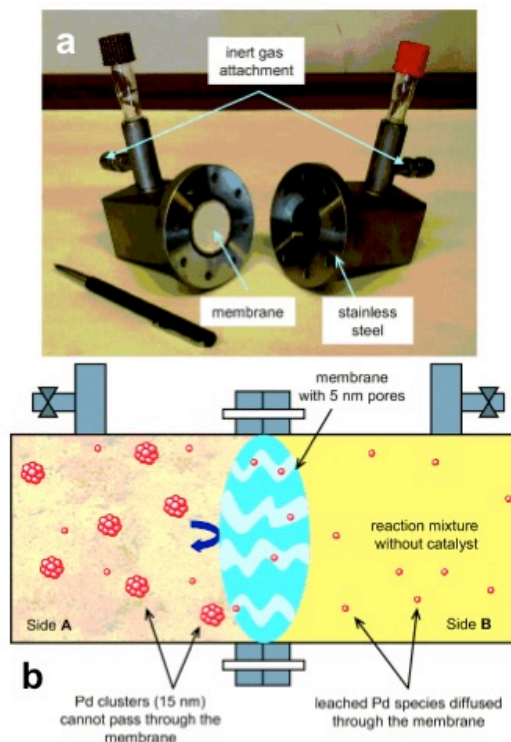


Figure 1.3 a) Photograph of the two-component reactor separated by alumina membrane and b) schematic diagram of the reactor showing the cluster-exclusion process.¹⁶⁸ (Reproduced with permission from ref 168. Copyright © 2006 WILEY-VCH Verlag GmbH & Co. KGaA, Weinheim.)

A thorough study of the leaching mechanism of Pd nanoparticles in coupling reactions was investigated using a 2-compartment reactor, shown in Figure 1.3 a.^{168, 169} This system separates the two compartments with an alumina membrane that only allows for passage of metal species of <5 nm.¹⁶⁹ As such, the nanocluster exclusion process was achieved in which only small Pd clusters, Pd⁰ atoms, and/or Pd²⁺ ions can traverse the alumina membrane, thereby monitoring and analysis of the leached species was possible (Figure 1.3 b). Pd nanoparticles were prepared by mixing the metal precursor, Pd(OAc)₂, with

tetraoctylammonium glycolate (TOAG) acting as both a stabilizer and a reducing agent to produce ~14 nm particles.¹⁶⁹ The C-C coupling initially studied using the unique reaction system was the Heck reaction between n-butyl acrylate and iodobenzene using DMF as the solvent and NaOAc as the base to generate n-butylcinnamate as the product. The two starting materials were added to both sides of the reaction chamber, except the solid base was placed only in side B and the Pd nanoparticles were fully contained in side A at the initiation of the reaction.¹⁶⁹ NaOAc base was necessary for the Heck coupling to occur so no product formation was expected in side A. Control studies showed that the solubility of NaOAc in DMF was negligible thus base diffusion from side B to side A was not observed.¹⁶⁸ In this system however, diffusion of the active Pd species to side B through the mesoporous membrane will allow the reaction to proceed. To this end, Heck coupling was observed for the reaction at side B generating 88% of the n-butylcinnamate product after 120 h, although a small amount of the product (4.9%) was also formed in the opposite side of the reaction chamber, which was attributed to the diffusion of the product from side B to side A.¹⁶⁹

To further verify the leaching of the Pd species through the membrane, another reaction was performed using the Suzuki coupling between phenylboronic acid and p-iodotoluene with the same conditions as the Heck coupling. Approximately 50% of the total anticipated product was formed on side B after 250 h of reaction time, indicating that the catalytic Pd species was abstracted from the nanoparticle cluster during oxidative addition and then subsequently transferred from side A to side B; however diffusion of the product from side B to side A was also observed similar to the Heck reaction albeit at a greater yield of ~ 20%.¹⁶⁹

The nature of the leached species was then investigated to determine whether Pd⁰ species, small Pd⁰ clusters, or both were released through the membrane. Initially, Pd nanoparticles were added to the DMF solvent in side A of the chamber while only DMF was placed on side B.¹⁶⁹ The leaching process was then monitored for 144 h at 100 °C by taking small aliquot of the reaction mixture in side B and analyzing the particles using inductively coupled plasma (ICP) and transmission electron microscopy (TEM).¹⁶⁹ TEM results indicated that small Pd clusters do not diffuse through the membrane, whereas only 20% of the total Pd was found on side B after 144 h, as determined by ICP analysis.¹⁶⁹ Only Pd⁰ species was observed in side B, forming irregular shaped aggregates stabilized by the presence of TOAG ions that were released from the nanoparticle surface and diffuse through the membrane due to concentration gradient.¹⁶⁹ This was verified by UV-vis experiment using samples from both sides of the reaction chamber wherein only a broad spectrum was observed for side B indicating the presence of Pd aggregates, while an absorbance shoulder at 390 nm was obtained from samples in side A suggesting the presence of Pd clusters in solution.¹⁶⁹

Another experiment was performed to probe the leaching of Pd²⁺ as a result of oxidative addition in the presence of aryl halides. To accomplish this study, iodobenzene was dissolve in DMF and placed on both sides of the reaction chamber with Pd nanoparticles added only to side A.¹⁶⁹ After 24 h, aliquots were taken from both reactions wherein it was observed that the black solution in side A turned into dark reddish color while the reaction in side B turned dark red after another 24 h indicating the migration of Pd species from side A to side B. As such, leaching of catalytically active Pd⁰ atom from the

nanoparticles was observed in the presence of oxidizing aryl iodide substrate, which supports an atom-leaching mechanism during oxidative addition for Pd nanoparticles.¹⁶⁹ From these studies, three different scenarios could occur for the transfer of Pd species from one side of the reactor to the other through an alumina membrane (Figure 1.4).¹⁶⁹ The first mechanism involves the fragmentation of Pd nanoparticles into smaller nanoclusters, which can then pass through the porous membrane; however, the results indicate that this process was not occurring, as there were no small Pd nanoclusters observed in side B of the reactor. Although the fragmentation of Pd nanoparticles results in the formation of small Pd clusters, these do not appear to be able to pass through the alumina membrane.¹⁶⁹

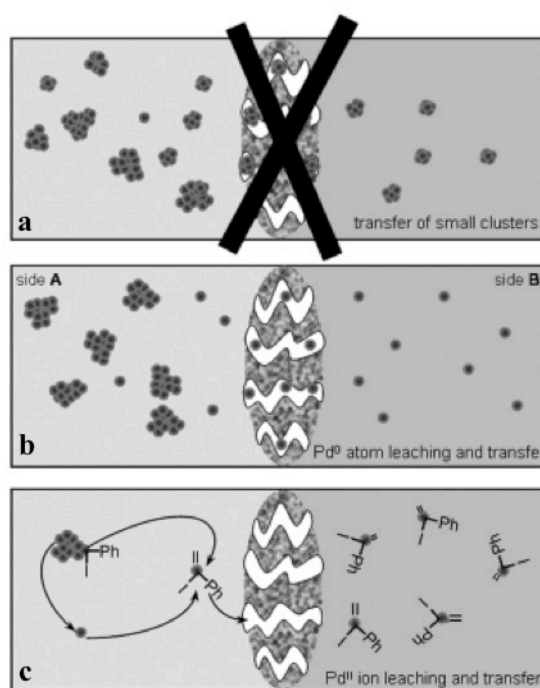


Figure 1.4 Possible transfer mechanisms of leached Pd species in a two-component reactor. a) nanoparticle fragmentation and transfer of small clusters does not occur, b) leaching of Pd⁰ atoms and ensuing transfer, and c) formation of Pd²⁺ complexes during oxidative addition and subsequent leaching and transfer.¹⁶⁹ (Reproduced with permission from ref 169. Copyright © 2007 WILEY-VCH Verlag GmbH & Co. KGaA, Weinheim.)

In the second mechanism, Pd⁰ atoms were leached from the nanoparticles under non-oxidizing conditions and then transferred to side B through the porous membrane as indicated by the experimental results.¹⁶⁹ In contrast, the third mechanism involved the leaching of Pd species from the nanoparticles surface under oxidizing conditions due to the presence of aryl halides in solution.¹⁶⁹ In this process, the oxidative attack of the aryl halides resulted in leaching of Pd species and formation of Pd²⁺ complexes that were then transferred to side B.¹⁶⁹ These Pd²⁺ complexes can then pass through the porous membrane and continue with the catalytic cycle in side B if the coupling components were present.¹⁶⁹ To this end, transfer of Pd species from side A to side B and their corresponding catalytic activity can be attributed to the leached Pd⁰ atoms and/or the Pd²⁺ complex.¹⁶⁹

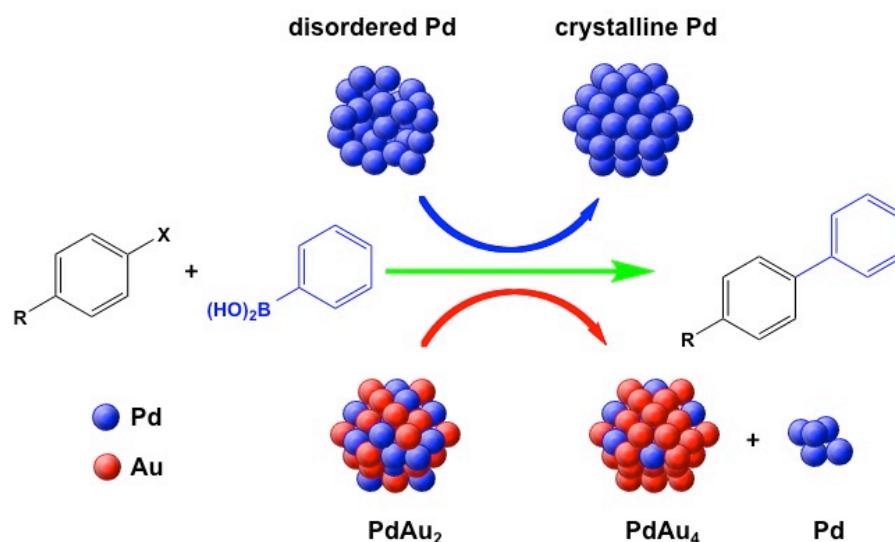


Figure 1.5 Representation of changes in crystallinity and morphology of Pd and Au-Pd nanoparticles as a result of the atom-leaching mechanism in Suzuki coupling.¹⁷⁰ (Reproduced with permission from ref 170. Copyright © 2012 WILEY-VCH Verlag GmbH & Co. KGaA, Weinheim.)

In another study by Niu *et al.*, the design of Pd nanoparticles was employed to probe the catalytic mechanism promoted by oxidative addition in the presence of aryl halide substrates.¹⁷⁰ Observations of tunable characteristics of the nanocatalysts such as crystallinity, composition, and surface structure were used for qualitative scrutiny of the reaction mechanism by employing two differently synthesized particles (Figure 1.5): 1. poorly crystalline (disordered) Pd nanoparticles and 2. bimetallic PdAu nanocrystals.¹⁷⁰ Using highly disordered nanoparticles in the coupling reaction, the overall change in the structure and crystallinity of the particles after the reaction was monitored from which information regarding the mechanism could be obtained.¹⁷⁰ Meanwhile, using bimetallic PdAu nanoparticles provided evidence concerning the catalytic mechanism by the formation of Pd nanostructures via phase segregation in the reaction as a result of leaching during oxidative addition.¹⁷⁰

These nanoparticles were employed in the Suzuki coupling reaction between iodoanisole and phenylboronic acid using Na_2CO_3 as base. In the case of the poorly crystalline Pd nanoparticles, HRTEM analysis, shown in Figure 1.6g and h, after the reaction illustrated sintering and crystallinity enhancements of the particles, which were very different from the original nanocatalysts (Figure 1.6d).¹⁷⁰ High resolution TEM (HRTEM) and selected area electron diffraction (SAED) experiments still did show some poorly crystalline nanoparticles, suggesting that not all of the materials were involved in the catalytic cycle.¹⁷⁰ The crystalline nanoparticles ranged from spherical to irregularly shaped structures with sizes between 3 – 22 nm, where SAED and energy-dispersive X-ray (EDX) analyses confirmed the formation of pure Pd nanocrystals as shown in Figure 1.3 f and j, respectively.¹⁷⁰

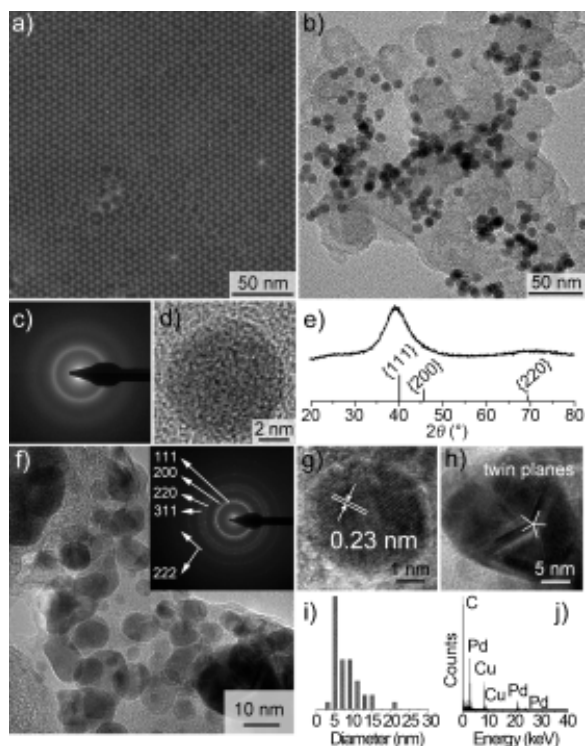


Figure 1.6 (a, b) TEM images, (c) SAED pattern, (d) HRTEM image, and (e) XRD analysis of the Pd nanoparticles before catalysis. (f) TEM image and SAED pattern (inset), (g and h) HRTEM images, (i) size distribution histogram, and (j) EDX spectrum of Pd nanoparticles after catalysis.¹⁷⁰ (Reproduced with permission from ref 170. Copyright © 2012 WILEY-VCH Verlag GmbH & Co. KGaA, Weinheim.)

To further probe the improved crystal structure of the Pd nanoparticles in the reaction, several control experiments were performed wherein the results indicated that the presence of aryl halides was responsible for crystallinity enhancement. In this process, the aryl halides abstract Pd atoms from the surface of the disordered nanoparticles during oxidative addition, generating nanoparticles with an enhanced crystalline structure. To this end, when aryl halides were removed from the reaction system, retention of poor crystallinity was observed for the Pd nanoparticles.¹⁷⁰ In a separate study, in a reaction system where only the aryl halide was present in the absence of the transmetalation reagent, nanoparticle crystallinity enhancement was again observed due to Pd leaching

during oxidative addition.¹⁷⁰ These results suggest that the catalytic mechanism driven by the Pd nanoparticles follows an atom-leaching process wherein the aryl halides oxidatively abstract Pd⁰ atoms. Following this, the leached complexes undergo transmetalation and reductive elimination, releasing the coupling product and free Pd⁰ atoms in solution. The Pd⁰ atoms can then undergo nucleation and growth to produce crystalline nanoparticles with no size and shape control due to the absence of stabilizing agents in the reaction system.¹⁷⁰ On the other hand, if the catalytic mechanism was exclusively a surface-based reaction, only minimal to no changes in nanoparticle morphology should be observed, with no formation of irregular shaped, crystalline Pd nanoparticles.¹⁷⁰

Inductively coupled plasma – mass spectrometry (ICP-MS) analysis was also performed to measure the concentration of soluble Pd species in the reaction solution with and without the aryl halide. Using the poorly crystalline Pd nanoparticles as the catalyst, 60 ppb Pd species was determined to be in solution for the reaction containing 4-iodoanisole; however, only 9 ppb Pd species was found in the reaction without the aryl halide substrate.¹⁷⁰ These results suggest that oxidative addition in the presence of aryl halides causes abstraction of Pd species from the nanoparticle surface, thereby increasing the amount of Pd released to solution. On the other hand, only minimal leaching was observed without aryl halides, which can be attributed to the inherent instability of the nanoparticles.

While the crystallinity results suggest leaching of Pd atoms during oxidative addition, further evidence was obtained using a bimetallic Pd-Au nanoparticle system. In this case, co-reduction of Pd and Au metal precursors was achieved by adding oleylamine at 230

°C to produce spherical nanoparticles with ~9 nm average diameter size.¹⁷⁰ HRTEM and EDX mapping analysis revealed that the particles were composed of a 31:69 Pd:Au ratio with lattice spacings between the expected value for face-centered cubic (fcc) Pd and Au.¹⁷⁰ Catalytic reactions between 4-iodoanisole and phenylboronic acid were used to probe the leaching process driven by the Pd-Au nanoparticles. TEM analysis of the bimetallic nanocatalyst after the reaction revealed that the shape and size of the particles remained the same; however, EDX results showed the Pd/Au atomic ratio to be 19:81, indicating a decreased amount of Pd atoms in the nanoparticles.¹⁷⁰ Interestingly, highly crystalline Pd nanoparticles of ~5 nm in size were formed in this system, as confirmed by TEM and EDX, suggesting that the Pd atoms were selectively abstracted from the bimetallic nanoparticle during the coupling reaction.¹⁷⁰ To verify the role of oxidative addition by the aryl halide in the leaching process, control reactions were done without 4-iodoanisole, wherein the EDX analysis of the materials after the process displayed a Pd/Au ratio of 27:73, which was similar to the original bimetallic ratio.¹⁷⁰ These results indicate that the aryl halides leached the Pd⁰ species during the oxidative addition process in the catalytic reaction.

Overall, the results of these studies indicated that the atom-leaching mechanism promoted by oxidative addition of the aryl halide was the likely catalytic process for Pd nanoparticles in the Suzuki coupling reaction. These results offer direct evidence using various analytical techniques and different types of Pd nanoparticles wherein atom abstraction during the catalytic cycle was both qualitatively and quantitatively analyzed. Aside from indirect processes such as monitoring the TOF values, these studies provided physical validation of an atom-leaching process for Pd nanoparticles.

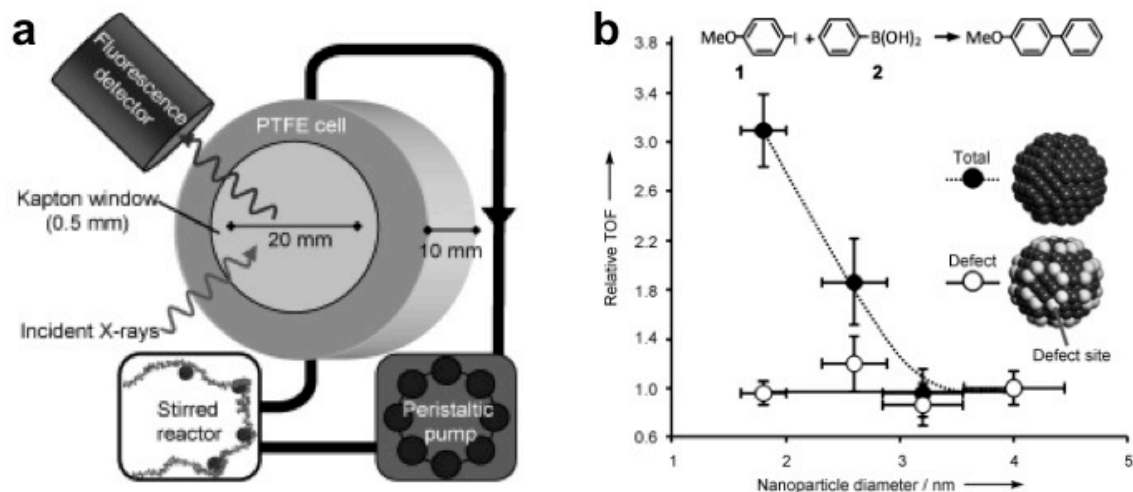


Figure 1.7 a) Schematic diagram of the recirculating reactor setup for XAS, b) normalized TOF data for Suzuki coupling reaction showing rate dependence on correct active sites and not on particle size.¹⁷¹ (Reproduced with permission from ref 171. Copyright © 2010 WILEY-VCH Verlag GmbH & Co. KGaA, Weinheim.)

The other side of the debate regarding the catalytic mechanism of Pd nanoparticles centers on the argument that the entire reaction occurs directly on the surface of the particles in a straightforward heterogeneous reaction. To this end, evidence of surface-based Suzuki coupling catalyzed by Pd nanoparticles was examined by monitoring of the local coordination environment of the metal in real time using a recirculating reactor set up for operando fluorescence X-ray absorption spectroscopy (XAS) illustrated in Figure 1.7a.¹⁷¹ Polymer-stabilized Pd nanoparticles were prepared by refluxing H_2PdCl_4 and polyvinylpyrrolidone (PVP) with water and ethanol to generate 1.8 – 4.0 nm Pd^0 particles.¹⁷¹ Suzuki coupling between iodoanisole and phenylboronic acid was monitored for these studies wherein the catalytic activity was expressed as turnover frequency (TOF) values. When the reactivity of the nanocatalyst was monitored with respect to particle diameter, the TOF values decreased as the size of the nanoparticles increased as expected; however, when the TOF values were normalized with respect to the edge and

vertex atoms on the surface of the nanoparticles, statistically similar TOF values were obtained regardless of particle size (Figure 1.7b).¹⁷¹ This suggests that the reactivity of Pd nanoparticles is associated with the defect atoms on the particle surface.

As such, monitoring of the possible leached species was performed using XAS, which can sensitively measure the average Pd-Pd coordination number (CN), as well as provide information concerning the particle size and morphology. From the extended X-ray absorption fine structure (EXAFS) intensities for simulated 1.8 nm Pd nanoparticles, a Pd-Pd CN value of 9.46 was calculated, which is in agreement with the observed value of 9.58.¹⁷¹ Leached Pd species, however, were not observed as there was neither sintering nor dissolution of Pd atoms since there is no change in the CN, which supported the stability of the nanoparticles in the reaction.¹⁷¹ HRTEM analysis before and after the reaction also illustrated no change in the size and shape of the nanoparticles.¹⁷¹ Simulation of analogous 1.8 nm particles with 48 Pd defect atoms removed into the solution would lead to a drop of CN to 7.23; however this phenomenon was not observed, which indicated that there was no solubilization and homogeneous contribution of catalytically active Pd species.¹⁷¹

To further probe the system with regards to leached Pd atoms, trace amounts of dissolved Pd(OAc)₂ were added to the reaction, which was expected to enhance the catalytic activity of the particles; however, no such enhancement was observed.¹⁷¹ On the other hand, adding Hg as a selective catalyst poison immediately inhibits the catalytic activity, suggesting that a surface-based process was occurring for the PVP-Pd nanoparticles.¹⁷¹ Analysis of the nanocatalyst using *ex situ* X-ray photoelectron spectroscopy (XPS) showed a 1:1 ratio between surface Pd and Hg atoms indicating full coverage of the

active catalytic sites.¹⁷¹ When the reaction was deliberately spiked with Pd(OAc)₂ atoms after addition of Hg, no additional catalytic activity was observed.¹⁷¹ These results indicated that the catalytic activity for PVP-Pd nanoparticles happens at the metal surface, while the additional Pd(OAc)₂ species were not catalytically reactive.

One final method was employed to study this leaching process. For this, thiolated porous silica was used to probe the nature of the active species wherein the sulfur-containing substrate should interact with soluble Pd species abstracted from the nanoparticles and prevent catalysis if the leached atoms were responsible for the reaction. Using these functionalized silica materials, the catalytic reaction of the nanocatalyst decreased; however, this was due to nanoparticle entrapment inside the pores of the silica beads and not due to the sequestration of Pd species by thiols.¹⁷¹ To this end, employing unfunctionalized silica with identical pore sizes over the thiolated silica resulted in the same catalytic rate decrease, indicating that the coupling reaction was inhibited by the nanocatalyst being trapped within the porous material, as confirmed via TEM, XAS, and XPS analyses.¹⁷¹ Kinetic studies comparing the reactivities of PVP-Pd nanoparticles and Pd(OAc)₂ showed a first-order dependence on Pd concentration for the former and negative-order dependence on the latter, suggesting that a surface-based catalytic reaction was at play.¹⁷¹ Furthermore, if the reaction was based on the dissolved or leached Pd species, a decrease in coupling rate would be observed as the amount of Pd loading was increased; however, the opposite results were obtained wherein increases in initial rates were directly proportional to the increased Pd concentration. Overall, the results of these studies offered a strong argument that the catalytic mechanism for C-C coupling

catalyzed by PVP-capped Pd nanoparticles happened at the metal surface in a heterogeneous fashion.

The studies of the reaction mechanism of Pd nanoparticles provide two different theories regarding the nature of active catalytic species wherein the reactions either proceeds exclusively in a heterogeneous or homogeneous manner. In a purely heterogeneous catalysis, the transformation reaction occurred at the surface of metal nanoparticles and, as such, changes in the morphology, crystallinity, and size of the nanocatalyst were minimal. On the other hand, in a homogeneous catalytic mechanism, the active species was abstracted from the nanoparticle surface during the oxidative addition resulting in morphological and crystallinity changes, as well as Pd black formation. These theories presented conflicting explanations regarding the catalytic mechanism of Pd nanoparticles in C-C coupling reaction. Although both of these explanations are plausible, further studies are required to fully elucidate the catalytic reactivity of Pd nanoparticles for C-C coupling. Understanding the actual reaction mechanism can provide valuable information for the design of new synthetic routes for the production of more efficient nanocatalysts.

1.4 Pd Nanoparticles in the Stille Coupling Reaction

The Stille coupling process was first reported in 1978 as a reaction between acid chlorides and organostannane reagents in the synthesis of ketones, catalyzed by phosphine-stabilized Pd catalysts.⁶⁰ Since then, various modifications to the phosphine ligands have been reported for this reaction,¹⁷²⁻¹⁷⁴ which takes advantage of the air- and moisture-stable nucleophilic partner to afford C-C bond formation with substrates

containing different functional groups. Typically, this transformation is performed at elevated temperatures (70 – 120 °C), in organic solvents, and with catalyst loadings of > 1 mol% Pd, which can be reduced *in situ*.¹⁷⁵ In the age of nanotechnology, however, milder reaction conditions are employed due to the nature of the ligand employed in material production. For example, using dendritic materials for the synthesis of Pd nanoparticles, Stille coupling was performed in water at room temperature with only 0.10 mol% Pd as the catalyst.⁸⁶ In this system, the Crooks group used hydroxyl-terminated fourth generation poly(amido amine) PAMAM dendrimers to encapsulate Pd nanoparticles using a 40:1 molar ratio of the PdCl₄⁻ metal precursor and the dendrimer (Figure 1.8a).⁸⁶ Upon reduction, ~40 Pd atoms were contained within the dendrimer, producing a nanoparticle with an average size of 1.7 ± 0.4 nm.⁸⁶ These dendrimer-encapsulated Pd nanoparticles (Pd DENs) were employed for Stille coupling between 4-iodobenzoic acid and phenyltin trichloride, generating a new C-C bond in the 4-biphenylcarboxylic acid product, as shown in Figure 1.8b. Quantitative yields were reported after a 15 h reaction time with constant stirring at room temperature.⁸⁶ Aryl halides with different halogen species and functional groups were also employed in the Stille reaction using the Pd DENs with results corresponding to the expected reactivity of each substrate. To this end, the aryl halide substrates with electron-withdrawing (–COOH) and iodide groups were more reactive than the corresponding bromide-substituted and phenolic substrates.⁸⁶ TOF values of 2000 ± 200 mol product (mol Pd × h)⁻¹ for 4-iodobenzoic acid was obtained, suggesting a highly efficient nanocatalyst.⁸⁶

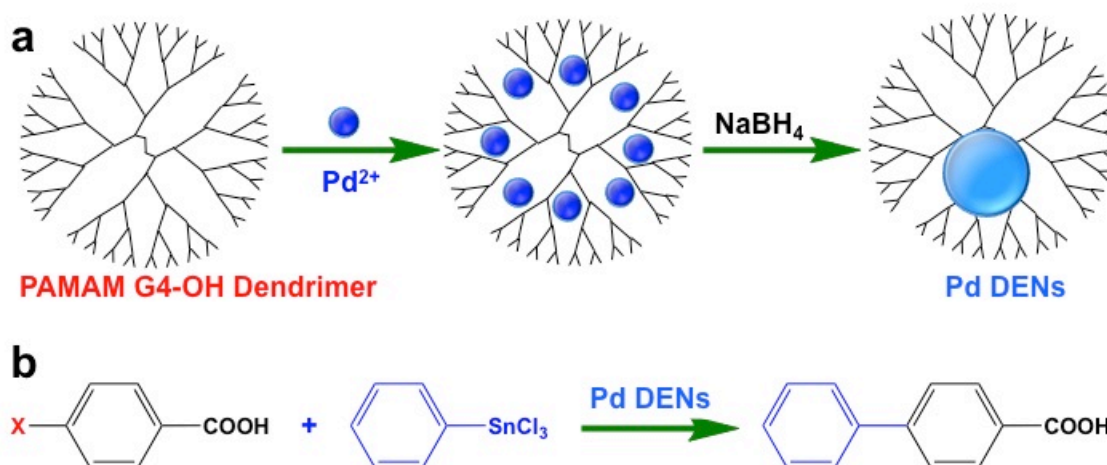


Figure 1.8 a) Synthesis of dendrimer-encapsulated Pd nanoparticles, b) Stille coupling reaction using Pd DENs.

An interesting control reaction was performed using Pd nanoparticles generated without the DENs to evaluate the role of the dendritic cage in catalytic reactivity. As such, K_2PdCl_4 was reduced with NaBH_4 in the absence of the dendrimers, thus producing polydisperse particles that generated a TOF value slightly lower than that of Pd DENs ($1800 \text{ mol product (mol Pd} \times \text{h)}^{-1}$).⁸⁶ This result suggests that the size control provided by the DENs enables the catalyst to have higher surface area than the particles without DENs to provide better catalytic reactivity.⁸⁶ TEM analyses of the Pd DENs before and after the catalytic reaction were performed, which showed a moderate increase in particle size and dispersity from $1.7 \pm 0.4 \text{ nm}$ to $2.7 \pm 1.1 \text{ nm}$.⁸⁶ These results indicated partial aggregation of the Pd nanoparticles as a consequence of the catalytic reaction that was attributed to leaching of Pd atoms during the catalytic cycle.⁸⁶ To confirm this, the Pd DENs were added to an identical reaction solution but without the substrates and allowed to proceed for 24 h. TEM analyses of the nanoparticles before and after the reaction

showed statistically similar particle diameter indicating that the catalytic reaction was responsible for increase in nanoparticle size.⁸⁶

When the Pd DENs were employed in Stille couplings at elevated temperatures, catalyst aggregation was observed by the appearance of black precipitate.⁸⁶ As such, product yields under these reaction conditions were lower than the reactions at room temperature, which could arise from dendrimer degradation.⁸⁶ Finally, the recyclability of the Pd DENs was also evaluated using sequential Stille coupling between two different substrates.⁸⁶ For this, the second substrate was added after the reaction of the initial substrate was concluded.⁸⁶ Specifically, a reaction solution containing 4-iodophenol and phenyltin trichloride was added to the Pd DENs and allowed to proceed for 15 h. After reaching completion, another reaction solution containing 4-iodobenzoic acid and phenyltin trichloride was added to the first mixture and allowed to proceed for 15 h such that in the end, two possible products can be observed if the Pd DENs remain active. Gas chromatography – mass spectrometry (GC-MS) analysis of the reaction demonstrated the quantitative formation of the anticipated two products (4-phenylphenol and 4-biphenylcarboxylic acid), indicating that the Pd DENs were still catalytically active after the initial cycle.⁸⁶ These studies showed that Pd DENs catalyzed Stille coupling under ambient reaction conditions, which could serve as model for designing catalytic systems.

In a separate study, the effect that the dendrimers possessed over the catalyst reactivity and selectivity was studied by comparing different precatalysts namely: Pd DENs, Pd(OAc)₂, and Pd²⁺-PAMAM complexes.⁹⁰ In Stille coupling reactions employing the same system Crooks and coworkers employed at a higher temperatures of 40 °C and 80 °C, results indicated that both Pd DENs and Pd(OAc)₂ have similar reactivity with

quantitative product yields after 24 h; however, the unreduced Pd²⁺-PAMAM complex only generated 18% product.⁹⁰ Furthermore, the DENs showed 100% selectivity for the conversion of 4-iodobenzoic acid to 4-biphenylbenzoic acid, while Pd(OAc)₂ generated both the anticipated Stille coupling product and the undesired homocoupling biphenyl.⁹⁰ When using less water-soluble substrates such as activated 4-iodoacetophenone, almost quantitative yields were obtained using the naked precatalyst at 40 °C, while a higher temperature of 80 °C was necessary for the DENs to generate 66% of the product with 100% selectivity.⁹⁰ Similar trends were determined using aryl halides with different functional groups, indicating that the simplest catalyst, Pd(OAc)₂, is the fastest system, but it was not selective for generating C-C bonds.⁹⁰ When the same precatalysts were used in recycling experiments, the materials were inactive after the initial catalytic cycle; however, the DENs were able to complete several reaction cycles with slightly diminished reactivity after multiple reactions.⁹⁰ TEM images taken after the fourth catalytic cycle showed an increase in the Pd nanoparticle size from 1.6 ± 0.3 nm to 2.3 ± 0.6 nm as a result of the reaction.⁹⁰ These indicated that the dendrimer was able to retain most of the Pd species to prevent bulk Pd black formation, but that migration of Pd materials between the dendrimers occurred.

In contrast with the aqueous-based Pd DENs, organic solvents have also been used in the preparation of dendrimer-stabilized Pd nanoparticles. The structural difference between DENs and dendrimer-stabilized materials is that DENs encapsulated the nanoparticle within the void space of the polymer, while dendrimer-stabilized materials bind multiple dendrimers to the particle surface to impart material stability. This system was prepared by co-dissolving phosphine-oxide dendrimers and a metal precursor, Pd(acac)₂, in THF at

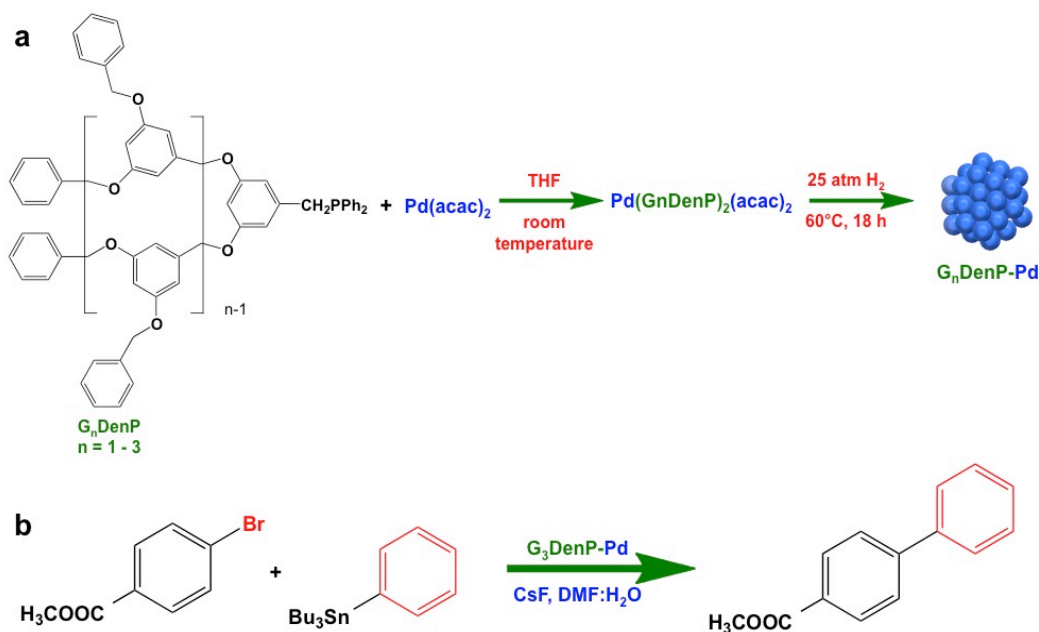


Figure 1.9 a) Scheme for the synthesis of $\text{G}_n\text{DenP-Pd}$ nanoparticles and b) their use in Stille coupling reaction between methyl-4-bromobenzoate and tributyl(phenyl)stannane.⁹³

room temperature as shown in Figure 1.9a.⁹³ The resulting complex was then reduced by H_2 at 60°C overnight producing a black solution of $\text{G}_n\text{DenP-Pd}$ ($n = 1 - 3$) with sizes of $5.0 \pm 0.4 \text{ nm}$, $4.6 \pm 0.5 \text{ nm}$ and $3.2 \pm 0.5 \text{ nm}$ for $\text{G}_1\text{DenP-Pd}$, $\text{G}_2\text{DenP-Pd}$ and $\text{G}_3\text{DenP-Pd}$ nanoparticles, respectively.⁹³ The dendritic-phosphine-based Pd nanoparticles were then used for Stille coupling using methyl-4-bromobenzoate and tributyl(phenyl)stannane (Figure 1.9b) with 1.5 mol% nanocatalyst at 40°C and DMF-water as the solvent.⁹³ Excellent yields of 98% after 5.0 h were reported for this model reaction, while 78 – 98% yields were obtained for an array of aryl bromides containing electron-donating and withdrawing substituents and heteroatom-containing substrates.⁹³ Reactivity over such a wide variety of reagents signifies the versatility of the $\text{G}_n\text{DenP-Pd}$ system for practical applications in organic synthesis. Furthermore, when the Stille reaction using aryl chlorides were used at 110°C , formation of products were observed with excellent yield

ranging from 78 – 95%.⁹³ This was quite remarkable as aryl chlorides are difficult to get to participate in C-C couplings. This suggests that the G_nDenP-Pd system presents a robust, highly efficient nanocatalyst with industrial and pharmaceutical applications for organic and materials synthesis.

As a complement to the dendrimer-based systems, an aqueous-based synthesis of Pd nanoparticle catalyts has also been accomplished using polymer ligands such as polyethelene glycol (PEG). In this process, K₂PdCl₄ interacted with the PEG, which was reduced by drop wise addition of a Fisher carbene complex, generating 7 – 10 nm spherical Pd nanoparticles.⁹⁷ For these materials, the Stille coupling between an aryl bromide and phenyltributylstannane was performed in an aqueous solution of K₂CO₃ at 80 °C for 2 – 3 h.⁹⁷ Product yields of ≥88% were obtained using different aryl bromide substrates with varying functional groups, indicating applicability in a wide array of reagents.⁹⁷

Imidazolium-based ionic polymers have also been used to stabilize Pd nanoparticles as a functionalized ionic liquid, producing 5.0 nm particles after NaBH₄ reduction.¹³⁵ The Pd nanocatalyst (Pd-IP-IL) was used in coupling reactions between different aryl halides and an organostannane reagent at 80 °C, producing quantitative yields for aryl iodides with a variety of functional groups.¹³⁵ The recyclability of the Pd-IP-IL nanoparticles was established wherein no loss of activity was reported after five reaction cycles.¹³⁵ This indicated that the catalyst was stable at elevated temperatures and is potentially viable for industrial use. Amine-rich ionic liquids, tetrabutylammonium bromide and tetrabutylammonium acetate, were also employed for the preparation of monodisperse, core-shell Pd nanoparticles composed of 3.3 nm metallic core and stabilized by

tetrabutylammonium cations, Br^- , and $[\text{PdBr}_4]^{2-}$.¹³⁴ These nanoparticles were used for Stille coupling using bromo- and chloro-arenes with tetrabutylphenylstannane. The starting materials were reacted in tetraheptylammonium bromide at elevated temperatures between 90 – 130 °C.¹³⁴ High product yields were generated from aryl bromides and activated aryl chlorides at 90 °C, while higher temperatures of up to 130 °C were needed to generate modest yields for deactivated electron-rich aryl chlorides.¹³⁴ Recycling experiments were performed after the initial catalytic cycle by first extracting the Pd nanoparticles with cyclohexane and the resulting viscous mixture was added with fresh starting materials.¹³⁴ The nanocatalyst was recycled five times with minimal loss of activity, suggesting a practical, easily recoverable and reusable catalyst, which were the main advantages of ionic liquid based Pd nanoparticles.¹³⁴

Another ligand system employed for nanocatalyst synthesis is Pd-substituted Keggin-type polyoxometallates. The precursor species, $\text{K}_5[\text{PdPW}_{11}\text{O}_{39}] \cdot 12\text{H}_2\text{O}$, was reacted with acetophenone at 200 °C for 4 h with an applied H_2 pressure of 30 bar, which produced a blue-black solid.¹⁷⁶ Due to the polymer's high anionic charge, the polymer-capped Pd nanoparticles were electrostatically stabilized, forming spherical clusters of ~15 – 20 nm in size.¹⁷⁶ The Stille reaction between 4-bromotoluene and tetraphenyltin was performed using these materials in a 50:50 DMF- H_2O mixture at 110 °C for 12.0 h.¹⁷⁶ Under these conditions, the reaction generated a nearly quantitative yield of 93% for the 4-methylbiphenyl product.¹⁷⁶ Similarly, coupling between 1-chloro-4-nitrobenzene and tetraphenyltin produced 92% 4-nitrobiphenyl under similar conditions.¹⁷⁶ Together, this suggests that these materials are highly reactive catalysts due to their reactivity with chloro-based reagents.

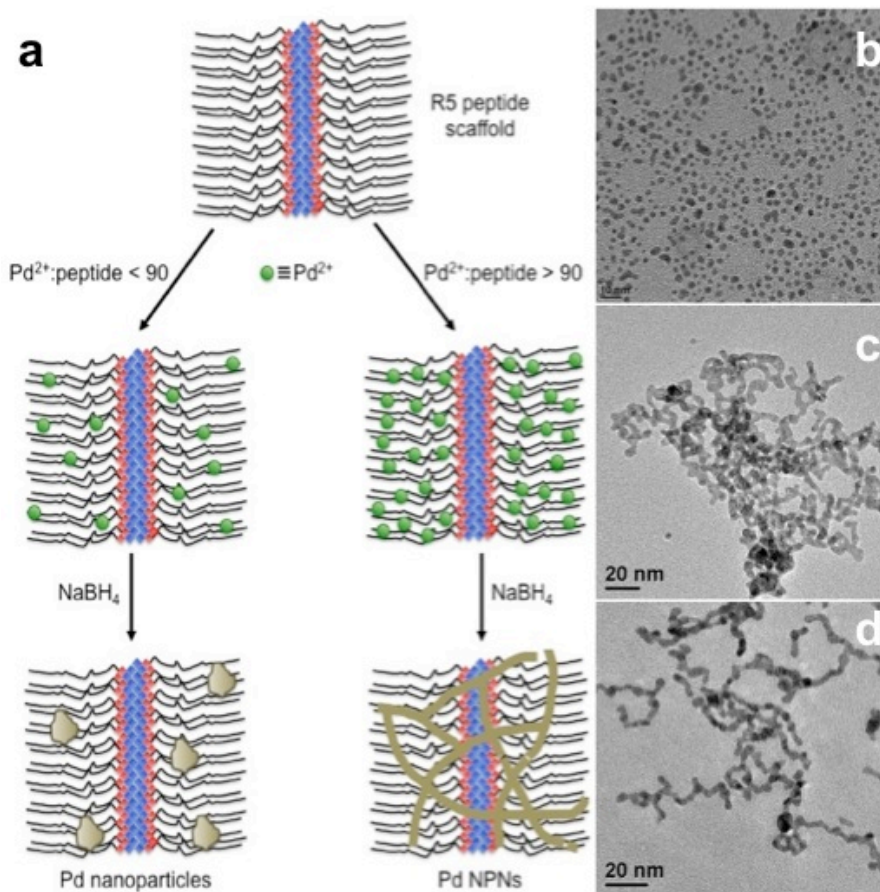


Figure 1.10 a) Schematic representation of the R5-templated synthesis of Pd NPNs, and TEM images of Pd materials produced using different Pd:peptide ratios: b) Pd60, c) Pd90, and d) Pd120.⁸⁷ [Jakhmola, A.; Bhandari, R.; Pacardo, D. B.; Knecht, M. R. *J. Mater. Chem.* **2010**, *20*, 1522-1531.] - Reproduced by permission of The Royal Society of Chemistry.

More recently, biological molecules have been employed for the synthesis of solvent-dispersible nanocatalysts due to their ability to interact and bind with target materials. The biotic/abiotic interaction displayed by the biological molecules and inorganic substrates was also observed in the silaffin proteins that precipitate silica in the cell walls of diatoms. The Kröger group isolated and identified the R5 peptide from the diatom *Cylindrotheca fusiformis* bearing multiple basic residues (sequence =

SSKKSGSYSGSKGSKRRIL).^{177, 178} This peptide self-assembles due to the hydrophobic RRIL motif to form a bioscaffold that can interact and stabilize metal nanomaterials as illustrated in Figure 1.10a.⁸⁷ In this regard, peptide-templated Pd nanostructures were synthesized by co-dissolving Pd²⁺ with the R5, followed by addition of NaBH₄ as the reducing agent.⁸⁷ Several Pd:peptide ratios were prepared, resulting in the generation of differently shaped materials, as shown in the TEM images of Figure 1.10.⁸⁷ Using a 60:1 Pd:peptide ratio (Pd60), nearly monodisperse and spherical nanoparticles were formed with an average diameter of 2.9 ± 0.6 nm (Figure 1.10b).⁸⁷ For a 90:1 ratio (Pd90), linear nanoribbons were observed with a width of 3.9 ± 0.8 nm (Figure 1.10c), while nanoparticle networks (NPNs) were generated at a 120:1 ratio (Pd120) with an average width of 4.1 ± 1.2 nm (Figure 1.10d).⁸⁷

The catalytic activity of these nanocatalysts was initially tested using the Stille coupling reaction between 4-iodobenzoic acid and phenyltin trichloride. Quantitative yields were observed after 24 h for reactions using low catalyst amounts (≥ 0.01 mol% Pd for all Pd:peptide ratios), suggesting that these materials were highly efficient under ambient conditions.⁸⁷ TOF analysis of the different peptide-templated structures generated modest values of ~ 450 mol product (mol Pd \times h)⁻¹ for both Pd60 and Pd120, while a value of ~ 350 mol product (mol Pd \times h)⁻¹ was obtained for Pd90.⁸⁷ Although these TOF values are lower than those reported by Crooks and colleagues⁸⁶ using the same reaction, it is worth noting that for the R5-templated Pd nanoparticles, lower catalyst amounts were required to generate quantitative product yields.

Employing biological molecules as tools for the biomimetic synthesis of metal nanoparticles could generate a model system for green nanocatalysis. As shown in the R5-

templated Pd nanoparticles, highly active nanocatalysts with different morphologies can be generated by exploiting the scaffold-like nature of the biomolecules; however, there are limited numbers of naturally-occurring biomolecules with affinity for inorganic substrates. Furthermore, biological molecules exhibit unspecific interactions with different of metal ions as exemplified by the R5 template, which showed templating/stabilizing ability in the synthesis of Si,¹⁷⁹ TiO₂,¹⁸⁰ Pd,^{37, 87} and Au¹⁸¹ nanomaterials.

1.5 Pd Nanoparticles in Suzuki Coupling Reaction

The Suzuki reaction was first reported in 1979 where the cross-coupling of alkenylboranes with aryl halides was performed using a phosphine-stabilized Pd catalyst in the presence of a base.⁶⁴ This provided a new synthetic strategy to produce stereoselective arylated alkene products from different aryl halides with activated alkenylboranes as the nucleophilic partner. The main advantages of this coupling reaction are the ability to tolerate different functional groups attached to the aryl ring, as well as the relatively low toxicity of the boron reagent.⁶⁴ In this reaction, the presence of a base is important as it converts the boronate species into its active form for transmetalation to occur; absence of the base results in no product formation.⁶⁴ In a separate paper, Suzuki and coworkers reported the coupling of alkenylboranes with alkenyl halides in the presence of a base and catalytic amount of tetrakis(triphenylphosphine) Pd to produce decent yields of conjugated dienes and enynes with high regio- and stereoselectivity.⁶³ From these simple borane compounds, the application of the Suzuki reaction was

expanded to different organoboranes such as boronic acids, boronate ester, and arylboranes, providing a wide array of applications in organic synthesis.

The application of Pd nanoparticles for Suzuki coupling was first introduced by the Reetz group.¹⁸² For this, tetrabutylammonium (R_4N^+)- or (PVP)-stabilized Pd nanocatalysts were employed for the reaction between aryl bromides and aryl chlorides with phenylboronic acid producing biaryl products.¹⁸² The R_4N^+ Pd clusters of 2 – 3 nm were initially employed for the Suzuki coupling reaction between bromobenzene and phenylboronic acid in DMF at 100 °C for 3.5 h.¹⁸² The results of these studies demonstrated 100% conversion of the starting material based on GC and thin layer chromatography (TLC) analyses with a 53% isolated yield for the product.¹⁸² Similar conversion capabilities were obtained from the same reaction using PVP-stabilized Pd materials, although significantly lower isolated yields were achieved.¹⁸²

In separate work, PVP-stabilized Pd nanoparticles were synthesized by El-Sayed and coworkers for applications in Suzuki coupling reactions in aqueous solution.⁹⁶ The TEM analysis displayed the formation of ~3.6 nm Pd nanoparticles after heating a solution of H_2PdCl_4 and PVP in 40% EtOH for 3.0 h.⁹⁶ Cross-coupling reactions between aryl iodides and arylboronic acids were performed in 40% EtOH and in the presence of Na_3PO_4 as the base under reflux conditions for 12 h using a lower catalyst loading of 0.3 mol% Pd.⁹⁶ In the reaction involving iodobenzene and phenylboronic acid, 95% yield of the biphenyl product was generated.⁹⁶ On the other hand, using sulfur-containing starting material such as 2-iodothiophene or 2-thiopheneboronic acid, resulted in decreased product yields ranging from 26% to 92%.⁹⁶ The decrease in product yield can be attributed to poisoning of the nanocatalyst by the thiol-groups in the reactants. Although

these reactions showed decent product yields for most of the substrates used, precipitation of Pd black was noted during the reaction, which was attributed to the high reaction temperatures. In another experiment, the initial rate of the coupling reaction between phenylboronic acid and iodobenzene in acetonitrile-water solvent was determined.⁹⁶ The results indicated that the reaction rate was directly proportional to the concentration of PVP-Pd nanocatalyst, from which the authors suggested that C-C bond formation occurred at the catalyst surface.⁹⁶ While the PVP-Pd nanoparticles were effective Suzuki coupling catalysts, the formation of Pd black decreased the overall efficiency of the catalyst.

Another polymer ligand used for the synthesis of Pd nanoparticles is the block copolymer polystyrene-*b*-poly(sodium acrylate) (PS-*b*-PANa).¹⁸³ The polymer structure was composed of a hydrophobic polystyrene component and a hydrophilic poly(sodium acrylate) component.¹⁸³ This amphiphilic polymer generates a micellar structure in solution that provides steric stabilization of nanoparticles. The block copolymer-stabilized Pd nanoparticles were synthesized by refluxing PS-*b*-PANa with H₂PdCl₄ in EtOH, producing a clear dark brown solution containing 3.0 ± 0.7 nm particles based upon TEM analysis.¹⁸³ Suzuki coupling reactions between 2-thiopheneboronic acid and iodobenzene were performed using a 0.6 mol% Pd catalyst loading with NEt₃ or NaOAc as the base, generating yields of 85% or 88%, respectively after 12.0 h under reflux.¹⁸³ Incidentally, the base influenced the stability of the Pd nanoparticles; NEt₃ provided additional nanoparticle stabilization, while NaOAc resulted in particle precipitation. As such, NEt₃ was used as base in subsequent Suzuki couplings between phenylboronic acid and bromothiophene using 3:1 acetonitrile-water as solvent. In this reaction, competitive

formation of the product (2-phenylthiophene) and homocoupling product (bithiophene) was observed, generating similar yields of 16% with no precipitation of Pd black.¹⁸³ In contrast, when PVP-Pd nanoparticles were employed for a similar reaction between bromothiophene and phenylboronic acid, only homocoupling products were generated; however, comparing the catalyst stability as a function of ligands, the PS-*b*-PANa-based nanoparticles were more stable than the PVP at these conditions as Pd black was not produced in the reaction.¹⁸³

PEG-stabilized Pd nanoparticles have also been employed for Suzuki coupling reactions in an aqueous medium between aryl halides and phenylboronic acid using K_2CO_3 as the base.⁹⁷ Initially, the reaction between *p*-bromoacetophenone and phenylboronic acid in a 1:5 dimethoxyethane (DME)/water solvent at room temperature generated the expected product with 95% isolated yield after 3.0 h. Subsequent reactions were performed in pure water using aryl halides with different electron-donating and electron-withdrawing groups, producing excellent yields within 2.0 h of reaction.⁹⁷ For instance, near quantitative yields were obtained for aryl iodides within 0.5 h of reaction at room temperature, indicating a superior catalytic reactivity for the nanocatalyst. On the other hand, higher temperatures were required for conversion of sterically hindered aryl bromides, while aryl chlorides were unreactive. Recycling of the catalyst was studied using the aqueous extract retained from product purification. Unfortunately, significant loss of catalytic activity was recorded from these systems with decreased yields from 90% to 40%.⁹⁷ This was attributed to metal leaching or incomplete extraction of the nanocatalyst.

Imidazolium-based ionic polymer-stabilized Pd nanoparticles in the functionalized Pd-IP-IL described above were also used in Suzuki coupling at 100 °C.¹³⁵ Aryl iodides, containing electron-donating or electron-withdrawing groups, were reacted with phenylboronic acid generating coupled products from 82% upto >99% using a 1.0 mol% Pd loading. As expected, lower yields were observed for substituted aryl bromides using similar reaction conditions, ranging from 6% to 99%.¹³⁵ On the other hand, when iodobenzene and bromobenzene were used, 90% and 55% yields were produced after 6 h of reaction.¹³⁵ Consequently, when the reaction was performed in water at 35 °C using aryl benzoic acids, the amount of Pd nanocatalyst required was reduced from 1.0 mol% to 0.5 mol%. Interestingly, the yields of the expected products for the aqueous-based reactions were similar to the yields of reactions in ionic liquids such that >99% yield was generated for iodobenzoic acid and 57% yield for bromobenzoic acid.¹³⁵ This suggests that the solvent played only a minor role in controlling the reactivity.

Seed-mediated nanoparticle synthesis methods in the ionic liquids were also used to prepare larger diameter (~10 – 20 nm) Pd nanoparticles (termed Pd-IP-IL-2).¹³⁵ These materials were then employed for Suzuki coupling between aryl iodides and phenylboronic acid wherein almost quantitative yields were obtained, similar to the yields noted for the initial Pd-IP-IL nanocatalysts. As expected, significantly lower yields were obtained when aryl bromides were employed as the substrate instead of the iodo-derivatives.¹³⁵ TEM analysis of the nanocatalyst after the coupling reaction revealed that the particle size decreased to ~5.0 nm, suggesting that the reaction was driven via the catalytic leaching mechanism.¹³⁵

A unique polymer-stabilized Pd nanocatalysts was prepared using polyaniline nanofibers (PANI), shown in Figure 1.11a, that function as both the reducing agent and particle support.¹⁸⁴ The synthesis was accomplished by incubating the metal precursor ($\text{Pd}(\text{NO}_3)_2$) with an aqueous dispersion of PANI nanofibers for one day. This reaction results in the formation of polycrystalline particles (Figure 1.11b) with a bimodal size distribution with two populations centered at ~ 2 nm and ~ 75 nm.¹⁸⁴ Once fully characterized, the Pd-PANI nanocatalyst system was then used for the coupling of aryl chlorides and phenylboronic acid with NaOH as the base in water at 80 – 100 °C for 2 – 6 h.¹⁸⁴ Using a highly activated substrate, 4-chlorobenzaldehyde, almost quantitative yields were obtained in the Suzuki reaction with phenylboronic acid.¹⁸⁴ On the other hand, when a deactivated substrate such as 4-chlorophenol was used for the reaction, a significant yield of 88% was generated.¹⁸⁴ Hetero-substituted substrates such as pyridyl chloride also generated yields of 89% and 96% of the expected coupling products from 4-chloropyridine and 2,6-dichloropyridine substrates, respectively.¹⁸⁴ The effect of changing the boronic acid substituent was also explored using the Pd-PANI nanoparticles such that when activated 3,5-di(trifluoromethyl)phenylboronic acid was used, a 92% yield was generated, while using 2,4-dimethoxyphenylboronic acid only produced a 70% product yield.¹⁸⁴ Taken together, these results indicate that this approach generated a highly reactive nanocatalyst, as aryl chlorides do not usually undergo coupling reactions under such mild conditions.

To further test the reactivity of the Pd-PANI nanoparticles, 1,4-difluorobenzene was used as substrate for coupling with phenylboronic acid as illustrated in Figure 1.9e. As expected, the Suzuki reaction using the fluoro-substituted substrates were much slower

compared with the aryl chlorides due to the stronger C-F bond. Remarkably, after 24 h at 100 °C, 60% product yield was obtained, whereas when fluorobenzene and phenylboronic acid were used for coupling reaction, 80% yield of the biphenylproduct was generated.¹⁸⁴ Finally, recycling of the nanoparticles was also accomplished, as studied using the coupling of 4-acetylphenyl chloride and phenylboronic acid. For this, minimal loss of activity was observed after ten reaction cycles, generating $\geq 89\%$ product yields with no noted catalyst aggregation as observed in the TEM analysis of the particles after two reaction cycles.¹⁸⁴ The decreased product yield was attributed to the degradation of the nanofiber support after several catalytic cycles.

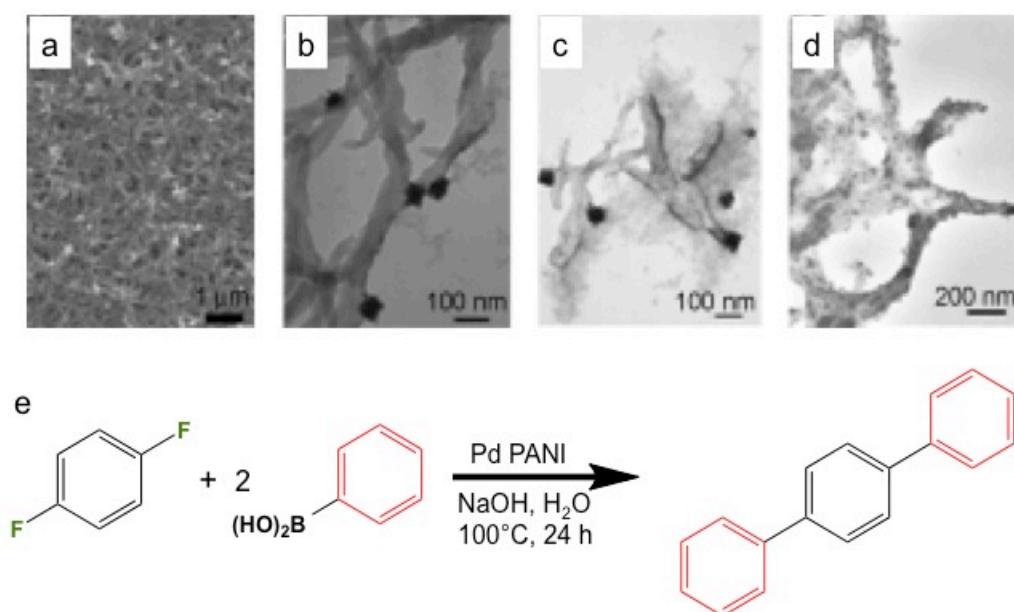


Figure 1.11 a) SEM image of PANI nanofibers, TEM images of Pd-PANI nanoparticles b) before the reaction, c) halfway through the reaction, and d) after two reaction cycles. e) Suzuki coupling reaction between 1,4-difluorobenzene and phenylboronic acid using Pd-PANI nanoparticles.¹⁸⁴ Reproduced with permission from ref 184. Copyright © 2007 WILEY-VCH Verlag GmbH & Co. KGaA, Weinheim.

While synthetic PANI was an excellent support for the catalytic nanoparticles, biologically derived nanofibers such as bacterial cellulose (BC) can also be used.¹⁸⁵ BC was produced by fermentation of *Acetobacter xylinum* with glucose as the carbon source.¹⁸⁵ The three-dimensional nanofibers interacted with metal ions to serve as a support for nanoparticle production. The one-pot synthesis involved mixing of metal precursors with BC nanofibers under an N₂ atmosphere at 140 °C.¹⁸⁵ Once complete, NaBH₄ was added, producing polydispersed, ~20 nm Pd nanoparticles deposited on the nanofibers (termed Pd-BC).¹⁸⁵ Initial catalytic analysis of the materials was performed using the coupling of iodobenzene and phenylboronic acid, generating almost quantitative yields of 98% after 3.5 h at 85 °C.¹⁸⁵ Recycling experiments using the same reactants showed no loss of activity after two reaction cycles with no visible Pd aggregation as observed by TEM; however, similar to the Pd-PANI nanoparticles, a decline in the quality of the nanofiber support was observed after extended recycling runs that resulted in lower product yields.¹⁸⁵

Suzuki reactions using aryl iodide and substituted phenylboronic acids were also studied with the Pd-BC nanocatalyst, which generated excellent yields between 88 – 99% of the expected coupling products depending on the substituent attached on the nucleophile.¹⁸⁵ To this end, when 3-methoxyphenylboronic acid was used in the reaction with iodobenzene, a 99% yield was obtained, whereas using 4-cyanophenylbenzoic acid generated a yield of only 88%.¹⁸⁵ Recycling experiments were again performed for the Pd-BC nanoparticles using the substituted nucleophiles wherein product yields > 86% were obtained after five catalytic.¹⁸⁵ To further explore the reactivity of Pd-BC nanoparticles, the least reactive substrate, aryl chloride, was employed for Suzuki

coupling with different substituted phenylboronic acids. Surprisingly, product yields between 75 – 92% were recorded, indicating that an extremely efficient nanocatalyst was developed.¹⁸⁵ Finally, leaching of the active catalyst was also studied using inductively coupled plasma – atomic emission spectroscopy (ICP-AES) analysis wherein the amount of Pd species before and after the five reaction cycles was quantitated. The results showed that the Pd concentration before the reaction was 5.29% and 5.26% after the reaction, indicating a negligible amount of Pd was leached during the reaction.¹⁸⁵ As such, the results of elemental analysis suggested that the BC nanofibers are good protecting ligands for the nanoparticles.

The Pd-substituted Keggin-type polyoxometalate-based nanoparticles, described above, were also used for the Suzuki reaction.¹⁷⁶ For this, aryl bromides and phenylboronic acid were reacted in an EtOH/water solvent with diisopropylamine as the base. Nearly quantitative yields of the expected biaryl coupling products were obtained for a variety of aryl bromide substrates in the reactions, which were heated to temperatures between 80 – 85 °C.¹⁷⁶ For example, the coupling reaction between 1-bromo-4-nitrobenzene and phenylboronic acid generated >99% yield of 4-phenylnitrobenzene product, while using 4-bromotoluene gave an 89% yield of 4-phenyltoluene, revealing the effects of electron-withdrawing and electron-donating groups on substrate reactivity.¹⁷⁶ On the other hand, when 1-chloro-4-nitrobenzene was employed as the starting material under similar reaction conditions, a 98% product yield was generated demonstrating the reactivity of the materials toward difficult to use substrates.¹⁷⁶

The effects of different stabilizers on the reactivity of Pd nanoparticles for the Suzuki reaction were also investigated using hydroxyl-terminated PAMAM dendrimers.¹⁸³ The

preparation of dendrimer-encapsulated Pd nanoparticles was similar to the process described by Crooks and coworkers, albeit with some modifications.¹⁸³ To this end, the hydroxyl-terminated PAMAM-dendrimer solution was added with an appropriate amount of K_2PdCl_4 ; prior to reduction, the pH of the solution was adjusted to 4.0 using HCl to ensure the coordination of Pd^{2+} ions with the interior tertiary amines of the polymer. Upon reduction using $NaBH_4$, 1.4 nm particles were formed using third (G3-OH(Pd)) and fourth generation (G4-OH(Pd)) hydroxyl-terminated dendrimers, while bigger nanoparticles (3.6 nm) were formed from second generation dendrimers (G2-OH(Pd)).¹⁸³ The Pd nanoparticles were then employed in the Suzuki coupling of phenylboronic acid (or 2-thiopheneboronic acid) and iodobenzene in 40% EtOH under reflux for 24.0 h. The results demonstrated that the G4-OH(Pd) nanoparticles were less efficient, generating $\leq 35\%$ of the expected products, compared with the G3-OH(Pd) and G2-OH(Pd) nanoparticles, which produced $\geq 69\%$ yields.¹⁸³ Interestingly, precipitation of inactive Pd black was generated during the reaction when using G3-OH(Pd) and G2-OH(Pd) nanoparticles; however, no such catalyst aggregation was observed for G4-OH(Pd) nanoparticles catalytic reaction. These results suggested that a trade off between catalyst stability and efficiency existed, wherein the fourth generation nanoparticles were more stable with limited substrate access to the metal surface; however, for the lower generation structures, higher catalytic efficiency and diminished stability was noted.¹⁸³ Among these materials, the third generation dendrimer provided the optimal mix of materials stability and catalytic efficiency, although Pd black formation was observed when using 2-thiopheneboronic acid as the substrate. This effect is possibly due to Pd

leaching during the reaction or through the thiol moiety of the substrate coordinating to the metallic material.

In another study of the hydroxyl-terminated dendrimer materials, Christensen and colleagues prepared the same dendrimer-based Pd nanoparticles using fourth generation dendrimers, where particles of ~3 nm were generated.¹⁸⁶ These structures were then employed for the coupling of iodobenzene and *p*-tolylboronic acid at 78 °C using EtOH as solvent. From this study, product yields of 98% were determined, thus a more efficient catalytic system was obtained using the nearly identical dendrimer-based materials,¹⁸⁶ which may arise from the different reagents employed. Interestingly, no precipitation of Pd black was noted during the reaction. Aryl bromides were also studied using this system; however, they were not as reactive as the iodo-based substrates, requiring higher temperatures and longer reaction time. Aryl chlorides were also shown to be completely unreactive.¹⁸⁶ Finally, the recyclability of the nanocatalyst was studied using the coupling of ethyl-4-iodobenzoate and *p*-tolylboronic acid wherein formation of Pd black during the subsequent reactions was observed resulting in decreased product yield, from 99% to 80%, after the third reaction cycle.¹⁸⁶

The Astruc group has developed a unique dendrimer-stabilized Pd nanoparticle system using 1,2,3-triazolylsulphonate dendrimers, synthesized through click chemistry.¹⁸⁷ In this system, Pd²⁺ was introduced to the triazole ligands producing two absorption bands in the UV-vis spectrum at 208 and 235 nm. Upon addition of NaBH₄, Pd nanoparticles of ~2 – 3 nm in diameter were generated using three different dendrimer generations (Pd-DSN-G₀, Pd-DSN-G₁, Pd-DSN-G₂).¹⁸⁷ TEM analysis showed that the nanoparticles sizes were larger than the size of the ligands, thus leading to a large degree of polydispersity

from the materials as the generation of the dendrimers increases. Room temperature Suzuki coupling reactions between iodobenzene and phenylboronic acid in a water/ethanol solvent were used to examine the reactivity of the dendrimer-stabilized materials. Using a 0.1 mol% Pd loading, product yields of 96%, 95%, and 70% were obtained using Pd-DSN-G₀, Pd-DSN-G₁ and Pd-DSN-G₂, respectively, suggestive of a decrease in catalytic efficiency with respect to increasing dendrimer generation.¹⁸⁷ Similar trends were observed when lower Pd loadings (0.01 mol%) were used in the reaction. TOF analysis employing the Pd-DSNs indicated that there was no significant difference in the values based upon dendrimer generation; however, significantly higher TOFs of 1167 – 1533 mol PhI (mol Pd × h)⁻¹ were obtained for the reaction employing 0.01 mol% Pd, while TOF values of 117 – 167 mol PhI (mol Pd × h)⁻¹ were generated when using 0.1 mol% Pd, demonstrating an effect based upon the Pd loading.¹⁸⁷ From on these results, the catalytic mechanism of Pd-DSNs was suggested to follow an atom-leaching process wherein the TOF values of the reaction decreases as the amount of Pd loading increases. Quantitative yields were also obtained in the coupling reaction using bromobenzene, but the reaction needed to be heated to 100 °C.¹⁸⁷

The phosphine-based dendrimers, G_nDenP-Pd, whose synthesis was discussed above, have also been used for Suzuki coupling.⁹³ The reaction between bromobenzene and phenylboronic acid was initially tested with different bases such as NEt₃, NaOAc, K₂CO₃, and K₃PO₄ to optimize the reaction conditions. As such, K₃PO₄ was determined to be the best base for the Suzuki reaction using the G_nDenP-Pd in dioxane as the solvent under refluxing conditions. Aryl iodides and aryl bromides with electron-withdrawing or electron-donating groups were reacted with different phenylboronic acids, which

generated nearly quantitative yields ($\geq 94\%$) of the expected coupling products using G₂DenP-Pd nanoparticles; however, when the reaction was performed using electron-deficient arylboronic acids, slightly lower yields of 88% to 92% were obtained.⁹³ Interestingly, sterically hindered ortho-substituted aryl halides generated excellent product yields between 86 – 99%.⁹³ Expanding the scope of G_nDenP-Pd catalytic activity to coupling reactions between different aryl chlorides and phenylboronic acid using G₃DenP-Pd nanoparticles resulted in good to excellent yields (81 – 94%) even with deactivated or ortho-substituted substrates.⁹³ Using heteroaryl bromides and chlorides as substrates in Suzuki coupling also generated excellent yields using G₃DenP-Pd nanoparticles, such as shown in the coupling between pyridine-derived aryl bromide and phenylboronic acid to generate phenylpyridine product. Interestingly, even pyridine-derived aryl chloride produces the expected product with an 82% yield.⁹³

The recyclability of the G₃DenP-Pd nanoparticles was also explored using 0.2 mol% of the catalyst in a model reaction between 4-hydroxyphenyl iodide and phenylboronic acid.⁹³ Using these materials, no loss of activity was observed during the first four cycles. Lower reaction yields were recorded after the fifth run (79% yield), but when the subsequent cycles were allowed to proceed at longer reaction times (from 20 h to 48 h), excellent product yields (94%) were generated for three cycles before decreased activity was observed, generating only 75% yield after the ninth cycle.⁹³ Furthermore, only a very small amount of Pd was leached during the recycling activity as measured by inductively coupled plasma X-ray fluorescence (ICP-XRF); however, TEM analysis of the nanoparticles after nine runs showed an increased particle size with irregular shape, which was suggestive of particle aggregation.⁹³

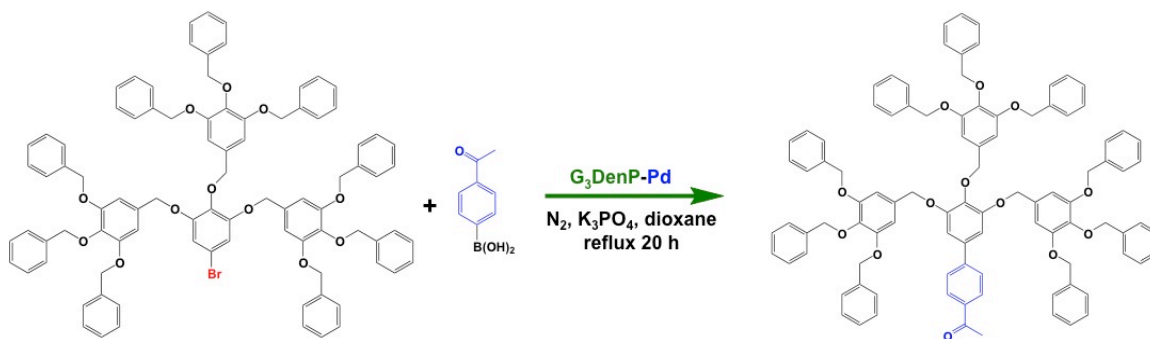


Figure 1.12 Suzuki coupling reaction using dendritic bromobenzene and 4-acetylphenylboronic acid.⁹³

The role of GnDenP-Pd nanoparticles in the coupling reaction was further probed by using a bulky dendritic aryl bromide substrate and 4-acetylphenylboronic acid (Figure 1.12) to determine the catalytic mechanism.⁹³ The bulky substrate was anticipated to ascertain if the catalytic reaction occurred on the metal surface inside the dendritic cage or through potentially leached Pd species. To this end, the formation of the coupling product will be minimized if the reaction mainly occurs on the nanoparticles surface. On the other hand, Suzuki coupling between the dendritic aryl halide and phenylboronic acid will proceed smoothly if the reaction follows the atom-leaching mechanism.

Interestingly, the results generated 96% yield of the coupling product, suggesting that the Suzuki reaction could not occur completely inside the dendritic box due to the bulky aryl substituent.⁹³ As such, the catalytically active Pd atom species must be leached from the G₃DenP-Pd nanoparticles during the reaction, resulting in near quantitative yields for the dendritic aryl halide substrate. To validate the results, a homogeneous catalytic complex, Pd(PPh₃)₄, was employed to drive a control analysis using the same bulky aryl halide and phenylboronic acid under similar reaction conditions. The results from this study

provided a 79% yield of the expected product, which was lower than the yield for G₃DenP-Pd nanoparticles.⁹³ These results suggested that the catalytic mechanism for G₃DenP-Pd nanoparticles was similar to the homogeneous catalyst although the former was much more efficient than the latter.

In a different synthetic approach, Pd nanoparticles were generated using perthiolated cyclodextrin (β -SH-CD) as surface passivants, where the materials were reactive for Suzuki coupling (Figure 1.13).⁹⁸ In this process, the metal precursor was added to a solution containing NaBH₄ and β -SH-CD in DMF, which resulted in the formation of 3.5 nm CD-capped Pd nanoparticles. The Suzuki coupling between aryl halides and arylboronic acid in a 1:1 (v/v) acetonitrile/water solvent were performed using the Pd nanoparticles under reflux for 2 h. Nearly quantitative yields were obtained for aryl iodides with different functional groups and, as expected, lower yields were obtained from aryl bromides even after longer reaction times.⁹⁸ TOF analysis demonstrated values ranging from 7.8 to 48 mol product (mol Pd \times h)⁻¹. These decreased values were likely due to the covalently bound CD ligands, which covered ~50% of the active surface, thus making it inaccessible for substrate interaction.⁹⁸

Another unique Suzuki reaction using these materials was performed using iodoferrocene, which can interact to form stable inclusion complexes with the surface-bound CD, as illustrated in Figure 1.13.⁹⁸ In the presence of Ba(OH)₂ as the base under an N₂ atmosphere, the coupling reaction between iodoferrocene and phenylboronic acid was performed using 1 mol% CD-capped Pd nanoparticles, generating a 70% isolated product yield of the product, phenylferrocene.⁹⁸ The attachment of the iodoferrocene to the CD receptor on the nanoparticle surface trapped the substrate at the active metal site,

thus generating high product yields. In this regard, a control reaction was performed wherein ferrocene was added to the system to compete with iodoferrocene for available CD receptors, resulting in a much lower product yield.⁹⁸ This nanoparticle system employed CD receptors as both a nanoparticle stabilizer and as a reagent gatekeeper wherein the specific binding between the receptor and substrates controlled the reactivity, leading to high degrees of specificity.

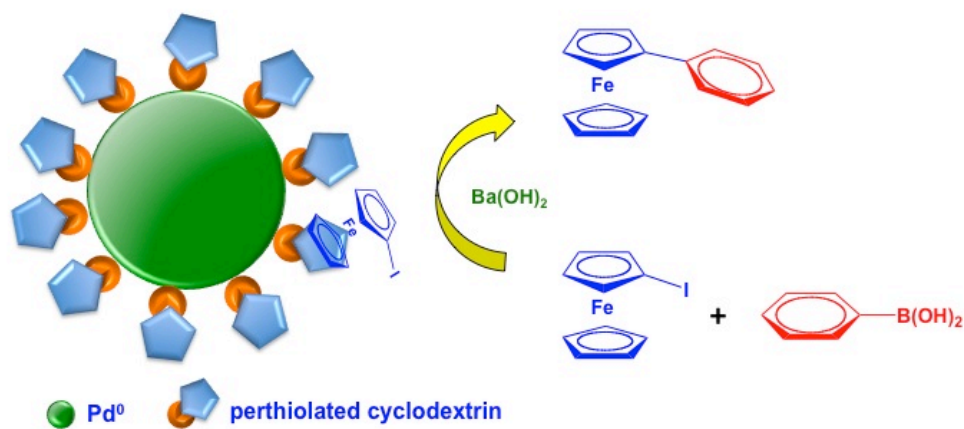


Figure 1.13 Perthiolated cyclodextrin-capped Pd nanoparticles used in the Suzuki coupling reaction between iodoferrocene and phenylboronic acid.⁹⁸

1.6 Pd Nanoparticles in Heck Coupling Reaction

Development of Pd nanoparticles for Heck coupling was pioneered by Reetz and coworkers wherein they used tetraalkylammonium salts such as $(C_8H_{17})_4NBr$ instead of organic phosphine, as stabilizers for soluble Pd clusters.¹⁸² Synthesis of the ligand-stabilized Pd nanoparticles was described above wherein 2 – 3 nm particles were produced.¹⁸² Heck coupling between iodobenzene and the acrylic acid n-butyl ester was performed using these materials in DMF at 30 °C to produce cinnamic acid ester. Nearly

quantitative product yields were generated after 14 h, providing initial catalytic results for the phosphine-free Pd nanocatalysts.¹⁸²

In expanding the scope of reactivity in Heck coupling using Pd nanocatalysts, another stabilizer was employed for the synthesis of nanoparticles using an electrochemical method and thermolysis.¹⁸⁸ For this, propylene carbonate (PC) was used for the production of Pd nanoclusters through electrochemical methods involving anodic dissolution of a Pd sheet at 60 °C, which formed monodisperse, nearly spherical, highly crystalline particles of 8 – 10 nm in diameter.¹⁸⁸ In a separate process, Pd(O₂CMe)₂ was mixed with PC at 100 °C while sonicating to form 8 – 10 nm particles with similar shapes through thermal decomposition. The catalytic activities for the PC-Pd nanoparticles were tested using the Heck reaction between aryl halides and styrene in the presence of a base at temperatures ranging from 130 – 160 °C.¹⁸⁸ The results showed excellent product yields of 96% and 97% for activated 4-bromonitrobenzene substrate in the presence of PC-Pd nanoparticles using NEt₃ and NaO₂CMe as the base, respectively. On the other hand, chlorobenzene was also able to generate significant product yields between 40% to 58%, but longer reaction times were required.¹⁸⁸

Dendrimer-based Pd nanoparticles have also been used for the Heck reaction; however, the higher temperatures that were required to accomplish the coupling necessitated the use of highly stable dendrimers.¹⁸⁹ As such, poly(propylene imine) (PPI) dendrimers were employed to passivate the Pd nanoparticles for reactions that require refluxing. The perfluorinated polyether-derivatized PPI DENs (third and fifth generation) were exposed to Pd²⁺ ions to coordinate to the dendrimer interior. Addition of a reducing agent resulted in the production of nearly monodisperse Pd nanoparticles of ~2 – 3 nm in diameter

according to TEM analysis.¹⁸⁹ The PPI-Pd nanoparticles were then used for Heck coupling between different aryl halides and n-butylacrylate to generate n-butyl-formylcinnamate using a fluorocarbon/hydrocarbon solvent and Et₃N as base at 90 °C. The results indicated that the PPI-Pd nanocatalyst was able to drive the coupling reaction generating modest yields; however, regioselectivity of the product was established to be 100% selective toward trans-n-butyl-formylcinnamate.¹⁸⁹ Interestingly, the fifth generation PPI-Pd nanoparticles catalyzed higher product yields compared with the third generation PPI-Pd nanoparticles even though the diameters of the particles were similar.¹⁸⁹ These results suggested that the fifth generation dendrimers provided larger encapsulated space wherein the coupling reaction could occur leading to the observed regioselectivity and higher product yields. In contrast, the third generation dendrimers contained less interior room such that slower reactions occurred, lowering the product yields. Nevertheless, product regioselectivity was maintained. As anticipated, lower yields were obtained when using aryl bromides compared with aryl iodides and no activation of aryl chlorides was noted.¹⁸⁹ Finally, para-nitro-substituted aryl bromides generated lower product yields compared with unsubstituted aryl reagents, which was attributed to the repulsive forces between the electron-donating nitro-group and the perfluorinated polyether dendrimer groups, making substrate incorporation difficult.¹⁸⁹ Taken together, these results suggested that Heck coupling using the PPI-Pd nanoparticles occurred at the dendrimer interior.

Since the reaction using the dendrimer nanocatalysts was performed in a fluorocarbon/hydrocarbon solvent, separation and recovery of the PPI-Pd nanoparticles was easily achieved.¹⁸⁹ To this end, the nanocatalysts remained dissolved in the fluoruous

phase of the solvent, as shown by the retention of the dark color of the catalyst, while the organic phase that contained the product was colorless. Recyclability of the nanocatalyst was performed using the separated particles in the fluoruous phase wherein significant loss of activity was observed with each reaction cycle.¹⁸⁹ This loss in reactivity was attributed to changes in the morphology of the Pd nanoparticles due to the redox cycling of Pd atoms in the Heck reaction. Control reactions were also performed to determine the effect of base identity on the reaction.¹⁸⁹ These results showed that even in the absence of Et₃N in the reaction, Heck coupling still occurred due to the interior tertiary amines in the dendrimers that acted as the base. Overall, the results of these initial studies of Pd DENs for Heck coupling showed highly regioselective intradendrimer catalytic reactivity under relatively ambient reaction conditions.

Further DEN effects for Pd nanoparticles were performed by Kaneda *et al.*, wherein the Pd complex was immobilized inside the dendrimer through ionic bonds (Figure 1.14).⁹¹ Initially, the peripheral amino groups of PPI dendrimers were functionalized with decanoyl chloride and 3,4,5-triethoxybenzoyl chloride to produce alkylated and arylated dendritic materials, respectively. On the other hand, Pd nanoparticles were exposed to 4-diphenylphosphinobenzoic acid as ligands, which can then form ionic bonds between the carboxylic acid moiety and the internal amino groups of the dendrimers. To this end, the phosphine-stabilized Pd nanoparticles were encapsulated at the interior of the functionalized PPI dendrimers and employed as nanocatalysts in the Heck reaction.⁹¹ Initially, the coupling between iodobenzene and n-butyl acrylate in toluene with KOAc was performed with the PPI modified Pd DENs. The results of the reaction showed that the dendrimer generation directly affected the reactivity where the reaction rate increased

with higher generations; however, when the molar ratio of phosphine ligand: Pd in the 5th-generation PPI Pd nanoparticles was increased from 1 to 4, product yields decreased from 92% to 19%.⁹¹ These results suggested that the large amounts of amino groups in higher generation dendrimers provided complexation with the active species and as such led to high stability and catalytic reactivity.

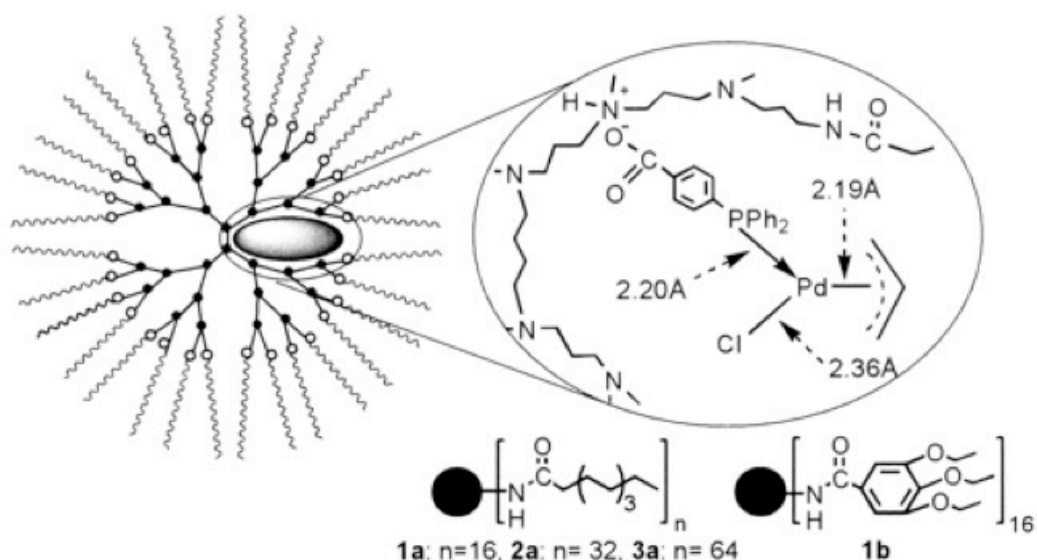


Figure 1.14 Schematic illustration of the Pd complex immobilized inside the dendrimer.⁹¹ Reprinted (adapted) with permission from ref. 91. Copyright 2004 American Chemical Society.

To further probe the reactivity, as well as the selectivity of the nanocatalyst, a second Heck coupling reaction was employed using *p*-diiodobenzene and *n*-butylacrylate with two possible products, mono- and di-substituted benzene.⁹¹ The results showed that in the presence of the nanocatalyst, only *n*-butyl-*p*-iodocinnamate, the mono-substituted product, was formed, indicating a highly reactive (86% yield) and selective (92%) nanocatalyst. Furthermore, the allylic amination of cinnamyl methyl carbonate was also catalyzed by the Pd DENs, demonstrating that the catalytic materials were quite

versatile.⁹¹ Finally, the recyclability of the catalyst was established wherein minimal loss of activity was observed after four reaction cycles.⁹¹

Expanding the scope of reactivity of the PPI-Pd nanoparticles for Heck coupling under environmentally friendly conditions was achieved using supercritical CO₂ (scCO₂) as the solvent.¹⁹⁰ The PPI dendrimer end groups were functionalized with a perfluoro-2,5,8,11-tetramethyl-3,6,9,12-tetraoxapentadecanoyl perfluoropolyether chain to enhance solubility with scCO₂, generating 1 – 2 nm Pd particles after reduction.¹⁹⁰ The modified PPI-Pd nanoparticles were then used as the coupling catalyst between iodobenzene and methylacrylate with Et₃N as the base at 75 °C and 5000 psi.¹⁹⁰ Formation of the possible products, methyl-2-phenylacrylate and cis/trans-cinnamate, was monitored using GC wherein 57% of the aryl iodide was consumed after 24 h.¹⁹⁰ Characterization of the reaction solution by ¹H NMR revealed that only the methyl-2-phenylacrylate product was formed and no cinnamate products or impurities were generated. These results indicated high selectivity for the nanocatalyst, which was attributed to steric environment of the dendrimer system.¹⁹⁰

Calculation of the turnover number (TON) generated a value of ~22 mol substrate/mol Pd only, which was suggestive of a slow reaction using the modified-PPI Pd nanoparticles.¹⁹⁰ A notable change in color of the scCO₂ solution containing the nanoparticles from dark-brown to dull-orange was observed after the reaction, which likely arises from Pd⁰ oxidized to Pd²⁺.¹⁹⁰ Upon treatment of this solution with NaBH₄, the formation of a dark-brown solution was observed, consistent with metal reduction and nanoparticle formation. The oxidation of the catalytically active Pd species explained the

low catalytic conversion driven by the modified PPI-Pd nanoparticles. When the reaction was extended to 52 h, no visible Pd precipitation was observed.¹⁹⁰

In contrast to the low TON values obtained in the Heck coupling reaction using the modified PPI-Pd nanoparticles, drastically higher TONs were generated using Pd-DENs with hydroxyl-terminated PAMAM dendrimers; however, the reaction was performed using DMA as the solvent instead of $scCO_2$.⁹² In this system, the reaction between aryl halides and acrylic acid was employed to determine the reactivity of Pd@[PAMAM G4-OH] in the presence of NaOAc as the base at 140 °C. Two different Pd:dendrimer ratios, Pd₆₀ and Pd₄₀, were used for the reaction, where similar product yields were obtained for both systems.⁹² The results of the coupling reaction showed significantly higher TON values depending on the halogen group in aryl halides such that iodobenzene gave a value of 30,000 mol product/mol Pd, while bromobenzene generated a TON of 14,000 mol product/mol Pd.⁹² No product formation was observed for chlorobenzene. As expected, electron-withdrawing substituents on the aryl halide generated higher product yields and TONs, while decreasing the catalyst loading resulted in the corresponding decrease in yields and TON values.⁹²

Aside from Pd DENs, other ligand stabilized Pd catalysts have also been employed for Heck coupling. For instance, PEG-Pd nanoparticles were used for the coupling of *t*-butylstyrene with aryl iodides and aryl bromides in the presence of K_2CO_3 in water under refluxing conditions (80 – 100 °C).⁹⁷ The results demonstrated excellent yields of 90 – 92% for the reaction using activated iodo- and bromo-arenes. Interestingly, even sterically hindered ortho-substituted aryl bromides generated relatively good yields of 72 – 80%, while the meta-substituted substrates produced poor (5%) product yields when

coupled with *t*-butylstyrene.⁹⁷ Overall, the PEG-Pd nanoparticles showed high reactivity for Heck coupling under relatively mild reaction conditions with water as the solvent, indicating a positive development towards environmentally friendly, but highly efficient nanoparticle catalysts.

Another polymer-based catalytic system used for Heck coupling was the ionic polymer-ionic liquid stabilized Pd nanoparticles, Pd-IP-IL.¹³⁵ The 5 nm Pd-IP-IL nanoparticles were used in the Heck reaction between aryl halides and ethyl acrylate using tributylamine as the base in the ionic liquid at 80 °C. The results displayed quantitative yields (>99 %) of the expected products were obtained from activated aryl halides after only 2 h. Iodobenzene, on the other hand, only managed to generate 49% of the product after 1.5 h, while increasing the reaction time to 4 h showed a corresponding yield increase to 81%.¹³⁵ These results indicated that the ionic liquid was a great solvent for the Heck reaction and the use of Pd-IP-IL nanoparticles show excellent reactivity under ambient reaction conditions.

Finally, the Keggin-type polyoxometallate-stabilized Pd nanoparticles were also employed for the Heck coupling reaction.¹⁷⁶ Initially, the reaction between bromotoluene and styrene was performed employing diisopropylamine as the base in a water/ethanol solvent. Interestingly, excellent yields of 95% were obtained for the Heck coupling product, stilbene, at 80 – 85 °C after 16 h. When activated aryl chloride, 1-chloro-4-nitrobenzene, was used under similar reaction conditions, a 91% product yield was obtained.¹⁷⁶ Similarly, for the Heck reaction between aryl halides and methyl acrylate, almost quantitative yields (97 %) of methyl cinnamate was generated from aryl bromide, while a 94% product yield was obtained using aryl chloride.¹⁷⁶ The mild reaction

conditions employed in the coupling reaction suggested a highly efficient nanocatalyst that was operational under environmentally friendly conditions.

1.7 Summary and Conclusions

In this chapter, we presented the recent advances in Pd nanoparticles research with regards to their applications in select C-C coupling reactions. Significant numbers of studies have been devoted in the development of new nanomaterials in the past few decades leading to the production of remarkably efficient nanocatalysts. The advantages of nanomaterials in catalytic transformations include the use of very low metal loading, their ability to catalyze reactions in ambient conditions, their use in energy-efficient reactions, and their recyclability with minimal activity loss; however, the catalytic mechanism driven by these Pd nanoparticles remains a subject of debate with two different theories suggested for C-C couplings. The surface-based mechanism invokes a truly heterogeneous catalyst in which the reaction occurs directly at the surface of the nanoparticles. As such, minimal morphological changes should be observed for these nanoparticles. In contrast, the atom-leaching mechanism indicates that the active Pd⁰ atoms are abstracted from the nanoparticle surface during the reaction. In this process, changes in size, shape and crystal structure should be observed during the catalytic cycle. Although each of these theories can be supported by available evidence, additional studies are necessary in order to verify the reaction mechanism. Compounding this issue, different reaction mechanisms may be possible for different materials, which may give rise to the disparate set of results present in the literature. Nevertheless, Pd nanoparticles

have demonstrated excellent reactivities for C-C coupling catalytic reactions, which may serve as model systems for the development of sustainable materials for future chemical transformations.

Chapter 2. Biomimetic Synthesis of Green Nanocatalyst for the Stille Coupling Reaction

2.1 Overview of Study

In this chapter, the results of the study on the biomimetic synthesis of Pd nanoparticles for use as models of green catalytic systems were presented. The nanomaterials are synthesized using peptides isolated via phage-display techniques that are specific to Pd surfaces. Using this synthetic strategy, peptide functionalized Pd nanoparticles of 1.9 ± 0.3 nm in diameter are produced, which are soluble and stable in aqueous solutions. Once characterized, these bio-based materials were then used as catalysts to drive the formation of C-C bonds using the Stille coupling reaction. Under the conditions of an aqueous solvent at room temperature, quantitative product yields were achieved within 24.0 h employing catalyst loadings of ≥ 0.005 mol% Pd. Additionally, high TOF values of $3,207 \pm 269$ mol product $(\text{mol Pd}\cdot\text{h})^{-1}$ have been determined for these materials. The catalytic reactivity was then examined over a set of substrates with substitutions for both functional group and halide substituents, demonstrating that the peptide-based Pd nanoparticles are reactive towards a variety of functionalities. Taken together, these bio-inspired materials represent unique model systems for catalytic studies to determine ecologically friendly reactive species and conditions.

2.2 Motivation

The fabrication of green catalysts that address environmental and energy concerns is both strategically and ecologically important.^{50, 51} Traditional homogenous and heterogeneous catalysts used on the industrial scale produce toxic waste materials that necessitate

specialized disposal means and can require thermal activation for reactivity, both of which can result in inflated production costs. To alleviate these costly conditions, highly active green catalytic systems that employ an aqueous medium at room temperature with low catalyst loadings are desirable.⁵² Metallic Pd nanoparticles have demonstrated some positive progression towards these goals;^{86, 187, 191} however, it is rare for one system to address all three principles simultaneously. One further compounding issue is the fact that different catalyst structures can be required for their individual activity;^{32, 192} therefore, a “magic bullet” system that can be employed for all reactions is unlikely. As a result, different catalytic architectures may be required for specific reactions, depending upon their structure-based functionality; however, a subset of reactions that follow similar pathways may be addressable by a single generated catalytic structure.

One area where a green reaction system is attractive is for catalytic C-C bond formation. A variety of reactions have been developed such as Stille coupling, Suzuki coupling, and Heck coupling that use Pd catalysts of similar morphologies.^{52, 86, 187, 191, 193} These reactions traditionally require single molecule Pd catalysts, either in zerovalent state or a Pd²⁺ oxidation state that is reduced *in situ*, which require high thermal activation temperatures (70-100 °C) and organic solvents such as toluene.^{52, 175} Since similar reaction mechanisms have been proposed for these reactions with only slight changes in specific steps, it may be possible to design and develop a single catalytic architecture that is functional for a select number carbon coupling reactions using green conditions. This would be highly desirable as these reactions are used as necessitated by the functionalities and specific reaction steps required during chemical synthesis. Previous results employing Pd nanomaterials as the catalyst with different surface protection techniques have

demonstrated a degree of success with these reactions individually.^{52, 86, 141, 187, 191, 192, 194-196}

Unfortunately, ideal materials that fully address the principles of green C-C coupling catalysis have yet to be isolated.

In contrast, biological systems have developed ambient synthetic routes to reactive nanostructures.¹⁹⁷⁻²⁰⁰ Through biomineralization processes,^{200, 201} highly intricate nanomaterials can be produced for structural, catalytic, and bioremediation purposes.

While a select number of inorganic minerals are fabricated biologically, a complete set of technologically interesting materials is not produced. To overcome this limitation, phage display technologies have been developed as a means to expand the toolkit of bionanotechnology through the isolation of non-natural peptide sequences with the ability to control the fabrication of nanomaterials under biological conditions.^{197-199, 202-205} From

this method, peptides responsible for the production of Ag,¹⁹⁹ Au,²⁰⁶ FePt,²⁰⁵ BaTiO₃,²⁰² as well as other technologically interesting materials have been elucidated. The synthetic methodologies employed for biomimetic fabrications are relatively green and produce quality nanomaterials with exacting control over their final structural properties.^{203, 207-210}

Indeed, multicomponent functional nanostructures have been fabricated such as PdAu bimetallic catalysts,²⁰⁹ Pt-CdS enzyme mimics,²¹¹ and Au-Co₃O₄ bio-batteries.²⁰³ These unique structures possess their intrinsic activities under biological-based conditions, suggesting that their activities can be tailored to address green technologies. While these materials may not be immediately feasible to replace current technologies, their final products can act as model systems to generate an understanding of the structure required for specific functionality. This may lead to the realization of next generation materials to address the current global environmental and energy concerns.

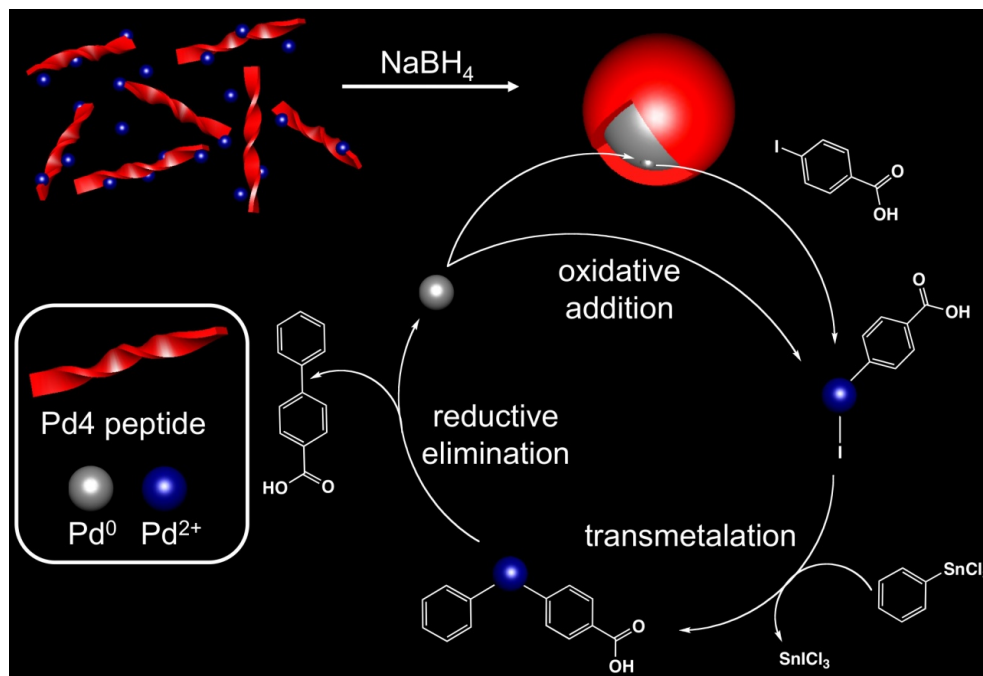


Figure 2.1 Biomimetic synthesis of Pd nanoparticles and their use for green Stille coupling.

Here we demonstrate that peptides isolated via phage-display are able to mediate the production of highly active model green Pd nanocatalysts, as shown in Figure 2.1. Using the peptide-based system, nearly monodisperse, and aqueously soluble peptide stabilized Pd nanoparticles are synthesized with a small average particle diameter of 1.9 ± 0.3 nm. This particle size is optimal for catalytic designs as it maximizes the surface-to-volume ratio without reaching the molecule to particle electronic transition of small nanomaterials.³² These nearly monodisperse bio-based nanoparticles were then catalytically tested for C-C bond formation activity using Stille coupling^{175, 212} under environmentally friendly reaction conditions. From this analysis, quantitative catalytic formation of C-C bonds was observed within 24.0 h in water, at room temperature, using catalyst loadings of ≥ 0.005 mol% Pd. These results are important as this representative system addresses all three green concerns, which is likely due to the peptide-metal

surface structure that can allow for interactions between the catalytic surface and the reagents in solution.²¹³ In addition, we demonstrate that the bio-inspired Pd materials are active with a variety of substrates, suggesting that the system is versatile and may translate to various other chemical reactions.

2.3 Methods

2.3.1 Chemicals

All Fmoc-protected amino acids used in peptide synthesis were purchased from Advanced ChemTech (Louisville, KY). NaBH₄ was purchased from EMD (Gibbstown, NJ), K₂PdCl₄, 2-iodobenzoic acid, 4-bromobenzoic acid, 4-iodophenol, and 4-tert-butylphenol were purchased from Sigma-Aldrich (Milwaukee, WI), and 4-iodobenzoic acid, 3-iodobenzoic acid, 4-chlorobenzoic acid, 4-bromophenol, 4-chlorophenol were purchased from TCI America (Wellesley Hills, MA). Phenyltin trichloride, N-methyl-N-(trimethylsilyl)trifluoroacetamide (MSTFA), CCl₃D, anhydrous Na₂SO₄, NaCl, and KOH were purchased from Fisher (Pittsburgh, PA). All reagents were used as received. Milli-Q water (18mΩ•cm; Millipore, Bedford, MA) was used throughout.

2.3.2 Peptide Synthesis

The Pd4 peptide was prepared using a Tetras peptide synthesizer (CreoSalus, Louisville, KY) employing standard Fmoc peptide synthesis protocols.

2.3.3 Preparation of Pd Nanoparticles

The Pd nanoparticles were prepared as follows. 100 μL of a 10.0 mg/mL Pd4 peptide solution was added to a vial containing 25.0 μl of 100 mM K_2PdCl_4 in 4.775 mL H_2O . The solution was completely mixed using a vortexer and allowed to stand for 30.0 min. The reaction was then reduced by adding 100 μl of a 0.100 M freshly prepared NaBH_4 solution. The reaction was then allowed to stand for 1.00 h at room temperature.

2.3.4 Catalytic Reaction

The coupling reaction of 4-iodobenzoic acid and phenyltin trichloride is presented as the model procedure in this analysis; however, identical protocols are used for all aryl halides employed. In 20.0 mL reaction vials, 124 mg (0.500 mmol) of 4-iodobenzoic acid and 98.5 μL (0.600 mmol) of phenyltin trichloride (PhSnCl_3) were dissolved in 6.00 mL of 3.00 M aqueous KOH and 2.00 mL H_2O . Different amounts of Pd nanoparticle catalyst were then added to the reaction mixtures, namely 1.00 mL (0.100 mol%), 0.500 mL (0.050 mol%), 100 μL (0.010 mol%), 50.0 μL (0.005 mol%), 10.0 μL (0.001 mol%), 5.00 μL (0.0005 mol%) and 1.00 μL (0.0001 mol%). The reactions were allowed to proceed for 24.0 h with constant stirring at room temperature. The reactions were then quenched with 50.0 mL of 5.00% aqueous HCl. The product of the reaction was extracted from the aqueous mixture using diethyl ether (thrice, 30.0 mL each). The organic layer was treated with saturated NaCl solution (twice, 20.0 mL each), dried with anhydrous Na_2SO_4 , and filtered. 75.0 mg (0.500 mmol) of 4-*t*-butylphenol was added to the organic layer to serve as the internal standard in determining the percent yield of the

reaction. The organic solvent was then removed using a rotary evaporator and the product was analyzed using GC-MS and ^1H NMR.

2.3.5 TOF Measurement

In determining the TOF of the catalyst, the reaction was monitored for 1.00 h at time intervals of 0.00, 5.00, 10.0, 15.0, 20.0, 25.0, 30.0, 40.0, 50.0, and 60.0 min. The coupling reaction between 4-iodobenzoic acid and phenyltin trichloride was scaled up by 10.0 fold and 8.00 mL aliquots were obtained after each time interval. In a 250 mL beaker, 1.240 g of 4-iodobenzoic acid (5.00 mmol) and 986 μL of PhSnCl_3 (6.00 mmol) were dissolved in 60.0 mL of 3.00 M aqueous KOH and 20.0 mL H_2O . Then, 5.00 mL of the Pd nanoparticle catalyst (0.050 mol%) was added to the reaction mixture and an 8.00 mL aliquot was immediately quenched with 50.0 mL of 5.00% aqueous HCl. Aliquots were then taken after the specified time intervals and extracted as described above.

2.3.5 Characterization

UV-vis spectra of the Pd nanoparticles were obtained on an Agilent 8453 UV-vis spectrometer using a 1.00 mm path length quartz cuvette (Starna). The spectra obtained were background subtracted against water. Electron microscopy images were obtained using a JEOL 2010F TEM operating at 200 keV with a point-to-point resolution of 0.19 nm. Samples were prepared on 400 mesh Cu grids coated with a thin layer of carbon (EM Sciences). The solution (5.00 μL) was pipetted onto the surface of the grid and allowed to dry in air.

GC-MS spectra of the products were obtained using an Agilent 6890N Network GC system with an Agilent 5973 Network Mass Selective Detector. Products possessing carboxylic acids and phenols were converted to their trimethyl silyl ester analogs prior to analysis. Approximately 3 – 6 mg of the product was added with 200 μ L of N-methyl-N-(trimethylsilyl)-trifluoroacetamide (MSTFA). The reaction was stirred for 2.00 h, which resulted in the complete dissolution of the product and formation of the trimethyl silyl ester. The reaction mixture was then diluted in CH_2Cl_2 and analyzed by GC-MS.

NMR spectra were obtained using a Varian Inova 400 MHz NMR with a quadruply-tuned switchable probe. The product (1.0 – 2.0 mg) was dissolved in 1.50 mL deuterated chloroform in a standard 5.00 mm NMR tube (Wilmad). The integration of the peak at δ 8.2 ppm (product) was compared with the integration of the peak at δ 6.8 ppm (internal standard) to obtain the percent yield of the reaction.

2.4 Results and Discussion

Pd-binding peptides were identified from a phage displayed combinatorial peptide library. Commercially available Pd nanopowder (particle size < 25 nm) was used as the target for identifying Pd-binding peptides from the peptide library using established procedures.^{197-199, 202} As shown in Table 1, two 12-mer sequences were identified, termed Pd2 and Pd4, respectively. Both peptide sequences possessed basic pI values; however, the Pd4 peptide sequence possessed more basic and hydroxyl-containing residues, comparatively. Additionally, theoretical modeling of the Pd4 peptide Pd surface binding capabilities suggests that the two histidine residues bind to the materials surface in a

pinched arrangement, which will likely lead to open interaction sites between the solution and the metallic surface.²¹³ As such interactions are key to catalysis, this peptide was selected for nanoparticle synthetic analysis. The linear peptide was produced using standard Fmoc synthesis, purified by HPLC methods, and confirmed by MALDI-TOF mass spectrometry. Upon sequence confirmation, the peptide was then dissolved in deionized water to a concentration of 10 mg/mL, from which 100 μ L was added to a vial containing 25.0 μ L of 100 mM K_2PdCl_4 in 4.775 mL H_2O . The solution was allowed to stand for 30.0 min, after which 100 μ L of a 100 mM $NaBH_4$ solution was added for metal reduction. Prior to reduction, the solution was a pale yellow color, owing to the $PdCl_4^{2-}$ in solution; however, after reductant addition, a rapid color change to brown was immediately observed. The solution was allowed to stand and reduce for 1.00 h prior to use.

peptide	amino acid sequence	pI ^a
Pd2	NFMSLPRLGHMH	9.8
Pd4	TSNAVHPTLRHL	9.5

^a pI calculated at <http://ca.expasy.org>.

Table 1 Pd binding peptide sequences identified using phage display.

Initial characterization was performed using UV-vis spectroscopy, as shown in Figure 2.2. The black spectrum presented for the peptide in solution displays a featureless absorbance spectrum as anticipated. Upon incubation of the Pd4 peptide with the Pd^{2+} ions, red spectrum of Figure 2, formation of an absorbance shoulder at 224 nm is observed. This absorbance is likely due to the ligand to metal charge transfer band

associated with Pd-amine binding. The Pd4 peptide possesses histidine and arginine residues, which are readily able to coordinate Pd²⁺ ions in solution to give rise to this spectral absorbance.^{214, 215} Upon reduction, represented by the blue spectrum, this band disappears with formation of a broad absorbance characteristic of nanoparticle formation.^{214, 216} An increase in absorbance towards lower wavelengths is observed for the reduced species, corresponding to the brown solution described above. Previous syntheses of small Pd nanoparticles have demonstrated similar colorimetric and UV-vis spectroscopic properties.^{32, 119} Additionally, no materials precipitation was observed at any point during the nanoparticle synthesis, suggesting that the interaction between the peptide and the nascent nanoparticle surface is sufficient in magnitude to prevent bulk material aggregation.

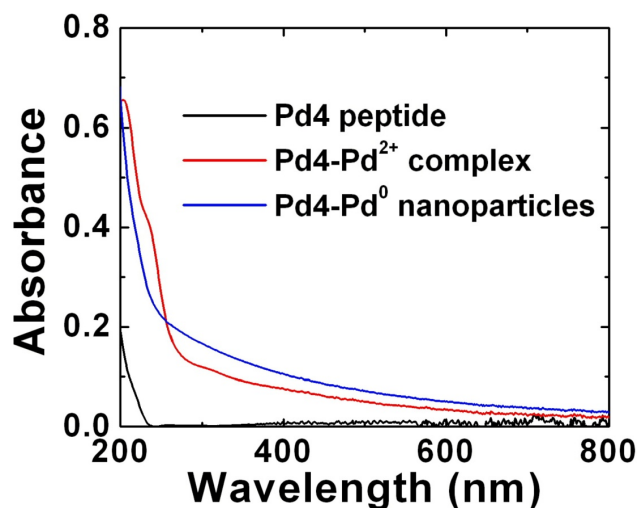


Figure 2.2 UV-vis spectra for the biomimetic synthesis of Pd nanoparticles. The black spectrum is for the Pd4 peptide, the red spectrum represents the Pd4-Pd²⁺ complex, while the blue spectrum corresponds to the Pd nanoparticles after reduction. All spectra were background subtracted against water.

TEM confirmed the fabrication of nanoparticles, as displayed in Figure 2.3a. Using this peptide, nearly monodisperse, spherical Pd nanoparticles are produced with an average

diameter of 1.9 ± 0.3 nm, which is highlighted in the particle size histogram presented in Figure 2.3b. Based upon theoretical calculations assuming an empirical Pd atomic radius of 140 pm, Pd nanoparticles of this size would contain approximately 312 metal atoms.²¹⁷ Such small particles are ideal for catalysis with their large surface-to-volume ratio for maximal catalytic activity. Additionally, the particles are large enough to avoid any undesired electronic effects that can be observed from smaller Pd nanostructures.³²

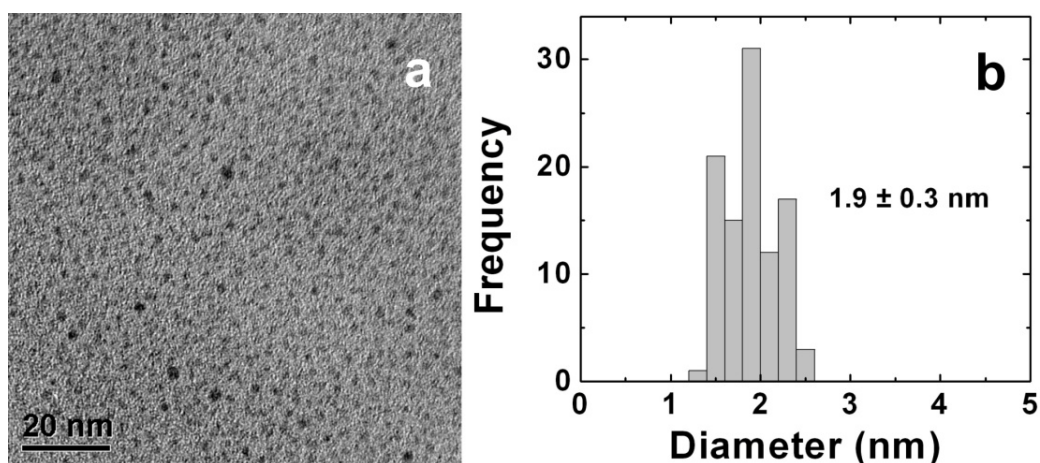


Figure 2.3 TEM analysis of the Pd nanoparticles. Part a) displays the TEM image of the Pd nanoparticles, while part b) presents their size distribution histogram.

To confirm that the synthetic protocol produced spherical Pd nanoparticles in response to the Pd4 peptide, rather than through generalized binding processes, control studies were conducted using a different peptide sequence of similar biological characteristics. In this analysis, the Pd4 peptide was substituted with the R5 peptide, which has been implicated in the biosilicification process of the diatom *Cylindrotheca fusiformis*.^{177, 179} Similar to the Pd4 peptide, the R5 peptide possesses a basic pI value (11.22) and a high percentage of basic and hydroxyl-terminated residues. Analysis of the materials prepared using this peptide resulted in the production of large, non-spherical Pd nanostructures of irregular

networks, which are shown in the Chapter 6, Figure 6.1. No spherical particles were observed and only wire-like structures were produced using the non-Pd specific peptide. This dramatic change in shape and dispersity results in a minimization of the Pd surface area for interactions with the catalytic reagents, whereby decreasing their overall reactivity. This indicates that the Pd4 peptide possess significant control over the fabrication of Pd nanomaterials, which can be synthetically preferred for the present catalytic applications.

Upon confirmation of the fabrication of Pd metallic nanostructures, the materials were studied for catalytic reactivity for the formation of C-C bonds. This family of reactions can follow various pathways; however, the overarching mechanism driving product generation is relatively similar from reaction to reaction. Initially, Stille coupling between an aryl halide and an organostannane compound was selected for analysis. This reaction was selected for three specific reasons. First, the final organic product of the catalytic reaction possesses a newly formed C-C bond, which is important for pharmaceutical production,²¹⁸ molecular electronics,²¹⁹ and fossil fuel processing.²²⁰ Second, previous reports have suggested that routes towards more environmentally responsible synthetic conditions for this carbon-coupling scheme may be readily achievable.⁵² Third, many of the reagents, both aryl halides and organostannanes, are commercially available to be used for facile characterization of the reactivity of the newly produced biomimetic Pd nanoparticles. Additionally, the solubility of the reagents can be tailored to fit a variety of solvent polarities and reaction conditions, thus facilitating a broad set of analyses of the Pd nanomaterial's catalytic activity.

For catalytic analysis of the biomimetic materials, green synthetic conditions were initially employed for the coupling of 4-iodobenzoic acid and phenyltin trichloride to produce biphenyl carboxylic acid (BPCA), which was used as a model system.⁸⁶ For this reaction, 0.500 mmol of the aryl halide was codissolved in solution with 0.600 mmol of phenyltin trichloride using 8.00 mL of 2.25 M aqueous KOH. To this solution, varying amounts of the Pd materials (0 – 0.500 mol% Pd) were added and the reaction was stirred for 24.0 h. In this sense, the mol% Pd refers to the amount of Pd in solution and not the concentration of nanoparticles, which would be quite lower. Once complete, the reaction was quenched with HCl, extracted using diethyl ether, and quantitated.

Initially, the model reaction was studied using 0.100 mol% Pd. This concentration was used to determine the feasibility of the reaction under the described synthetic conditions employing the peptide-stabilized Pd nanoparticles. Visual monitoring of the solution during the reaction occurred from which the precipitation of a fine white solid within <10.0 min after initiation was observed. This event suggests that a successful catalytic reaction is progressing as the final product, BPCA, is not soluble in the hydrophilic solution. After reaction workup from which the organically soluble materials were extracted into diethyl ether, the final products were analyzed using GC-MS and ¹H NMR. For GC-MS analysis, the carboxylic acid containing species were converted into trimethyl silyl esters to prevent hydrogen bonding and increase the volatility for gas chromatographic analysis. Figure 2.4a presents the gas chromatogram of the reaction after functionalization. In this sample, 4-*t*-butyl phenol (TBP) was added as an internal standard. The chromatogram possesses two distinct peaks at elution times of 7.29 and 11.04 min, which were analyzed by mass spectrometry in Figures 2.4b and c,

respectively. Analysis of the materials from the 7.29 min peak (Figure 2.4b) indicates that it is the TBP internal standard, with an $m/z = 222$. The second peak observed at 11.04 min and analyzed in Figure 2.4c, possessed an $m/z = 270$, which is in agreement with the calculated mass of the anticipated final BPCA product with the silyl-derivatized carboxylic acid. Additionally, no peak was isolated for the starting materials. While these results indicate a successful coupling reaction, spectroscopic characterization of the final product is required to confirm its identity.

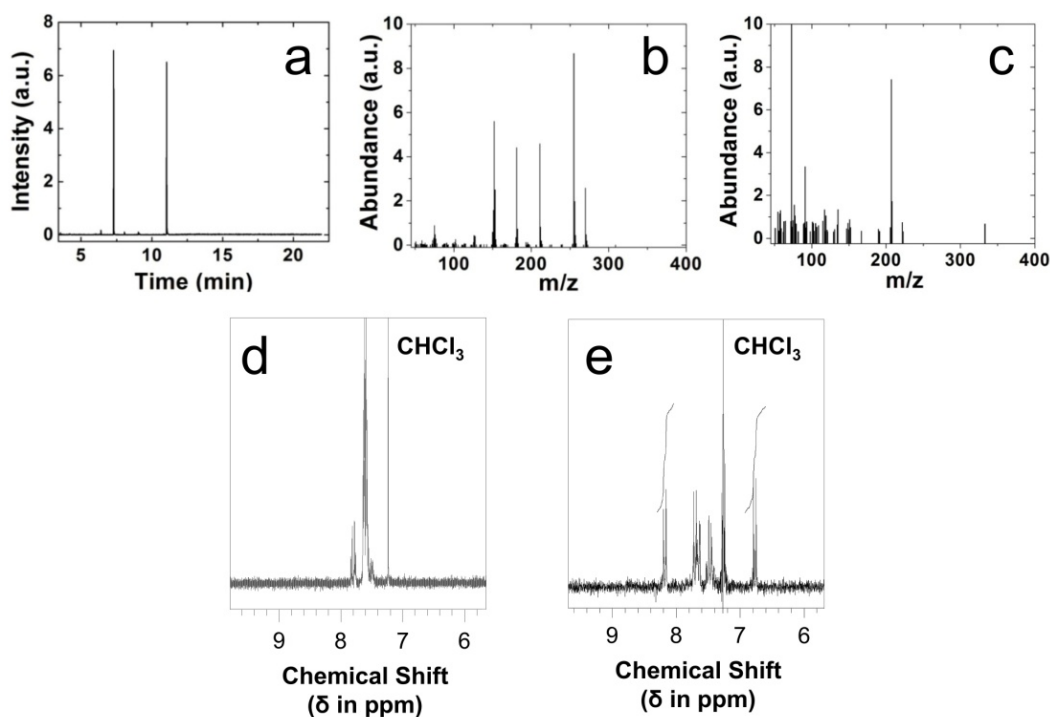


Figure 2.4 Characterization of the catalytic reaction between 4-iodobenzoic acid and phenyltin trichloride to produce BPCA. Part a) displays the gas chromatogram for the final products after addition of the TBP internal standard. Part b) presents the mass spectrum of the 7.29 min peak of the chromatogram, while part c) presents the mass spectrum of the 11.04 min peak of the chromatogram. Analysis of each spectrum confirms that part b) represents the TBP internal standard, while part c) represents the anticipated silyl-functionalized BPCA final product. Part d) presents the NMR spectrum of the physical mixture of 4-iodobenzoic acid and phenyltin trichloride prior to catalyst addition and part e) displays the NMR spectrum of the materials attained after catalytic reactivity with the bio-inspired Pd nanoparticles. A new signal is observed at 8.2 ppm, consistent with the BPCA product.

Spectroscopic identification of the final materials was conducted using 400 MHz ^1H NMR. Figure 2.4d presents the NMR spectrum of a mixture of the 4-iodobenzoic acid and phenyltin trichloride starting materials prior to catalysis initiation dissolved into a CDCl_3 solution. In this spectrum, peaks are observed at 7.78 and 7.87 ppm with a coupling constant of $J = 8.8$ Hz. Such results are anticipated for the *para* disubstituted benzene ring of the aryl halide substituent. The signals observed over the 7.5 – 7.7 ppm region are consistent with the known spectrum of the organostannane species.⁸⁶ Taken together, this indicates that only signals directly attributable to the starting materials are present, confirming that no reaction has taken place in the absence of the Pd nanoparticles. Analysis of the extracted products post-reaction is shown in Figure 2.4e. This NMR spectrum demonstrates that the starting material peaks have disappeared and are replaced by a new signal at 8.17 ppm. Such clear results are consistent with the BPCA final product,⁸⁶ thus indicating that a successful catalytic carbon coupling reaction occurred in the presence of the bio-inspired Pd nanomaterials. For this spectrum, an additional peak at 6.80 ppm is due to the TBP internal standard, whose individual spectrum was attained and is presented in the Chapter 6, Figure 6.2. The reaction was quantitated using the TBP, which indicates that a 100% product yield is attained within the 24.0 h reaction time frame.

To determine the extent of catalytic reactivity of the peptide functionalized Pd nanoparticles, the model reaction was conducted at decreasing catalyst-loading values. This process was studied down to a loading of 0.001 mol% Pd with surprising product yields. As shown in Figure 2.5a, quantitative reaction yields were consistently achieved after a 24.0 h reaction time period down to a catalyst loading value of 0.005 mol% Pd.

Note that this percentage represents the amount of Pd atoms in solution, not the concentration of Pd nanoparticles; therefore, the loading value is even further minimized for the nanoparticle catalyst species. Remarkably, when a catalyst loading of 0.001 mol% was studied, an average product yield of ~64% was observed. While such catalyst loadings are below traditional values, these reactions were also conducted in an aqueous solvent at room temperature, suggesting that the bio-inspired Pd nanomaterials may represent a model catalytic system for understanding the structural requirements of green catalysts. To confirm that the observed results were facilitated by the Pd nanoparticles rather than by an uncontrolled autocatalytic event, a control study was conducted in which no Pd nanoparticles were added to the two starting materials in a typical reaction solution. After 24.0 h, the sample was quenched and extracted using the standard purification and reaction procedures. Final analysis of the resultant materials indicated that no product was generated and that only the initial starting materials were retained.

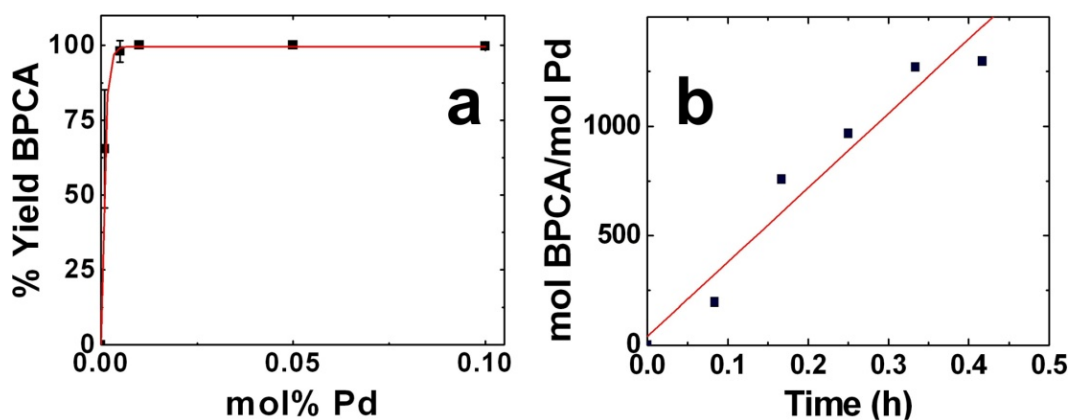
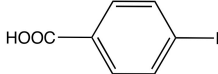
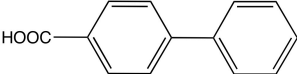
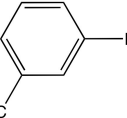
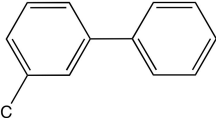
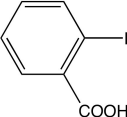
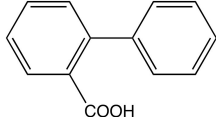
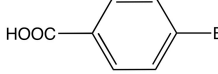
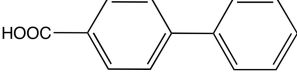
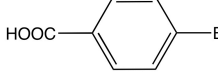
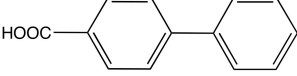
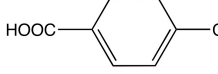
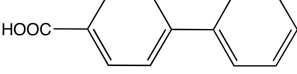
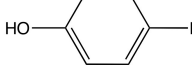
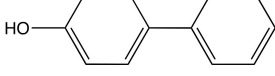
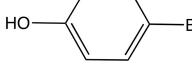
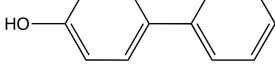
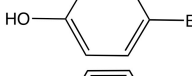
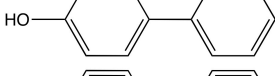
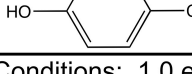
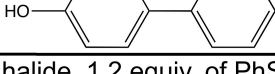


Figure 2.5 Analysis of the catalytic reactivity of the peptide functionalized Pd nanoparticles. Part a) displays the effect of Pd catalyst loading on the model reaction for the production of BPCA, while part b) displays the TOF determination employing a catalyst loading of 0.050 mol% Pd for the model reaction.

To determine the efficiency of the peptide functionalized Pd nanomaterials, the turnover frequency (TOF) of the reaction was determined. For this study, a Pd loading of 0.050 mol% was employed in a scaled up reaction volume of 80.0 mL. This system was used where the ratio of starting materials to catalyst remained constant to allow for additional time-based aliquot removal and analysis. Immediately after catalyst addition, one 8.00 mL aliquot was extracted from the reaction and quenched. From that time point, aliquots were taken and analyzed at 5.00 min intervals for 30.0 min and then at 10.0 min intervals for a total time of 1.00 h. The quantitation of the reaction yields at time points < 30.0 min are plotted in Figure 2.5b, which represents the linear region of the analysis. The TOF value of this catalyst can then be extrapolated from the slope of the line over this portion of the plot as the y-axis incorporates both the mols of final product and catalyst. From this analysis, a TOF value of $3,207 \pm 269$ mol BPCA (mol Pd•h)⁻¹ was determined for the model reaction system. This value is larger than those previously reported for similar systems and represents an enhancement in reactivity.^{86,191}

An expanded analysis of the catalyst reactivity and specificity was further studied, as demonstrated in Table 2. For this analysis, the aryl halide was substituted at different positions and the halide functionality was varied over I, Br, and Cl substituents. Switching of the iodo substituent to the 3-position (Entry 2) over the 4-position (Entry 1) retained activity; however, when the iodo group was placed at the 2-position (Entry 3), no product was generated. A lack of reactivity for this molecule was not unexpected due to irreversible binding to the Pd surface through the electronic interactions of the closely spaced functional groups.^{86, 187, 191} Substitution of the halide for bromide or chloride functionalities resulted in a decrease in reactivity. Such results were anticipated due to the

lesser activity of the lighter halides.^{175, 212} For the bromo-species, when 0.100 mol% (Entry 4) catalyst was used, a 7.9% or 43.2% yield was observed after 72 or 168 h of reactivity at room temperature, respectively. However, when 0.500 mol% (Entry 5) catalyst was employed, an increased yield of 40.0% or 84.7% was attained after 72 or 168 h, respectively. Unfortunately, the 4-chlorobenzoic acid species (Entry 6) was non-reactive towards carbon cross coupling.

Entry	Aryl Halide	Product	Yield
1			100
2			100
3			0
4 ^b			7.9 (43.2) ^c
5 ^d			40.0 (84.7) ^c
6 ^b			0
7			100
8 ^b			6.23 (26.8) ^c
9 ^d			12.8 (48.4) ^c
10 ^b			0

^a Reaction Conditions: 1.0 equiv. of aryl halide, 1.2 equiv. of PhSnCl₃, 0.05 mol% Pd, 8.0 mL of 2.25 M KOH, 25 °C, t = 24 h; ^b 0.1 mol% Pd nanoparticles; ^c t = 72 h or 168 h in parenthesis; ^d 0.5 mol% Pd nanoparticles

Table 2 Stille cross coupling reactions using the bio-inspired Pd nanoparticles.

Further reactivity was probed using aryl-phenols. Again, quantitative yields for the 4-iodo species (Entry 7) were observed after 24.0 h. Substitution of the halide similarly resulted in decreased reaction yields; however, a significant product yield was still observed for the bromo-species at either 0.100 mol% (Entry 8) or 0.500 mol% (Entry 9) catalyst after 72 – 168 h. The changes with this species, as compared to the carboxylic acid species, is likely due to the electronics of the molecule,^{175, 212} as well as catalyst concentration effects,¹⁹⁴ both of which are known to alter reactivity in solution. Overall, while varying yields can be achieved with differently substituted starting materials, final products are readily producible using green synthetic conditions catalyzed by the bio-inspired Pd materials.

Based upon the hydrophilic peptide coating of the biomimetic Pd nanoparticles, the system is likely to be optimized for aqueous-based reactivity. To probe this level of functionality, the model reaction using 4-iodobenzoic acid was studied in a solvent mixture of 3 EtOH: 1 H₂O. This reaction system was required to permit solubility of all the reagents and the peptide-functionalized nanocatalysts, while being able to be compared to the aqueous-based results to generate an understanding of solvent effects. Using these conditions and a catalyst loading of 0.050 mol% Pd, at a reaction time of 24 h, a BPCA final product yield of only 44.9% was achieved (Chapter 6, Figure 6.16). This is significantly lower than the quantitative yields observed under aqueous conditions. These results are likely due to the solvent polarity, which can cause changes to the particle surface, such as tighter ligand packing, to alter the specific interactions that drive the chemical reactions in solution.

The above catalytic results indicate that the inorganic metallic surface must be solvent exposed in some manner. If the surface was completely bound and passivated by the peptides, then specific reactivity would not be observed. Previous computational studies have suggested that the two histidine residues of the Pd₄ peptide are responsible for the surface binding ability.²¹³ As such, it may be possible for the peptides to form a bidentate interaction, thus arranging in a specific fashion on the three-dimensional Pd nanoparticle surface. Due to steric and geometric constraints of the large peptide framework, it would be unlikely for the peptides to tightly pack on the small particle surface; therefore, pockets of exposed metallic regions are likely to exist. It is from these regions that the initial oxidative addition process can occur to drive the Stille coupling reaction. While it is known that the reaction does occur, it is difficult to determine whether this process is progressing at the surface of the particle, or whether Pd-ions are chemically extracted from the nanomaterial and the reaction is driven by these liberated species in solution.⁵² Future research on this mechanism is required and presently being conducted.

The catalytic reaction conditions demonstrated herein adhere to green synthetic conditions; however, the peptide synthesis required to achieve the templating ligands employs traditional synthetic organic mechanisms. While such routes are less than desirable, the main focus is to understand the materials structure of the peptide functionalized Pd nanoparticles in an attempt to generate an image of the structural requirements for enhanced green catalyst. As such, the peptide functionalized Pd nanoparticles represent unique models to understand these structural properties as they possess inherently efficient nearly green catalytic abilities. In addition, further steps to enhance the green aspects of these catalytic conditions can be achieved by

using less harmful boron reagents in Suzuki coupling over the organotin species of Stille coupling. Further research is required; however, the initial steps towards this goal have been demonstrated.

2.4 Summary and Conclusions

Herein we have demonstrated the use of peptides for the specific fabrication of highly active model green catalysts. These materials were synthesized using basic peptide sequences isolated via phage display techniques with the ability to recognize and bind metallic Pd surfaces. Using standard reduction techniques, small, monodisperse Pd nanoparticles are formed. These materials are reactive for Stille coupling employing the environmentally friendly conditions of a water-based solvent at room temperature, using low Pd loadings of ≥ 0.001 mol% Pd. Large TOF values have also been achieved using these materials, indicative of active catalysts. Additionally, these biomimetic Pd nanocatalysts have demonstrated reactivity across a set of chemical compounds, suggesting that their activity may be open to a variety of chemical reactions. This unique catalytic property is likely dependent upon the nanoparticle surface structure, which is directly controlled by the orientation and surface binding of the Pd4 peptide. Theoretical calculations show that only the histidine residues of the peptide bind to the surface,²¹³ suggesting that a significant fraction of the surface Pd atoms are solvent exposed. While varying reaction yields were observed with chemically different starting materials, the main message is that the reaction efficiently progresses with a variety of species. The methods described represent only

a fraction of those that can be employed while retaining environmentally friendly conditions. Small changes can be used for enhanced reactivity from the starting point described herein, which are presently being studied.

“Reprinted (adapted) with permission from (Pacardo, D. B.; Sethi, M.; Jones, S. E.; Naik, R. R.; Knecht, M. R. *ACS Nano* 2009, 3, 1288-1296). Copyright (2009) American Chemical Society.”

Chapter 3. Interrogating the Catalytic Mechanism of Nanoparticle Mediated Stille Coupling Reactions Employing Bio-inspired Pd Nanocatalysts

3.1 Overview of the Study

In this chapter, the results of mechanistic studies of peptide-capped Pd nanoparticles were presented. To address issues concerning the global environmental and energy state, new catalytic technologies must be developed that translate ambient and efficient conditions to heavily used reactions. To achieve this, the structure/function relationship between model catalysts and individual reactions must be critically discerned to identify structural motifs responsible for the reactivity. This is especially true for nanoparticle-based systems where this level of information remains limited. Here we present evidence indicating that peptide-capped Pd nanoparticles drive Stille C-C coupling reactions via Pd atom leaching. Through a series of reaction studies, the materials are shown to be optimized for reactivity under ambient conditions where increases in temperature or catalyst concentration deactivate reactivity due to the leaching process. A quartz crystal microbalance analysis demonstrates that Pd leaching occurs during the initial oxidative addition step at the nanoparticle surface by aryl halides. Together, this suggests that peptide-based materials may be optimally suited for use as model systems to isolate structural motifs responsible for the generation of catalytically reactive materials under ambient synthetic conditions.

3.2 Motivation

Nanoparticles are uniquely positioned for catalysis due to their high surface to volume ratio that maximizes catalyst exposure.^{52, 221, 222} Beyond the size of the particle, the inorganic/ligand interface also plays a significant role in the reactivity by controlling particle stability and facilitating the molecular interactions between the surface and substrates in solution.^{33, 94, 223, 224} To that end, the ligands must be designed to allow inorganic surface exposure; however, this exposure must be displayed in such a manner as to prevent nanoparticle aggregation. Such an ability remains challenging using present day nanocatalyst synthetic approaches, which either results in unstable nanoparticles or catalytically poisoned surfaces. We have used a unique peptide-based approach²⁰¹ towards the synthesis of Pd nanoparticle catalysts employing the Pd4 peptide (TSNAVHPTLRHL) isolated via phage display.^{88, 94} Theoretical calculations suggest that the Pd4 peptide anchors to the Pd surface through the binding of the histidine residues, which generates a kinked-loop structure to expose the reactive surface.²¹³ Once fabricated, these materials are highly efficient for Stille coupling^{175, 212} reactions between aryl halides and organostannanes employing a water-based solvent at room temperature with ultra low Pd concentrations (0.001 mol% Pd).⁸⁸ Consequently, this system is suited for studies concerning the reactivity of nanocatalysts under conditions that are both eco-friendly and energy neutral, which represents major milestones for the advancement of catalytic technologies.^{220, 225, 226} More recently, we have demonstrated that modifications to the peptide binding at the histidine residues can be used to modulate reactivity. Here, alanine substitution of the

histidine at the sixth position results in an approximate doubling of reactivity, while modification of the histidine at the eleventh position produces materials with diminished reactivity,⁹⁴ thus directly correlating with the modeling data.²¹³ Unfortunately, the actual mechanism of Stille coupling driven by these structures remains unclear. By elucidating this mechanism, key structural motifs of the peptide/inorganic surface could be extrapolated to expand the reactivity. Such an understanding of the peptide interface is also important in the development of biomimetic materials for other applications, which are poised to make significant advancements.^{201, 203, 210, 211, 222, 227, 228}

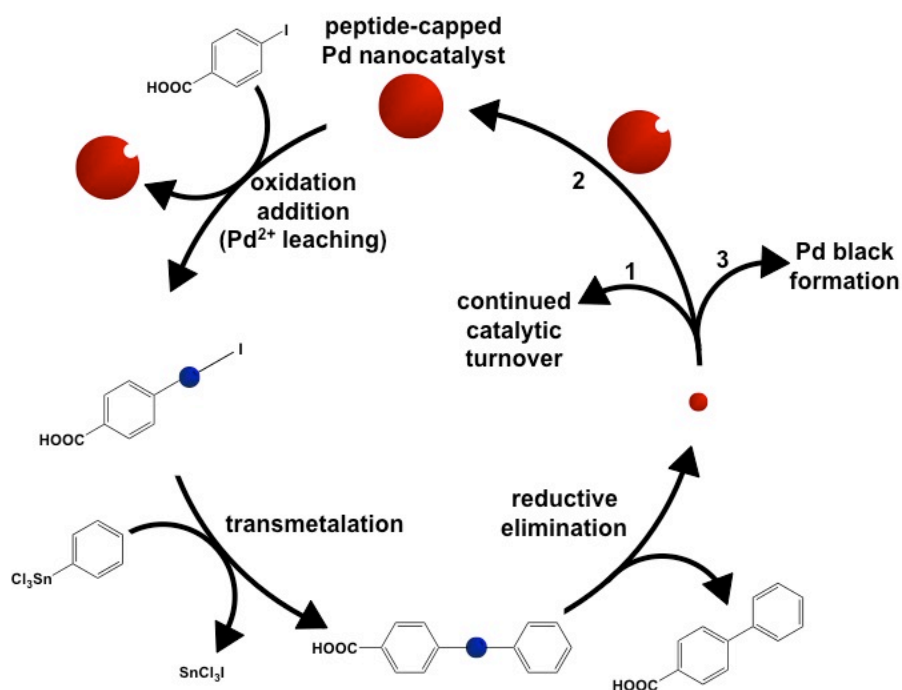


Figure 3.1 Schematic diagram of the atom leaching mechanism for the Stille coupling reaction employing the Pd bionanocatalysts.

Previous studies of nanoparticle driven C-C coupling mechanisms have focused on the Heck reaction,^{52, 194, 229-232} which couples aryl halides with alkenes, and Suzuki

coupling^{169, 171, 187, 191} between aryl halides and organoboranes. At present, to the best of our knowledge, very little information is available concerning the Stille mechanism.⁸⁶ While these three reactions are similar, they are optimized for different substrates, thus a critical analysis of each individual mechanism is important as subtle differences could yield substantial variations in reactivity. For the Heck and Suzuki reactions using a variety of nanoparticles with different surface ligands, two possible mechanisms have been proposed.⁵² In the first method, the reaction occurs directly on the nanoparticle surface,^{171, 233} thus maintaining the structure of the material. While such a process would seem to be reasonable, other evidence suggests against a simple surface reaction, wherein Pd atom leaching drives the process.^{52, 86, 191, 194, 232} In this approach, oxidative addition oxidizes a Pd atom to Pd²⁺, which is then abstracted from the nanoparticle surface to solution. After this step, the reaction cycle proceeds in which a bare Pd-atom is released to solution. At this point, the Pd atoms can follow one of the three paths as illustrated in Figure 3.1 following traditional Stille coupling. In path one, if the concentration of starting materials is high, the Pd atom can be recycled through the reaction; however, as the reagents become exhausted in path two, the Pd atoms can be quenched by the remaining nanoparticles.⁵² Path three is achieved if a high concentration of nanocatalysts is employed. In this event, excessive Pd leaching can occur to generate a large Pd atom concentration resulting in the precipitation of catalytically dead Pd black. Based upon these two different mechanisms, altered reactivity is envisioned, which could control the catalytic capabilities of the materials; therefore, it is essential to determine the mechanism and effects of solution conditions to optimize and enhance each reaction. It should be

noted that leaching for Heck and Suzuki coupling has been proposed for a variety of nanoparticles with vastly different passivating ligands; however, different TOF values can be achieved for the individual reactions. This suggests that while the ligand surface controls the catalytic activity, the actual mechanism of the reaction is independent of the surface structure.

While the mechanisms of Heck and Suzuki couplings may provide insight towards the pathway employed by the Stille reaction, it is probable that significant differences are present. For instance, nanoparticle driven Heck coupling requires very high reaction temperatures (80 °C – 130 °C) and organic solvents to activate the reaction.^{52, 230-232} Furthermore, most Suzuki reaction studies also employ organic solvents or co-solvents,^{52, 166, 187, 191} however, they have recently been processed at room temperature.^{187, 191} Changes in temperature and solvent are known to alter catalytic pathways, especially for C-C coupling reactions due to changes in solvent shielding and intermolecular forces.^{88, 175, 212} In contrast to these reaction conditions, the peptide-capped Pd materials employ low temperatures and aqueous conditions, which could significantly change the catalytic pathway. Additionally, different transmetalation reagents are employed for Stille coupling, where various mechanisms have been proposed for this single step.²¹² To advance this model Stille system that operates under highly desirable conditions, it is important to fully elucidate the mechanism employed from the initial oxidative addition to the final reductive elimination. Once a step-by-step mechanism is determined, it could then be exploited for selective catalytic abilities, which would find immediate use in fine-chemical synthesis applications.

Here we present studies that indicate that Pd atom leaching controls the reactivity of the biomimetic Pd nanoparticles for Stille coupling (Figure 3.1), which is optimized for ambient and energy neutral conditions. By monitoring the TOF values of the system as a function of reagent identity, Pd concentration, and temperature, we have observed key effects that support a temperature and Pd concentration sensitive leaching mechanism that is not observed for other coupling reactions. The results indicate that the initial oxidative addition step at the nanoparticle abstracts a Pd species; however, the leached Pd²⁺/aryl halide complexes are highly sensitive to the reaction temperature and Pd concentration. To that end, when the reaction is processed at temperatures >60°C or at Pd concentrations of >0.050 mol% Pd, rapid consumption of the catalyst to Pd black occurs to attenuate the catalytic capabilities. Furthermore, a highly unique aspect of this study is that the leaching process was analytically confirmed to occur during oxidative addition of the aryl halide via a quartz crystal microbalance (QCM) analysis. These results suggest that the bio-based Pd materials may be optimally situated for reactivity under eco-friendly and energy efficient conditions.

3.3 Methods

3.3.1 Chemicals

FMOC-protected amino acids and WANG resins substituted with the first amino acid were purchased from Advanced ChemTech (Louisville, KY). K₂PdCl₄, 4-bromobenzoic acid, 4-biphenylcarboxylic acid, phenyltin trichloride (PhSnCl₃), and

4-*t*-butylphenol were purchased from Sigma-Aldrich (St. Louis, MO), while NaBH₄ was purchased from EMD (Gibbstown, NJ) and 4-bromophenol was purchased from TCI America (Portland, OR). Divinyln tin dichloride (DVT) was purchased from Alfa Aesar (Ward Hill, MA). Anhydrous Na₂SO₄, CCl₃D, 4-iodobenzoic acid, NaCl, and KOH were purchased from Fisher (Pittsburgh, PA). All reagents were used as received. Milli-Q water (18mΩ•cm; Millipore, Bedford, MA) was used throughout.

3.3.2 Preparation of Pd Nanoparticles

The Pd4 peptide was prepared using a TETRAS synthesizer (CreoSalus, Louisville, KY) employing automated Fmoc protocols, purified via HPLC, and confirmed by MALDI TOF.²³⁴ To fabricate the Pd nanoparticles using the peptides, a previously reported synthesis was used.⁸⁸ To a vial, 100 μL of a 10 mg/mL Pd4 peptide solution was diluted with 4.775 mL of water, to which 25.0 μL of 0.10 M K₂PdCl₄ in water was added. The solution was completely mixed and allowed to stand for 30.0 min. The reaction was then reduced by adding 100 μL of a 0.10 M freshly prepared NaBH₄ solution. The reaction was allowed to stand for 1.00 h at room temperature to ensure complete Pd²⁺ reduction. UV-vis characterization of the materials was conducted using an Agilent 8453 spectrometer employing a 1 cm quartz cuvette. Transmission electron microscopy (TEM) analysis of the materials was performed using a JEOL 2010F TEM operating at 200 kV. 5.0 μL of the Pd materials were pipetted onto a Cu grid coated with a thin layer of carbon and allowed to dry in a desiccator.

3.3.3 TOF Measurements

Determination of TOF values for the Stille coupling of 4-iodobenzoic acid and PhSnCl_3 was achieved using previously described methods.⁸⁸ Briefly, in a 250 mL beaker, 1.24 g of 4-iodobenzoic acid (5.00 mmol) and 986 μL of PhSnCl_3 (6.00 mmol) were co-dissolved in 80.0 mL of 2.25 M aqueous KOH. The required amount of Pd nanocatalyst was then added to the reaction mixture for each concentration (10.0 mL for 0.100 mol% Pd, 7.50 mL for 0.075 mol% Pd, 5.00 mL for 0.050 mol% Pd, 1.00 mL for 0.010 mol% Pd, and 0.500 mL for 0.005 mol% Pd). For each concentration, additional water was added such that the total volume of the reaction mixture was 90.0 mL. An 8.00 mL aliquot was immediately quenched with 50.0 mL of a 5.00% aqueous HCl solution, which represented a 0.00 min time point. Aliquots were then taken and quenched after selected time intervals.

The product of the quenched aliquot was extracted three times using diethyl ether (30.0 mL). The organic layer was twice treated with a saturated NaCl solution (20.0 mL), dried with Na_2SO_4 , and filtered. 75.0 mg (0.500 mmol) of 4-*t*-butylphenol was then added to the organic layer as an internal standard for product yield determination. The organic solvent was removed using a rotary evaporator and the product was quantified using a Varian Inova 400 MHz NMR. The product (~1.0 – 2.0 mg) was dissolved in 1.00 mL of CCl_3D in a standard 5.00 mm NMR tube. The integration of the peak at δ 8.17 ppm (product) was compared with the integration of the peak at δ 6.80 ppm (internal standard) to obtain the yield.

3.3.4 Temperature Controlled Stille Coupling

The coupling between 4-bromobenzoic acid and PhSnCl_3 was analyzed at seven temperatures (30 °C, 40 °C, 50 °C, 60 °C, 70 °C, 80 °C, and 90 °C), and at four Pd loadings (0.005 mol%, 0.010 mol%, 0.050 mol%, and 0.100 mol%). The reaction was performed using 20.0 mL vials containing 100.5 mg of 4-bromobenzoic acid (0.500 mmol) and 98.5 μL of PhSnCl_3 (0.600 mmol) dissolved in 8.0 mL of 2.25 M aqueous KOH. The Pd nanoparticles were then added to the reactions to achieve the desired loading (1.00 mL for 0.100 mol%, 0.500 mL for 0.050 mol%, 100 μL for 0.010 mol%, and 50 μL for 0.005 mol%). The reaction vials were then placed in an oil bath thermostated at the specified temperature for 24.0 h with vigorous stirring. Upon completion, the reactions were quenched and the product was extracted and characterized using the procedure described above. The exact same procedure was followed for the coupling reaction of 4-bromophenol (86.5 mg, 0.500 mmol) and PhSnCl_3 ; however, 4-biphenylcarboxylic acid was employed as the internal standard. For this system, ^1H NMR-based product characterization was completed using the peaks at δ 6.88 ppm for the product and δ 8.17 ppm for the internal standard.

3.3.5 Effect of the Transmetalation Agent

The Stille coupling reaction between 4-iodobenzoic acid and DVT was monitored at room temperature using different loadings of the Pd nanoparticles. The same conditions were employed as described above; however, the PhSnCl_3 was substituted with 82.9 μL of DVT (0.600 mmol). The mixture was allowed to stir for 24.0 h at room temperature. The reaction was then quenched and the product was extracted as

described above, using 4-biphenylcarboxylic acid as the internal standard. The percent yield was determined by comparing the ^1H NMR peak at δ 8.05 ppm (product) with that of δ 8.17 (internal standard).

3.3.6 QCM Analysis

QCM analysis was completed using a Au resonator chip coated with Pd. The Pd surface was prepared with a thickness of 100 – 200 Å via sputter coating on a Au sensor (QSX-301 from Q-Sense). The final Pd film was cleaned in a heated solution of 5:1:1 water, 25% ammonia, and 30% H_2O_2 for 10.0 min, followed by thorough rinsing with water and 99% EtOH to remove any bound organic contaminants. QCM was then completed at room temperature using a Q-Sense E4 system with dissipation (QCM-D). In an open QCM sensor module, 4-iodobenzoic acid was added to the system (5.00 mmol in 2.25 M KOH) and the third overtone resonance frequency was monitored from which the mass loss of Pd over time was calculated using the Sauerbrey equation.

3.4 Results and Discussion

The peptide-capped Pd nanoparticles were prepared and employed for Stille coupling using standard procedures.^{88, 94} Figure 3.2 presents a complete TEM analysis of the materials prepared at a Pd:peptide ratio of 3.3. As shown in Figure 3.2a, a low-resolution micrograph displays highly dispersed Pd nanoparticles. Particle size distribution analysis, displayed in Figure 3.2c, indicates that the materials are nearly

monodisperse with a size distribution of 2.0 ± 0.4 nm. Such a value is consistent with previous studies.⁸⁸ Figure 3.2b presents a high-resolution analysis of the materials displaying a resolved image of the material's crystal structure. In the inset of the figure, a single particle is presented where the fringes of the Pd (111) plane are displayed with a d-spacing of 2.4 \AA , consistent with the face-centered cubic structure of zero valent Pd.⁸⁷ Furthermore, from this image, it is evident that the peptide-capped Pd nanoparticles are single crystalline, which suggests a highly controlled synthetic process is occurring to mediate the final structure.

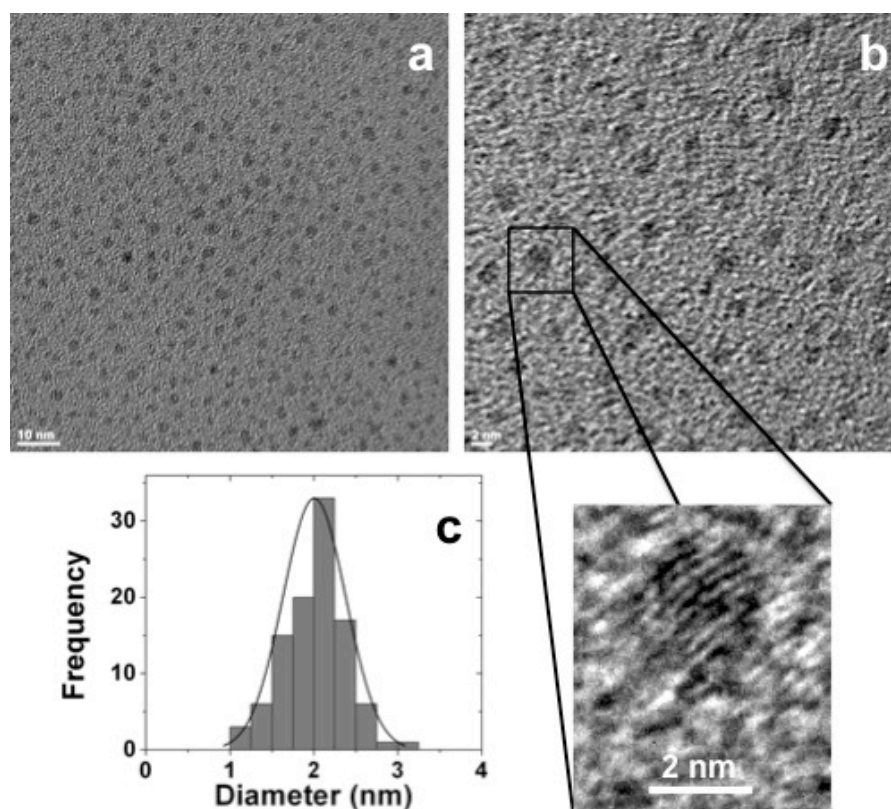


Figure 3.2 TEM analysis of the Pd nanocatalysts prepared using the Pd4 peptide. Part a) presents a low magnification micrograph, while b) presents a high-resolution image. The inset of b) presents the (111) lattice fringes of a single crystal particle. Part c) displays the particle size distribution analysis for the materials with an average of 2.0 ± 0.4 nm.

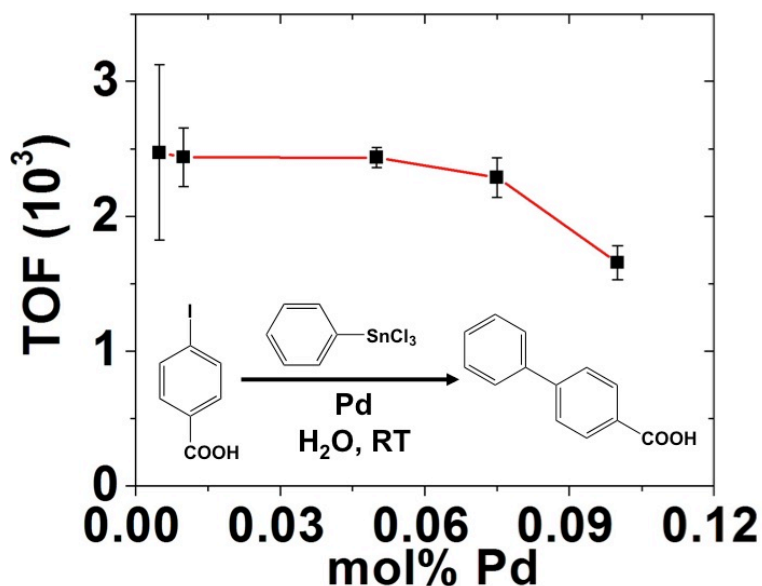


Figure 3.3 Comparison of the TOF value as a function of Pd concentration for the model Stille reaction displayed in the insert employing 4-iodobenzoic acid as the aryl halide.

With confirmation of the materials structure, the catalytic mechanism of nanoparticle-driven Stille coupling was probed. To discriminate between the two possible pathways, the TOF for the model reaction of 4-iodobenzoic acid coupling with PhSnCl_3 to produce biphenylcarboxylic acid (BPCA) was studied as a function of nanoparticle loading between 0.005 mol% Pd and 0.100 mol% Pd. As shown in Figure 3.3, using a loading of 0.050 mol% Pd, a TOF value of 2436 ± 74 mol product $(\text{mol Pd} \times \text{h})^{-1}$ was achieved, which is consistent with previous results.^{88, 94} As the Pd reaction concentration decreases, the TOF value remains constant. Here, TOFs of 2438 ± 218 mol product $(\text{mol Pd} \times \text{h})^{-1}$ and 2473 ± 651 mol product $(\text{mol Pd} \times \text{h})^{-1}$ were achieved for the reactions with Pd loadings of 0.010 mol% and 0.005 mol%, respectively. Since equivalent TOF values are achieved, this suggests that the TOF is being normalized to the actual reactive sites for Stille coupling as previously demonstrated for nanoparticle-driven reactions.^{32, 171} Note that the TOF value is

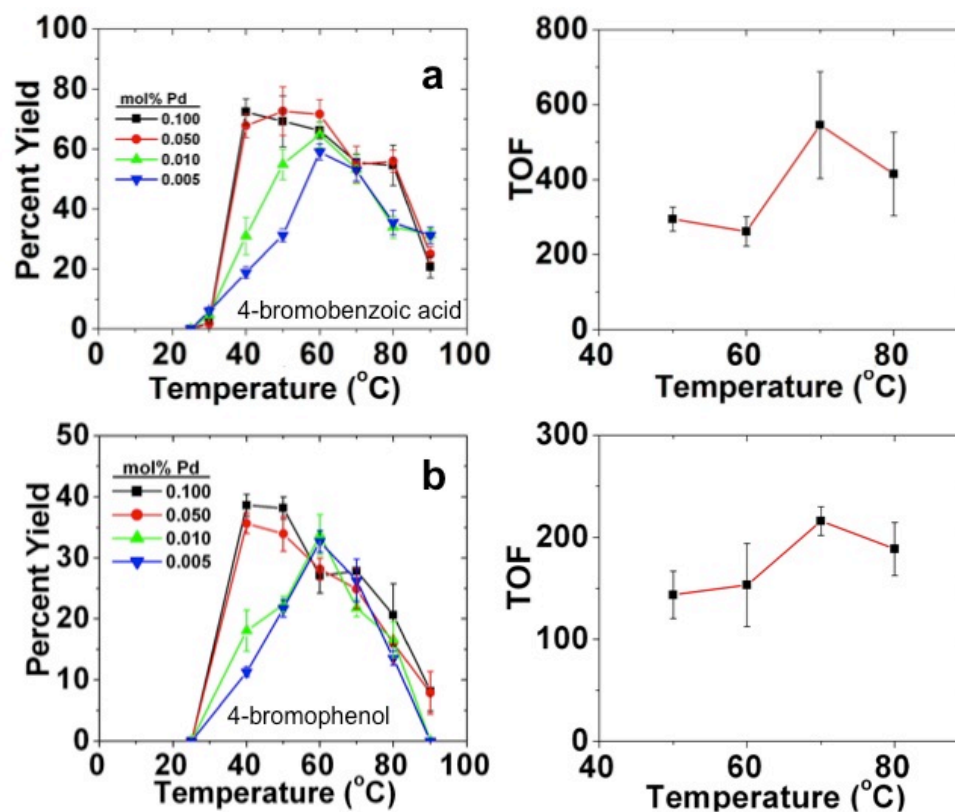


Figure 3.4 Effects of the reaction temperature for the Stille coupling of a) 4-bromobenzoic acid and b) 4-bromophenol with PhSnCl_3 . The left figure presents the overall reaction yield, while the right figure displays the TOF values at specific temperatures using a Pd loading of 0.050 mol%.

determined using the total Pd concentration in solution and not the nanoparticle concentration, consistent with previous studies.^{86, 88, 94, 191} Interestingly, as the concentration of Pd increases above 0.05 mol%, a decrease in the TOF is observed. For instance, using a Pd loading of 0.075 mol%, a TOF of 2290 ± 148 mol product $(\text{mol Pd} \times \text{h})^{-1}$ was observed that further decreased to 1656 ± 126 mol product $(\text{mol Pd} \times \text{h})^{-1}$ at 0.100 mol% Pd. While quantitative BPCA production is observed under these conditions,⁸⁸ the decrease in TOF suggests that an altered catalytic process is occurring at higher Pd concentrations as compared to those studied at loadings ≤ 0.05 mol% Pd. Note that for previous studies of Heck and Suzuki coupling using

nanoparticle catalysts, the TOF value continued to increase at lower Pd loadings,^{52, 191, 194, 232} which is quite different than the presently observed trend.

As is evident from above TOF data, the reaction rapidly takes place using 4-iodobenzoic acid as the aryl halide reagent; however, a Br substitution has been shown to result in significantly lower product yields.⁸⁸ To achieve observable product amounts for 4-bromobenzoic acid, a catalyst loading of 0.500 mol% Pd and 7.0 days was required for a product yield of 84.7%.⁸⁸ To optimize the activity, the reaction was heated between 25°C and 90°C, where the BPCA yield after 24 h was quantitated (Figure 3.4a). This experiment was anticipated to significantly increase the BPCA yield, proportional to the reaction temperature, until saturation of product generation was achieved. The black plot of Figure 3.4a shows the product percent yields achieved using a loading of 0.100 mol% Pd. For this reaction, negligible BPCA was produced at room temperature; however, when the reaction was studied at 30°C, a product yield of $2.4 \pm 0.4\%$ was determined. Surprisingly, when the reaction was gently heated to 40°C, a dramatic increase in the product yield was observed to $72.4 \pm 4.3\%$. This degree of reactivity was maintained through a reaction temperature of 60°C; however, at higher temperatures, the amount of BPCA produced steadily decreased. At 70°C, a yield of $55.6 \pm 2.7\%$ was determined that further diminished to $20.6 \pm 3.5\%$ at 90°C. A nearly identical trend was observed for a Pd loading of 0.050 mol%, but a slightly altered trend was observed for those reactions with lower Pd concentrations. For the 0.010 mol% and 0.005 mol% Pd reactions, higher temperatures are required to reach maximum product yields. These effects are likely due to the lower concentration of catalytic species in the reaction.

The right panel of Figure 3.4a demonstrates the effect of temperature on the TOF values for reactions with 0.050 mol% Pd at temperatures between 50°C and 80°C. At 50°C, a TOF of 294 ± 31 mol product $(\text{mol Pd} \times \text{h})^{-1}$ was observed, which is significantly lower than the values achieved when using 4-iodobenzoic acid. As the reaction temperature increased to 60°C, a similar TOF was achieved; however, a jump in the TOF was observed at 70°C to 546 ± 142 mol product $(\text{mol Pd} \times \text{h})^{-1}$. This is quite intriguing as product yields are maximized at 60°C, but begin to decrease at temperatures $\geq 70^\circ\text{C}$. Note that TOF values are calculated at short time frames immediately after Pd nanoparticle addition. This suggests that while the rate of Stille coupling is initially faster at temperatures $\geq 70^\circ\text{C}$, the catalytic species is consumed during the reaction to give diminished product yields. Such effects are different than the reactivity observed for other C-C coupling reactions where higher temperatures are required for reaction activation, especially for Heck coupling.^{52, 230-232} Recent studies of nanoparticle driven Suzuki coupling at room temperature do demonstrate product formation;¹⁹¹ however, higher temperatures can also be employed, which are within the range that result in dramatic catalyst deactivation of the present study.⁵² Similar effects were observed when an identical temperature-based analysis was conducted using 4-bromophenol (Figure 3.4b). Employing this substrate, lower product yields were achieved, consistent with previous results,⁸⁸ due to changes in the aryl halide electronic structure. For the 0.100 mol% Pd reaction, negligible yields were achieved after 24.0 h at room temperature; however, a $38.7 \pm 1.8\%$ yield was observed when the reaction temperature was increased to 40°C. Similar product yields were obtained at 50°C, but at subsequently higher reaction temperatures, a linear

decrease in product formation was noted until an $8.1 \pm 3.2\%$ yield was determined at 90°C . Similar trends were observed for the lower Pd loadings; however, for the 0.010 mol% and 0.005 mol% samples, maximum product yields were not achieved until 60°C due to the lower catalyst concentration. Consistent with the lower product yields, TOF values were observed as a function of temperature that were lower than those determined for the 4-bromobenzoic acid substrate. For this system, a TOF of 144 ± 23 mol product $(\text{mol Pd} \times \text{h})^{-1}$ was observed for the 0.050 mol% Pd reaction at a temperature of 50°C that increased to 216 ± 14 mol product $(\text{mol Pd} \times \text{h})^{-1}$ at 70°C . This trend of increasing TOF values with lower product yields is consistent for both brominated species, thus suggesting that the actual mechanism plays a role in the reactivity. Furthermore, while such results suggest optimized activity at slightly elevated temperatures, heating of the reaction system to significantly higher temperature causes catalyst deactivation.

While the results above suggest that the reaction temperature plays a unique role in the reactivity, such observations could arise from the degradation of the biomimetic Pd nanoparticles at the elevated temperatures, thus spontaneously releasing reactive species to solution. In addition, at the highest temperatures, particle aggregation may occur to deactivate the materials, leading to the low product yields. To ensure that the materials remain unaltered at elevated temperatures, UV-vis and TEM analyses were conducted, as presented in Figure 3.5. Here, a fresh solution of the peptide-capped Pd nanoparticles was synthesized. Immediately after reduction, a UV-vis spectrum of the materials was obtained, which was identical to previous results.⁸⁸ Next, the solution was then heated at 70°C for 24.0 h, from which the materials were analyzed by UV-

vis and TEM at selected time points. Throughout the heating process, identical UV-vis spectra of the materials were observed (Figure 3.5a), as compared to the spectrum taken immediately after reduction. TEM analysis of the materials after 0.0 h, 12.0 h, and 24.0 h of heating are shown in Figures 3.5b, c and d, respectively. Here, a particle size distribution of 2.2 ± 0.6 nm was observed prior to heating, while values of 2.1 ± 0.5 nm and 2.0 ± 0.5 nm were observed after 12.0 h and 24.0 h of heating, respectively, thus indicating that the biomimetic Pd nanoparticles remain stable in solution under the high temperature reaction conditions.

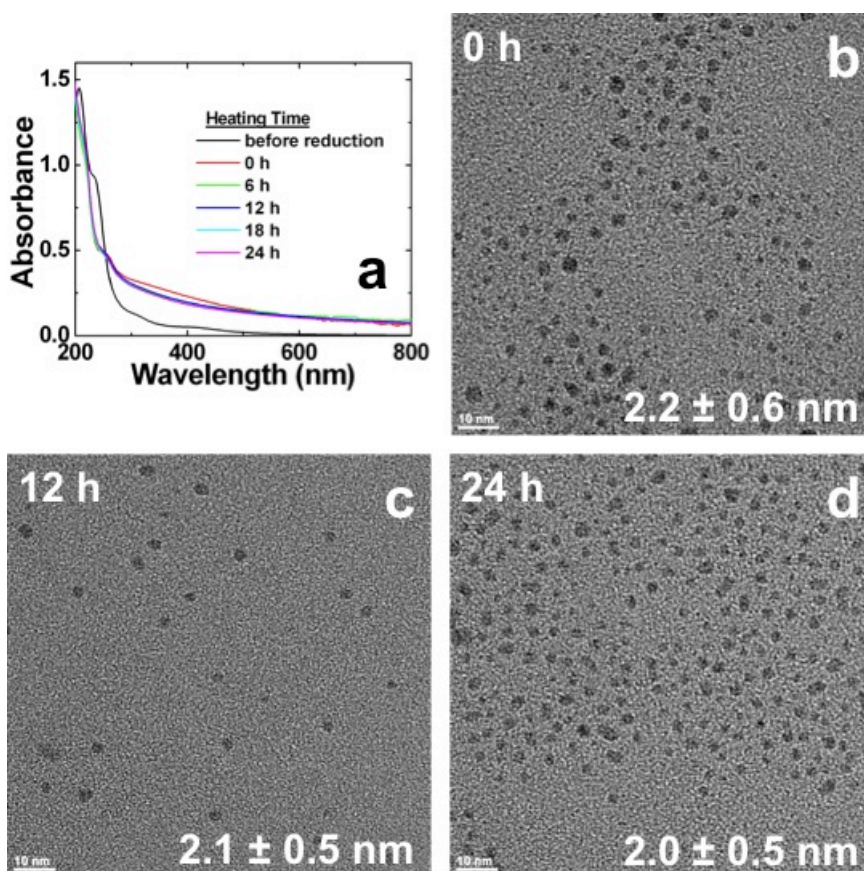


Figure 3.5 Analysis of the stability of peptide-capped Pd nanoparticles after heating at 70 °C for 24.0 h. Part a) presents the UV-vis spectra of the materials before reduction (black spectrum) and at various time points after reduction during the heating process that demonstrates no significant changes. Parts b-d present TEM images of the materials at time points b) 0.0 h, c) 12.0 h, and d) 24.0 h. Minimal to no changes in the particle size distribution are observed during the heating process.

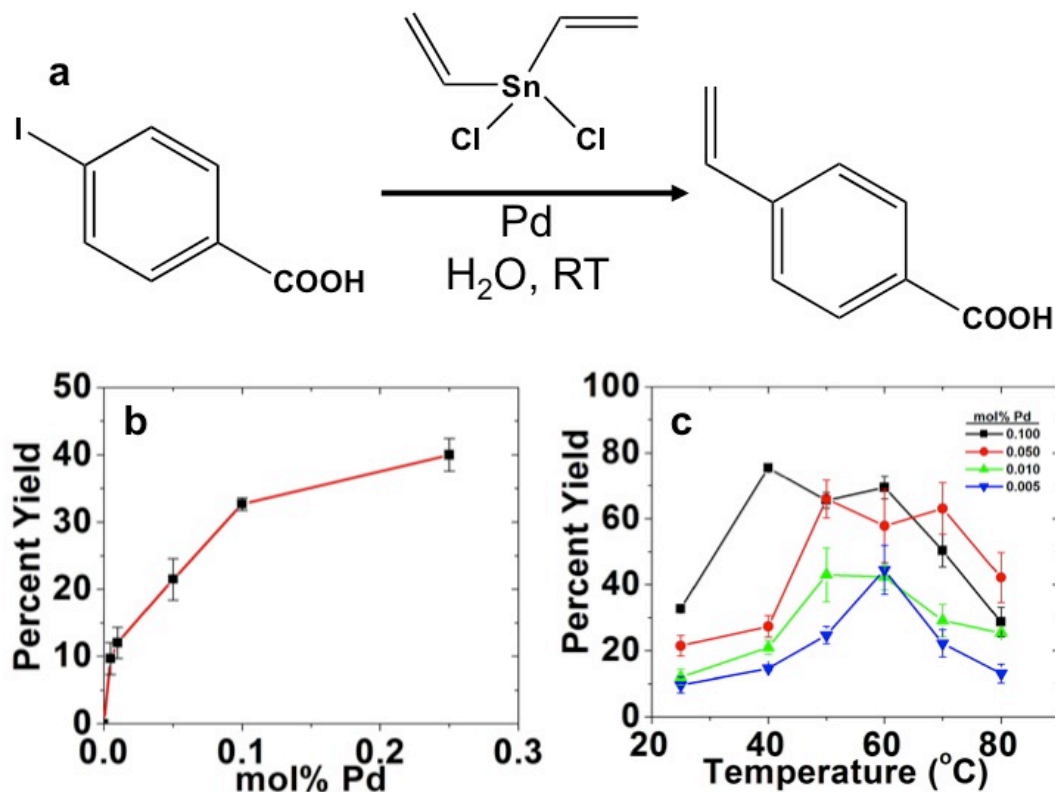


Figure 3.6 Reactivity analysis using DVT. Part a) presents the reaction scheme, part b) displays the percent yield of the 4-vinylbenzoic acid product as a function of catalyst concentration at room temperature, while part c) presents the product yield as a function of reaction temperature for a set of catalyst loadings.

While we have monitored the effects of the aryl halide, the tin complex used for transmetalation could play a large role in the reactivity and catalytic mechanism. Typically, PhSnCl_3 is employed, but other reagents are available, including DVT. As shown in Figure 3.6a, using this reagent with 4-iodobenzoic acid, 4-vinylbenzoic acid (VBA) is the anticipated product. Studying this specific reaction with the bionanocatalysts at room temperature, production of VBA was observed with Pd loadings ≥ 0.005 mol% (Figure 3.6b). Interestingly, lower yields were achieved using DVT as compared to PhSnCl_3 ; however, as the Pd concentration increased, the overall product yield also increased to a maximum of $40.0 \pm 2.4\%$ for a Pd loading of 0.250

mol%. To achieve larger VBA yields, the reaction was processed at temperatures between 20°C and 90°C, with Pd loadings ranging from 0.005 mol% to 0.100 mol%, (Figure 3.6c). For the reactions employing 0.100 mol% Pd at room temperature, a VBA percent yield of $32.7 \pm 0.92\%$ is quantitated; however, when the temperature was raised to 40°C, the product yield increased to $75.4 \pm 1.1\%$. As the temperature was further increased to $\leq 60^\circ\text{C}$, equivalent amounts of the product were achieved, but at a temperature $> 60^\circ\text{C}$, a decrease in the product amount was observed. It is worth noting that this is the same temperature where the percent yield decreased for the temperature-based studies of 4-bromobenzoic acid. Such results are consistent with the PhSnCl_3 results that show a proportional increase in product yields with Pd loadings and similar trends in product yields as a function of reaction temperature until catalyst deactivation at the highest temperatures.

The effects of catalyst concentration and reaction conditions demonstrate critical information regarding two features of the bionanocatalysts: the degree of reactivity and the mechanism for Stille coupling employing nanoparticles. The results suggest that the biomimetic materials possess a broad reactivity for Stille coupling with significant yields achieved using very low catalyst concentrations. Furthermore, the materials display a degree of sensitivity for the halogen identity of the aryl halide. While the iodo-based reagents readily react at room temperatures, bromo-based substrates require slightly elevated temperature conditions to drive the catalytic cycle. As a result, selective reactivity is envisioned based upon the reaction temperature, which could prove to be useful for complex synthetic protocols. In addition, reactivity is achieved across both electron donating and withdrawing groups,⁸⁸ as well as a

variety of tin compounds, which represent a diverse set of possible reagent candidates for low-temperature (< 50.0 °C) catalytic reactivity.

A second intriguing aspect is the implication of the results on the catalytic mechanism of nanoparticle-based Stille coupling. Two mechanisms are possible where the reaction occurs on the nanoparticle surface, or Pd²⁺ ions are abstracted from the nanoparticle to drive the reaction in solution. The two pathways are quite different where the altered steps could affect the reactivity and possible applications. In the second mechanism, the nanoparticle would serve as a catalyst reservoir where the reactive species must be extracted through the ligand shell, thus raising the importance of understanding the effects of the surface peptides. Our recent results indicate that the peptides strongly influence the reactivity due to their binding and orientation.⁹⁴ To fully elucidate these effects, which may have implications in other biomimetic materials,^{201, 222} it is critical to determine the fundamental reaction mechanism, which has proven to be challenging due to limited analytical techniques that probe such small materials (< 5.0 nm) at highly dilute concentrations.^{52, 86, 191, 194} Based upon these results, an atom leaching mechanism is most likely employed by the peptide-capped nanoparticles for Stille coupling (Figure 3.1). Furthermore, the results suggest that these materials are optimized for reactivity under green conditions, thus indicating that they may serve as model catalytic materials for future studies. The leaching mechanism for Stille coupling likely begins with Pd atom abstraction induced by oxidative addition at the nanoparticle surface. This is facilitated by the peptide ligands that form the kinked-loop structure, as discussed in the introduction, which expose the catalytic surface to drive the chemical process. After reductive

elimination, a free Pd⁰ atom is generated in solution. The fate of the atom depends upon two reaction conditions: the ratio of starting materials to Pd atoms and the free Pd atom concentration. If there is a significant excess of reagents, the Pd atoms can be recycled into the catalytic process (Figure 3.1, path 1). As the reaction ensues, the amount of starting material decreases. When a minimal reagent concentration is reached, the Pd atoms can no longer cycle through the reaction. As a result, highly reactive Pd atoms will accumulate in solution. If this concentration is low, based upon the amount of nanoparticles initially used, then it is likely that the atoms could be quenched with the remaining Pd particles (Figure 3.1, path 2). Additionally, if all of the Pd is leached such that no particles remain, the Pd⁰ peptide remains in solution, which would be responsible for controlling the renucleation and growth of the particles upon completion of the Stille coupling. Note that for reactions at elevated temperatures, particle nucleation and growth could be altered as compared to the process that occurs at room temperature. If the concentration of free Pd atoms is high, then uncontrolled aggregation could occur, resulting in the production of non-reactive Pd black during the catalytic process (Figure 3.1, path 3).^{194, 232} Such an event would be anticipated when the concentration of the Pd nanoparticles used in the reaction is high.

The results obtained from the present study correlate well with the catalytic leaching mechanism. As shown in Figure 3.3, at low concentrations of Pd in the reaction, a stable TOF was observed. As the TOF is normalized to reactive sites and the total Pd concentration was used to calculate this values, this suggests that nearly all of the Pd from the particles is leached to drive the reaction. At Pd loading values ≥ 0.075

mol%, a steady decrease in the TOF was indicated, which could result from two different possibilities. First, incomplete leaching of Pd from the particles could occur, thus some of the Pd could remain sequestered from the Stille coupling. In this case, the TOF value would decrease as not all of the Pd would be directly involved in the reaction. In the second case, at the high nanoparticle concentrations, significant Pd leaching would occur, thus generating a very high concentration of unstable, highly reactive Pd atoms in solution that would favor the formation of bulk Pd black, thus lowering the amount of active catalyst over time. Interestingly, for the reactions with lower TOF values (≥ 0.075 mol% Pd), a black precipitate was observed, thus suggesting that consumption of the catalyst occurs to generate the non-reactive bulk species. While quantitative product yields are achieved, it is likely that some Pd does remain in solution to drive the reaction during bulk precipitation. If a surface based mechanism was driving the reaction, no change in TOF would occur, regardless of the Pd concentration, as catalyst degradation would not be anticipated due to the stabilizing effects of the surface-bound peptides. Furthermore, these effects are similar to other nanoparticle-catalyzed coupling reactions that have been suggested to follow a leaching mechanism, which demonstrated larger TOF values with diminishing Pd concentrations.^{194, 232}

In addition, the results of the temperature studies are likely consequences of Pd⁰ leaching. For both 4-bromobenzoic acid and 4-bromophenol at room temperature, minimal product generation occurs; however, heating at $< 70^{\circ}\text{C}$ considerably increases product yields. This effect enhances the Stille reaction rate to maximize product yields; however, at $\geq 70^{\circ}\text{C}$, diminishing production is observed where Pd

black formation is likely maximized that competes with the catalysis. While the Stille TOF is higher at the elevated temperatures as anticipated, such values are measured at very short time periods after reaction initiation. In addition to this increase, the rate of bulk Pd black formation is also enhanced at the higher temperatures to diminish the number catalytic moieties. To that end, the reactive species are continually being depleted throughout the reaction, where such negative effects would be enhanced at longer time periods. As a result, lower yields are observed.

While a catalytic leaching mechanism is postulated for the biomimetic nanoparticles in the Stille reaction, significant differences are noted as compared to other C-C coupling processes that suggest that these materials are optimal choices for environmentally friendly and energy efficient reactivity. As is evident from the results above, optimal reactivity for these materials occurs at low concentrations of the precious metal catalysts (<0.050 mol% Pd), with temperatures that consume minimal to no energy (40°C), in a biologically and environmentally preferred medium (water). In fact, should these be changed towards harsher conditions, the reactivity can become inhibited. For instance, heating of the system to levels required to drive Heck coupling using nanoparticles ($>60^{\circ}\text{C}$)^{230, 231} causes rapid consumption of the reactive species to decrease product yields. Furthermore, the present system reaches a saturation point for the activity (TOF) at low catalyst concentrations. This suggests that at Pd loadings of ≤ 0.050 mol%, the leached Pd species are stable in solution to drive the process. Should the formation of Pd black be occurring at these values to produce the non-reactive bulk species, saturation would not occur. In this event, the rate of Pd black formation would continually decrease for lower catalyst

concentrations, thus allowing for a higher percentage of the Pd atoms to participate in the reaction. To that end, a continual increase in the TOF value at progressively lower Pd concentrations would be noted, which is observed for Heck and Suzuki coupling where TOF saturation typically does not occur at the low Pd concentrations of the present study.^{52, 187, 191, 194} This suggests that the peptide-based nanomaterials and the leached species are likely to be more stable against bulk Pd formation, to allow for nearly all of the leached Pd materials to participate in the reaction rather than precipitate as unreactive aggregates. Finally, consistent with previous results, the peptide-capped materials present maximum activity in an aqueous solvent.⁸⁸ Should organic co-solvents be added, decreased product yields are achieved, which likely is due to changes at the bio/nano interface as a result of the solvent dielectric. Overall, the present results indicate that the biomimetic nanoparticles are likely to be optimized model materials for efficient reactivity under green conditions.

To physically demonstrate the effects of the leaching mechanism, TEM and QCM analyses were employed to monitor the Pd abstraction process. As changes in the particle size are possible from the leaching mechanism,^{52, 86} we first attempted to observe the materials by TEM after the reaction. At the highest concentrations, we know that the particle size does increase due to bulk precipitation; however at the lower Pd concentrations, no precipitation is detected. This is likely due to the reformation of Pd nanoparticles upon Stille coupling completion, thus possibly resulting in altered particle size distributions. Due to the extremely low nanoparticle concentrations in these reactions, no materials were able to be observed by TEM post-reaction. To fully characterize these effects, *in situ* spectroscopic methods are

required,²¹⁴ which are presently being conducted; however, QCM analysis of a Pd source indicates that the leaching process does occur during the reaction.

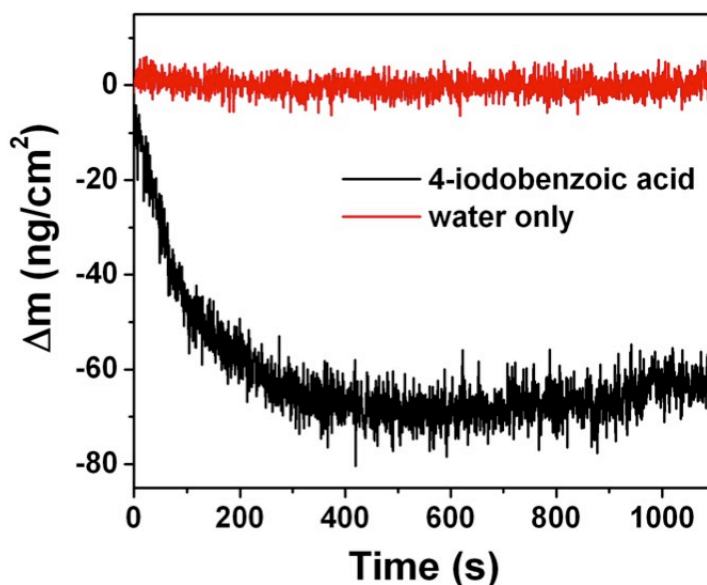


Figure 3.7 QCM analysis demonstrating the mass loss from a bare planar Pd surface during oxidative addition with 4-iodobenzoic acid. As a control, when no aryl halide reagent is added to the system, no change in the mass of the Pd surface is noted.

To address Pd leaching, QCM analysis was used to measure and quantify the metallic mass loss from a bare Pd surface during the course of oxidative addition with 4-iodobenzoic acid. QCM is a highly sensitive technique used to probe surface interactions upon the adsorption or desorption of molecules by measuring a change in frequency of an oscillating quartz crystal. QCM has been successfully used to monitor the dissolution and extraction of metal atoms from a Au coated quartz crystal in the presence of low concentrations of cyanide.²³⁵ In this case, the dissolution of Au by cyanide produced a reasonable increase in the resonance frequency of the metal coated quartz chip due to a loss of mass from the bulk Au surface. This suggests that similar studies could be employed to confirm and monitor Pd leaching during the

oxidative addition step of Stille coupling using a Pd coated surface. To that end, as shown in Figure 3.7, the mass loss of Pd from a cleaned metallic source (100 – 200 Å thick Pd film) mounted in an open QCM sensor module was directly studied in the presence of 4-iodobenzoic acid using a QCM with dissipation at room temperature. Consequently, in the presence of aryl halide, the frequency of the third overtone resonance increased by 4 to 47 Hz over three independently prepared Pd coated surfaces, which is equal to a mass loss of between 62 ng/cm² and 834 ng/cm², respectively. This significant loss in mass and the large range of values is likely attributable to the slight differences in the thicknesses of the individual Pd surfaces. Ultimately, these results support a catalytic mechanism of nanoparticle mediated Stille coupling involving abstraction of Pd atoms during the oxidative addition step, which is controlled by the aryl halide.

3.5 Summary and Conclusions

In conclusion, from a catalytic reaction analysis, critical information concerning the reactivity and mechanism of C-C coupling employing biomimetic Pd nanoparticles has been achieved. These results suggest that the materials are highly reactive for Stille coupling and that they follow an atom leaching mechanism that is highly sensitive to the reaction conditions. By elucidating the reaction mechanism, a more complete analysis of the peptide-capped surface can be completed to understand the role of the biotic/abiotic interface in controlling and optimizing the functionality of bio-inspired nanomaterials. Such structures represent promising materials for future

eco-friendly and energy efficient processes and may serve as model systems to isolate surface structural motifs responsible for driving these applications. Furthermore, these results may serve as a basis for understanding the catalytic mechanism of nanoparticle-based Stille C-C coupling, which could prove to be useful in the design of selective and enhanced catalytic approaches for applications ranging from pharmaceutical production to molecular electronics design. To more fully determine the mechanistic aspects of the nanoparticle-driven reaction, *in situ* analysis of kinetic rates is required, which is presently being conducted in our labs and will be reported shortly.

“Pacardo, D. B.; Slocik, J. M.; Kirk, K. C.; Naik, R. R.; Knecht, M. R. *Nanoscale* 2011, 3, 2194-2201. – Reproduced by permission of The Royal Society of Chemistry.”

Chapter 4. Exploring the Mechanism of Stille C-C Coupling via Peptide-capped Pd Nanoparticles Results in Low Temperature Reagent Selectivity

4.1 Overview of the Study

In this chapter, we systematically probed the atom-leaching mechanism of Pd nanoparticle-driven Stille coupling to further elucidate the fate of the highly active Pd⁰ atoms released in solution. In this regard, initial oxidative addition at the particle surface results in Pd atom abstraction for reactivity in solution. As a result, two reaction sites are present, the particle surface and pre-leached Pd atoms, thus differing degrees of reactivity are possible. This effect was probed via aryl halide combinations that varied the halogen identity allowing for oxidative addition of two substrates simultaneously. The results demonstrate that the system was highly reactive for iodo-based compounds in the mixture at room temperature; however, reactivity at bromo-based substrates was only observed at slightly elevated temperatures of 40.0 °C. As such, substrate selectivity was evident from the catalytic materials that can be controlled based upon the aryl halide composition and reaction temperature. Furthermore, both *intermolecular* and *intramolecular* selectivity is possible, thus raising the degree of reaction complexity that can be achieved.

4.2 Motivation

Recent advances in nanotechnology have enabled the design and fabrication of new materials with unique properties for a wide range of applications. An emerging important application for nanomaterials focuses on their use in catalytic technologies.⁵² For

instance, a variety of different materials have been realized for reactivity in C-C coupling,^{58, 86, 88, 95, 134, 233, 236-239} olefin hydrogenation,^{31, 32, 223, 240} nitro-group reduction,^{36, 37, 241} and remediation of trichloroethene.²⁴²⁻²⁴⁴ This reactivity typically arises from the inorganic core; however, catalytic activity can also be achieved via the ligands bound to the particle surface.^{245, 246} While the basic catalytic properties of these materials have been demonstrated, enhancing and/or expanding their functionality is highly desirable. Typically, this can be achieved in two manners: optimization for reactivity under ambient/green conditions or increasing the degree of catalytic selectivity based upon the reagents.²⁴⁷⁻²⁵⁰ Together, such approaches are important as they lower the environmental impact of catalysis, minimize energy consumption required to drive the reaction, as well as limit the degree of separation steps required to purify the final product. The latter point of separations is critically linked to catalyst selectivity that minimizes byproduct formation, thus also enhancing the carbon efficiency of the reaction. To achieve these capabilities, it is important to fully understand and exploit the mechanism employed by the catalytic nanomaterials, which can be challenging to study due to the complexity of the system and the limited analytical techniques available. Through this understanding, individual steps of the catalytic cycle could be exploited to enhance the system and/or realize reagent selectivity.

We have previously reported the biomimetic synthesis of nanocatalysts designed using Pd-specific peptides that bind directly to the nanoparticle surface.^{88, 251} In this regard, the Pd4 peptide (TSNAVHPTLRHL) caps growing Pd nanoparticles upon recognition of the face centered cubic (fcc) metallic structure through the strong interactions of the histidine residues.^{83, 88, 94, 213, 251, 252} From this approach, ~2 nm Pd nanoparticles can be generated

that are highly reactive for the Stille C-C coupling reaction.⁸⁸ As such, the reaction can be employed to elucidate important surface structural effects of the biotic/abiotic interface of the materials that would be difficult to study. Using the Pd₄-capped Pd nanoparticles for Stille coupling under non-traditional conditions of an aqueous solvent at room temperature, quantitative product yields were observed at low catalyst loadings (> 0.001 mol% Pd).^{88, 251} Furthermore, both the particle size and catalytic reactivity can be tuned as a function of the peptide sequence, where minor structural changes can result in significant alterations in the catalytic functionality.^{83, 94, 252} Taken together, these materials represent a model system for studying ligand-capped catalysts that could address environmental and energy concerns.^{88, 251}

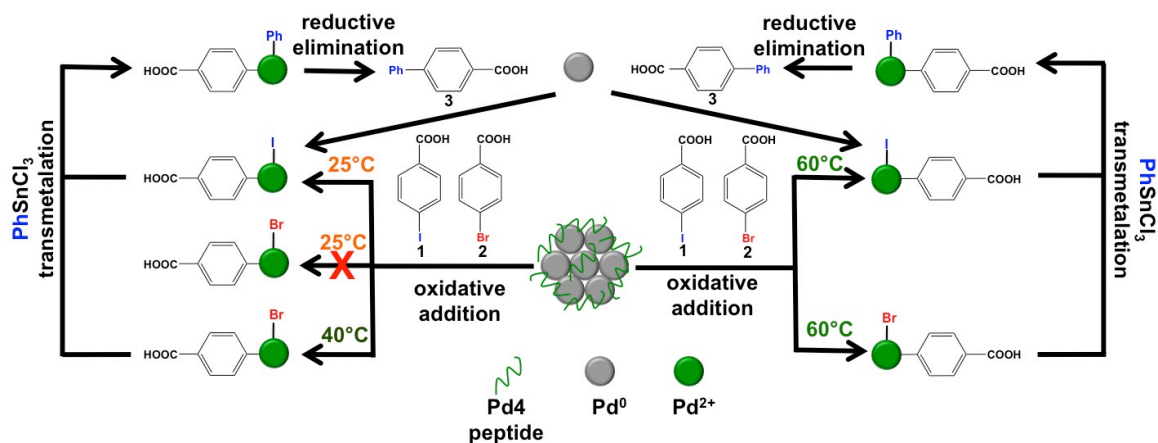


Figure 4.1 Representative scheme for reagent selectivity of the peptide-capped Pd nanoparticles for two aryl halide substrates at different reaction temperatures based upon the catalytic mechanism.

Given the advantages of generating efficient catalytic systems, it is important to understand the underlying principles driving the reaction. Recent studies of the Stille coupling reaction using the Pd₄-capped Pd nanoparticles suggest that an atom-leaching

mechanism is possible (Figure 4.1).²⁵¹ In this mechanism, the particles act as catalytic reservoirs containing the active metal species, which has been similarly proposed for other C-C coupling reactions.^{52, 86, 251, 253, 254} During the initial oxidative addition step of the reaction, Pd atoms are abstracted from the nanoparticles, from which the catalytic cycle can then occur in solution to produce the final product and regenerate the Pd⁰ species. These free Pd⁰ atoms can then be recycled through the catalytic process until reaction completion, upon which the atoms are quenched by the remaining particles.^{52, 94, 251} These Pd nanoparticles also demonstrated varying degrees of reactivity with aryl halides as a function of the halogen group. To that end, iodo-derivatives are typically reactive for Stille coupling at room temperature, while bromo-based species require a slight increase in temperature to 40.0 °C for reactivity.²⁵¹ This temperature effect could be directly related to the bond dissociation energies of the carbon-halogen bond wherein C-Br (285 kJ/mol) > C-I (232 kJ/mol).²⁵⁵ While it is clear that aryl bromides are unable to abstract Pd⁰ atoms from the nanoparticle surface at room temperature,²⁵¹ it is unclear if the abstracted Pd⁰ atoms can insert across the C-Br bond to drive the reaction under such conditions. As such, to more fully understand and elucidate the fundamental catalytic properties of the system and the overall mechanism, additional studies are required that could be used to enhance the reactivity of the materials.

Here we report on the reactivity and substrate selectivity of peptide-capped Pd nanoparticles in a mixture of reagents. This study provides important information concerning the catalytic reaction mechanism and degree of reactivity. By employing different aryl halide substrates, Stille coupling with an organostannane reagent can be achieved, where selectivity is observed as a function of the reaction temperature, aryl

halide composition, and the catalytic mechanism. As summarized in Figure 4.1, the Pd nanoparticles selectively couple aryl iodide substrates over bromo- or chloro-derivatives in the same reaction mixture at room temperature generating the anticipated product; however, a mild increase in system temperature to 40.0 °C enables reactivity at the bromo substrate. These results indicate functional group catalytic selectivity that is inversely related to the strength of the carbon-halogen bond. By increasing the reaction temperature to 60.0 °C, catalytic selectivity is lost wherein reactivity at both iodo and bromo substituents is observed. Furthermore both *intermolecular* (separate reagents) and *intramolecular* (two reactive sites in a single reagent) selectivity is observed, raising the level of reaction complexity possible under low-temperature conditions using the peptide-capped materials. This selectivity is achieved based upon the catalytic leaching mechanism, where an apparent energy barrier is present that prevents bromo-based reactivity at room temperature.

This suggests that oxidative insertion of the Pd⁰ materials across the C-Br bond is prevented, regardless of whether the metallic component is constrained within the zerovalent particle or pre-leached into solution. These results are important for advancing catalytic nanotechnologies to achieving energy- and carbon-efficient systems.

4.3 Methods

4.3.1 Chemicals

4-iodobenzoic acid (**1**), NaBH₄, CDCl₃, NaCl, 4-tert-butylphenol, KOH, *N*-methyl-*N*-(trimethylsilyl) trifluoroacetamide (MSTFA), and dichloromethane were purchased from

Acros Organics. 4-bromobenzoic acid (**2**) was acquired from Alfa Aesar. 4-chlorobenzoic acid (**4**) and 3-bromo-5-iodobenzoic acid (**5**) were purchased from TCI America. 3-chloro-5-iodobenzoic acid (**8**), 3-bromo-5-chlorobenzoic acid (**10**) and 2-chloro-5-iodobenzoic acid (**19**) were obtained from Oakwood Products, while 3,5-diiodobenzoic acid (**11**) was acquired from Spectra Group Limited. PhSnCl_3 , K_2PdCl_4 , 3,5-dibromobenzoic acid (**13**), 2-bromo-5-iodobenzoic acid (**17**) and 2-chloro-4-iodobenzoic acid (**21**) were obtained from Sigma-Aldrich. Finally, 2,5-diiodobenzoic acid (**14**) was purchased from MP Biomedicals. Diethyl ether was obtained from VWR and 18 m Ω •cm water (Millipore) was employed throughout. All reagents were used as received without additional purification.

4.3.2 Characterization

The reaction products were characterized using GC-MS and ^1H NMR. For GC-MS analysis, ~1 mg of the product was dissolved in 200 μL of MSTFA, which was allowed to react for 2.00 h.⁸⁸ The sample was then diluted with 2.00 mL of dichloromethane before analysis using an Agilent 5975C GC-MS system. All products, including those generated using both the mono- and di-substituted aryl halides, were processed using this approach. For ^1H NMR analysis, a Bruker 400 MHz spectrometer with an autotuning multinuclear probe was employed. The percent yields of the products were determined by comparing the peaks of the internal standard (*t*-butyl phenol) with the product peak. For the reactions using **1** and **2**, the peak at 8.17 ppm corresponds to the biphenylcarboxylic acid (**3**) product while the peak at 6.7 ppm corresponds to the internal standard. The ratio of the integration of these two peaks was used to calculate the percent

yield of the reaction as previously demonstrated.⁸⁸ Furthermore, the amount of unreacted starting materials was determined by comparing the ratio of the peaks at 7.8 ppm (**1**), 7.93 ppm (**2**), and 8.0 ppm (**4**) with that of *t*-butyl phenol. For the di-substituted aryl halides, identical methods were employed where peaks associated with the mono- and di-substituted products were used to determine the product yield.

4.3.3 Catalytic Reactions with Multiple Aryl Halides

For all reactions, Pd nanoparticles capped with the Pd4 peptide were prepared at a Pd:peptide ratio of 3.3 using previously described methods.⁸⁸ For the catalytic reactions involving two separate aryl halide substrates, a system composed of **1** and **2** is described; however, identical procedures and conditions were employed for reactions with two reagents. In a reaction flask at room temperature, 5.00 mmol of **1** and 5.00 mmol of **2** were co-dissolved in 160 mL of 2.25 M KOH. To this solution, 12.0 mmol of PhSnCl₃ was added, followed by the direct injection of 10.0 mL of the freshly prepared Pd4-capped Pd nanoparticles. Under these conditions, a reaction with 0.05 mol% Pd was generated with respect to the total aryl halide concentration in solution. Immediately upon nanoparticle addition, 8.00 mL aliquots were extracted, separated into vials, reacted while stirring, and subsequently quenched with 50.0 mL of 5% HCl at specified time intervals. After 2.0 h at room temperature, the remaining reaction vials were placed in an oil bath at 40.0 °C and then quenched at selected time points. For all of the quenched reactions, the product was extracted, characterized, and quantitated by ¹H NMR and GC-MS.

This same system was also studied at 60.0 °C throughout the reaction to determine the effect of higher temperature. In this set up, the reaction was prepared and mixed in the flask, from which the aliquots that were transferred to separate vials were immediately placed in an oil bath heated to 60.0 °C. At selected time points, the reactions were quenched and the products were extracted and quantitated using the standard approach.

4.3.4 Aryl Dihalide Reactivity

The effects of multiple halogen functional groups within a single molecule on both the catalytic mechanism and the reaction selectivity were initially studied using **5**. In a reaction vial, 0.25 mmol of **5** and 0.6 mmol of PhSnCl₃ were dissolved in 6.00 mL of 1.5 M KOH. To this mixture, 0.25 mL of the freshly prepared Pd nanoparticles (0.05 mol% Pd) was added and the reaction was stirred at room temperature for 24.0 h. Once complete, the reaction was quenched using 50.0 mL of 5% HCl. The products of the reaction were extracted and quantitated as described above. Additional variations to this basic procedure were also studied by changing the Pd catalyst concentration and/or reaction temperature while holding all other conditions constant. The same procedure was employed for the following aryl dihalides: **8**, **10**, **14**, **17**, **19** and **21**. For **11** and **13**, identical procedures were also used; however, the starting materials were dissolved using 15.0 mL of 1.0 M KOH and 7.0 mL of 1.5 M KOH, respectively, due to reagent solubility.

The time-resolved formation of the coupling products between **5** and PhSnCl₃ was monitored by scaling up the reaction and extracting aliquots at selected time intervals. Specifically, 3.75 mmol of **5** and 9.0 mmol PhSnCl₃ were co-dissolved in 90.0 mL of

1.50 M KOH. When the reagents were dissolved, 5.00 mL of the freshly prepared Pd nanoparticles (0.05 mol% Pd) was added. 6.00 mL aliquots were then taken and quenched every 30.0 min for 5.0 h followed by product extraction and quantitation. A similar procedure was used for **11**; however, product formation was monitored every 10.0 min for 1.00 h, followed by 30.0 min intervals over an additional 2.00 h.

4.4 Results and Discussion

Based upon the proposed Pd leaching mechanism, aryl halide oxidative addition occurs at two specific locations: at the nanoparticle surface and at free Pd⁰ atoms in solution.^{52, 86, 251, 253, 254} Initially, oxidative addition at the nanoparticle surface occurs to leach the Pd atoms to solution, from which subsequent oxidative addition processes can occur with additional aryl halide reagents.²⁵¹ Intrinsicly, the reactivity for these two steps could be significantly different based upon the aryl halide substrate. For instance, from previous studies using the peptide-capped materials, it is known that aryl iodides can oxidatively add to the Pd metal at the nanoparticle surface, while aryl bromides cannot,^{88, 251} however, different reactivity for the leached Pd⁰ atoms could be observed as a function of the halogen group.

In this regard, while no reaction is observed for aryl bromides with the Pd nanoparticles, Stille coupling could be noted from such reagents using the leached Pd⁰ atoms. Such mechanistic information could be quite useful in the design of selective catalytic materials. As such, equal amounts of aryl halides that varied the halogen only were co-reacted with the peptide-capped Pd nanoparticles to monitor product formation. Initially,

1, **2**, and **4** were used since the substrates exhibited different levels of reactivity: **1** is known to readily react for Stille coupling at room temperature, slightly higher temperatures of 40.0 °C are required to drive the same reaction with **2**, while **4** does not typically react.^{88, 251}

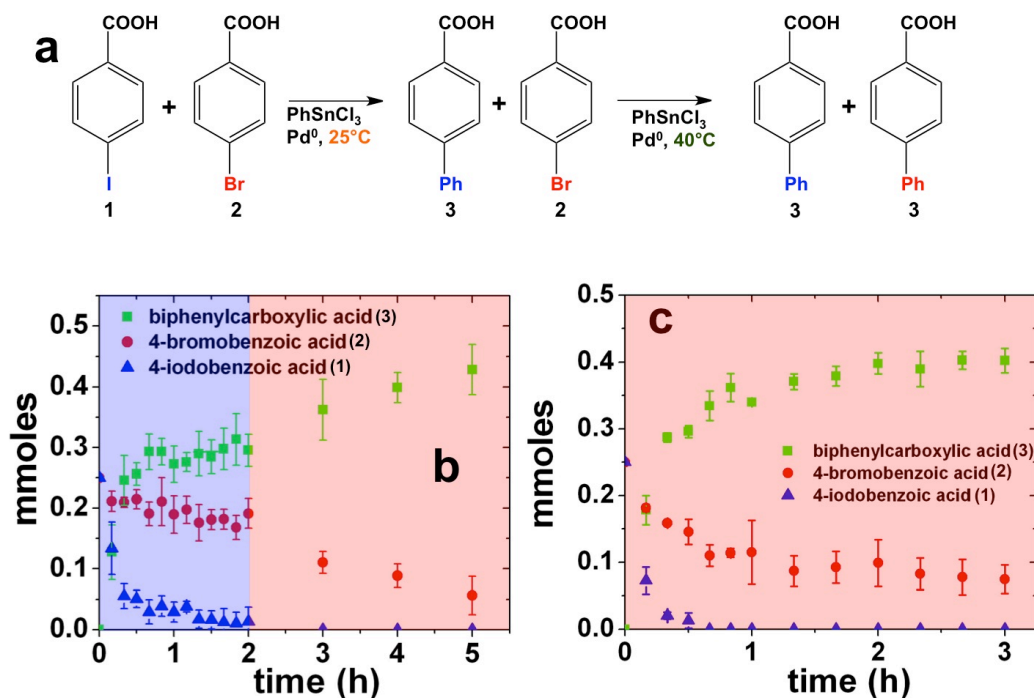


Figure 4.2 Effects of aryl halide mixtures for the Stille coupling reaction using peptide-capped Pd nanoparticle catalysts. Part (a) presents the reaction between **1** and **2** at the indicated temperatures. Part (b) displays the time based analysis for the reactions using **1** and **2** at 25.0 °C (blue region) for 2.0 h, followed by heating the reaction to 40.0 °C (red region), while part (c) presents the Stille coupling analysis over time using **1** and **2** at 60.0 °C throughout the study.

Figure 4.2a schematically presents the process employed for using two different aryl halide substrates in the reaction. For this, **1** and **2** are commixed in the reaction medium with PhSnCl₃ and sufficient Pd nanoparticles to reach a concentration of 0.05 mol% Pd. The reaction is initially monitored at room temperature (~25.0 °C), followed by heating

to 40.0 °C after 2.00 h. The progress of the reaction, monitored at selected time points, is shown in Figure 4.2b. The plot represents the amount, in mmoles, of **1** (blue triangles), **2** (red circles), and of the product, **3** (green squares), present in the reaction at the given time. Immediately after catalyst addition at room temperature, rapid consumption of **1** was observed as shown by the exponential decrease in the amount of reagent in the reaction. After 1.0 h, only trace amounts of this reagent were present in the mixture, which reached complete consumption at 2.0 h. Consequently, the quantity of product **3** rapidly increased over the initial 1.0 h time frame to eventually saturate. Conversely, the amount of **2** remained constant for the first 2.0 h of the reaction at room temperature. A minor decrease may be present; however, this is within the statistical noise of the study. After 2.0 h at room temperature, the reaction was mildly heated to 40.0 °C, where previous results demonstrated maximal reactivity for **2**.²⁵¹ At the elevated temperature, the bromo-based substrate is consumed, concomitant with an increase in the product quantity. Interestingly, the rate of consumption of **2** at 40.0 °C was slower than the consumption of **1** at room temperature, suggesting a change in the reaction rate as a function of halogen identity.

These results indicate that the peptide-capped Pd nanoparticles preferentially drive coupling at the iodo-derivative over the bromo-species at room temperature, regardless of whether Pd⁰ atoms are pre-leached into solution. Pd⁰ atoms are abstracted from the nanoparticle surface by aryl iodide oxidative addition, thus they would be available for reactivity with the aryl bromide compound upon completion of the first Stille coupling cycle. As such, this suggests that an energy barrier exists for aryl bromide oxidative addition at both the nanoparticle surface and the highly reactive Pd⁰ atoms in solution.

To probe this mechanistic observation, additional studies of different aryl halide combinations and selected reaction temperatures were employed. Initially, an identical coupling system was studied with **1** and **2**; however, the reaction was processed at 60.0 °C throughout the experiment. At this temperature, both substrates should readily undergo coupling to generate common product **3**, as shown in Figure 4.2c. In this study, rapid consumption of **1** is observed, faster than at room temperature, resulting in complete reagent consumption within 40.0 min. Additionally, immediate coupling is observed for **2**; however, the rate of the reaction for the bromo-derivative is slower compared to the iodo-derivative. Complete exhaustion of **2** is not observed, resulting in ~70% of the substrate generating product, consistent with previous studies.²⁵¹ Further co-reactivity studies were also conducted using a mixture of **1** and **4**, as presented in Figure 4.3. Figure 4.3a specifically presents the study of the reaction at room temperature, while Figure 4.3b presents the analysis of the reaction at 60.0 °C. As anticipated, when the reaction was processed at room temperature, rapid formation of product **3** (green squares) was observed from **1** (blue triangles), with complete reagent consumption at 2.00 h, while no coupling was noted from **4** (black diamonds) throughout the process. When the reaction was studied at the elevated temperature of 60.0 °C (Figure 4.3b), rapid consumption of **1** was noted over a 40.0 min time frame with no product formation arising from the chloro-derivative. Additional Stille coupling studies of mixtures of **2** and **4** were performed using the peptide-capped Pd nanoparticle catalysts. Figure 4.3c presents the catalytic analysis for the Stille coupling reaction using these two reagents at room temperature with a 0.05 mol% Pd catalyst concentration. Under these conditions, no coupling product is observed after 5.00 h. When the reaction was studied at a

temperature of 60.0 °C, Figure 4.3d, consumption of **2** is noted (red circles) along with an increase in the formation of **3** (green squares). Again, no reactivity from **4** is observed even at the higher temperature with leached Pd⁰ present in the medium. Figure 4.3e, presents the scheme for the competition reaction between **2** and **4** at different temperatures.

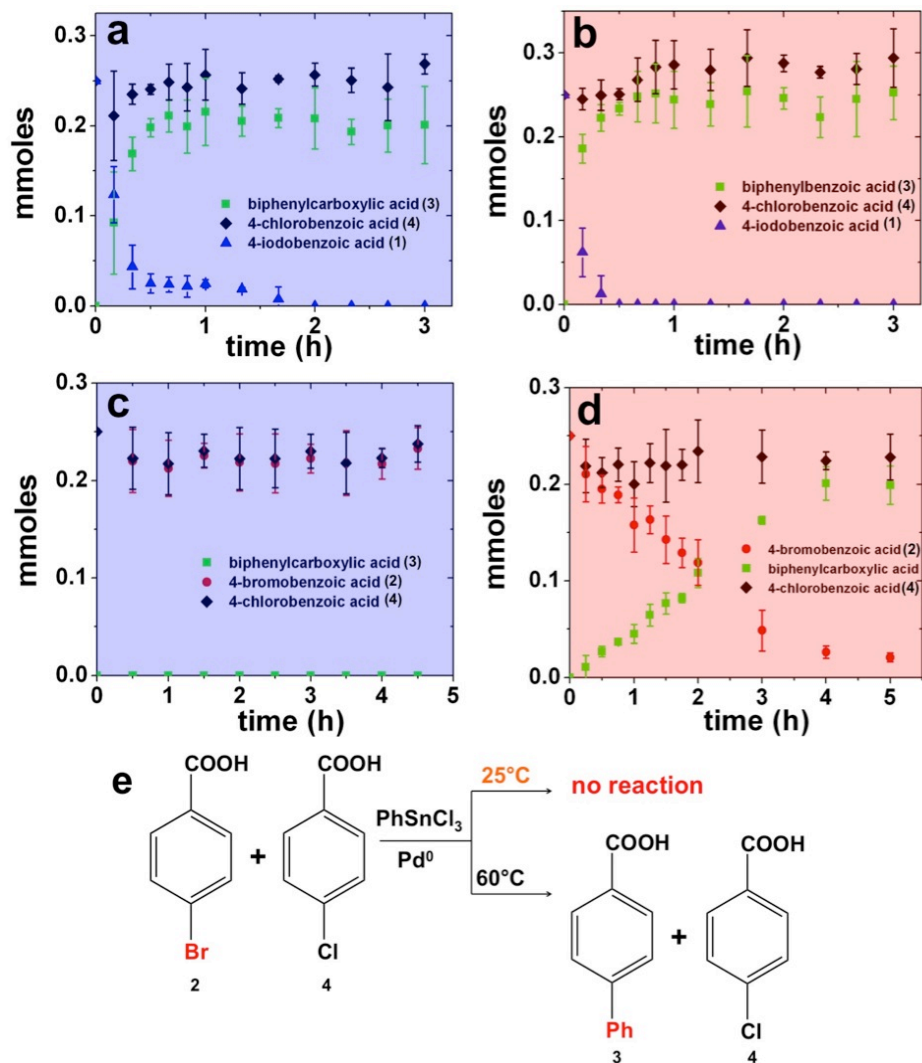
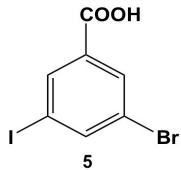
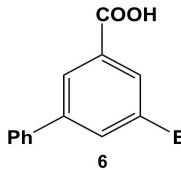
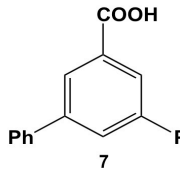
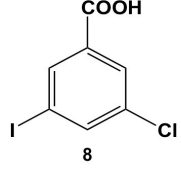
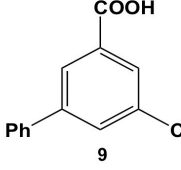
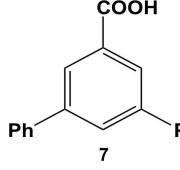
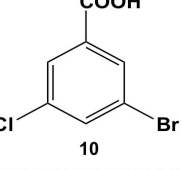
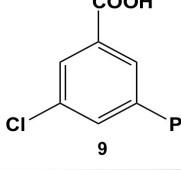
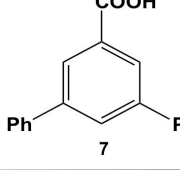
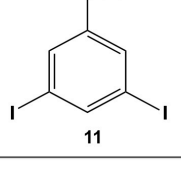
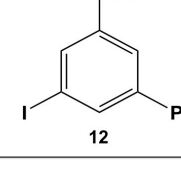
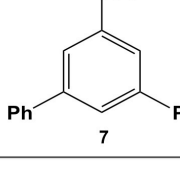
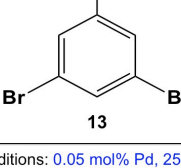
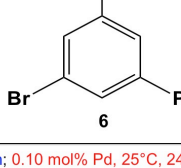
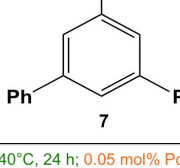


Figure 4.3 Parts a) and b) present the time resolved analysis of the Stille coupling process employing mixtures of **1** and **4** at room temperature and at 60.0 °C, respectively, while parts c) and d) display the same temperature analysis for mixtures of **2** and **4** at the same temperatures. The scheme for the reaction of **2** and **4** at different temperatures is shown in part e).

Taken together, these studies demonstrate important results concerning the reactivity of Pd nanoparticles for C-C coupling reactions based upon the catalytic mechanism. In the proposed leaching mechanism (Figure 4.1), aryl halide oxidative addition occurs at the nanoparticle surface, which abstracts reactive Pd species. After completion of the catalytic cycle, highly reactive Pd⁰ components are released in the reaction medium, from which secondary oxidative addition with additional substrates can occur to recycle through the process. Eventually, these reactive Pd⁰ species are quenched by the remaining particles in the mixture; however, two different oxidative addition steps are present that are likely to be both thermodynamically and kinetically different. These results indicate that while the two oxidative additions are indeed different, the reactivity for the separate processes remains similar. To that end, aryl iodides are reactive for oxidative addition at room temperature at both the nanoparticle surface and the leached Pd⁰ atoms, while elevated temperatures are required for reactivity in both processes for aryl bromides. Regardless of the oxidative addition step, aryl chlorides remain unreactive. Such results are likely to be related to the relative values of the C-X bond dissociation energies associated wherein C-I (232 kJ/mol) < C-Br (285 kJ/mol) < C-Cl (338 kJ/mol).²⁵⁵ As such, in the Stille coupling reaction, the aryl iodide substrate reacts rapidly at room temperature, indicating that both oxidative addition steps readily occur without the need for thermal activation. On the other hand, the bromo-species require mild heating to 40.0 °C for the coupling reaction to occur due to the stronger C-Br bond. The aryl chloride, however, does not undergo coupling even at 60.0 °C due to the greater energy required for activation of the C-Cl bond. Mechanistically, these results provide a greater understanding of the different factors that affect the oxidative addition processes and

could potentially be applied to different C-C coupling reactions. Furthermore, these capabilities could also be exploited to engender the biomimetic system with catalytic selectivity. In that regard, these studies suggest selectivity for iodo-based substrates over bromo- and chloro-based reagents as a function of temperature. This selective reactivity is based upon the mechanism of the reaction and the thermodynamics of the system. While this was observed for *intermolecular* reaction systems, *intramolecular* reactivity and selectivity may also be possible; however, the electronics of the system may change the degree of reactivity.

The reactivity of aryl dihalide substrates was initially studied using a benzoic acid derivative containing two different halide groups, **5** (Table 3, entry 1). In this reaction, the effect of having two reaction centers on the aryl ring was investigated through the formation of two likely products, 3-bromo-5-phenylbenzoic acid (**6**) and 3,5-diphenylbenzoic acid (**7**); the former is generated from the reaction of the iodo-component of the substrate, while the latter from the reaction of both the iodo- and bromo-components. A third product is possible, 3-iodo-5-phenylbenzoic acid; however, this product is unlikely based upon the observed reactivity of iodo over bromo groups. Using 0.05 mol% Pd at 25.0 °C, 70.8 ± 0.9% of **6** and 22.1 ± 2.5% of **7** was produced after 24.0 h. These results suggest that the iodo-component of the aryl dihalide preferentially undergoes Stille coupling at room temperature leading to the formation of the mono-substituted product. Interestingly, the generation of the di-substituted product at room temperature indicates that the C-Br bond in the mono-substituted product is potentially activated to undergo oxidative addition and eventual Stille coupling (discussed below).

Entry	Aryl Dihalides	Possible Products			
		Mono-substituted	Percent Yield	Di-substituted	Percent Yield
1			70.8 ± 0.9 33.6 ± 1.9 19.3 ± 6.0 12.9 ± 11.2		22.1 ± 2.5 60.9 ± 1.3 80.6 ± 6.4 69.8 ± 11.5
2			88.2 ± 4.6 89.2 ± 9.0 97.2 ± 3.5 95.5 ± 7.8		0.0 0.0 0.0 0.0
3			0.0 0.0 0.0 0.0		0.0 0.0 0.0 0.0
4			0.0 0.0 0.0 0.0		88.6 ± 9.0 87.5 ± 7.4 96.6 ± 3.8 82.4 ± 13.9
5			0.0 0.0 32.5 ± 3.0 30.9 ± 3.2		0.0 0.0 24.6 ± 3.7 39.5 ± 1.4

Reaction conditions: 0.05 mol% Pd, 25°C, 24 h; 0.10 mol% Pd, 25°C, 24 h; 0.10 mol% Pd, 40°C, 24 h; 0.05 mol% Pd, 60°C, 24 h

Table 3 Stille coupling analysis of reactions using aryl dihalide substrates and the peptide-capped Pd nanoparticle catalyst.

To further understand the dynamics of the system, time-based analysis for the reaction was employed to monitor product formation (Figure 4.4). Over the first 5.00 h of the reaction at room temperature, formation of mono-substituted product **6** (blue circles) is observed from coupling at the iodo-group of **5** (green squares). Minor formation of the di-substituted product, **7** (red triangles) is observed 1.50 h after reaction initiation. Note

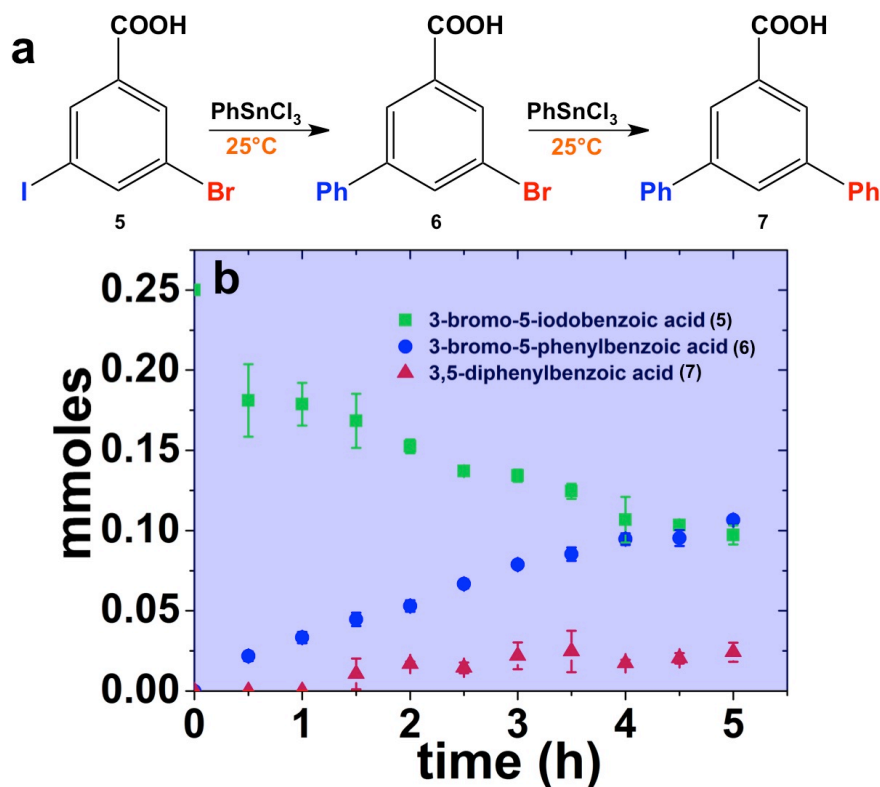


Figure 4.4 Part a) presents the likely reaction scheme for the Stille coupling process using the peptide-capped Pd nanoparticles employing **5** as the aryl dihalide reagent, while part b) displays the time-based results for the reaction at room temperature.

that the formation of the mono-substituted product is noted first, followed by production of the di-substituted species. Furthermore, the rates of C-C coupling are also quite slower as compared to **1** and **2** above. As such, these results suggest that coupling at aryl dihalides provides changes to the electronics of the system that impact the coupling reactions; however, the general selectivity of the catalyst remains. This results in slower coupling reactions, as well as activation of the second halogen group within the ring system. To that end, the electron-donating phenyl ring in **6** possibly activates the bromo-component at room temperature. As a result, a weakening of the C-Br bond could occur, thus making it more susceptible to oxidative addition. The C-Br species from **6** could then participate in the atom abstraction process or react with the free Pd⁰ atoms available

in solution after the initial catalytic cycle of reaction at the iodo-component; however, only minimal di-substituted product yields are observed.

When the same reaction was performed at a higher catalyst loading of 0.10 mol% Pd, the amount of di-substituted product **7** generated increased to $60.9 \pm 1.3\%$, while that of mono-substituted product **6** decreased to $33.6 \pm 1.9\%$ (Table 3, entry 1). Such changes are likely due to more rapid product formation rates based upon the higher catalyst loading. Further shifting of the reaction towards the di-substituted product (**7**) was observed by heating the reaction system. When studying the process at $40.0\text{ }^{\circ}\text{C}$ using 0.10 mol% Pd, the yields of **7** reached $80.6 \pm 6.4\%$, while the yields for **6** were $19.3 \pm 6.0\%$. When the reaction was heated to $60.0\text{ }^{\circ}\text{C}$, the yields of the two products were statistically similar to the results at $40.0\text{ }^{\circ}\text{C}$, indicating a potential saturation point for product formation at higher temperatures. These results suggest that at elevated temperatures, the formation of di-substituted product **7** increases due to the additional thermal energy where both the C-I and C-Br bonds can now undergo oxidative addition with both the particle surface and leached Pd⁰ atoms. This process, however, could still occur in a step-wise fashion due to the more rapid reaction event at iodo group over the bromo group, giving rise to the formation of intermediate **6**. Furthermore, no evidence of the 3-iodo-5-phenylbenzoic acid intermediate was ever observed. These results demonstrate that *intramolecular* selectivity is possible for the peptide-capped Pd nanocatalyst at ambient/low temperature conditions using low catalyst concentrations based upon the reaction mechanism and system thermodynamics.

Expanding the scope of the *intramolecular* selectivity of the nanocatalyst was explored using different derivatives of benzoic acid dihalides (Table 3). For the reaction using **8**,

only the mono-substituted product, 3-chloro-5-phenylbenzoic acid (**9**) was generated at an $88.2 \pm 4.6\%$ yield after 24.0 h at room temperature using 0.05 mol% Pd (Table 3, entry 2). Increasing the catalyst loading and/or raising the reaction temperature generated increasing amounts of mono-substituted product **9** to nearly quantitative yields. As expected, the chloro-component of the reagent was not reactive, thereby the formation of di-substituted product **7** was not observed; the formation of intermediate **9** did not significantly activate the C-Cl bond to facilitate coupling. Interestingly, when employing **10** as the substrate, no coupling was observed for either the bromo or chloro groups under any reaction conditions (Table 3, entry 3). Such results may arise from inductive effects of the electronegative chloro-component, which could cause deactivation of the bromo-component, even at higher temperatures. In general, the different halide groups of the aryl dihalide systems follow a similar trend observed above with the mono-substituted reagents. In this regard, the Pd nanoparticles generally react at the iodo-component first, followed by the bromo-component, with no reactivity for the chloro-component under the selected conditions. Activation of the second functional group is also possible, but the low coupling rates at these positions still allow for selective coupling at the initial reactive site (*i.e.* iodo over bromo).

Reactions of aryl dihalide substrates with the same halogen group at the 3 and 5 positions were also studied. Initially, **11** was employed for Stille coupling using 0.05 mol% Pd at room temperature (Table 3, entry 4). The two highly reactive iodo-components generated di-substituted product **7** at $88.6 \pm 9.0\%$ yield, after 24.0 h. A general increase in the formation for the di-phenyl product was observed proportional to the catalyst loading and

reaction temperature, as anticipated. Interestingly, the mono-substituted intermediate, 3-iodo-5-phenylbenzoic acid (**12**), was never observed under any conditions.

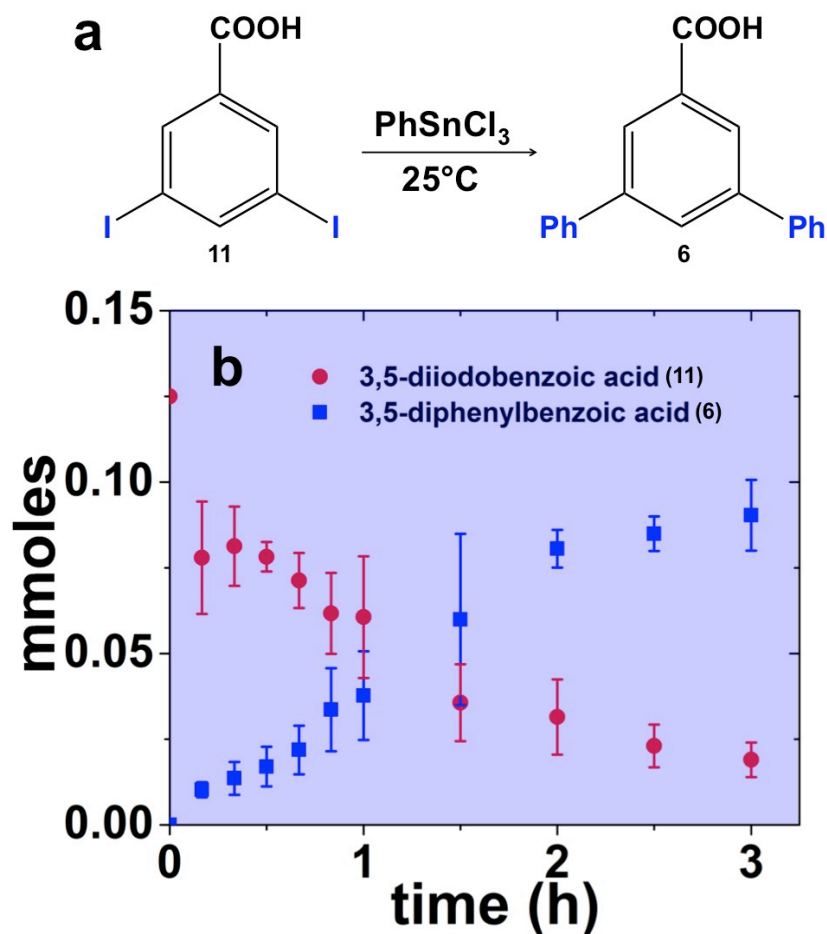


Figure 4.5 Part a) presents the likely reaction scheme for the Stille coupling reaction using the peptide-capped Pd nanoparticles employing **11** as the aryl dihalide reagent, while part b) displays the time-based results for the reaction at room temperature.

To probe the reaction mechanism for **11**, a time-based analysis of the reaction at room temperature with a catalyst loading of 0.05 mol% Pd was studied, as shown in Figure 4.5a. The results (Figure 4.5b) indicate that after 10.0 min, the di-substituted product, **7** (blue squares), was the only isolated product of the coupling reaction; an increase in formation of **7** over the time frame of the study was observed with a complementary

consumption of the starting material (**11**, red circles). Throughout the study, mono-substituted intermediate **12** from coupling at a single iodo group was never observed. To produce such results two likely reaction mechanisms are possible: 1. simultaneous coupling at both iodo- groups using separate catalytic Pd materials or 2. coupling at a single group to produce intermediate **12** that activates the second iodo-group to substantially increase the second-step reaction rate. Based upon the results of the coupling reaction for **5**, the latter mechanism for the di-iodo reagent is more likely. In this regard, the initial attachment of the phenyl group from the coupling reaction of one of the iodo-species produces the bi-aryl ring system that activates the second C-I bond. This then results in exceedingly rapid coupling, generating the di-substituted product (**7**). In this regard, the coupling at the first iodo-group is likely to be the rate-limiting step, otherwise mono-substituted product **12** should have been observed. This step-wise reactivity is more probable due to the kinetic consideration of the atom-leaching mechanism wherein there is a higher probability of a single halogen site reacting with a Pd atom, rather than the two halogens simultaneously coupling with separate catalysts.

Changing the halogen groups to bromides such as in **13** demonstrated an additional change in reactivity. For this system, the two possible products, **6** and **7** from coupling at either one or both of the halogens, respectively, were not obtained at room temperature using either 0.05 or 0.10 mol% Pd (Table 3, entry 5). Such results were expected based upon the energy required for oxidative addition using bromo-based reagents. When the reaction was heated to 40.0 °C with 0.10 mol% Pd, however, the reactivity of the di-bromo substrate was increased, generating both the mono-substituted intermediate **6** and the di-substituted final product **7** with yields of $32.5 \pm 3.0\%$ and $24.6 \pm 3.7\%$,

respectively, after 24.0 h. When the reaction was performed at 60.0 °C with 0.05 mol% Pd, the yield of the di-substituted product increased to $39.5 \pm 1.4\%$, with a mono-substituted product yield of $30.9 \pm 3.2\%$. The increase in the amount of **7** at 60.0 °C was attributed to the activating effect of the biphenyl moiety in the mono-substituted intermediate to the C-Br bond and the increased thermal energy, driving the catalytic reaction to produce more of the di-substituted product.

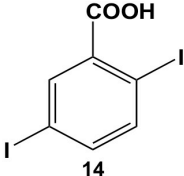
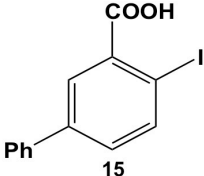
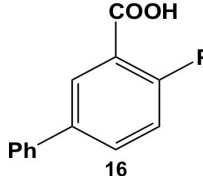
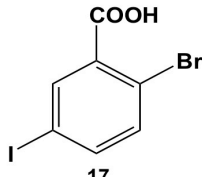
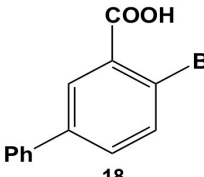
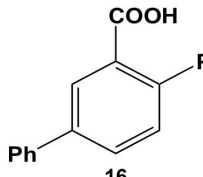
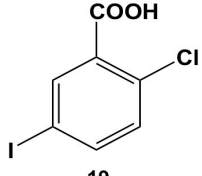
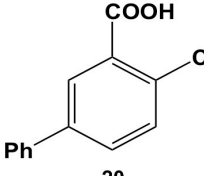
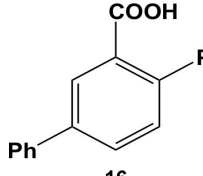
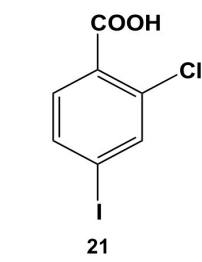
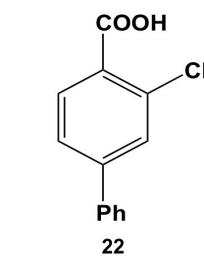
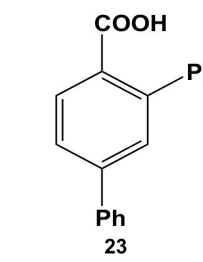
Entry	Aryl Dihalides	Possible Products			
		Mono-substituted	Percent Yield	Di-substituted	Percent Yield
1	 14	 15	0.0 0.0 0.0 0.0	 16	0.0 0.0 0.0 0.0
2	 17	 18	0.0 6.8 ± 0.9 23.3 ± 1.6 41.3 ± 1.4	 16	0.0 0.0 0.0 0.0
3	 19	 20	0.0 70.1 ± 15.8 83.1 ± 6.0 88.0 ± 8.3	 16	0.0 0.0 0.0 0.0
4	 21	 22	73.9 ± 4.0 92.8 ± 4.3 97.9 ± 2.4 95.5 ± 5.5	 23	0.0 0.0 0.0 0.0
Reaction conditions: 0.05 mol% Pd, 25°C, 24 h; 0.10 mol% Pd, 25°C, 24 h; 0.10 mol% Pd, 40°C, 24 h; 0.05 mol% Pd, 60°C, 24 h					

Table 4 Effects of the halogen group position in the aryl ring for the Stille coupling reaction employing peptide-capped Pd nanoparticles.

The reactivity of the Pd nanoparticles towards aryl dihalides was further explored using substrates containing halogen groups at different positions in the benzoic acid ring. Initially, the 2,5-orientation of halide groups was studied using the Stille coupling reaction of **14** with PhSnCl₃; however, no reactivity was observed at either iodo group (Table 4, entry 1). This is likely due to irreversible binding of the carboxylic acid moiety to the nanoparticle surface during the oxidative addition of the iodo group in the 2-position. This binding event allows for the additional interaction of the acid group with the Pd surface leading to catalyst deactivation. When the halide at the 2-position was changed to bromide in **17**, no reactivity was observed for coupling at either position after 24.0 h at room temperature using 0.05 mol% Pd (Table 4, entry 2). Interestingly, when the catalyst loading was increased to 0.10 mol% Pd, a $6.8 \pm 0.9\%$ yield of the mono-substituted product, 2-bromo-5-phenylbenzoic acid (**18**) was obtained. Increasing the temperature of the reaction to 40.0 °C with a Pd loading of 0.10 mol% resulted in a substantial increase in the formation of **18**, generating a $23.3 \pm 1.6\%$ yield after 24.0 h. When the reaction was performed at 60.0 °C with a catalyst loading of 0.05 mol% Pd, a further increase in the yield of **18** ($41.3 \pm 1.4\%$) was obtained after 24.0 h. No indication of reactivity towards the bromo-substituent was noted under any of the reaction conditions. Catalytic poisoning of the nanoparticle surface was not observed due to the required thermal activation of the C-Br bond for reactivity and due to the more reactive C-I bond driving oxidative addition. As a result, the interaction between the carboxylic acid functional group and the Pd surface was minimized. When **19** was used in the reaction (Table 4, entry 3), no detectable product was generated at room temperature with 0.05 mol% Pd; however, when the catalyst loading was increased to 0.10 mol% Pd, the

mono-substituted product, 2-chloro-5-phenylbenzoic acid (**20**) was generated with a yield of $70.1 \pm 15.8\%$ over 24.0 h. Increasing the temperature of the reaction generated an increasing amount of **20** with $83.1 \pm 6.0\%$ (0.10 mol% Pd) and $88.0 \pm 8.3\%$ (0.05 mol% Pd) yields at 40.0 °C and 60.0 °C, respectively. Since the chloro-component was not reactive under the given conditions, catalyst surface poisoning was not observed. The reactivity differences between the iodo-component in these two compounds likely arise from changes in the electronics of the rings structure.

The 2,4-position of the halide groups in benzoic acid was also examined using **21** (Table 4, entry 4). The initial reaction was performed at room temperature using 0.05 mol% Pd, generating 2-chloro-4-phenylbenzoic acid (**22**) with $73.9 \pm 4.0\%$ yield after 24.0 h. When the catalyst load was increased to 0.10 mol% Pd, the yield increased to $92.8 \pm 4.3\%$ after 24.0 h, while at elevated temperatures, almost quantitative yields were obtained for mono-substituted product **22** at the selected catalyst loadings. The increase in the product yield for the reaction of iodo-component **21** compared with **19** suggests that the coupling reaction was accelerated by the combined effect of the chloro-component in the 2-position and electron-withdrawing carboxylic acid moiety, which is *para* to the iodo group.

The results of the aryl dihalide reactions demonstrate the degree of *intramolecular* selectivity of the peptide-capped Pd nanocatalysts given two different halide groups in the same substrate. Similar to the results of the *intermolecular* reactivity, the observed trend for the catalyst selectivity towards aryl dihalides directly relates to the increasing bond strength of the C-X species; however, the orientation of the two halogens within the ring structure can lead to activating and/or deactivating effects. The reactivity of the aryl

dihalide substrates likely follows a step-wise process wherein the mono-substituted intermediate was generated first by the reaction of the more active C-I component. To this end, the orientation of the halide groups in the aryl dihalide substrate affects the reactivity of the halide components, but not the selectivity of the nanocatalyst. The 1,4-position of the halogens tends to deactivate the carbon-halogen bond such that higher Pd loadings are required to drive the reaction at room temperature; however, the 1,3-orientation likely activates the bond for the coupling reaction using less Pd. The presence of activating or deactivating groups in the aryl ring did not alter the selectivity of the Pd nanocatalyst with respect to halide identity.

4.5 Summary and Conclusions

We have studied the reactivity of different aryl halide substrates in a single reaction system to probe the reactivity, catalytic mechanism, and selectivity of peptide-capped Pd nanoparticles. While a variety of catalytic nanoparticles have been studied for C-C coupling reactions,^{86, 95, 134, 239} the peptide-based materials are interesting as they react in an aqueous-based solvent, with very low Pd concentrations and reaction temperatures. To further such materials for enhanced reactivity, a fundamental understanding of the reaction mechanism is required. In this sense, the release of free Pd⁰ atoms to the solution after the initial catalytic cycle of highly active iodo-components does not allow for coupling at less active bromo-groups. The results indicate that the oxidative addition of the C-Br bond requires thermal activation at 40.0 °C, suggesting that an energy barrier must be overcome to enable coupling, thereby allowing for a degree of thermal-control

for reaction selectivity at low temperatures. In both *intermolecular* and *intramolecular* systems, the selectivity trend for the Pd nanoparticles directly correlates to the strength of the C-halide bond dissociation energy wherein the weakest C-I bond readily reacts at room temperature, while the C-Br bond requires mild heating and the C-Cl bond does not readily react. Consequently, in aryl dihalide systems, the presence of activating/deactivating groups in the ring alters the electronics and reactivity of the halide components, but the selectivity of the catalyst is generally retained with regards to the halide identity. These results present a deeper understanding of the catalytic mechanism for nanoparticle-driven C-C coupling reactions, which could be useful for the design of optimized systems.

“Pacardo, D. B.; Knecht, M. R. *Catal. Sci. Technol.* **2013**, *3*, 745 – 753. – Reproduced by permission of The Royal Society of Chemistry.”

Chapter 5. Probing the Reactivity of Peptide-templated Pd Nanoparticles as Catalyst for Hydrogenation Reaction of Olefinic Alcohols

5.1 Overview of the Study

In this chapter, we present the results of the studies on the catalytic applications of the R5-templated Pd nanomaterials with different morphologies towards hydrogenation of olefinic alcohols employing mild reaction conditions of aqueous solvent, room temperature and low catalyst loading. Different primary, secondary and tertiary alcohols were employed for hydrogenation reactions using biotemplated Pd nanomaterials wherein TOF analysis showed similar values for each substrate regardless of catalyst morphology. However, low TOF values were obtained for the primary alcohols with increasing TOFs for secondary and tertiary alcohols. These results were attributed to the degree of isomer formation, the highest of which was observed in primary alcohols, that hindered the formation of hydrogenated products. For the competition reaction between allyl alcohol and a secondary olefinic substrate, the biotemplated Pd nanomaterials exhibit non-specific catalytic activity, wherein simultaneous product formation from the two substrates occur on the surface of the nanostructures. Furthermore, the reactivities of substrates with two reactive centers were explored using 1,4-pentadien-3-ol and 3-methyl-1-pentyn-3-ol resulting in step-by-step hydrogenation for the biotemplated nanomaterials.

5.2 Motivation

The catalytic application of transition metal organometallic small molecules has been greatly studied due to their unique ability to enable industrially significant chemical transformations such as C-C couplings,^{58, 86-88, 94} hydrogenations,^{13, 31, 120, 159, 240, 256, 257} hydrodesulfurization,²⁵⁸⁻²⁶¹ and oxidations.^{262, 263} These processes are employed in applications such as materials synthesis,²⁶⁴ petrochemical refinement,²⁶⁵ pharmaceutical production,^{53, 54} natural products synthesis,²⁶⁶ and bioremediation;²⁶⁷ however, harsh reaction conditions that employ organic solvents, high temperatures, and significant catalyst loadings are typically required. As a result of the high production costs and environmental impacts, these reactions have become unsustainable over the long term.^{50, 51} Given their necessity, however, studies have been conducted to diminish the ecological effects and energy consumption of these reaction systems to conserve limited resources.⁵² For this, new catalytic materials that are reactive under milder conditions without sacrificing efficiency are required. Furthermore, significantly increased catalytic functionality is desirable to employ lower catalysts loadings, especially for limited precious metal systems.

A unique avenue to realize these sustainable systems is through the use of nanoscale materials that maximize the surface-to-volume ratio. By manipulating the particle structure, incorporation of highly reactive surface defect atoms may be possible, which could prove to be critically important for catalysis. Both size- and shape-controls for the synthesis of nanomaterials are dictated by using different surface passivating ligands.²⁶⁸⁻

²⁷⁰ These functional molecules, typically composed of thiols, amines, and carboxylic

acids, interact with the metal surface, thus inhibiting particle growth to generate the final stable materials. In a separate area, the use of molecular templates has become increasingly important for nanocatalysis, where semi-hollow dendrimer represent a model template.²⁷¹ To this end, the nanoparticle guests are encapsulated within the void interior space of the dendrimer host, thus sterically stabilizing the materials to more efficiently expose the catalytic structures to the reagents. In recent years, the use of biological templates has been explored for the production of nanocatalytic materials.^{31, 222, 238, 272, 273} One such species is the naturally occurring and self assembling R5 peptide (SSKKSYSYSGSKGSKRRIL), responsible for silica precipitation in diatoms.^{177, 178} The peptide was isolated via HF-extraction from the cell walls of *Cylindrotheca fusiformis*,^{177, 178} where previous studies have shown that the –RRIL motif at the C-terminus of the sequence enhances peptide self assembly in water, resulting in the formation of a biotemplate for nanostructure encapsulation.^{87, 179} A particularly interesting catalytic system templated by the R5 scaffold is that of Pd, which can control the morphology of the metallic materials via the reaction conditions.⁸⁷ In this process, the biomolecule is dissolved in water, resulting in peptide assembly and template formation.⁸⁷ To this, Pd²⁺ ions are added, which can complex to the functional groups of the template that are presented at the interior of the structure. Upon the incorporation of a strong reducing agent, NaBH₄, formation of the zerovalent materials occurs.⁸⁷ Interestingly, the morphology of the inorganic structures is directly dependent upon the Pd:R5 ratio employed during the synthesis.^{87, 274} For instance, at a Pd:R5 ratio of 60 (termed Pd60), spherical nanoparticles are formed, while when the ratio was increased to 90 (Pd90), linear Pd nanoribbons can be obtained.^{87, 274} Conversely, at the highest stable ratio of 120

(Pd120), branched nanoparticle networks (NPNs) are generated within the bioscaffold.^{87, 274} These different metallic morphologies are observed due to the template-based synthesis. In this regard, immediately after Pd²⁺ reduction, zerovalent Pd nanoparticles are formed within the bioframework. At low Pd:R5 ratios, the particle density is low, thus the interparticle distance is high.^{87, 274} As this ratio increases, the number of particles deposited within the scaffold increase, thus decreasing the interparticle distance.^{87, 274} When this distance is sufficiently small, the particles can aggregate, likely in a linear pattern due to the template structure.^{87, 274} As the Pd:R5 ratio is further increased, more particle aggregation is anticipated, leading to NPN formation at the highest ratios.^{87, 274} Initial catalytic applications for the R5-templated Pd nanoparticles involved the Stille coupling reaction between aryl halides and organostannanes.⁸⁷ For this, the reaction efficiency depended upon both the metallic surface area and the penetration depth of the reagents to reach the catalytic structure within the bioscaffold.^{37, 87} As such, the Pd60 nanospheres and Pd120 NPNs displayed similar catalytic activities as determined by the turnover frequency (TOF) analysis due to their enhancement of the metallic surface area (Pd60) or minimization of the penetration depth and reagent diffusion (Pd120).^{37, 87} For the Pd90 nanoribbons, slower reactivity was evident as both of these structural characteristics are not optimized.^{37, 87} Similar reactivity results were observed for a separate reaction, 4-nitrophenol reduction, which displayed an identical trend for catalyst performance.³⁷ Interestingly, the R5-templated Pd materials have also demonstrated reactivity for the hydrogenation of allyl alcohol to 1-propanol; however, no dependence upon the material structure was evident.²⁷⁴ For this reaction, the catalytic surface is saturated with hydrogen before introducing the olefin substrate.^{256, 274} The substrate, such

as an alkene, is then reduced at the metallic surface to produce the hydrogen-saturated product. As noted, the differences in material morphology of the R5-templated Pd structures did not have significant effects on the hydrogenation of allyl alcohol.²⁷⁴ These results were attributed to the small size of the substrate that allowed for it to rapidly diffuse through the bioscaffold, as well as the exceedingly fast rate of the hydrogenation reaction itself.²⁷⁴ Together, these effects are anticipated to mask any structural-based rate limiting factors observed for the different reactions that are significantly slower and more sensitive to the material morphology based upon their bulkier reagents. Unfortunately, the effects of substrate molecular structure remain unclear using the biotemplated materials, which could be important for reactivity control.

Here we explore the reactivity of the biotemplated Pd nanostructures for the hydrogenation reaction based upon the molecular size, composition, and reactive groups of the substrate. Initially, olefinic alcohols were examined due to their broad range of synthetic use. The TOF analysis of each substrate revealed that the different olefinic alcohols reacted across all of the Pd nanostructures; however, an interesting trend was noted based upon the substitution of the molecule. To this end, when primary alcohols were employed as the starting materials, lower TOF values, on average, were observed that increased for secondary and tertiary alcohol substrates. Such effects were attributed to isomerization events that impeded the intended hydrogenation reaction. Furthermore, competition reaction studies were performed using a combination of allyl alcohol with a secondary olefin reagent in a single solution. These results indicated that the interaction between substrate and catalytic surface was important for controlling the overall reactivity, which may serve as a structural source to direct complex functional reactions.

Finally, the hydrogenation reaction was explored using both a diolefin, 1,4-pentadien-3-ol, and an alkyne, 3-methyl-1-pentyn-3-ol, to explore the multistep reactivity of the materials. Both systems demonstrated a stepwise reaction, resulting in the final fully saturated product after short reaction times. Taken together, such results are important for three key factors. First, high degrees of reactivity are demonstrated for a variety of different substrates in aqueous solvents, where minimal material structural effects are apparent. Second, from the competition studies, important nanomaterial structural information is presented, which indicates that the reactivity and interactions with the material surface may be sensitive to the morphology of the materials (spherical versus linear). Third, multistep reactivity is presented from the biotemplated nanomaterials, indicating a high degree of reactivity over short time scales using ambient conditions. Together, such materials may prove to be important as models for sustainable reactivity.

5.3. Methods

5.3.1 Chemicals

K_2PdCl_4 , anti-foam SE-15, allyl alcohol, 3-buten-1-ol, 4-penten-1-ol, 3-buten-2-ol, 1-penten-3-ol, 2-methyl-3-buten-2-ol, 3-methyl-2-penten-3-ol, 1-propanol, 1-butanol, 1-pentanol, 2-butanol, 3-pentanol, 2-methyl-2-butanol, 3-methyl-3-pentanol, propionaldehyde, crotyl alcohol, 2-butanone, and 3-pentanone were purchased from Sigma-Aldrich, while $NaBH_4$ was obtained from Acros Organics. All reagents were used as received. Finally, Milli-Q water ($18m\Omega\cdot cm$) was used throughout.

5.3.2 Synthesis of Peptide-templated Pd Nanoparticles

The fabrication of the peptide-templated Pd nanomaterials was processed using standard methods.^{87, 274} Briefly, 4.93 μL of a 10.0 mg/mL R5 peptide stock solution was diluted in 3.0 mL of water. To this solution, 14.7, 22.0, and 29.4 μL of a freshly prepared 0.10 M K_2PdCl_4 aqueous solution was then added, corresponding to a Pd:peptide ratio of 60, 90, and 120, respectively. After 15 min of stirring at room temperature to allow for complexation of the metal ions to the bioscaffold, 75.0 μL of a freshly prepared 0.10 M NaBH_4 solution was added. The reactions were allowed to reduce 1.0 h, after which the nanostructures were dialyzed overnight using Spectra/Por[®] dialysis tubing with MWCO of 12k – 14k.

5.3.3 Catalytic Hydrogenation Reactions

The olefin hydrogenation reactions were carried out using previously described methods with appropriate modifications.²⁵⁶ Specifically, 1.316 mL of the templated Pd nanostructures was added to 25.0 mL of water in a three-neck round bottom flask, along with 20 μL of anti-foam SE-15, a 10% solution of active silicone polymer and non-ionic emulsifier, with constant stirring at room temperature. This nanostructure solution volume was selected to result in a final catalyst loading of 0.05 mol % Pd in the reaction. Next, 50 kPa of H_2 gas was bubbled through the system for 30 min using a standard gas dispersion tube. After saturation of the solution with H_2 , 25.0 mL of a 50 mM olefinic alcohol solution prepared in water was introduced to the reaction vessel. Immediately after addition, a 1.0 mL aliquot was extracted and transferred to a vial to mark the start of the reaction ($t = 0$ min). Subsequent aliquots were then taken at selected time points,

where they were directly injected into the gas chromatograph (GC) and the products were characterized and quantitated as described below.

The hydrogenation reaction of two different olefinic alcohols was also carried out using the R5-templated materials. For this setup, identical reaction conditions and product characterization methods were employed; however, the 50 mM substrate solution was composed of equimolar amounts (25 mM) of the two selected alcohols.

5.3.4 Characterization and Retention Factor Determination

Characterization of hydrogenation products was accomplished using an Agilent 7820A GC operated with a DB-ALC1 column and a flame ionization detector. Using this system, the reaction solution was directly injected into the GC without further purification. The percent yield of the hydrogenation reaction was calculated using previously described methods by the Bruening group.²⁵⁶ Initially, the GC retention times of the olefinic alcohols and their expected products and isomers (if available) were established using standard solutions of each component. The retention factors (k) were then determined by GC analysis of a standard solution containing equimolar amounts of the starting material, expected product, and main isomer. Once the retention factors were determined, the hydrogenation percent yield during the reaction can be calculated using the peak areas of the starting material, product, and isomer, using established methods.²⁵⁶

5.4 Results and Discussion

R5-templated Pd nanostructures were prepared using established procedures.^{87, 274} For this, three different nanomaterials were synthesized using Pd:R5 ratios of 60, 90 and 120

to span the range of known structural morphologies prepared via this approach: nanoparticles, nanoribbons, and NPNs, respectively.^{87, 274} In this method, the amount of R5 peptide was held constant while varying the amount of Pd²⁺ added, followed by the addition of a strong reducing agent, NaBH₄.^{87, 274} Characterization using TEM, as shown in Figure 5.1, demonstrated the formation of different morphologies as a function of the amount of added metal precursor, consistent with previous results. For instance, the generation of spherical Pd nanoparticles (Figure 5.1a) was achieved for the Pd60 sample due to a high interparticle distance in the biotemplate as a result of low metal concentration. In contrast, at higher Pd:R5 ratios, such as in the Pd90 and Pd120 samples, decreased interparticle separation occurred, resulting in the formation of nanoribbons (Figure 5.1b) and Pd NPNs (Figure 5.1c), respectively. Upon confirmation of their unique morphology, the materials were employed as catalysts for olefin hydrogenation.

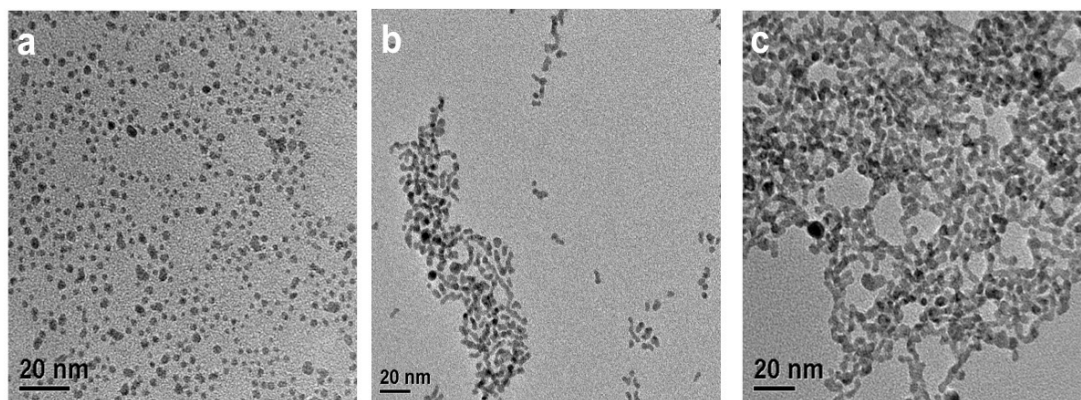


Figure 5.1 TEM images for the R5-templated Pd nanomaterials showing a) Pd60 nanospheres, b) Pd90 nanoribbons, and c) Pd120 NPNs.

The hydrogenation reaction was initially performed using allyl alcohol as the smallest olefinic substrate. In this reaction, a solution containing 0.05 mol% Pd from the different

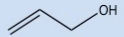
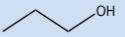


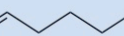
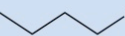
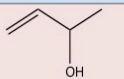
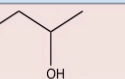
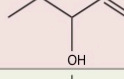
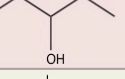
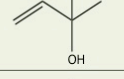
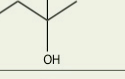
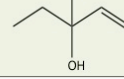
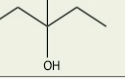
Entry #	Starting Material	Product	TOF mol product (mol Pd·h) ⁻¹			
			Pd/C	Pd60	Pd90	Pd120
1			1232 ± 43	3019 ± 120	3012 ± 76	2961 ± 101
2			1064 ± 405	3099 ± 86	3150 ± 231	2992 ± 80
3			1380 ± 182	2996 ± 292	3311 ± 38	2993 ± 618
4			1681 ± 242	3458 ± 30	3451 ± 148	3456 ± 251
5			1615 ± 50	3292 ± 298	3328 ± 409	2632 ± 283
6			1676 ± 256	4892 ± 433	4418 ± 736	4426 ± 1439
7			1315 ± 272	3748 ± 469	3912 ± 350	3256 ± 474

Table 5. TOF analysis for hydrogenation of olefinic alcohols using biotemplated Pd nanomaterials

Pd nanostructures was saturated with H₂ for 30 min under constant stirring at room temperature.^{256, 274} Once complete, a 50 mM allyl alcohol solution was added and 1.0 mL aliquots were taken at specific time points to be quantitated via GC methods.²⁵⁶ In the case of allyl alcohol, both the expected product, 1-propanol, and the propionaldehyde isomer were observed during the reaction; however, the isomer was eventually fully converted to the final product. Using this method, TOF values for the reaction can be calculated, thus allowing for a direct comparison of the reactivity between the different substrates. The catalytic TOF results for the three different biotemplated Pd nanostructures using allyl alcohol as the substrates are presented in entry 1 of Table 1. For this, the three different systems demonstrated TOFs of 3019 ± 120, 3012 ± 76, and 2961 ± 101 mol product (mol Pd × h)⁻¹ for the Pd60, Pd90, and Pd120 materials, respectively. These TOF values, which showed no differences based upon the structure of

the materials, were equivalent with previously reported results for this reaction.²⁷⁴ This suggests that the small allyl alcohol substrate can readily diffuse through the bioscaffold and react at the hydrogen-saturated metal surface. Comparing these results with a control reaction employing commercially available Pd on C (Pd@C) as the catalyst, a TOF of 1232 ± 43 mol product (mol Pd \times h)⁻¹ was obtained, indicating a much slower hydrogenation process, likely due to the larger size of the metallic materials. Furthermore, in the absence of the Pd, no catalytic turnover was noted, as anticipated.

Interestingly, when the substrate was changed to another primary alcohol in 3-buten-1-ol, the TOF values (Table 1, entry 2) obtained were similar to those of allyl alcohol: 3099 ± 86 , 3150 ± 231 and 2992 ± 80 mol product (mol Pd \times h)⁻¹, for Pd60, Pd90, and Pd120, respectively. The subtle, one carbon chain difference between allyl alcohol and 3-buten-1-ol did not have any effect on the reactivity of this substrate, generating similar TOF values for all three of the templated metallic structures. Again using the Pd@C control materials with 3-buten-1-ol, a TOF of 1064 ± 405 mol product (mol Pd \times h)⁻¹ was observed, which was nearly equivalent to the value calculated for allyl alcohol. To further probe the reactivity of peptide-templated Pd nanoparticles with respect to primary alcohol substrate, 4-penten-1-ol was employed as the hydrogenation substrate. For this substrate, formation of two isomers, 2-penten-1-ol and 3-penten-1-ol, were observed and as such, calculation of TOF values was modified as shown in Supporting Information, S1. Interestingly, the TOF results for this reagent (Table 1 entry 3) showed similar values as those of the other two smaller chained primary alcohols. For instance, a TOF of 2996 ± 292 mol product (mol Pd \times h)⁻¹ was calculated when using Pd60, while the values for the Pd90 nanoribbons and Pd120 NPNs were 3311 ± 38 and 2993 ± 618 mol product (mol Pd

$\times \text{h})^{-1}$, respectively. Again, diminished reactivity was noted from the Pd@C control, consistent with the smaller chained primary alcohol substrates.

Expanding the scope of the catalytic reactivity of the peptide-templated Pd materials towards secondary alcohols was further studied to increase the complexity of the substrate. Initially, 3-buten-2-ol was employed, as shown in Table 1, entry 4. Identification of the retention factors for this reaction was done using standard solutions of the substrate, the expected product, 2-butanol, and the isomer, 2-butanone. Like the other alcohol substrates, TOF analysis generated similar values of 3458 ± 30 mol product $(\text{mol Pd} \times \text{h})^{-1}$ for Pd60, 3451 ± 148 mol product $(\text{mol Pd} \times \text{h})^{-1}$ for Pd90, and 3456 ± 251 mol product $(\text{mol Pd} \times \text{h})^{-1}$ for Pd120. These TOF values were slightly higher than those obtained for the primary alcohols. Similarly, the control reaction using Pd@C showed a slightly higher average TOF value of 1681 ± 242 mol product $(\text{mol Pd} \times \text{h})^{-1}$, as compared to the control reactions using the primary alcohol substrates. Further studies of the catalytic activity of peptide-templated nanomaterials employed another secondary alcohol substrate, 1-penten-3-ol. To determine the TOF values using the GC method, retention factors for the reagent, the 3-pentanol anticipated product, and the 3-pentanone isomer were determined and subsequently used. From this study, TOF values (Table 1 entry 5) of 3292 ± 298 , 3328 ± 409 , and 2632 ± 283 mol product $(\text{mol Pd} \times \text{h})^{-1}$ were determined for the Pd60, Pd90, and Pd120 materials, respectively. Interestingly, the TOF results for the Pd60 and Pd90 materials were similar; however, the Pd120 structures demonstrated a diminished TOF, which was still higher than the Pd@C control that demonstrated a TOF value of 1615 ± 50 mol product $(\text{mol Pd} \times \text{h})^{-1}$.

To further broaden the extent of the catalytic activity for R5-templated Pd nanoparticles, tertiary alcohols were employed in the hydrogenation reaction. Initially, 2-methyl-3-buten-2-ol was used as the substrate, where 2-methyl-2-butanol was anticipated as the product, and no isomer was produced. Interestingly, this reaction generated even higher TOF values (Table 1, entry 6) of 4892 ± 433 mol product $(\text{mol Pd} \times \text{h})^{-1}$ for Pd60, 4418 ± 763 mol product $(\text{mol Pd} \times \text{h})^{-1}$ for Pd90, and 4426 ± 1439 mol product $(\text{mol Pd} \times \text{h})^{-1}$ for Pd120. In contrast, the control reaction using Pd@C produced a much lower TOF value of 1676 ± 256 mol product $(\text{mol Pd} \times \text{h})^{-1}$, similar to the range of values obtained for the control reactions using the secondary alcohols. Finally, a second tertiary alcohol substrate was studied, 3-methyl-1-penten-3-ol, which was converted to 3-methyl-3-pentanol during the reaction with no isomer formation. Note that this substrate is nearly identical to that of entry 5 of Table 1; however, one additional methyl group is present in the structure. Results of the TOF analysis (Table 1 entry 7) generated TOF values for the Pd60, Pd90, and Pd120 materials of 3748 ± 469 , 3912 ± 350 , and 3256 ± 474 mol product $(\text{mol Pd} \times \text{h})^{-1}$, respectively.

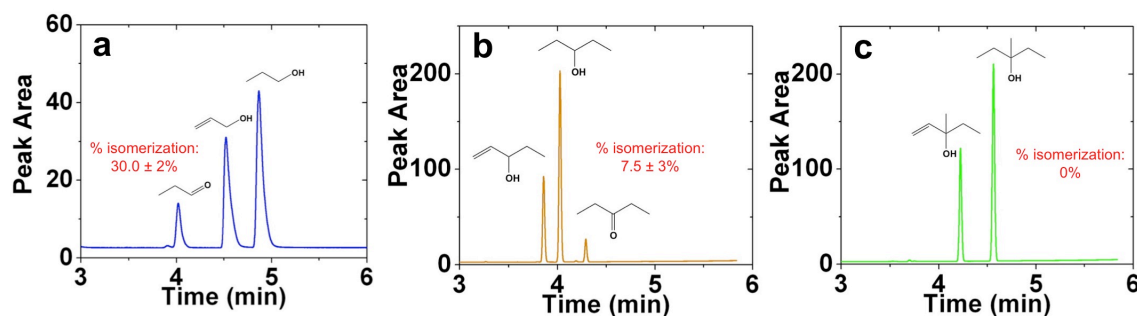


Figure 5.2 GC chromatograms illustrating isomer formation during hydrogenation reaction using Pd60 at 20.0 min for a) allyl alcohol, b) 1-penten-3-ol, and c) 3-methyl-1-penten-3-ol.

Taken together, these results provide important information concerning the catalytic reactivity of the biotemplated materials. In general, when considering a single substrate, similar degree of catalytic reactivity were observed for the Pd60, Pd90, and Pd120 materials, regardless of the nanomorphology; however, a general trend of increasing TOF with increasing the alcohol order (primary, secondary, and tertiary) was noted. These surprising results are likely due to the degree of isomerization observed in each alcohol system. To this end, the primary alcohols form the greatest amount of isomers among the three groups, followed by the secondary alcohols that produce more modest amounts of isomers. Finally, the tertiary alcohols do not isomerize in the reaction at all. Figure 5.2 specifically presents the GC chromatograms of the reactions using the indicated olefinic alcohols illustrating the degree of isomerization at 20.0 min of reaction employing the Pd60 sample as the nanocatalyst. For allyl alcohol (Figure 5.2a), $30.0 \pm 2\%$ of the isomer was formed midway through the reaction while for the secondary alcohol, 1-penten-3-ol, only $7.5 \pm 3\%$ (Figure 5.2b) of the substrate was converted to the isomer. On the other hand, the tertiary alcohol, 3-methyl-1-penten-3-ol, did not form any isomers throughout the reactions. As such, those reactions in which isomers were formed resulted in lower TOF values. Furthermore, the degree of isomerization had an effect on the overall TOF such that those systems that generated greater isomer amounts generally yielded lower reaction TOFs. Note that regardless of the amount of isomerization, each system studied resulted in 100% product yields of the anticipated saturated product in ~ 1.0 h. This isomerization process requires interactions with the catalytic surface to drive the process, thus occupying the site to prevent the hydrogenation reaction from occurring. Those systems with increased amounts of isomerization occurring thus more substantially

compete for the catalytic surface with the intended reaction, thus lowering the TOF values, which is observed in Table 5 and Figure 5.2 for the peptide-templated materials.

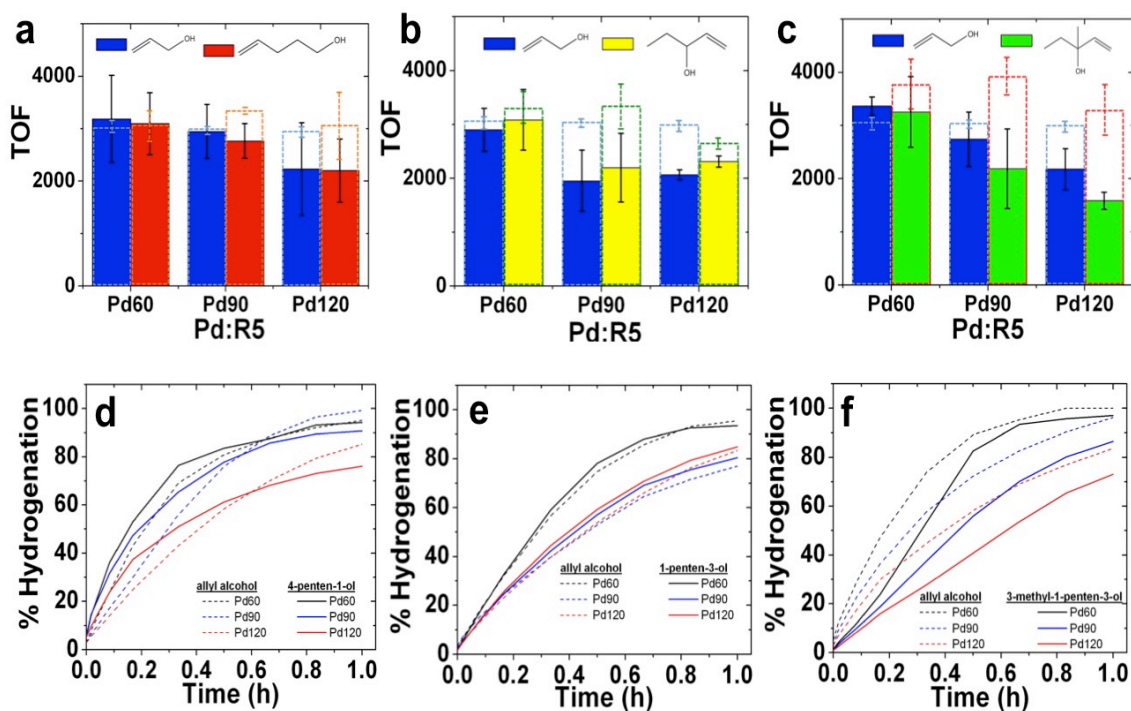


Figure 5.3 Parts a – c show the TOF analysis for hydrogenation competition reactions while parts d – e show the reaction profiles for allyl alcohol and 4-penten-1-ol (a and d), allyl alcohol and 1-penten-3-ol (b and e), and allyl alcohol and 3-methyl-1-penten-3-ol (c and f).

Once the TOF analysis of individual olefinic alcohols was better understood, competition experiments were performed between multiple substrates in the same reaction system. In this method, allyl alcohol was combined with equimolar amounts of each of the following substrates: 4-penten-1-ol (primary alcohol), 1-penten-3-ol (secondary alcohol), and 3-methyl-1-penten-3-ol (tertiary alcohol). With this mixture, hydrogenation reactions were performed using the peptide-templated Pd materials under the standard conditions, from which TOF values for the two different substrates were quantitated. The resulting TOF

values from the competition reactions could then be compared with the values for the individual hydrogenation reactions to determine the catalytic effects of the mixtures. Initially, the competition between two primary alcohols, allyl alcohol and 4-penten-1-ol, was employed. Figure 5.3a presents a bar chart of the analysis where the calculated TOF values of each substrate in the competition experiment are represented by a solid bar, which is superimposed with the TOF values from the individual hydrogenation reactions, presented as an empty bar. For the allyl alcohol substrate (blue plot) using the Pd60 nanospheres, a similar TOF value was obtained from the competition experiment (3187 ± 833 mol product (mol Pd \times h)⁻¹) as compared to the value obtained when the substrate was hydrogenated separately (3019 ± 120 mol product (mol Pd \times h)⁻¹). Similarly, the 4-penten-1-ol substrate (red plot) generated a comparable TOF value of 3098 ± 593 mol product (mol Pd \times h)⁻¹ in the competition reaction as to the TOF calculated in the individual reaction (2996 ± 292 mol product (mol Pd \times h)⁻¹). When the Pd90 nanoribbons were employed, however, a more substantial difference in the TOFs was noted for the larger substrate. To this end, only a minor change in values for allyl alcohol were observed (3012 ± 76 mol product (mol Pd \times h)⁻¹ versus 2949 ± 516 mol product (mol Pd \times h)⁻¹); however, the TOF for 4-penten-1-ol decreased from 3311 ± 38 mol product (mol Pd \times h)⁻¹ to 2766 ± 330 mol product (mol Pd \times h)⁻¹ in the competition experiment. Finally, for the Pd120 NPNs, both substrates demonstrated roughly equally diminished TOFs in the competition experiment as compared with the values obtained in individual reactions.

The second competition reaction experiment was performed using a mixture of allyl alcohol and the secondary alcohol 1-penten-3-ol, as presented in Figure 5.3b. For this

combination of alcohols, negligible changes in the TOF values for the Pd60 nanospheres was again observed. To this end, TOF values in the competition experiment for the allyl alcohol and 1-penten-3-ol substrates were 2904 ± 399 mol product $(\text{mol Pd} \times \text{h})^{-1}$ and 3086 ± 564 mol product $(\text{mol Pd} \times \text{h})^{-1}$, respectively, which are quite similar to the values of Table 1. When the competition studies were carried out using the linear Pd90 and Pd120 materials, however, a marked decrease in reactivity was observed for both alcohols. For instance, for the Pd90 nanoribbons, the allyl alcohol substrate displayed a TOF value of 1951 ± 570 mol product $(\text{mol Pd} \times \text{h})^{-1}$, while the 1-penten-3-ol demonstrated a value of 2199 ± 637 mol product $(\text{mol Pd} \times \text{h})^{-1}$. This continued for the larger Pd120 NPNs, where the co-hydrogenation of the two substrates resulted in TOFs of 2066 ± 94 mol product $(\text{mol Pd} \times \text{h})^{-1}$ for allyl alcohol and 2312 ± 105 mol product $(\text{mol Pd} \times \text{h})^{-1}$ for 1-penten-3-ol.

For the final competition experiment, allyl alcohol was co-reacted with 3-methyl-1-penten-3-ol, a tertiary alcohol starting material. Similar to the results of other competition reactions for Pd60, retention of reactivity was observed, as shown in Figure 5.3c. To this end, the allyl alcohol reagent demonstrated a TOF value of 3364 ± 169 mol product $(\text{mol Pd} \times \text{h})^{-1}$, while the 3-methyl-1-penten-3-ol substrate resulted in a value of 3254 ± 667 mol product $(\text{mol Pd} \times \text{h})^{-1}$. Meanwhile, using the Pd90 structures, a significant decrease in reactivity was noted for the tertiary alcohol, but only a minor change in the reactivity for the allyl alcohol substrate was noted. For instance, when hydrogenating allyl alcohol in the competition experiment, a TOF of 2742 ± 511 mol product $(\text{mol Pd} \times \text{h})^{-1}$ was determined, which is similar to the value presented in Table 1. When using 3-methyl-1-penten-3-ol in the presence of allyl alcohol, however, the reactivity decreased to $2189 \pm$

748 mol product (mol Pd × h)⁻¹, as compared to 3912 ± 350 mol product (mol Pd × h)⁻¹ achieved for this substrate when reacted in isolation. Similar results were observed for the Pd120 materials, but with more reactivity decreases for allyl alcohol. To this end, TOF values of 2180 ± 387 mol product (mol Pd × h)⁻¹ and 1583 ± 161 mol product (mol Pd × h)⁻¹ were noted for allyl alcohol and 3-methyl-1-penten-3-ol in the competition experiment, where a significant reactivity decrease for both substrates was noted.

In general, the changes in the reactivity observed in the competition experiments as compared to the single substrate studies is likely due to a combination of two factors: substrate isomerization and molecular size. When considering the competition reaction of allyl alcohol, a primary alcohol, and 3-methyl-1-penten-3-ol, the effects of isomerization and substrate size are most apparent. To this end, both substrates coreact on the particle surface, which is displayed in Figure 5.3f. As such, no selectivity between the two substrates was observed; however, based upon the data of Figure 5.2, no isomerization is noted for the tertiary alcohol, while the most significant isomerization of the present study was indicated from allyl alcohol. In this regard, the allyl alcohol substrate spends a greater amount of time reacting at the surface, either through the hydrogenation reaction itself, or through the isomerization reaction. Furthermore, the propionaldehyde isomer itself must then compete for the surface, either to reisomerize back to allyl alcohol or to hydrogenate the aldehyde to an alcohol; at present, it is unclear which stepwise reaction is required to reach the final saturated 1-propanol product. From this, TOF decreases would be anticipated for the 3-methyl-1-penten-3-ol substrate, which does not isomerize, requiring less time at the particle surface for the hydrogenation process. That said, the tertiary alcohol substrate is larger in size, thus while it is reacting at the Pd surface, it is

anticipated to cover a more substantial surface area per molecule as compared to the significantly smaller allyl alcohol. From this, less availability of reactive Pd metal would be present for the primary alcohol, resulting in the observed diminishment of its TOF value. As such, similar effects are anticipated for the competition reactions employing allyl alcohol and the other primary and secondary reagents (Figures 5.3 a and b); however, these reaction effects are somewhat more complicated as both reagents can now isomerize, which works in combination with molecular size effects to explain the observed TOF differences for the selected substrates. Note that for all of these experiments, both substrates coreact at the particle surface simultaneously (Figures 5.3d-f), supporting the effects of isomerization and molecular size. While general trends for the competition reaction studies are prevalent, it is interesting to point out that these two effects of the substrates are somewhat diminished for the spherical Pd60 materials, as compared to the linear Pd90 nanowires and Pd120 NPNs. This is indicated by the very minimal differences in the TOF values for the competition experiments as compared to the reactions done with a single substrate. Such results may be due to particle curvature effects altering the interactions between the substrate and the metallic surface; however, further studies are required to confirm this hypothesis.

Once single step reactions were analyzed, multistep reactive substrates were studied, first employing the di-ene alcohol 1,4-pentadien-3-ol. In this experiment, the formation of two products is possible: an intermediate 1-penten-3-ol and the final 3-pentanol species (Figure 5.4a). Initially, the retention factors were determined such that the equation for

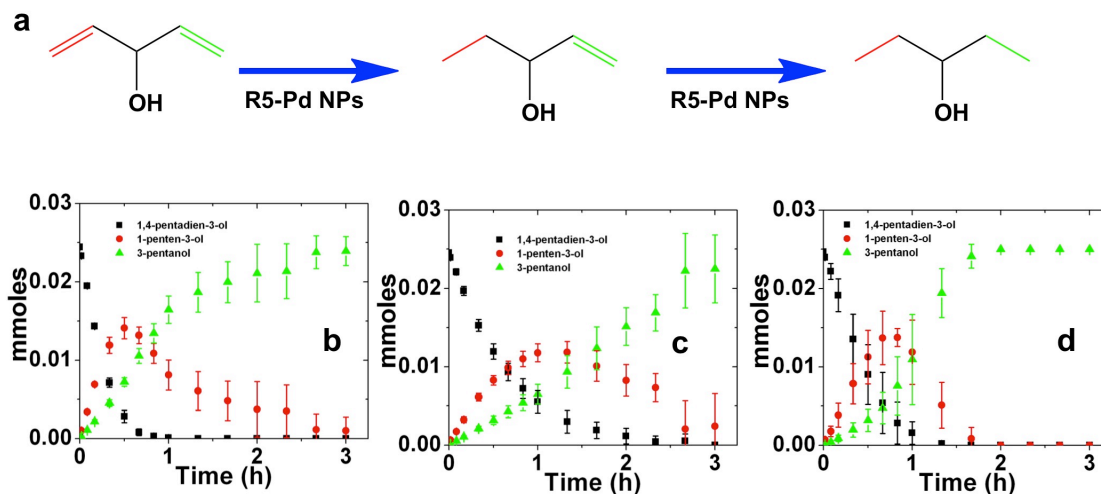


Figure 5.4 a) Reaction scheme for the hydrogenation of 1,4-pentadien-3-ol. Plots of the results of hydrogenation reaction of 1,4-pentadien-3-ol using biotemplated Pd nanomaterials b) Pd60, c) Pd90, and d) Pd120.

percent hydrogenation could be used to determine the moles of the starting material, intermediate, and final product (Supporting Information, S2). The hydrogenation reaction was then performed similar to the method used for other systems; however, the reaction time was probed for up to 3.0 h due to the multistep nature of the system. The results of the study for the diene are presented in Figure 5.4. Analysis of the reaction using the spherical Pd60 materials is specifically presented in Figure 5.4b. For this, a rapid decrease in the amount of the starting material was noted, such that the initial substrate was fully consumed in 1.0 h. From this consumption, the formation of the mono-hydrogenated intermediate, 1-penten-3-ol, was noted at the onset of the reaction. Rapid formation of 1-penten-3-ol was observed, reaching a maximum at 30 min, at a value of 0.014 mmoles (~60% yield). After this time point, the intermediate is fully consumed, resulting in production of the final, saturated 3-pentanol product. Full consumption of the intermediate was not noted until the 3.0 h time point. Interestingly, the formation of 3-pentanol was noted 5.0 min after reaction initiation, indicating that the hydrogenation of

both the initial substrate and the intermediate are occurring simultaneously at the Pd surface. After this time, the amount of the final product continually increased until reaching quantitative yields at 3.0 h.

When the linear Pd90 nanoribbons were used as the catalyst, similar stepwise reactivity was observed; however, changes in the reaction profile were noted. To this end, while the 1,4-pentadien-3-ol was consumed at the beginning of the reaction, the rate of consumption decreased, and was not fully consumed until 140 min. From this consumption, generation of the 1-penten-3-ol intermediate was observed in the reaction reaching a maximum amount of 0.012 mmoles at 80 min, representing 47% yield. After this time, the intermediate was again consumed to the final 3-propanol product, but complete consumption was not observed after 3.0 h of reaction, where 10% of the intermediate remained. Finally, formation of the final product was noted throughout the reaction, which linearly increased to near quantitative values, again indicating simultaneous hydrogenation of the initial substrate and intermediate. As anticipated, quantitative product yields were not observed over the time frame of the study as a small fraction of the intermediate remained unreacted. Interestingly, when the Pd120 NPNs were employed as the catalyst, increased degrees of reactivity were noted. To this end, the reaction of the 1,4-pentadien-3-ol reagent was similar to the Pd60 nanospheres; however, the consumption of the intermediate was significantly faster. This is noted by the exhaustion of the 1-penten-3-ol intermediate in the reaction system at a time of 100 min, compared to 3.0 h or greater for the Pd60 and Pd90 materials, respectively. As a result, quantitative final product yields were observed at 2.0 h after reaction initiation for the Pd120 NPNs.

From the results of the diene alcohol hydrogenation, a stepwise mechanism was observed starting with the formation of the 1-penten-3-ol intermediate, followed by production of the fully hydrogenated 3-pentanol product. Interestingly, based on the reaction profile, the Pd60 and Pd120 materials demonstrated similar degrees of reactivity wherein the starting material was rapidly consumed to generate the intermediate product that was quickly converted to the final product. In contrast, the Pd90 nanoribbons took nearly twice the time to consume the starting materials completely and the intermediate was slowly converted to the fully hydrogenated product.

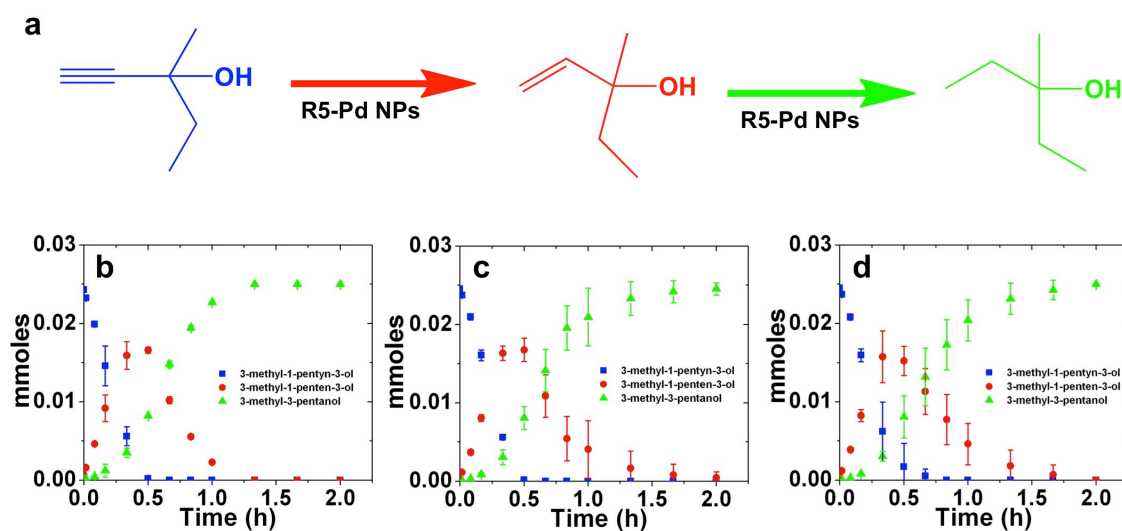


Figure 5.5 a) Reaction scheme for the stepwise hydrogenation of 3-methyl-1-pentyn-3-ol. Plots of the results of hydrogenation reaction of 3-methyl-1-pentyn-3-ol using R5-templated Pd nanomaterials a) Pd60, b) Pd90, and c) Pd120.

In the second multistep hydrogenation reaction system, the reactivity of the R5-templated Pd nanomaterials was explored using an alkyne alcohol, 3-methyl-1-pentyn-3-ol, as the starting material. In this reaction, the first step involves the hydrogenation of the alkyne group to an alkene, producing 3-methyl-1-penten-3-ol as the initial product, after which

the alkene is converted to the fully saturated 3-methyl-3-pentanol product, as illustrated in Figure 5.5a. For this stepwise hydrogenation reaction, the conversion of the substrate to products was monitored for 2.0 h as the reaction was faster as compared to the 1,4-pentadien-3-ol system. This observation can likely be attributed to placement of the reactive functional groups for hydrogenation, which were at the same location in the substrate molecular structure, as compared for the di-enes that positioned the reactive groups at different regions of the molecule. Using the Pd60 nanospheres as the catalyst, the starting material was rapidly hydrogenated in the reaction resulting in an exponential decay such that full consumption was observed at 30 min, as shown in Figure 5.5b. Consequently, the intermediate, 3-methyl-1-penten-3-ol, was immediately formed reaching a maximum yield of 0.017 mmoles, representing a 66% yield, at this time point. In contrast, the fully hydrogenated product, 3-methyl-3-pentanol, was not formed in significant amounts until ~20.0 min; however, rapid generation of this final product was observed after 30 min such that quantitative yields were obtained after 1.0 h. Interestingly, similar reaction profiles were observed when using the Pd90 nanoribbons (5.5c) and Pd120 NPNs (Figure 5.5d) as the catalyst. For Pd90, the starting material was completely consumed at 30 min, while the intermediate product reached maximum yield of 67% also this time point. Conversely, for the Pd120 NPNs, a rapid decrease in the amount of starting material was observed at the onset of the reaction with complete consumption at 40.0 min; however, the formation of the intermediate product peaked at 20.0 min generating a yield of 63%.

Generally, the results showed that the hydrogenation of 3-methyl-1-pentyn-3-ol to 3-methyl-1-penten-3-ol and eventually 3-methyl-3-pentanol occurred in a stepwise fashion

using the peptide-templated Pd nanomaterials as the catalyst. For this system, the reaction was much faster than the 1,4-pentadien-3-ol substrate due to the positioning of the reactive functionalities within the molecule. Additionally, the reaction profiles for Pd60, Pd90 and Pd120 were nearly identical, indicating a similar reaction mechanism for the biotemplated Pd nanostructures; in contrast with the diene reaction discussed above, the reactivity of Pd90 was comparable with the catalytic activities of Pd60 and Pd120.

5.5 Summary and Conclusions

In conclusion, these studies have expanded the catalytic application of peptide-templated Pd nanomaterials towards new substrates that demonstrated highly interesting results based upon the molecular substitution. The results indicated that the inherent reaction TOF values for olefinic alcohols depended directly upon the substitution of the molecule. In this regard, the TOF values of primary alcohols, were generally lower compared with those of secondary and tertiary alcohols, due to the degree of isomerization that hampered product formation. In the competition reaction between allyl alcohol and another olefinic alcohol substrate, non-specific reactivity of the Pd nanomaterials was observed wherein the two substrates undergo hydrogenation reaction at the same time. However, the effects of isomer formation and substrate molecular size were significant factors in the catalytic activities of Pd nanomaterials. To this end, considerable decreases in TOF values were observed for bulkier substrates due to the competition from allyl alcohol hydrogenation and isomerization reactions occurring simultaneously at the catalyst surface, rendering limited availability of reactive Pd atoms. Furthermore, stepwise reaction mechanism was

observed for the peptide-templated Pd nanomaterials for the hydrogenation of substrates containing two reactive centers such as di-substituted olefinic and alkyne alcohols. Overall, the results generated important information on the catalytic versatility of biotemplated Pd nanomaterials in hydrogenation reactions based upon the substrate size, composition and molecular substitution.

Chapter 6. Additional Information

6.1 Supporting information to Chapter 2.

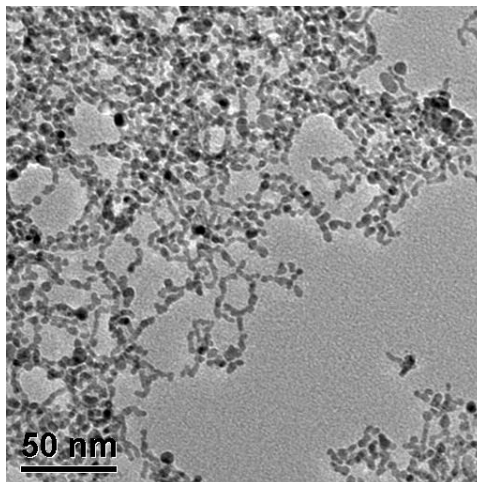


Figure 6.1 Irregular Pd nanostructures produced when the Pd4 peptide is substituted with the R5 peptide.

4-iodobenzoic acid

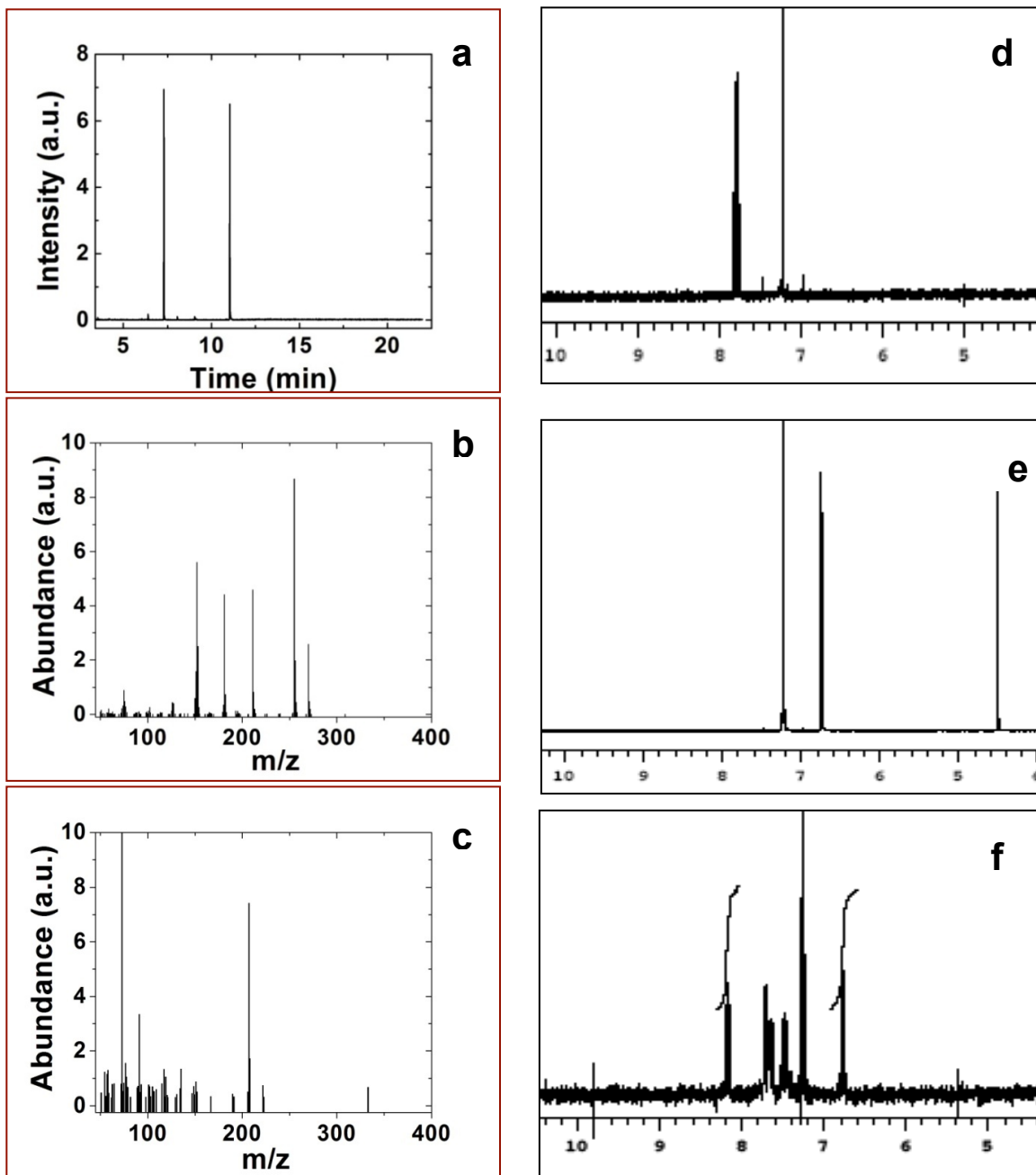


Figure 6.2 (a) GC chromatogram and (b) mass spectrum of the crude product of the Stille reaction using 4-iodobenzoic acid and PhSnCl_3 (0.005 mol% Pd, 24 h), after derivatization with MSTFA. The mass spectrum (b) of the peak at 11.04 min, corresponds to the biphenyl-4-carboxylic acid trimethylsilyl ester ($m/z = 270$). The mass spectrum (c) of the peak at 7.29 min corresponds to the internal standard 4-tertbutylphenol (TBP) trimethylsilyl derivative ($m/z = 222$). ^1H NMR spectrum of 4-iodobenzoic acid (d), TBP (e) and the crude product of the Stille reaction added with 0.5 mmols of TBP (f). The integration of the peak at δ 8.15 ppm (product) was compared with the integration of the peak at δ 6.74 ppm (TBP) to obtain the percent yield of the reaction.

3-iodobenzoic acid

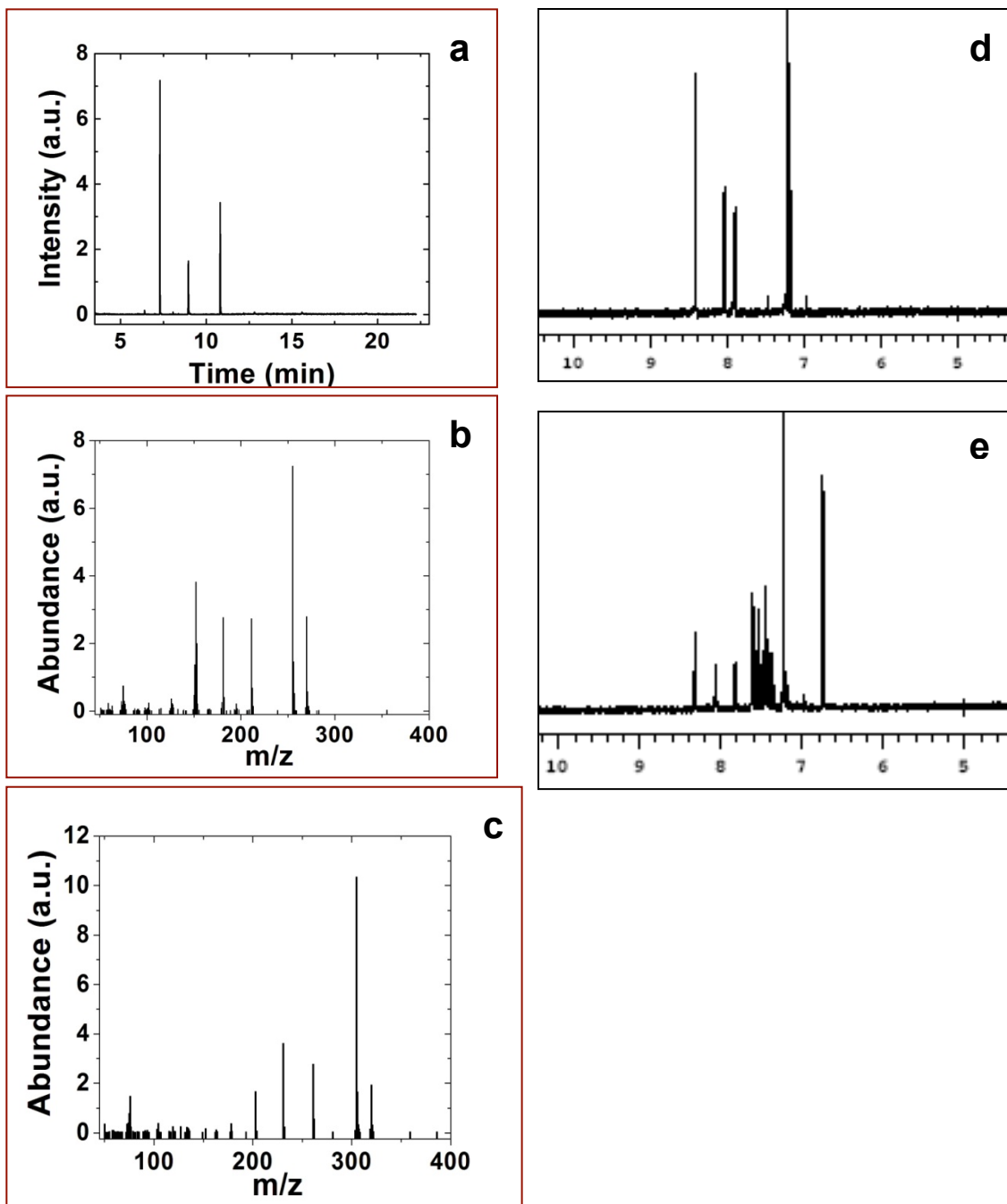


Figure 6.3 (a) GC chromatogram and (b) mass spectrum of the crude product of the Stille reaction using 3-iodobenzoic acid and PhSnCl_3 (0.05 mol% Pd, 24 h), after derivatization with MSTFA. The mass spectrum (b) of the peak at 10.81 min, corresponds to the biphenyl-3-carboxylic acid trimethylsilyl ester ($m/z = 270$). The mass spectrum (c) of the peak at 8.95 min corresponds to the starting material, 3-iodobenzoic acid ($m/z = 320$). ^1H NMR spectrum of 3-iodobenzoic acid (d) and the crude product of the Stille reaction added with 0.5 mmols of TBP (e). The integration of the peak at δ 8.15 ppm (product) was compared with the integration of the peak at δ 6.74 ppm (TBP) to obtain the percent yield of the reaction.

2-iodobenzoic acid

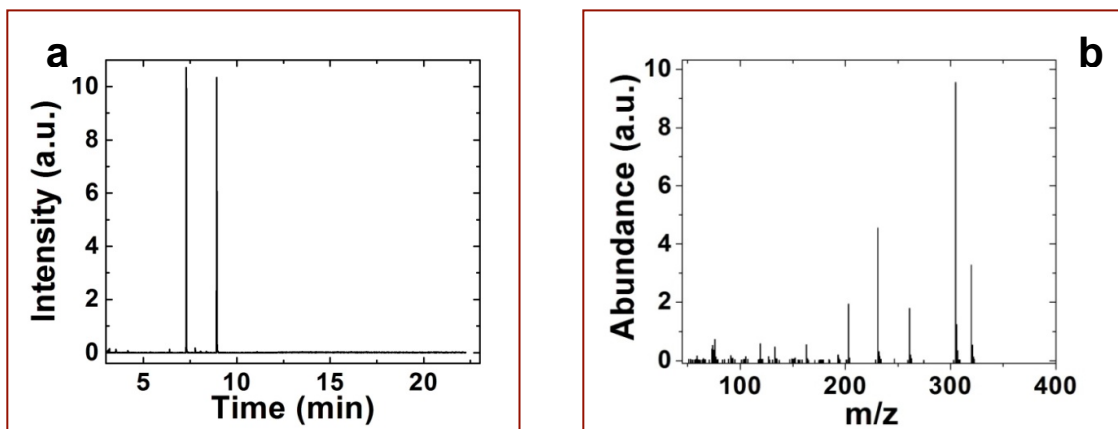


Figure 6.4 (a) GC chromatogram and (b) mass spectrum of the crude product of the Stille reaction using 2-iodobenzoic acid and PhSnCl_3 (0.05 mol% Pd, 24 h), after derivatization with MSTFA. The mass spectrum (b) of the peak at 8.93 min, corresponds to the 2-iodobenzoic acid trimethylsilyl ester ($m/z = 320$). No product is formed in this reaction.

4-bromobenzoic acid, 0.10 mol% Pd, 3.0 d

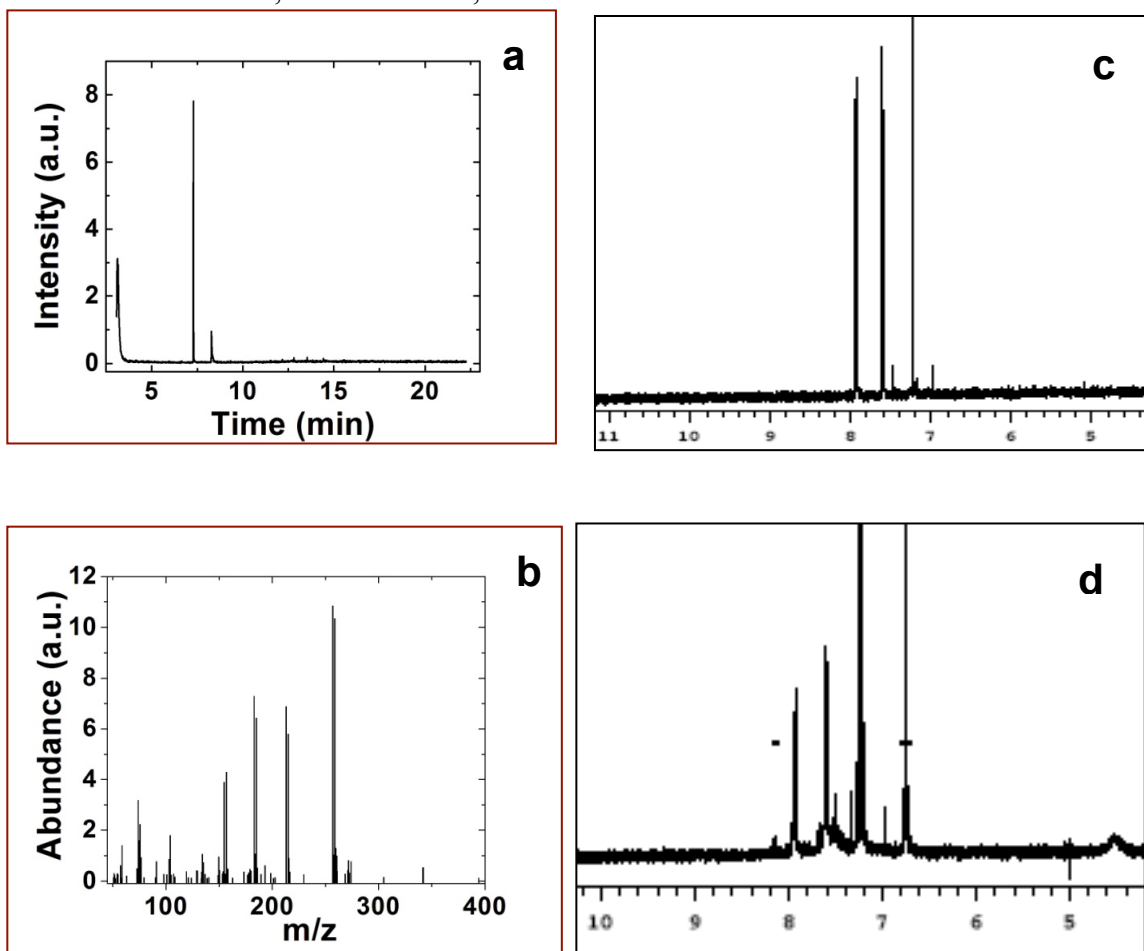


Figure 6.5 (a) GC chromatogram and (b) mass spectrum of the crude product of the Stille reaction using 4-bromobenzoic acid and PhSnCl_3 (0.10 mol% Pd, 3.0 d), after derivatization with MSTFA. The mass spectrum (b) of the peak at 8.28 min, corresponds to the 4-bromobenzoic acid trimethylsilyl ester ($m/z = 272$). ^1H NMR spectrum of 4-bromobenzoic acid (c) and the crude product of the Stille reaction added with 0.5 mmols of TBP (d). The integration of the peak at δ 8.15 ppm (product) was compared with the integration of the peak at δ 6.74 ppm (TBP) to obtain the percent yield of the reaction.

4-bromobenzoic acid, 0.10 mol% Pd, 7.0 d

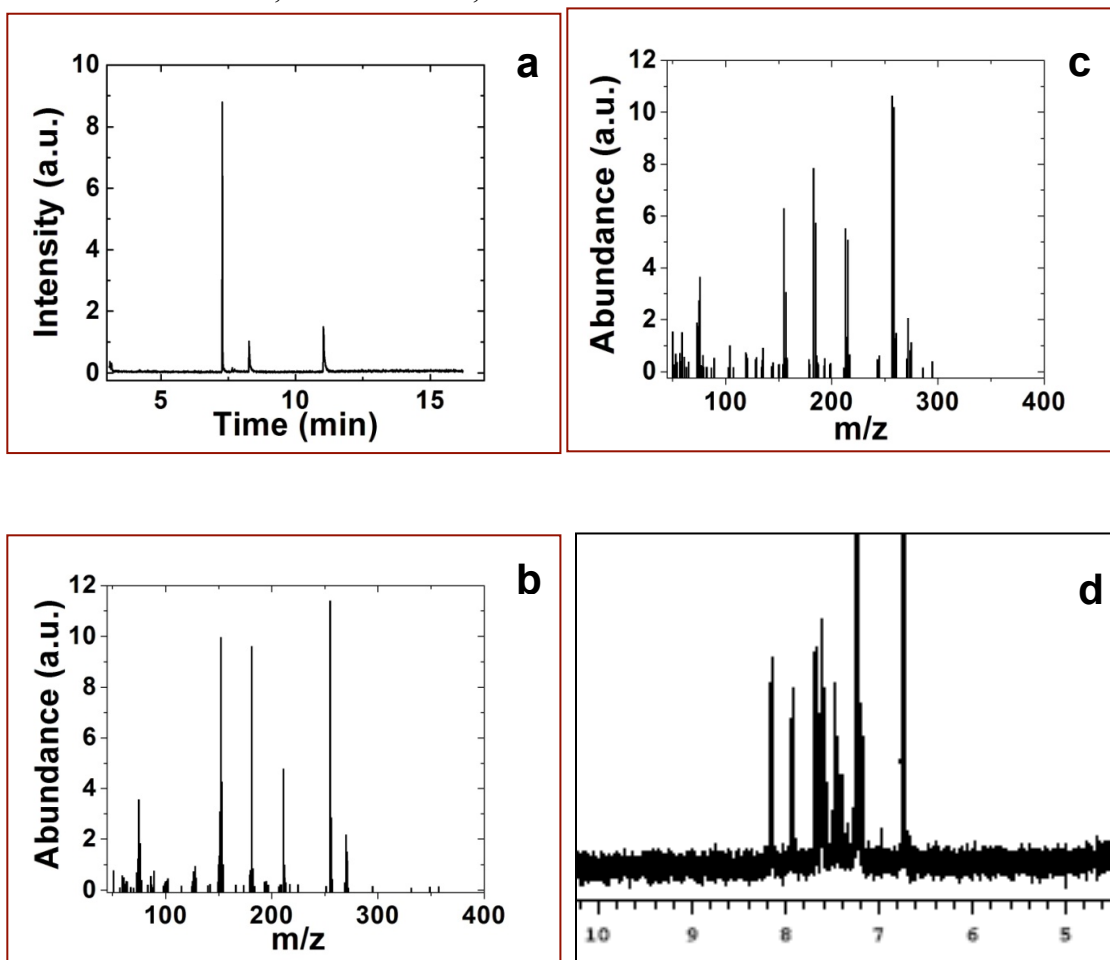


Figure 6.6 (a) GC chromatogram and (b) mass spectrum of the crude product of the Stille reaction using 4-bromobenzoic acid and PhSnCl_3 (0.10 mol% Pd, 7.0 d), after derivatization with MSTFA. The mass spectrum (b) of the peak at 11.03 min, corresponds to the biphenylcarboxylic acid trimethylsilyl ester ($m/z = 270$). The mass spectrum (c) of the peak at 8.28 min corresponds to the 4-bromobenzoic acid trimethylsilyl ester ($m/z = 272$). (d) ^1H NMR spectrum of the crude product of the Stille reaction added with 0.5 mmol of TBP. The integration of the peak at δ 8.15 ppm (product) was compared with the integration of the peak at δ 6.74 ppm (TBP) to obtain the percent yield of the reaction.

4-bromobenzoic acid, 0.50 mol% Pd, 3.0 d

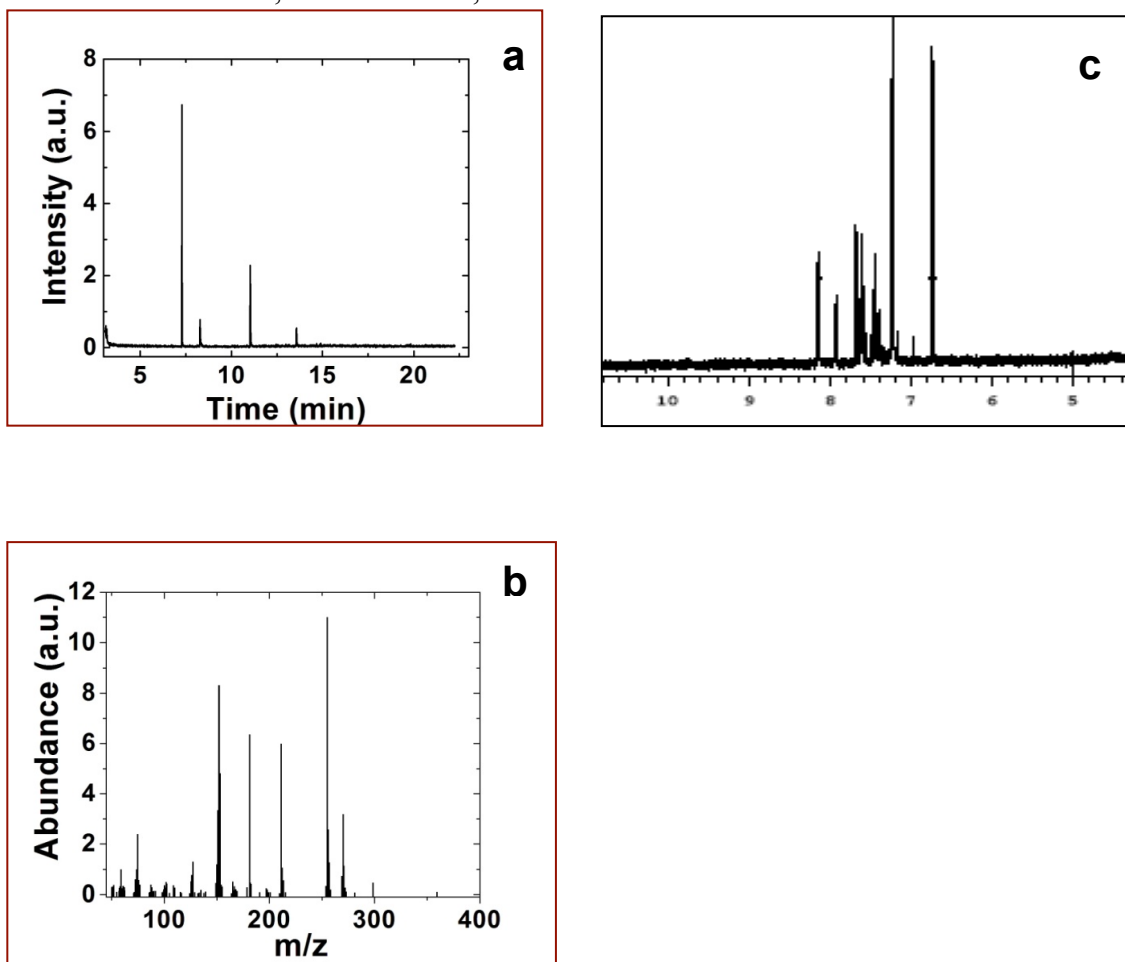


Figure 6.7 (a) GC chromatogram and (b) mass spectrum of the crude product of the Stille reaction using 4-bromobenzoic acid and PhSnCl_3 (0.50 mol% Pd, 3.0 d), after derivatization with MSTFA. The mass spectrum (b) of the peak at 11.03 min, corresponds to the biphenyl-4-carboxylic acid trimethylsilyl ester ($m/z = 270$). (c) ^1H NMR spectrum of the crude product of the Stille reaction added with 0.5 mmols of TBP. The integration of the peak at δ 8.15 ppm (product) was compared with the integration of the peak at δ 6.74 ppm (TBP) to obtain the percent yield of the reaction.

4-bromobenzoic acid, 0.50 mol% Pd, 7.0 d

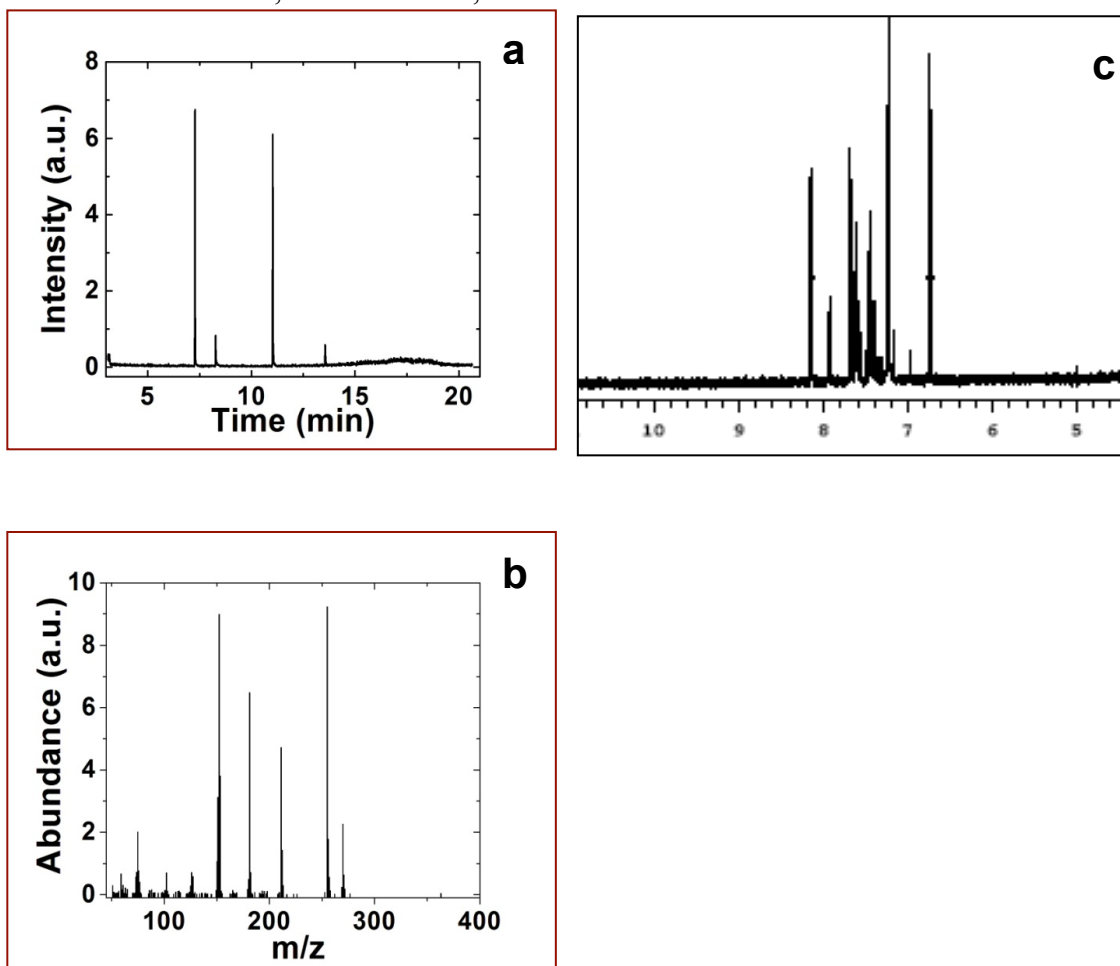


Figure 6.8 (a) GC chromatogram and (b) mass spectrum of the crude product of the Stille reaction using 4-bromobenzoic acid and PhSnCl_3 (0.50 mol% Pd, 7.0 d) after derivatization with MSTFA. The mass spectrum (b) of the peak at 11.03 min, corresponds to the biphenyl-4-carboxylic acid trimethylsilyl ester ($m/z = 270$). (c) ^1H NMR spectrum of the crude product of the Stille reaction added with 0.5 mmols of TBP. The integration of the peak at δ 8.15 ppm (product) was compared with the integration of the peak at δ 6.74 ppm (TBP) to obtain the percent yield of the reaction.

4-chlorobenzoic acid

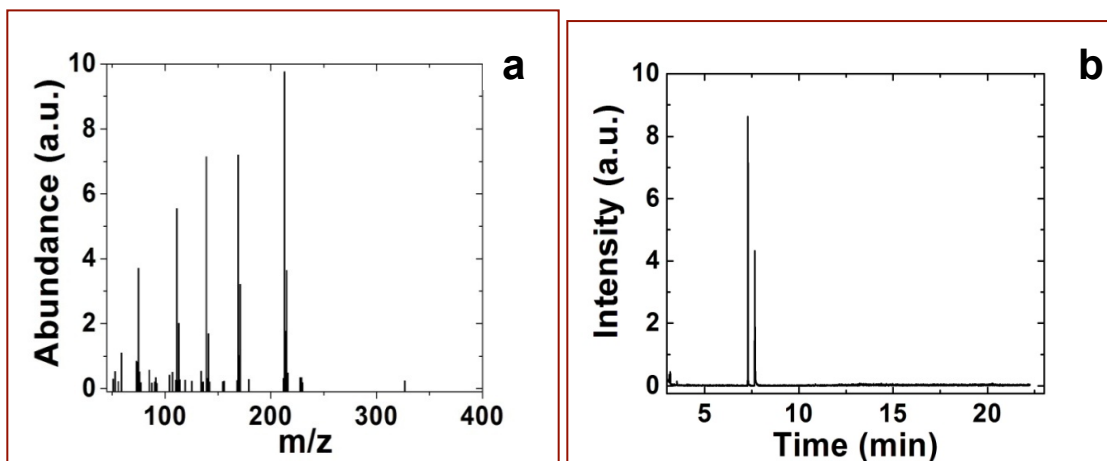


Figure 6.9 (a) GC chromatogram and (b) mass spectrum of the crude product of the Stille reaction using 4-chlorobenzoic acid and PhSnCl_3 (0.05 mol% Pd, 24 h), after derivatization with MSTFA. The mass spectrum (b) of the peak at 7.66 min corresponds to the 4-chlorobenzoic acid trimethylsilyl ester ($m/z = 242$). No product is formed in this reaction.

4-iodophenol

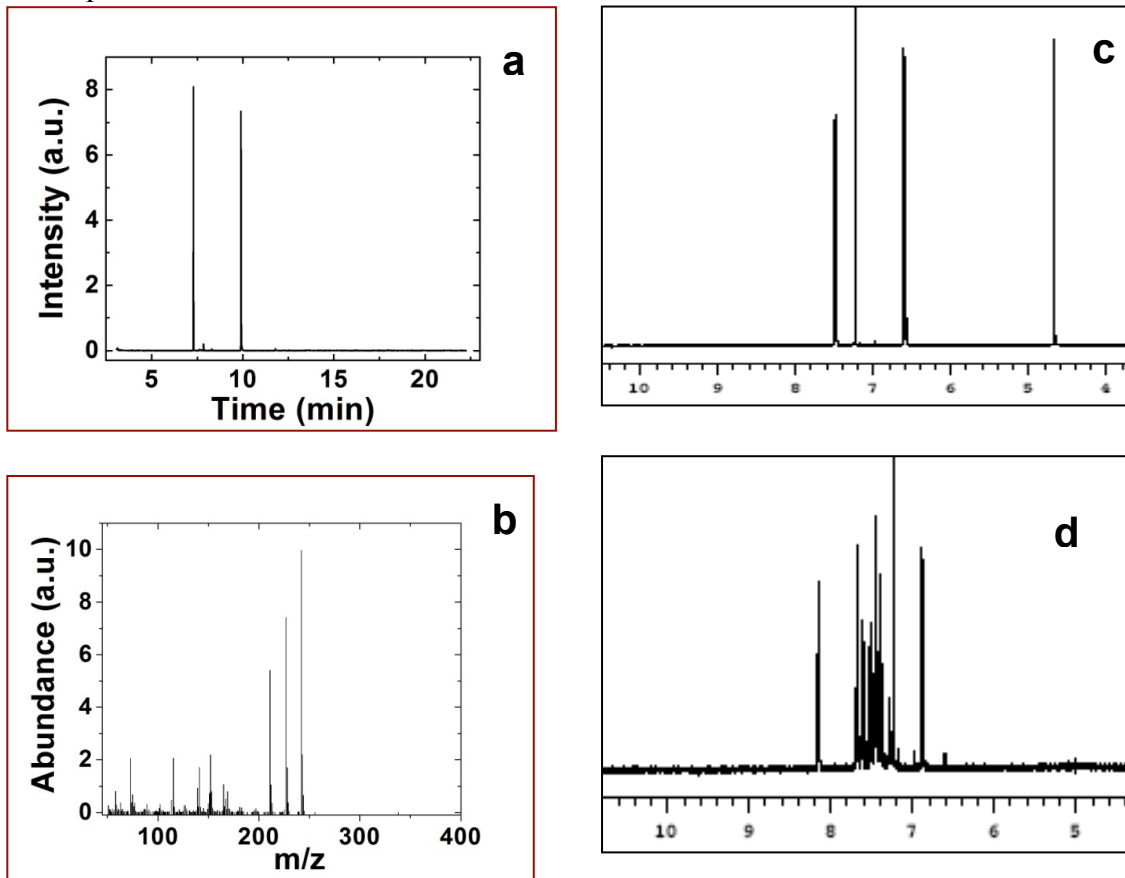


Figure 6.10 (a) GC chromatogram and (b) mass spectrum of the crude product of the Stille reaction using 4-iodophenol and PhSnCl_3 (0.05 mol% Pd, 24 h) after derivatization with MSTFA. The mass spectrum (b) of the peak at 9.90 min corresponds to the 4-phenylphenol trimethylsilyl ester derivative ($m/z = 242$). ^1H NMR spectrum of 4-iodophenol (c) and the crude product of the Stille reaction added with 0.5 mmols of biphenylcarboxylic acid (BPCA) (d). The integration of the peak at δ 6.88 ppm (product) was compared with the integration of the peak at δ 8.15 ppm (BPCA) to obtain the percent yield of the reaction.

4-bromophenol, 0.10 mol% Pd, 3.0 d

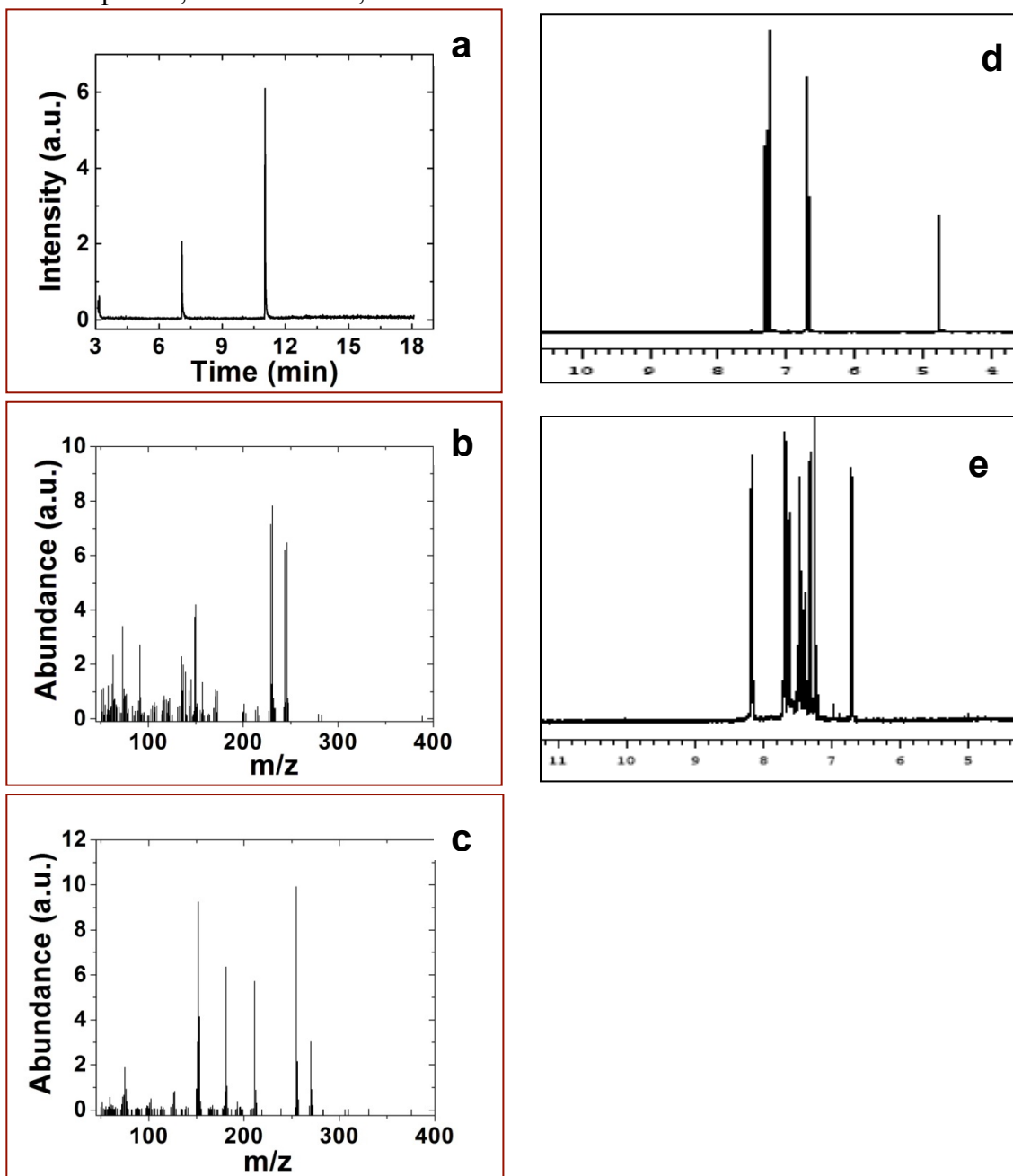


Figure 6.11 (a) GC chromatogram of the crude product of the Stille reaction using 4-bromophenol and PhSnCl_3 (0.10nmol% Pd, 3.0 d) after derivatization with MSTFA. The mass spectrum (b) of the peak at 7.09 min corresponds to the 4-bromophenol trimethylsilyl ester derivative ($m/z = 246$). The mass spectrum (c) of the peak at 11.03 min, corresponds to the internal standard biphenylcarboxylic acid (BPCA). ^1H NMR spectrum of 4-bromophenol (d) and the crude product of the Stille reaction added with 0.5 mmols of BPCA (e). The integration of the peak at δ 6.88 ppm (product) was compared with the integration of the peak at δ 8.15 ppm (BPCA) to obtain the percent yield of the reaction.

4-bromophenol, 0.10 mol% Pd, 7.0 d

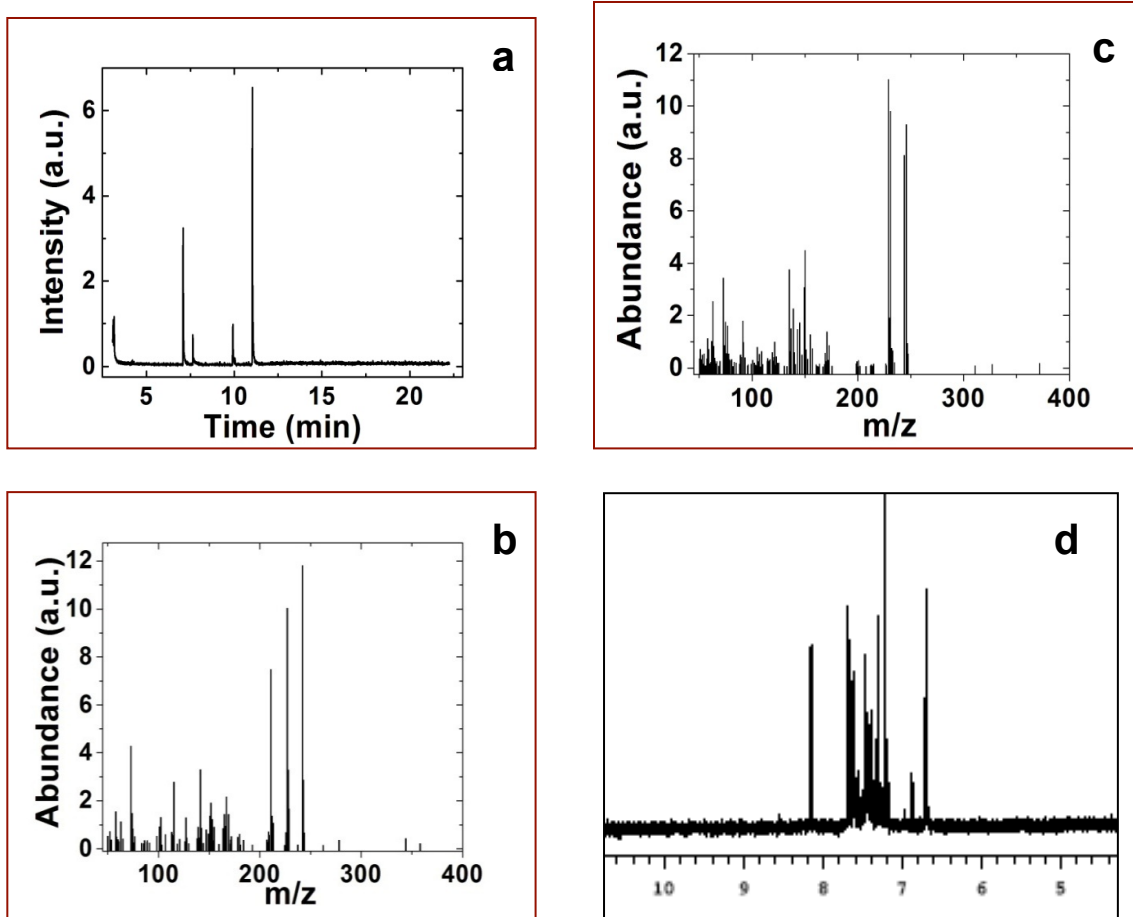


Figure 6.12 (a) GC chromatogram and (b) mass spectrum of the crude product of the Stille reaction using 4-bromophenol and PhSnCl_3 (0.10 mol% Pd, 7.0 d) after derivatization with MSTFA. The mass spectrum (b) of the peak at 9.90 min, corresponds to the 4-phenylphenol trimethylsilyl derivative ($m/z = 242$). The mass spectrum (c) of the peak at 7.09 min, corresponds to the 4-bromophenol trimethylsilyl derivative ($m/z = 246$). (d) ^1H NMR spectrum of the crude product of the Stille reaction added with 0.5 mmols of BPCA. The integration of the peak at δ 6.88 ppm (product) was compared with the integration of the peak at δ 8.15 ppm (BPCA) to obtain the percent yield of the reaction.

4-bromophenol, 0.50 mol% Pd, 3.0 d

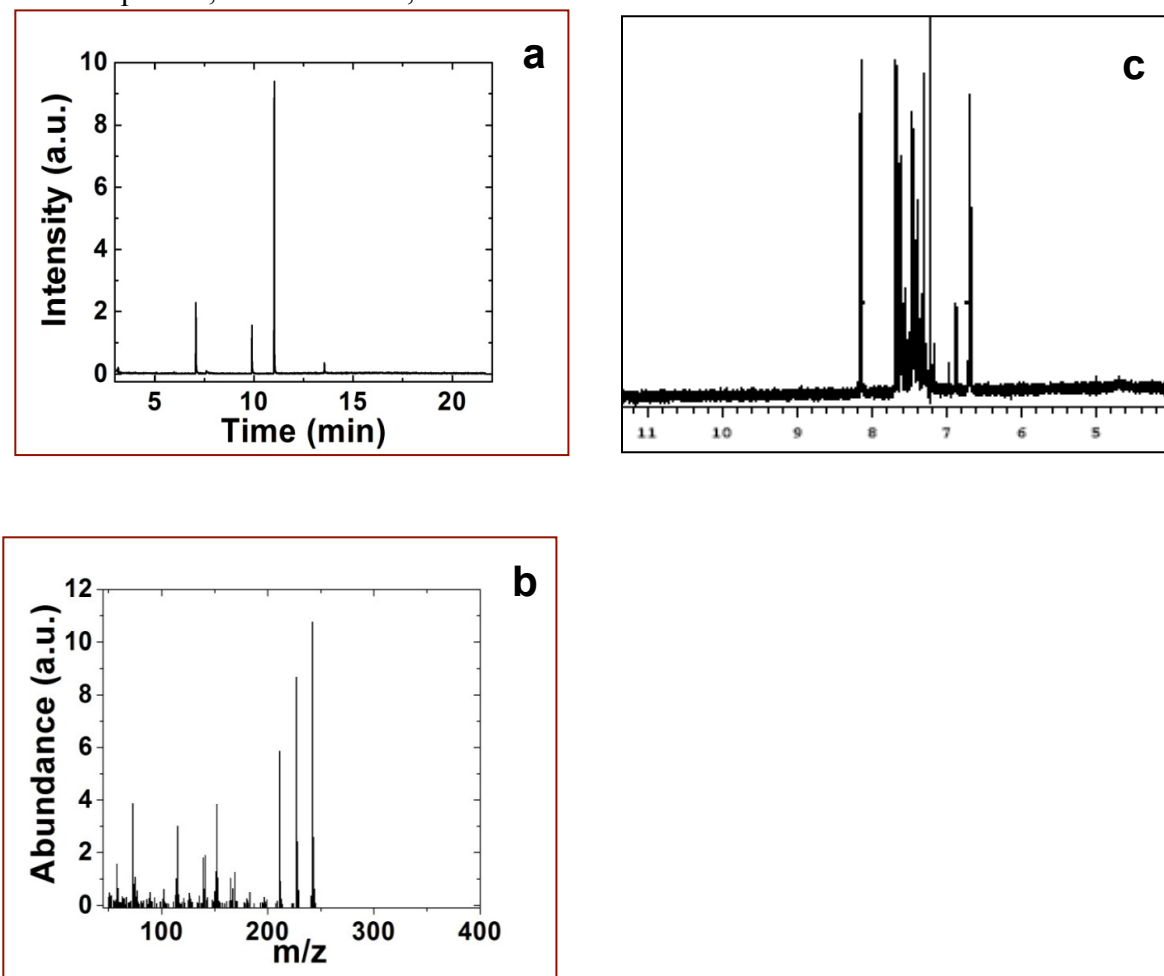


Figure 6.13 (a) GC chromatogram and (b) mass spectrum of the crude product of the Stille reaction using 4-bromophenol and PhSnCl_3 (0.50 mol% Pd, 3.0 d) after derivatization with MSTFA. The mass spectrum (b) of the peak at 9.90 min, corresponds to the 4-phenylphenol trimethylsilyl derivative ($m/z = 242$). (c) ^1H NMR spectrum of the crude product of the Stille reaction added with 0.5 mmols of BPCA. The integration of the peak at δ 6.88 ppm (product) was compared with the integration of the peak at δ 8.15 ppm (BPCA) to obtain the percent yield of the reaction.

4-bromophenol, 0.50 mol% Pd, 7.0 d

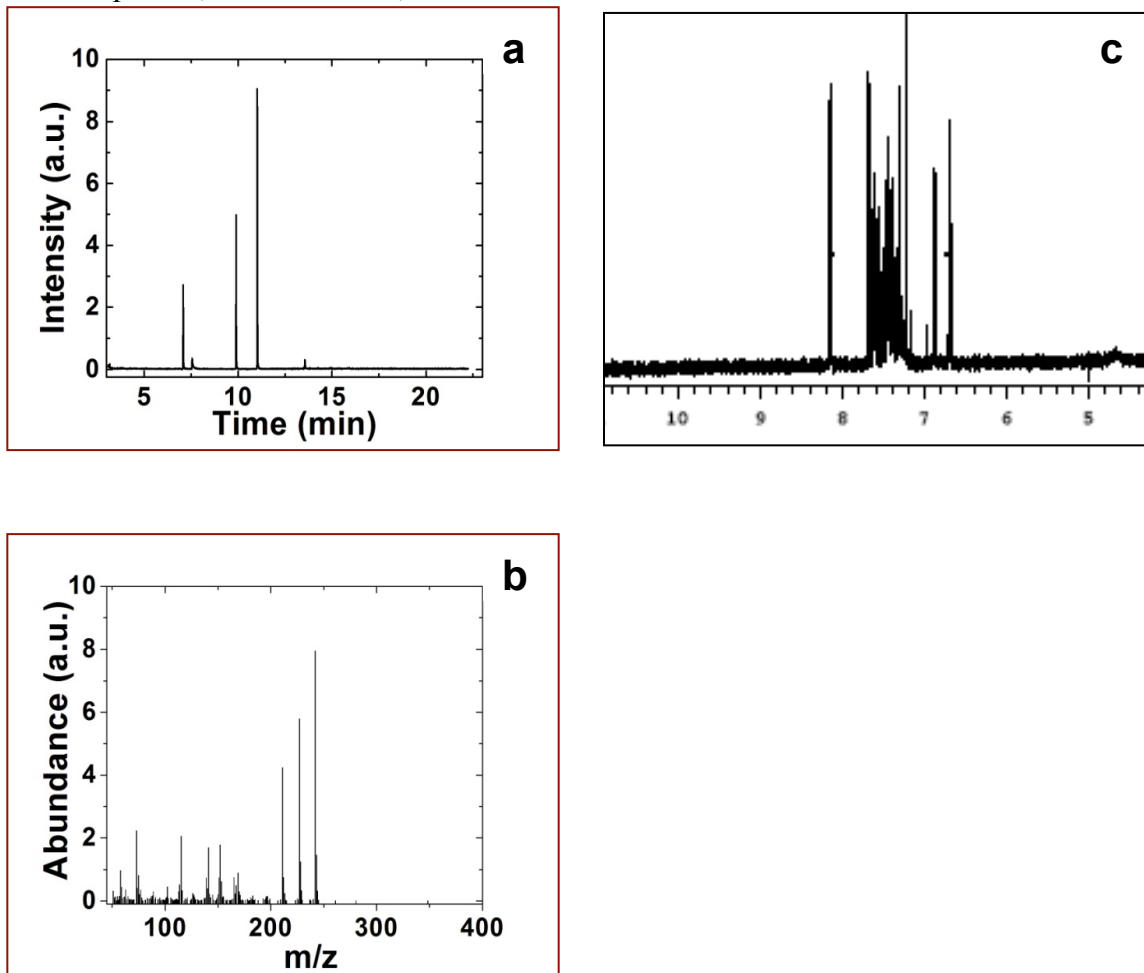


Figure 6.14 (a) GC chromatogram and (b) mass spectrum of the crude product of the Stille reaction using 4-bromophenol and PhSnCl_3 (0.50 mol% Pd, 7.0 d) after derivatization with MSTFA. The mass spectrum (b) of the peak at 9.90 min, corresponds to the 4-phenylphenol trimethylsilyl derivative ($m/z = 242$). (c) ^1H NMR spectrum of the crude product of the Stille reaction added with 0.50 mmols of BPCA. The integration of the peak at δ 6.88 ppm (product) was compared with the integration of the peak at δ 8.15 ppm (BPCA) to obtain the percent yield of the reaction.

4-chlorophenol

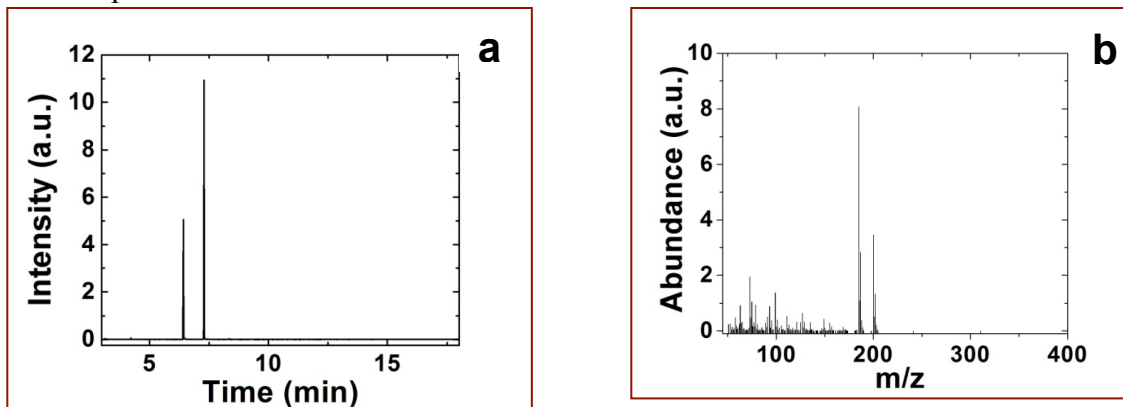


Figure 6.15 (a) GC chromatogram and (b) mass spectrum of the crude product of the Stille reaction using 4-chlorophenol and PhSnCl_3 (0.05 mol% Pd, 24 h), after derivatization with MSTFA. The mass spectrum (b) of the peak at 6.42 min corresponds to the 4-chlorophenol trimethylsilyl derivative ($m/z = 200$). No product is formed in this reaction.

Stille Coupling Reaction in Ethanol/KOH

4-iodobenzoic acid, 0.05mol% Pd, 24 h

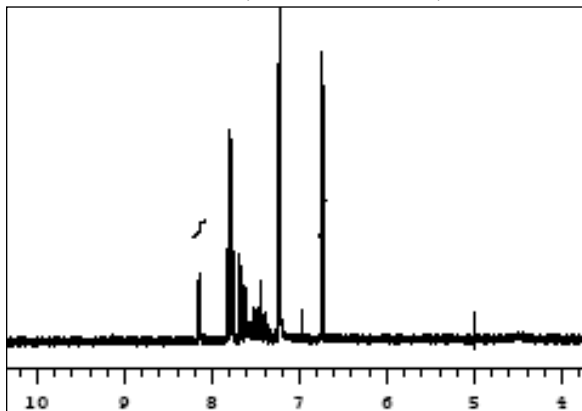


Figure 6.16 ^1H NMR spectrum of the crude product of the Stille reaction in ethanol/KOH solvent added with 0.50 mmols of TBP. The integration of the peak at δ 8.15 ppm (BCA) was compared with the integration of the peak at δ 6.74 ppm (TBP) to obtain the percent yield of the reaction.

6.2 Supporting information to Chapter 5.

6.2.1 Calculation of response factors and % hydrogenation for 4-penten-1-ol.

(Adapted from Bhattacharjee, S.; Bruening, M. L. *Langmuir* **2008**, *24*, 2916.)²⁵⁶

$$\frac{C_p k_1}{C_r} = \frac{S_p}{S_r}$$

$$\frac{C_{i1} k_2}{C_r} = \frac{S_{i1}}{S_r}$$

$$\frac{C_{i2} k_3}{C_r} = \frac{S_{i2}}{S_r}$$

where: C_p = concentration of product, 1-pentanol

C_r = concentration of starting material, 4-penten-1-ol

C_{i1} = concentration of isomer 1, 2-penten-1-ol

C_{i2} = concentration of isomer 2, 3-penten-1-ol

S_p = peak area corresponding to 1-pentanol

S_r = peak area corresponding to 4-penten-1-ol

S_{i1} = peak area corresponding to 2-penten-1-ol

S_{i2} = peak area corresponding to 3-penten-1-ol

k_1 = response factor of product to starting material

k_2 = response factor of isomer 1 to starting material

k_3 = response factor of isomer 2 to starting material

$$\% \text{ hydrogenation} = \frac{C_p}{C_p + C_r + C_{i1} + C_{i2}} \times 100\%$$

$$\% \text{ hydrogenation} = \frac{S_p k_2 k_3}{(S_p k_2 k_3) + (S_r k_1 k_2 k_3) + (S_{i1} k_1 k_3) + (S_{i2} k_1 k_2)} \times 100\%$$

6.2.2 Calculation of number of moles for each component of the stepwise hydrogenation reaction.

(Adapted from Bhattacharjee, S.; Bruening, M. L. *Langmuir* **2008**, *24*, 2916.)²⁵⁶

$$\frac{C_{p1} k_1}{C_r} = \frac{S_{p1}}{S_r}$$

$$\frac{C_{p2} k_1}{C_r} = \frac{S_{p2}}{S_r}$$

where: C_{p1} = concentration of intermediate product

C_{p2} = concentration of final product

C_r = concentration of starting material

S_{p1} = peak area corresponding to intermediate product

S_{p2} = peak area corresponding to final product

S_r = peak area corresponding to starting material

k_1 = response factor of intermediate product to starting material

k_2 = response factor of final product to starting material

$$\% \text{ starting material} = \frac{C_r}{C_r + C_{p1} + C_{p2}} \times 100\% = \frac{S_r k_1 k_2}{(S_r k_1 k_2) + (S_{p1} k_2) + (S_{p2} k_1)} \times 100\%$$

$$\text{mmol of starting material} = \frac{\% \text{ starting material} \times 0.025 \text{ mmol}}{100}$$

Similarly, the amount of intermediate and final products were calculated as follows:

$$\% \text{ intermediate product} = \frac{S_{p1} k_2}{(S_r k_1 k_2) + (S_{p1} k_2) + (S_{p2} k_1)} \times 100\%$$

$$\text{mmol of intermediate product} = \frac{\% \text{ intermediate product} \times 0.025 \text{ mmol}}{100}$$

$$\% \text{ final product} = \frac{S_{p2} k_1}{(S_r k_1 k_2) + (S_{p1} k_2) + (S_{p2} k_1)} \times 100\%$$

$$\text{mmol of final product} = \frac{\% \text{ final product} \times 0.025 \text{ mmol}}{100}$$

References

1. Kember, M. R.; Williams, C. K. *J. Am. Chem. Soc.* **2012**, *134*, 15676-15679.
2. Hanada, N.; Ichikawa, T.; Fujii, H. *J. Phys. Chem. B* **2005**, *109*, 7188-7194.
3. Ganguly, A.; Trinh, P.; Ramanujachary, K. V.; Ahmad, T.; Mugweru, A.; Ganguli, A. K. *J. Colloid Interface Sci.* **2011**, *353*, 137-142.
4. Patil, A. B.; Bhanage, B. M. *Catal. Commun.* **2013**, *36*, 79-83.
5. López, C.; Corma, A. *ChemCatChem* **2012**, *4*, 751-752.
6. Sonnenberg, J. F.; Coombs, N.; Dube, P. A.; Morris, R. H. *J. Am. Chem. Soc.* **2012**, *134*, 5893-5899.
7. Torres Galvis, H. M.; Bitter, J. H.; Khare, C. B.; Ruitenbeek, M.; Dugulan, A. I.; de Jong, K. P. *Science* **2012**, *335*, 835-838.
8. Lastella, S.; Jung, Y. J.; Yang, H.; Vajtai, R.; Ajayan, P. M.; Ryu, C. Y.; Rider, D. A.; Manners, I. *J. Mater. Chem.* **2004**, *14*, 1791-1794.
9. Moglie, Y.; Vitale, C.; Radivoy, G. *Tetrahedron Lett.* **2008**, *49*, 1828-1831.
10. Shimizu, K.-i.; Kon, K.; Onodera, W.; Yamazaki, H.; Kondo, J. N. *ACS Catal.* **2012**, *3*, 112-117.
11. Wang, H. Y.; Lua, A. C. *J. Phys. Chem. C* **2012**, *116*, 26765-26775.
12. Li, P.-Z.; Aijaz, A.; Xu, Q. *Angew. Chem., Int. Ed.* **2012**, *51*, 6753-6756.
13. Alonso, F.; Osante, I.; Yus, M. *Adv. Synth. Catal.* **2006**, *348*, 305-308.
14. Wang, A.; Yin, H.; Lu, H.; Xue, J.; Ren, M.; Jiang, T. *Catal. Commun.* **2009**, *10*, 2060-2064.
15. Zhang, W.; Qi, H.; Li, L.; Wang, X.; Chen, J.; Peng, K.; Wang, Z. *Green Chem.* **2009**, *11*, 1194-1200.
16. Geukens, I.; Fransaer, J.; De Vos, D. E. *ChemCatChem* **2011**, *3*, 1431-1434.
17. Chen, Y.; Crawford, P.; Hu, P. *Catal. Lett.* **2007**, *119*, 21-28.

18. Guzzi, L.; Horvath, D.; Paszti, Z.; Toth, L.; Horvath, Z. E.; Karacs, A.; Peto, G. *J. Phys. Chem. B* **2000**, *104*, 3183-3193.
19. Kidwai, M.; Bansal, V.; Kumar, A.; Mozumdar, S. *Green Chem.* **2007**, *9*, 742-745.
20. Kidwai, M.; Bhardwaj, S. *Appl. Catal., A* **2010**, *387*, 1-4.
21. Mitsudome, T.; Noujima, A.; Mizugaki, T.; Jitsukawa, K.; Kaneda, K. *Chem. Commun.* **2009**, *0*, 5302-5304.
22. Pasquato, L.; Rancan, F.; Scrimin, P.; Mancin, F.; Frigeri, C. *Chem. Commun.* **2000**, *0*, 2253-2254.
23. Wang, L.; Meng, X.; Wang, B.; Chi, W.; Xiao, F.-S. *Chem. Commun.* **2010**, *46*, 5003-5005.
24. Jiang, X.; Xie, Y.; Lu, J.; Zhu, L.; He, W.; Qian, Y. *Langmuir* **2001**, *17*, 3795-3799.
25. Mikami, Y.; Noujima, A.; Mitsudome, T.; Mizugaki, T.; Jitsukawa, K.; Kaneda, K. *Tetrahedron Lett.* **2010**, *51*, 5466-5468.
26. Mikami, Y.; Noujima, A.; Mitsudome, T.; Mizugaki, T.; Jitsukawa, K.; Kaneda, K. *Chem. Lett.* **2010**, *39*, 223-225.
27. Saha, S.; Pal, A.; Kundu, S.; Basu, S.; Pal, T. *Langmuir* **2010**, *26*, 2885-2893.
28. Sutton, A.; Franc, G.; Kakkar, A. *J. Polym. Sci., Part A: Polym. Chem.* **2009**, *47*, 4482-4493.
29. Steffan, M.; Jakob, A.; Claus, P.; Lang, H. *Catal. Commun.* **2009**, *10*, 437-441.
30. Kim, A. Y.; Bae, H.; Park, S.; Park, S.; Park, K. *Catal. Lett.* **2011**, *141*, 685-690.
31. Ueno, T.; Suzuki, M.; Goto, T.; Matsumoto, T.; Nagayama, K.; Watanabe, Y. *Angew. Chem., Int. Ed.* **2004**, *43*, 2527-2530.
32. Wilson, O. M.; Knecht, M. R.; Garcia-Martinez, J. C.; Crooks, R. M. *J. Am. Chem. Soc.* **2006**, *128*, 4510-4511.
33. Niu, Y.; Yeung, L. K.; Crooks, R. M. *J. Am. Chem. Soc.* **2001**, *123*, 6840-6846.
34. Galow, T. H.; Drechsler, U.; Hanson, J. A.; Rotello, V. M. *Chem. Commun.* **2002**, *0*, 1076-1077.

35. Semagina, N.; Kiwi-Minsker, L. *Catal. Lett.* **2009**, *127*, 334-338.
36. Mei, Y.; Lu, Y.; Polzer, F.; Ballauff, M.; Drechsler, M. *Chem. Mater.* **2007**, *19*, 1062-1069.
37. Bhandari, R.; Knecht, M. R. *ACS Catal.* **2011**, *1*, 89-98.
38. Harish, S.; Mathiyarasu, J.; Phani, K. L. N.; Yegnaraman, V. *Catal. Lett.* **2009**, *128*, 197-202.
39. Faticanti, M.; Cioffi, N.; Rossi, S. D.; Ditaranto, N.; Porta, P.; Sabbatini, L.; Blevè-Zacheo, T. *Appl. Catal., B* **2005**, *60*, 73-82.
40. Glaspell, G.; Fuoco, L.; El-Shall, M. S. *J. Phys. Chem. B* **2005**, *109*, 17350-17355.
41. Park, J.-N.; Forman, A. J.; Tang, W.; Cheng, J.; Hu, Y.-S.; Lin, H.; McFarland, E. W. *Small* **2008**, *4*, 1694-1697.
42. Schalow, T.; Brandt, B.; Laurin, M.; Schauermaun, S.; Libuda, J.; Freund, H. J. *J. Catal.* **2006**, *242*, 58-70.
43. Wang, H.; Jusys, Z.; Behm, R. J. *J. Phys. Chem. B* **2004**, *108*, 19413-19424.
44. Xu, B.; Guo, J.; Jia, H.; Yang, X.; Liu, X. *Catal. Today* **2007**, *125*, 169-172.
45. Inkaew, P.; Zhou, W.; Korzeniewski, C. *J. Electroanal. Chem.* **2008**, *614*, 93-100.
46. Mostafa, S.; Croy, J. R.; Heinrich, H.; Cuenya, B. R. *Appl. Catal., A* **2009**, *366*, 353-362.
47. Li, J.; Liang, X.; King, D. M.; Jiang, Y.-B.; Weimer, A. W. *Appl. Catal., B* **2010**, *97*, 220-226.
48. Long, N.; Ohtaki, M.; Nogami, M.; Hien, T. *Colloid Polym. Sci.* **2011**, *289*, 1373-1386.
49. Wu, H.; Tang, R.; He, Q.; Liao, X.; Shi, B. *J. Chem. Technol. Biotechnol.* **2009**, *84*, 1702-1711.
50. Armor, J. N. *Appl. Catal., A* **2000**, *194*, 3-11.
51. Centi, G.; Ciambelli, P.; Perathoner, S.; Russo, P. *Catal. Today* **2002**, *75*, 3-15.
52. Astruc, D. *Inorg. Chem.* **2007**, *46*, 1884-1894.

53. Barnard, C. *Platinum Met. Rev.* **2008**, *52*, 38-45.
54. Colacot, T. J. *Platinum Met. Rev.* **2009**, *53*, 183-188.
55. Jin, R. The impacts of nanotechnology on catalysis by precious metal nanoparticles. *Nanotechnology Reviews*, 2012; Vol. 1, p 31.
56. Yin, J. *Applications of Transition Metal Catalysis in Drug Discovery and Development*, John Wiley & Sons, Inc.: 2012; pp 97-163.
57. Heck, R. F.; Nolley, J. P. *J. Org. Chem.* **1972**, *37*, 2320-2322.
58. Balanta, A.; Godard, C.; Claver, C. *Chem. Soc. Rev.* **2011**, *40*, 4973-4985.
59. Sonogashira, K.; Tohda, Y.; Hagihara, N. *Tetrahedron Lett.* **1975**, *16*, 4467-4470.
60. Milstein, D.; Stille, J. K. *J. Am. Chem. Soc.* **1978**, *100*, 3636-3638.
61. Negishi, E.; King, A. O.; Okukado, N. *J. Org. Chem.* **1977**, *42*, 1821-1823.
62. Hayashi, T.; Konishi, M.; Kumada, M. *Tetrahedron Lett.* **1979**, *20*, 1871-1874.
63. Miyaura, N.; Yamada, K.; Suzuki, A. *Tetrahedron Lett.* **1979**, *20*, 3437-3440.
64. Miyaura, N.; Suzuki, A. *J. Chem. Soc., Chem. Commun.* **1979**, *0*, 866-867.
65. Colacot, T. J. *Platinum Met. Rev.* **2011**, *55*, 84 - 90.
66. *Nat Mater* **2011**, *10*, 333-333.
67. Qing, F.; Sun, Y.; Wang, X.; Li, N.; Li, Y.; Li, X.; Wang, H. *Polym. Chem.* **2011**, *2*, 2102-2106.
68. Thanh, N. C.; Ikai, M.; Kajioka, T.; Fujikawa, H.; Taga, Y.; Zhang, Y.; Ogawa, S.; Shimada, H.; Miyahara, Y.; Kuroda, S.; Oda, M. *Tetrahedron* **2006**, *62*, 11227-11239.
69. van Mullekom, H. A. M.; Vekemans, J. A. J. M.; Meijer, E. W. *Chem. Eur. J.* **1998**, *4*, 1235-1243.
70. Thornton, P. D.; Brown, N.; Hill, D.; Neuenswander, B.; Lushington, G. H.; Santini, C.; Buszek, K. R. *ACS Comb. Sci.* **2011**, *13*, 443-448.
71. Deore, P. S.; Argade, N. P. *J. Org. Chem.* **2011**, *77*, 739-746.
72. Bentoumi, W.; Helhaik, J.; Ple, G.; Ramondenc, Y. *Tetrahedron* **2009**, *65*, 1967-1970.

73. Zeng, F.; Negishi, E. *Org. Lett.* **2001**, *3*, 719-722.
74. Danishefsky, S. J.; Masters, J. J.; Young, W. B.; Link, J. T.; Snyder, L. B.; Magee, T. V.; Jung, D. K.; Isaacs, R. C. A.; Bornmann, W. G.; Alaimo, C. A.; Coburn, C. A.; Di Grandi, M. J. *J. Am. Chem. Soc.* **1996**, *118*, 2843-2859.
75. Hong, C. Y.; Kado, N.; Overman, L. E. *J. Am. Chem. Soc.* **1993**, *115*, 11028-11029.
76. Barluenga, J.; Tomás-Gamasa, M.; Moriel, P.; Aznar, F.; Valdés, C. *Chem. Eur. J.* **2008**, *14*, 4792-4795.
77. Pomeisl, K.; Holy, A.; Pohl, R.; Horska, K. *Tetrahedron* **2009**, *65*, 8486-8492.
78. Burda, C.; Chen, X.; Narayanan, R.; El-Sayed, M. A. *Chem. Rev.* **2005**, *105*, 1025-1102.
79. Perez-Juste, J.; Pastoriza-Santos, I.; Liz-Marzan, L. M.; Mulvaney, P. *Coord. Chem. Rev.* **2005**, *249*, 1870-1901.
80. Xia, Y.; Xiong, Y.; Lim, B.; Skrabalak, S. E. *Angew. Chem., Int. Ed.* **2009**, *48*, 60-103.
81. Rycenga, M.; Cogley, C. M.; Zeng, J.; Li, W.; Moran, C. H.; Zhang, Q.; Qin, D.; Xia, Y. *Chem. Rev.* **2011**, *111*, 3669-3712.
82. You, H.; Yang, S.; Ding, B.; Yang, H. *Chem. Soc. Rev.* **2013**, *42*, 2880-2904.
83. Coppage, R.; Slocik, J. M.; Briggs, B. D.; Frenkel, A. I.; Naik, R. R.; Knecht, M. R. *ACS Nano* **2012**, *6*, 1625-1636.
84. Daniel, M.-C.; Astruc, D. *Chem. Rev.* **2003**, *104*, 293-346.
85. Huang, X.; Tang, S.; Mu, X.; Dai, Y.; Chen, G.; Zhou, Z.; Ruan, F.; Yang, Z.; Zheng, N. *Nat Nano* **2011**, *6*, 28-32.
86. Garcia-Martinez, J. C.; Lezutekong, R.; Crooks, R. M. *J. Am. Chem. Soc.* **2005**, *127*, 5097-5103.
87. Jakhmola, A.; Bhandari, R.; Pacardo, D. B.; Knecht, M. R. *J. Mater. Chem.* **2010**, *20*, 1522-1531.
88. Pacardo, D. B.; Sethi, M.; Jones, S. E.; Naik, R. R.; Knecht, M. R. *ACS Nano* **2009**, *3*, 1288-1296.
89. Astruc, D. *Tetrahedron: Asymmetry* **2010**, *21*, 1041-1054.

90. Bernechea, M.; de Jesus, E.; Lopez-Mardomingo, C.; Terreros, P. *Inorg. Chem.* **2009**, *48*, 4491-4496.
91. Ooe, M.; Murata, M.; Mizugaki, T.; Ebitani, K.; Kaneda, K. *J. Am. Chem. Soc.* **2004**, *126*, 1604-1605.
92. Rahim, E. H.; Kamounah, F. S.; Frederiksen, J.; Christensen, J. B. *Nano Lett.* **2001**, *1*, 499-501.
93. Wu, L.; Li, Z.-W.; Zhang, F.; He, Y.-M.; Fan, Q.-H. *Adv. Synth. Catal.* **2008**, *350*, 846-862.
94. Coppage, R.; Slocik, J. M.; Sethi, M.; Pacardo, D. B.; Naik, R. R.; Knecht, M. R. *Angew. Chem., Int. Ed.* **2010**, *49*, 3767-3770.
95. Dutta, P.; Sarkar, A. *Adv. Synth. Catal.* **2011**, *353*, 2814-2822.
96. Li, Y.; Hong, X. M.; Collard, D. M.; El-Sayed, M. A. *Org. Lett.* **2000**, *2*, 2385-2388.
97. Sawoo, S.; Srimani, D.; Dutta, P.; Lahiri, R.; Sarkar, A. *Tetrahedron* **2009**, *65*, 4367-4374.
98. Strimbu, L.; Liu, J.; Kaifer, A. E. *Langmuir* **2003**, *19*, 483-485.
99. Liang, C.; Xia, W.; van den Berg, M.; Wang, Y.; Soltani-Ahmadi, H.; Schlüter, O.; Fischer, R. A.; Muhler, M. *Chem. Mater.* **2009**, *21*, 2360-2366.
100. Liang, C.; Xia, W.; Soltani-Ahmadi, H.; Schlüter, O.; Fischer, R. A.; Muhler, M. *Chem. Commun.* **2005**, *0*, 282-284.
101. Binder, A.; Seipenbusch, M.; Muhler, M.; Kasper, G. *J. Catal.* **2009**, *268*, 150-155.
102. Cristoforetti, G.; Pitzalis, E.; Spiniello, R.; Ishak, R.; Giammanco, F.; Muniz-Miranda, M.; Caporali, S. *Appl. Surf. Sci.* **2012**, *258*, 3289-3297.
103. Mortazavi, S. Z.; Parvin, P.; Reyhani, A.; Golikand, A. N.; Mirershadi, S. *J. Phys. Chem. C* **2011**, *115*, 5049-5057.
104. Hwang, C.-B.; Fu, Y.-S.; Lu, Y.-L.; Jang, S.-W.; Chou, P.-T.; Wang, C. R. C.; Yu, S. J. *J. Catal.* **2000**, *195*, 336-341.
105. Allmond, C. E.; Sellinger, A. T.; Gogick, K.; Fitz-Gerald, J. M. *Appl. Phys. A: Mater. Sci. Process.* **2007**, *86*, 477-480.

106. Fujimoto, T.; Terauchi, S.-y.; Umehara, H.; Kojima, I.; Henderson, W. *Chem. Mater.* **2001**, *13*, 1057-1060.
107. Okitsu, K.; Yue, A.; Tanabe, S.; Matsumoto, H. *Chem. Mater.* **2000**, *12*, 3006-3011.
108. Kijima, N.; Takahashi, Y.; Akimoto, J.; Tsunoda, T.; Uchida, K.; Yoshimura, Y. *Chem. Lett.* **2005**, *34*, 1658-1659.
109. Arul Dhas, N.; Gedanken, A. *J. Mater. Chem.* **1998**, *8*, 445-450.
110. Okitsu, K.; Mizukoshi, Y.; Bandow, H.; Yamamoto, T. A.; Nagata, Y.; Maeda, Y. *J. Phys. Chem. B* **1997**, *101*, 5470-5472.
111. Pan, W.; Zhang, X.; Ma, H.; Zhang, J. *J. Phys. Chem. C* **2008**, *112*, 2456-2461.
112. Wu, C.-C.; Chan, D.-S.; Yang, C.-C.; Chiou, H.-P.; Chen, H.-R.; Lee, C.-L. *J. Electrochem. Soc.* **2011**, *158*, D616-D620.
113. Zhang, P.; Sham, T. K. *Appl. Phys. Lett.* **2003**, *82*, 1778.
114. Liu, J.; He, F.; Gunn, T. M.; Zhao, D.; Roberts, C. B. *Langmuir* **2009**, *25*, 7116-7128.
115. Zhang, Y.; Chang, G.; Liu, S.; Tian, J.; Wang, L.; Lu, W.; Qin, X.; Sun, X. *Catal. Sci. Technol.* **2011**, *1*, 1636-1640.
116. Kou, J.; Varma, R. S. *RSC Adv.* **2012**, *2*, 10283-10290.
117. Chen, J.; Li, Z.; Chao, D.; Zhang, W.; Wang, C. *Mater. Lett.* **2008**, *62*, 692-694.
118. Han, J.; Zhou, Z.; Yin, Y.; Luo, X.; Li, J.; Zhang, H.; Yang, B. *CrystEngComm* **2012**, *14*, 7036-7042.
119. Scott, R. W. J.; Ye, H.; Henriquez, R. R.; Crooks, R. M. *Chem. Mater.* **2003**, *15*, 3873-3878.
120. Zhao, M.; Crooks, R. M. *Angew. Chem., Int. Ed.* **1999**, *38*, 364-366.
121. Li, Z.; Gao, J.; Xing, X.; Wu, S.; Shuang, S.; Dong, C.; Paa, M. C.; Choi, M. M. F. *J. Phys. Chem. C* **2010**, *114*, 723-733.
122. Turkenburg, D. H.; Antipov, A. A.; Thathagar, M. B.; Rothenberg, G.; Sukhorukov, G. B.; Eiser, E. *Phys. Chem. Chem. Phys.* **2005**, *7*, 2237-2240.
123. Mazumder, V.; Sun, S. *J. Am. Chem. Soc.* **2009**, *131*, 4588-4589.

124. Lu, F.; Ruiz, J.; Astruc, D. *Tetrahedron Lett.* **2004**, *45*, 9443-9445.
125. Chen, S.; Huang, K.; Stearns, J. A. *Chem. Mater.* **2000**, *12*, 540-547.
126. Cliffel, D. E.; Zamborini, F. P.; Gross, S. M.; Murray, R. W. *Langmuir* **2000**, *16*, 9699-9702.
127. Zamborini, F. P.; Gross, S. M.; Murray, R. W. *Langmuir* **2001**, *17*, 481-488.
128. Kim, S.-W.; Park, J.; Jang, Y.; Chung, Y.; Hwang, S.; Hyeon, T.; Kim, Y. W. *Nano Lett.* **2003**, *3*, 1289-1291.
129. Tamura, M.; Fujihara, H. *J. Am. Chem. Soc.* **2003**, *125*, 15742-15743.
130. Son, S. U.; Jang, Y.; Yoon, K. Y.; Kang, E.; Hyeon, T. *Nano Lett.* **2004**, *4*, 1147-1151.
131. Drinkel, E.; Souza, F. D.; Fiedler, H. D.; Nome, F. *Curr. Opin. Colloid Interface Sci.* **2013**, *18*, 26-34.
132. Zapp, E.; Souza, F. D.; Souza, B. S.; Nome, F.; Neves, A.; Vieira, I. C. *Analyst* **2013**, *138*, 509-517.
133. Souza, B. S.; Leopoldino, E. C.; Tondo, D. W.; Dupont, J.; Nome, F. *Langmuir* **2012**, *28*, 833-840.
134. Calo, V.; Nacci, A.; Monopoli, A.; Montingelli, F. *J. Org. Chem.* **2005**, *70*, 6040-6044.
135. Yang, X.; Fei, Z.; Zhao, D.; Ang, W. H.; Li, Y.; Dyson, P. J. *Inorg. Chem.* **2008**, *47*, 3292-3297.
136. Zeng, Y.; Wang, Y.; Xu, Y.; Song, Y.; Jiang, J.; Jin, Z. *Catal. Lett.* **2013**, *143*, 200-205.
137. Huang, J.; Jiang, T.; Gao, H.; Han, B.; Liu, Z.; Wu, W.; Chang, Y.; Zhao, G. *Angew. Chem., Int. Ed.* **2004**, *43*, 1397-1399.
138. Oh, S.-K.; Niu, Y.; Crooks, R. M. *Langmuir* **2005**, *21*, 10209-10213.
139. Huang, X.; Wang, Y.; Liao, X.; Shi, B. *Chem. Commun.* **2009**, *0*, 4687-4689.
140. Umpierre, A. P.; Machado, G.; Fecher, G. H.; Morais, J.; Dupont, J. *Adv. Synth. Catal.* **2005**, *347*, 1404-1412.

141. Karousis, N.; Tsotsou, G.-E.; Evangelista, F.; Rudolf, P.; Ragoussis, N.; Tagmatarchis, N. *J. Phys. Chem. C* **2008**, *112*, 13463-13469.
142. Tessonnier, J.-P.; Pesant, L.; Ehret, G.; Ledoux, M. J.; Pham-Huu, C. *Appl. Catal., A* **2005**, *288*, 203-210.
143. Yoon, B.; Wai, C. M. *J. Am. Chem. Soc.* **2005**, *127*, 17174-17175.
144. Kim, J. Y.; Jo, Y.; Kook, S.-K.; Lee, S.; Choi, H. C. *J. Mol. Catal. A: Chemical* **2010**, *323*, 28-32.
145. Scott, R. W. J.; Wilson, O. M.; Crooks, R. M. *Chem. Mater.* **2004**, *16*, 5682-5688.
146. Willis, N. G.; Guzman, J. *Appl. Catal., A* **2008**, *339*, 68-75.
147. Moussa, S.; Abdelsayed, V.; Samy El-Shall, M. *Chem. Phys. Lett.* **2011**, *510*, 179-184.
148. Wang, H.-F.; Kaden, W. E.; Dowler, R.; Sterrer, M.; Freund, H.-J. *Phys. Chem. Chem. Phys.* **2012**, *14*, 11525-11533.
149. Lee, S.-S.; Park, B.-K.; Byeon, S.-H.; Chang, F.; Kim, H. *Chem. Mater.* **2006**, *18*, 5631-5633.
150. Mori, K.; Furubayashi, K.; Okada, S.; Yamashita, H. *RSC Adv.* **2012**, *2*, 1047-1054.
151. Webb, J. D.; MacQuarrie, S.; McEleney, K.; Crudden, C. M. *J. Catal.* **2007**, *252*, 97-109.
152. Komhom, S.; Mekasuwandumrong, O.; Praserttham, P.; Panpranot, J. *Catal. Commun.* **2008**, *10*, 86-91.
153. Kidambi, S.; Bruening, M. L. *Chem. Mater.* **2005**, *17*, 301-307.
154. Feng, H.; Libera, J. A.; Stair, P. C.; Miller, J. T.; Elam, J. W. *ACS Catal.* **2011**, *1*, 665-673.
155. Mori, K.; Miura, Y.; Shironita, S.; Yamashita, H. *Langmuir* **2009**, *25*, 11180-11187.
156. Domine, M. E.; Hernandez-Soto, M. C.; Navarro, M. T.; Perez, Y. *Catal. Today* **2011**, *172*, 13-20.
157. Li, F.; Zhang, Q.; Wang, Y. *Appl. Catal., A* **2008**, *334*, 217-226.

158. Ghiaci, M.; Ansari, F.; Sadeghi, Z.; Gil, A. *Catal. Commun.* **2012**, *21*, 82-85.
159. Drelinkiewicz, A.; Waksmundzka, A.; Makowski, W.; Sobczak, J. W.; Krol, A.; Zieba, A. *Catal. Lett.* **2004**, *94*, 143-156.
160. Ding, J. H.; Gin, D. L. *Chem. Mater.* **2000**, *12*, 22-24.
161. Xing, R.; Liu, Y.; Wu, H.; Li, X.; He, M.; Wu, P. *Chem. Commun.* **2008**, *0*, 6297-6299.
162. Choi, H. R.; Woo, H.; Jang, S.; Cheon, J. Y.; Kim, C.; Park, J.; Park, K. H.; Joo, S. H. *ChemCatChem* **2012**, *4*, 1587-1594.
163. Anderson, K.; Cortinas Fernandez, S.; Hardacre, C.; Marr, P. C. *Inorg. Chem. Commun.* **2004**, *7*, 73-76.
164. Chtchigrovsky, M.; Lin, Y.; Ouchaou, K.; Chaumontet, M.; Robitzer, M.; Quignard, F.; Taran, F. *Chem. Mater.* **2012**, *24*, 1505-1510.
165. Zhang, Z.; Wang, Z. *J. Org. Chem.* **2006**, *71*, 7485-7487.
166. Phan, N. T. S.; Van Der Sluys, M.; Jones, C. W. *Adv. Synth. Catal.* **2006**, *348*, 609-679.
167. Zhao, F.; Bhanage, B. M.; Shirai, M.; Arai, M. *Chem. Eur. J.* **2000**, *6*, 843-848.
168. Thathagar, M. B.; ten Elshof, J. E.; Rothenberg, G. *Angew. Chem., Int. Ed.* **2006**, *45*, 2886-2890.
169. Gaikwad, A. V.; Holuigue, A.; Thathagar, M. B.; ten Elshof, J. E.; Rothenberg, G. *Chem. Eur. J.* **2007**, *13*, 6908-6913.
170. Niu, Z.; Peng, Q.; Zhuang, Z.; He, W.; Li, Y. *Chem. Eur. J.* **2012**, *18*, 9813-9817.
171. Ellis, P. J.; Fairlamb, I. J. S.; Hackett, S. F. J.; Wilson, K.; Lee, A. F. *Angew. Chem., Int. Ed.* **2010**, *49*, 1820-1824.
172. Menzel, K.; Fu, G. C. *J. Am. Chem. Soc.* **2003**, *125*, 3718-3719.
173. Zhao, H.; Wang, Y.; Sha, J.; Sheng, S.; Cai, M. *Tetrahedron* **2008**, *64*, 7517-7523.
174. Pal, A.; Ghosh, R.; Adarsh, N. N.; Sarkar, A. *Tetrahedron* **2010**, *66*, 5451-5458.
175. Stille, J. K. *Angew. Chem., Int. Ed.* **1986**, *25*, 508-524.

176. Kogan, V.; Aizenshtat, Z.; Popovitz-Biro, R.; Neumann, R. *Org. Lett.* **2002**, *4*, 3529-3532.
177. Kröger, N.; Deutzmann, R.; Sumper, M. *Science* **1999**, *286*, 1129-1132.
178. Kröger, N.; Lorenz, S.; Brunner, E.; Sumper, M. *Science* **2002**, *298*, 584-586.
179. Knecht, M. R.; Wright, D. W. *Chem. Commun.* **2003**, *0*, 3038-3039.
180. Sewell, S. L.; Wright, D. W. *Chem. Mater.* **2006**, *18*, 3108-3113.
181. Bhandari, R.; Knecht, M. R. *Catal. Sci. Technol.* **2012**, *2*, 1360-1366.
182. Reetz, M. T.; Breinbauer, R.; Wanninger, K. *Tetrahedron Lett.* **1996**, *37*, 4499-4502.
183. Li, Y.; El-Sayed, M. A. *J. Phys. Chem. B* **2001**, *105*, 8938-8943.
184. Gallon, B. J.; Kojima, R. W.; Kaner, R. B.; Diaconescu, P. L. *Angew. Chem., Int. Ed.* **2007**, *46*, 7251-7254.
185. Zhou, P.; Wang, H.; Yang, J.; Tang, J.; Sun, D.; Tang, W. *RSC Adv.* **2012**, *2*, 1759-1761.
186. Pittelkow, M.; Moth-Poulsen, K.; Boas, U.; Christensen, J. r. B. *Langmuir* **2003**, *19*, 7682-7684.
187. Ornelas, C.; Ruiz, J.; Salmon, L.; Astruc, D. *Adv. Synth. Catal.* **2008**, *350*, 837-845.
188. Reetz, M. T.; Lohmer, G. *Chem. Commun.* **1996**, *0*, 1921-1922.
189. Yeung, L. K.; Crooks, R. M. *Nano Letters* **2000**, *1*, 14-17.
190. Yeung, L. K.; Lee Jr, C. T.; Johnston, K. P.; Crooks, R. M. *Chem. Commun.* **2001**, *0*, 2290-2291.
191. Diallo, A. K.; Ornelas, C.; Salmon, L.; Ruiz Aranzaes, J.; Astruc, D. *Angew. Chem., Int. Ed.* **2007**, *46*, 8644-8648.
192. Narayanan, R.; El-Sayed, M. A. *J. Phys. Chem. B* **2005**, *109*, 12663-12676.
193. Crabtree, R. H. *The Organometallic Chemistry of the Transition Metals*. 3rd ed.; John Wiley & Sons: New York, 2001.
194. Reetz, M. T.; de Vries, J. G. *Chem. Commun.* **2004**, *0*, 1559-1563.

195. Srimani, D.; Sawoo, S.; Sarkar, A. *Org. Lett.* **2007**, *9*, 3639-3642.
196. Xu, S.; Yang, Q. *J. Phys. Chem. C* **2008**, *112*, 13419-13425.
197. Dickerson, M. B.; Jones, S. E.; Cai, Y.; Ahmad, G.; Naik, R. R.; Kröger, N.; Sandhage, K. H. *Chem. Mater.* **2008**, *20*, 1578-1584.
198. Lee, S.-W.; Mao, C.; Flynn, C. E.; Belcher, A. M. *Science* **2002**, *296*, 892-895.
199. Naik, R. R.; Stringer, S. J.; Agarwal, G.; Jones, S. E.; Stone, M. O. *Nat. Mater.* **2002**, *1*, 169-172.
200. Slocik, J. M.; Knecht, M. R.; Wright, D. W. *The Encyclopedia of Nanoscience and Nanotechnology*, Nalwa, H. S., Ed. American Scientific Publishers: Stevenson Ranch, CA, 2004; pp 293 - 308.
201. Dickerson, M. B.; Sandhage, K. H.; Naik, R. R. *Chem. Rev.* **2008**, *108*, 4935-4978.
202. Ahmad, G.; Dickerson, M. B.; Cai, Y.; Jones, S. E.; Ernst, E. M.; Vernon, J. P.; Haluska, M. S.; Fang, Y.; Wang, J.; Subramanyam, G.; Naik, R. R.; Sandhage, K. H. *J. Am. Chem. Soc.* **2007**, *130*, 4-5.
203. Nam, K. T.; Kim, D.-W.; Yoo, P. J.; Chiang, C.-Y.; Meethong, N.; Hammond, P. T.; Chiang, Y.-M.; Belcher, A. M. *Science* **2006**, *312*, 885-888.
204. Sarikaya, M.; Tamerler, C.; Jen, A. K. Y.; Schulten, K.; Baneyx, F. *Nat. Mater.* **2003**, *2*, 577-585.
205. Reiss, B. D.; Mao, C.; Solis, D. J.; Ryan, K. S.; Thomson, T.; Belcher, A. M. *Nano Lett.* **2004**, *4*, 1127-1132.
206. Slocik, J. M.; Stone, M. O.; Naik, R. R. *Small* **2005**, *1*, 1048-1052.
207. Nam, K. T.; Lee, Y. J.; Krauland, E. M.; Kottmann, S. T.; Belcher, A. M. *ACS Nano* **2008**, *2*, 1480-1486.
208. Slocik, J. M.; Govorov, A. O.; Naik, R. R. *Angew. Chem., Int. Ed.* **2008**, *120*, 5415-5419.
209. Slocik, J. M.; Naik, R. R. *Advanced Materials* **2006**, *18*, 1988-1992.
210. Slocik, J. M.; Zabinski, J. S.; Phillips, D. M.; Naik, R. R. *Small* **2008**, *4*, 548-551.
211. Slocik, J. M.; Govorov, A. O.; Naik, R. R. *Angew. Chem., Int. Ed.* **2008**, *47*, 5335-5339.

212. Espinet, P.; Echavarren, A. M. *Angew. Chem., Int. Ed.* **2004**, *43*, 4704-4734.
213. Pandey, R. B.; Heinz, H.; Feng, J.; Farmer, B. L.; Slocik, J. M.; Drummy, L. F.; Naik, R. R. *Phys. Chem. Chem. Phys.* **2009**, *11*, 1989-2001.
214. Knecht, M. R.; Weir, M. G.; Frenkel, A. I.; Crooks, R. M. *Chem. Mater.* **2008**, *20*, 1019-1028.
215. Slocik, J. M.; Moore, J. T.; Wright, D. W. *Nano Lett.* **2002**, *2*, 169-173.
216. Creighton, J. A.; Eadon, D. G. *J. Chem. Soc., Faraday Trans.* **1991**, *87*, 3881-3891.
217. Kim, Y.-G.; Oh, S.-K.; Crooks, R. M. *Chem. Mater.* **2004**, *16*, 167-172.
218. Nicolaou, K. C.; Bulger, P. G.; Sarlah, D. *Angew. Chem., Int. Ed.* **2005**, *44*, 4442-4489.
219. Anthony, J. E. *Angew. Chem., Int. Ed.* **2008**, *47*, 452-483.
220. Energy, U. S. D. o. *Basic Research Needs: Catalysis for Energy*; 2007.
221. Knecht, M. R.; Pacardo, D. B. *Anal. Bioanal. Chem.* **2010**, *397*, 1137 - 1155.
222. Sethi, M.; Pacardo, D. B.; Knecht, M. R. *Langmuir* **2010**, *26*, 15121-15134.
223. Mizugaki, T.; Murata, M.; Fukubayashi, S.; Mitsudome, T.; Jitsukawa, K.; Kaneda, K. *Chem. Commun.* **2008**, *0*, 241-243.
224. Scott, R. W. J.; Wilson, O. M.; Crooks, R. M. *J. Phys. Chem. B* **2005**, *109*, 692-704.
225. Dahl, J. A.; Maddux, B. L. S.; Hutchison, J. E. *Chem. Rev.* **2007**, *107*, 2228-2269.
226. Energy, U. S. D. o. *New Science for a Secure and Sustainable Energy Future*; 2008.
227. Lee, Y. J.; Lee, Y.; Oh, D.; Chen, T.; Ceder, G.; Belcher, A. M. *Nano Lett.* **2010**, *10*, 2433-2440.
228. Lee, Y. J.; Yi, H.; Kim, W.-J.; Kang, K.; Yun, D. S.; Strano, M. S.; Ceder, G.; Belcher, A. M. *Science* **2009**, *324*, 1051-1055.
229. Alimardanov, A.; Schmieder-van de Vondervoort, L.; de Vries, A. H. M.; de Vries, J. G. *Adv. Synth. Catal.* **2004**, *346*, 1812-1817.

230. de Vries, A. H. M.; Mulders, J. M. C. A.; Mommers, J. H. M.; Henderickx, H. J. W.; de Vries, J. G. *Org. Lett.* **2003**, *5*, 3285-3288.
231. de Vries, A. H. M.; Parlevliet, F. J.; Schmieder-van de Vondervoort, L.; Mommers, J. H. M.; Henderickx, H. J. W.; Walet, M. A. M.; de Vries, J. G. *Adv. Synth. Catal.* **2002**, *344*, 996-1002.
232. de Vries, J. G. *Dalton Trans.* **2006**, 421-429.
233. Narayanan, R.; El-Sayed, M. A. *J. Am. Chem. Soc.* **2003**, *125*, 8340-8347.
234. Chan, W. C.; White, P. D. *Fmoc Solid Phase Peptide Synthesis: A Practical Approach*. Oxford University Press: New York, 2000.
235. Cimpoa, G. V.; Radulescu, C.; Popescu, I. V.; Dulama, I. D.; Bancuta, I.; Gheboianu, A. I.; Cimpoa, M.; Staicu, L. AIP Conf. Proc., 2009; pp 415-420.
236. Park, J. C.; Heo, E.; Kim, A.; Kim, M.; Park, K. H.; Song, H. *J. Phys. Chem. C* **2011**, *115*, 15772-15777.
237. Tatumi, R.; Akita, T.; Fujihara, H. *Chem. Commun.* **2006**, 3349-3351.
238. Coker, V. S.; Bennett, J. A.; Telling, N. D.; Henkel, T.; Charnock, J. M.; van der Laan, G.; Patrick, R. A. D.; Pearce, C. I.; Cutting, R. S.; Shannon, I. J.; Wood, J.; Arenholz, E.; Lyon, I. C.; Lloyd, J. R. *ACS Nano* **2010**, *4*, 2577-2584.
239. Li, J.-H.; Tang, B.-X.; Tao, L.-M.; Xie, Y.-X.; Liang, Y.; Zhang, M.-B. *J. Org. Chem.* **2006**, *71*, 7488-7490.
240. Kidambi, S.; Dai, J.; Li, J.; Bruening, M. L. *J. Am. Chem. Soc.* **2004**, *126*, 2658-2659.
241. Esumi, K.; Isono, R.; Yoshimura, T. *Langmuir* **2004**, *20*, 237-243.
242. He, F.; Zhao, D. *Environ. Sci. Technol.* **2005**, *39*, 3314-3320.
243. Li, S.; Fang, Y.-L.; Romanczuk, C. D.; Jin, Z.; Li, T.; Wong, M. S. *Appl. Catal., B* **2012**, *125*, 95-102.
244. Nutt, M. O.; Hughes, J. B.; Wong, M. S. *Environ. Sci. Technol.* **2005**, *39*, 1346-1353.
245. Bhandari, R.; Coppage, R.; Knecht, M. R. *Catal. Sci. Technol.* **2012**, *2*, 256-266.
246. Zhang, Z.; Fu, Q.; Li, X.; Huang, X.; Xu, J.; Shen, J.; Liu, J. *J. Biol. Inorg. Chem.* **2009**, *14*, 653-662.

247. Budarin, V. L.; Clark, J. H.; Luque, R.; Macquarrie, D. J.; White, R. J. *Green Chem.* **2008**, *10*, 382-387.
248. Chen, Z.; Cui, Z. M.; Li, P.; Cao, C. Y.; Hong, Y. L.; Wu, Z.; Song, W. G. *J. Phys. Chem. C* **2012**, *116*, 14986-14991.
249. Malysheva, Y. B.; Gushchin, A. V.; Mei, Y.; Lu, Y.; Ballauff, M.; Proch, S.; Kempe, R. *Eur. J. Inorg. Chem* **2008**, 379-383.
250. Yang, C.; Manocchi, A. K.; Lee, B.; Yi, H. *J. Mater. Chem.* **2011**, *21*, 187-194.
251. Pacardo, D. B.; Slocik, J. M.; Kirk, K. C.; Naik, R. R.; Knecht, M. R. *Nanoscale* **2011**, *3*, 2194-2201.
252. Coppage, R.; Slocik, J. M.; Briggs, B. D.; Frenkel, A. I.; Heinz, H.; Naik, R. R.; Knecht, M. R. *Journal of the American Chemical Society* **2011**, *133*, 12346-12349.
253. Astruc, D.; Lu, F.; Aranzaes, J. R. *Angew. Chem., Int. Ed.* **2005**, *44*, 7852-7872.
254. Xu, J.; Wilson, A. R.; Rathmell, A. R.; Howe, J.; Chi, M.; Wiley, B. J. *ACS Nano* **2011**, *5*, 6119-6127.
255. Darwent, B. d. *Bond Dissociation Energies in Simple Molecules*. U.S. Department of Commerce, National Bureau of Standards: Washington, DC, 1970.
256. Bhattacharjee, S.; Bruening, M. L. *Langmuir* **2008**, *24*, 2916-2920.
257. Kidambi, S.; Bruening, M. L. *Chem. Mater.* **2004**, *17*, 301-307.
258. Bezverkhyy, I.; Afanasiev, P.; Danot, M. *J. Phys. Chem. B* **2004**, *108*, 7709-7715.
259. Bezverkhyy, I.; Afanasiev, P.; Lacroix, M. *J. Catal.* **2005**, *230*, 133-139.
260. Sharma, R. K.; Rana, B. S.; Varma, D.; Kumar, R.; Tiwari, R.; Jha, M. K.; Sinha, A. K. *Microporous Mesoporous Mater.* **2012**, *155*, 177-185.
261. Yi, Y.; Zhang, B.; Jin, X.; Wang, L.; Williams, C. T.; Xiong, G.; Su, D.; Liang, C. *J. Mol. Catal. A: Chem.* **2011**, *351*, 120-127.
262. Hansen, H. A.; Varley, J. B.; Peterson, A. A.; Nørskov, J. K. *J. Phys. Chem. Lett.* **2013**, *4*, 388-392.
263. Iwakura, C.; Takezawa, S.; Inoue, H. *J. Electroanal. Chem.* **1998**, *459*, 167-169.
264. Wong, K.-T.; Hung, T. S.; Lin, Y.; Wu, C.-C.; Lee, G.-H.; Peng, S.-M.; Chou, C. H.; Su, Y. O. *Org. Lett.* **2002**, *4*, 513-516.

265. Tomina, N. N.; Nikul'shin, P. A.; Tsvetkov, V. S.; Pimerzin, A. A. *Kinet. Catal.* **2009**, *50*, 220-227.
266. Bonazzi, S.; Eidam, O.; Güttinger, S.; Wach, J.-Y.; Zemp, I.; Kutay, U.; Gademann, K. *J. Am. Chem. Soc.* **2010**, *132*, 1432-1442.
267. Khin, M. M.; Nair, A. S.; Babu, V. J.; Murugan, R.; Ramakrishna, S. *Energy Environ. Sci.* **2012**, *5*, 8075-8109.
268. Bastús, N. G.; Comenge, J.; Puentes, V. *Langmuir* **2011**, *27*, 11098-11105.
269. Focsan, M.; Gabudean, A. M.; Canpean, V.; Maniu, D.; Astilean, S. *Mater. Chem. Phys.* **2011**, *129*, 939-942.
270. Lara, P.; Philippot, K.; Chaudret, B. *ChemCatChem* **2013**, *5*, 28-45.
271. Crooks, R. M.; Zhao, M.; Sun, L.; Chechik, V.; Yeung, L. K. *Acc. Chem. Res.* **2001**, *34*, 181-190.
272. Qu, K.; Wu, L.; Ren, J.; Qu, X. *ACS Appl. Mater. Interfaces* **2012**, *4*, 5001-5009.
273. Slocik, J. M.; Naik, R. R. *Adv. Mater.* **2006**, *18*, 1988-1992.
274. Bhandari, R.; Pacardo, D. B.; Bedford, N. M.; Naik, R. R.; Knecht, M. R. *J. Phys. Chem. C* **2013**, *accepted*.